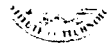
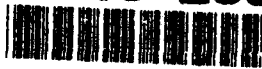


AD-A243 288



CAMBRIDGE, MASSACHUSETTS 02139-4307

RESEARCH LABORATORY of ELECTRONICS
MITTS INSTITUTE OF TECHNOLOGY

November 15, 1991

DTIC
ELECTE
NOV 21 1991
S C D

Dr. Charles A. Luther, Code 1121RS
Scientific Officer
Office of the Chief of Naval Research
800 North Quincy Street
Arlington, VA 22217

Re: Contract N00014-89-J-1107

Type of Material: Annual Technical Report

Title: Active and Passive Remote Sensing of Ice

Submitted By: J.A. Kong

Period Covered: October 1, 1990 - September 30, 1991

No. of copies: Three plus form 298

Distribution: Navy Distribution List (9)

Mary S. Greene
RLE Publications Office
Room 36-412

cc: J.A. Kong (1)
D. Duffy
A.F. Favaloro, E19-702
File (1)

OSP 71367

DISTRIBUTION STATEMENT A

Approved for public release;
Distribution Unlimited

91-16073
[Barcode]

91 1120 059

| REPORT DOCUMENTATION PAGE | | | Form Approved OMB No. 0704-0188 | |
|---|---|--|------------------------------------|--|
| <small>Public reporting burden for this collection of information is estimated to average 1 hour per response, including the time for reviewing instructions, searching existing data sources, gathering and maintaining the data needed, and completing and reviewing the collection of information. Send comments regarding this burden estimate or any other aspect of this collection of information, including suggestions for reducing this burden, to Washington Headquarters Services, Directorate for Information Operations and Reports, 1215 Jefferson Davis Highway, Suite 1204, Arlington, VA 22202-4302, and to the Office of Management and Budget, Paperwork Reduction Project (0704-0188), Washington, DC 20503.</small> | | | | |
| 1. AGENCY USE ONLY (Leave blank) | 2. REPORT DATE 11-15-91 | 3. REPORT TYPE AND DATES COVERED Annual 10/1/90 - 9/30/91 | | |
| 4. TITLE AND SUBTITLE Active and Passive Remote Sensing of Ice | | 5. FUNDING NUMBERS N00014-89-J-1107 | | |
| 6. AUTHOR(S) Prof. J.A. Kong | | 425F023-03 | | |
| 7. PERFORMING ORGANIZATION NAME(S) AND ADDRESS(ES) Research Laboratory of Electronics Massachusetts Institute of Technology 77 Massachusetts Avenue Cambridge, MA 02139 | | 8. PERFORMING ORGANIZATION REPORT NUMBER | | |
| 9. SPONSORING / MONITORING AGENCY NAME(S) AND ADDRESS(ES) Office of Naval Research 800 North Quincy Street Arlington, VA 22217 | | 10. SPONSORING / MONITORING AGENCY REPORT NUMBER | | |
| 11. SUPPLEMENTARY NOTES The view, opinions and/or findings contained in this report are those of the author(s) and should not be construed as an official Department of the Army position, policy, or decision, unless so designated by other documentation. | | | | |
| 12a. DISTRIBUTION / AVAILABILITY STATEMENT Approved for public release; distribution unlimited. | | 12b. DISTRIBUTION CODE | | |
| 13. ABSTRACT (Maximum 200 words) Work by Prof. J.A. Kong and his collaborators is summarized here | | | | |
| 14. SUBJECT TERMS | | 15. NUMBER OF PAGES | | |
| | | 16. PRICE CODE | | |
| 17. SECURITY CLASSIFICATION OF REPORT UNCLASSIFIED | 18. SECURITY CLASSIFICATION OF THIS PAGE UNCLASSIFIED | 19. SECURITY CLASSIFICATION OF ABSTRACT UNCLASSIFIED | 20. LIMITATION OF ABSTRACT UL | |

ANNUAL REPORT

Title: ACTIVE AND PASSIVE REMOTE SENSING OF ICE

Sponsored by: Department of the Navy
Office of Naval Research

Contract number: N00014-89-J-1107

Research Organization: Center for Electromagnetic Theory and Applications
Research Laboratory of Electronics
Massachusetts Institute of Technology

OSP number: 71367

Principal Investigator: J. A. Kong

Author of Report: H. C. Han

Period covered: October 1, 1990 — September 30, 1991



| | |
|--------------------|-------------------------|
| Accession For | |
| NTIS GRA&I | |
| DTIC TAB | |
| Unannounced | |
| Justification | |
| By | |
| Distribution/ | |
| Availability Codes | |
| Dist | Avail and/or Special |
| A-1 | |

ACTIVE AND PASSIVE REMOTE SENSING OF ICE

ANNUAL REPORT

This annual report covers research under the sponsorship of the ONR contract N00014-89-J-1107 from October 1, 1990 to September 30, 1991. We have published 15 journal and conference papers and 3 student theses during this period.

1. Multi-Layer Random Medium Model for Sea Ice

Fully polarimetric scattering of electromagnetic waves from snow and ice is studied with a multi-layered random medium model and applied to interpret experimental data obtained under laboratory controlled conditions such as CRRELEX. The snow layer is modeled as an isotropic random medium. The sea ice is described as an anisotropic random medium due to the nonspherical shape of brine inclusions. The underlying sea water is considered as a homogeneous half-space. The random media in both layers are characterized by three-dimensional correlation functions with variances and correlation lengths corresponding to the fluctuation strengths and the physical geometries of the inhomogeneities, respectively. The strong fluctuation theory is used to calculate the effective permittivities of the random media. The distorted Born approximation is then employed to obtain the covariance matrix which represents the fully polarimetric scattering properties of the snow-ice media. It has been shown that the polarimetric covariance matrix contains more information than the conventional scattering coefficients on the remotely sensed media.

In saline ice sheets under quiescent condition, the background ice grows in columnar form and saline water is trapped between ice platelets in the form of brine inclusions

which are usually ellipsoidal. The ice tends to grow vertically downward rendering the ellipsoidal inclusions aligned preferably in the vertical direction and the crystallographic C axes parallel to the horizontal plane. In this case, the C axes are, however, random in azimuthal direction. The strong fluctuation theory is extended to account for vertically aligned ellipsoidal brine inclusions with C axes randomly oriented in the horizontal direction. The brine inclusions are described by three-dimensional local correlation functions. The configuration average over the azimuthal orientation angles is carried out in the process of deriving the global correlation tensor. The distorted Born approximation is applied to obtain the covariance matrix for the multi-layered snow-ice configuration. The theoretical results show non-zero cross-polarized returns under the first-order distorted Born approximation. We have also compared the results with experimental data obtained by the US Army Cold Regions Research and Engineering Laboratory (CRREL).

In sea ice, the scatterers can have various shapes, sizes, and permittivities. We have also investigated the modeling of radar backscatter from random media with multiple scatterer species. We consider each type of scatterers as a species which can take on a shape, size, and complex permittivity different from other species. The multiple species in the random medium are considered as randomly oriented ellipsoids and described by multiple three-dimensional ellipsoidal local correlation functions. The variances and correlation lengths of the correlation functions characterize the fluctuation strengths and the physical geometries of each species of scatterers. The effective permittivity of the random medium is derived under the strong fluctuation theory and the polarimetric scattering coefficients are calculated for the layer configuration with the distorted Born approximation. Due to the non-spherical shape and the random orientation of the scatterers, the correlation coefficient between the HH and VV returns has a magnitude different from unity and a small phase angle. The scattering coefficients are also used to calculate the Mueller matrix for synthesis of polarization signatures. The co-polarized signature of the random medium has a rather straight distortion track and a recognizable pedestal.

2. Polarimetric Radar Calibration

Accurate calibration of polarimetric radar systems is essential for the polarimetric remote sensing of earth terrain. Polarimetric calibration algorithms using in-scene reflectors and distributed targets are studied. The transmitting and receiving ports of the polarimetric radar are modeled by two unknown polarization transfer matrices. These unknown matrices are determined using the measured scattering matrices from the calibration targets. For the case of polarimetric calibration using three in-scene reflectors, a Polarization-basis Transformation (PT) technique is introduced to find out a new transmitting and receiving polarization basis under which the scattering matrices of the calibration targets will fall into one of six simpler sets. The calibration solution can then be solved easily in the new polarization basis and converted to obtain the solution in the original polarization basis. The uniqueness of polarimetric calibration using three targets is addressed for all possible target combinations. The PT technique can also be applied to the polarimetric calibration using a combination of arbitrary in-scene reflectors and distributed targets. The effect of misalignment of calibration targets and the sensitivity of polarimetric calibration algorithms to the noise are illustrated by investigating several sets of calibration targets.

3. Classification Studies of Polarimetric SAR Images

We have studied the SAR image classification by using the neural network methods. Supervised methods, including both conventional Maximum Likelihood (ML) and more recent multi-layer perceptron neural network classifiers have yielded higher accuracy than unsupervised techniques, but suffer from the need for human interaction to pre-determine classes and training regions. In contrast, unsupervised methods determine classes automatically, but generally show limited ability to accurately divide terrain into natural

classes. We introduced a new terrain classification technique to discriminate sea ice signatures in polarimetric SAR images by utilizing unsupervised neural networks to provide automatic classification, but employing an iterative algorithm which overcomes the poor accuracy of other unsupervised techniques.

Several types of unsupervised neural networks are first applied to the classification of SAR images, and the results are compared with those of more conventional unsupervised methods. Neural network approaches include Adaptive Resonance theory (ART), Learning Vector Quantization (LVQ), and Kohonen's self-organizing feature map. Conventional classifiers utilized are the migrating means clustering algorithm and the K-means clustering method. Preprocessing is performed with the SAR images to reduce speckle noise and stabilize the training process for the neural networks. Results after preprocessing show that LVQ and Kohonen's self-organizing feature map outperform the conventional unsupervised classifiers, but are still inferior to supervised methods.

To overcome this poor accuracy, an iterative algorithm is constructed where the SAR image is reclassified using a Maximum Likelihood (ML) classifier. Training of the ML classifier is performed using a training data set first classified by the above unsupervised method, thus, requiring no human intervention, and preserving the unsupervised nature of the overall classification scheme. The process is then repeated iteratively, training a second ML classifier using data classified by the first. It is shown that this algorithm converges rapidly, and significantly improves classification accuracy. Performance after convergence is seen to be comparable to that obtained with a supervised ML classifier, while maintaining the advantages of an unsupervised technique.

The unsupervised and iterative techniques developed have been applied to the polarimetric SAR images of Beaufort sea ice acquired by the C-, L-, and P-band SAR instruments of Jet Propulsion Laboratory. The results obtained with the new algorithms

are compared with the results obtained with other techniques by classifying terrain features in polarimetric SAR images.

4. K-Distribution and Polarimetric Terrain Radar Clutter

A multivariate K-distribution has been developed to model the statistics of fully polarimetric radar data from earth terrain with polarizations HH, HV, VH, and VV. In this approach, correlated polarizations of radar signals, as characterized by a covariance matrix, are treated as the sum of N n-dimensional random vectors; N obeys the negative binomial distribution with a parameter α and mean \bar{N} . Subsequently, an n-dimensional K-distribution, with either zero or nonzero mean, is developed in the limit of infinite \bar{N} or illuminated area. The probability density function (PDF) of the K-distributed vector normalized by its Euclidean norm is independent of the parameter α and is the same as that derived from a zero-mean Gaussian-distributed random vector. The above model is well supported by experimental data provided by MIT Lincoln Laboratory and the Jet Propulsion Laboratory in the form of polarimetric measurements. The results are illustrated by comparing the higher-order normalized intensity moments and cumulative density functions (CDF) of the experimental data with theoretical results of the K-distribution.

5. Composite Volume and Surface Scattering Model

Among the various theoretical models applied to study the electromagnetic wave scatterings from geophysical terrain, such as snow and ice, the radiative transfer theory has drawn intensive attention in the microwave remote sensing society during the past years. In most of the scattering models, the volume scattering and the surface scattering effects have been investigated separately. Recently, there has been a growing interest in the construction of composite models which can take into account both types of scattering.

We derived the first order iterative solution to the vector radiative transfer equations for a two-layer medium with a diffuse top boundary and an irregular bottom boundary of Gaussian roughness. The Kirchhoff approximation and the geometrical optics approach with shadowing correction are used in formulating the boundary conditions. To demonstrate the utilities of the theory, randomly oriented spheroidal discrete scatterer model is used to calculate the backscattering coefficients from soybean field in different growing stages and compared to the experimental measurements. Good agreement has been achieved for both the co-polarized and the cross-polarized data. It is observed that the presence of the rough surface can significantly enhance the backscattering at small incident angles and increase the cross-polarized returns. The polarization signatures calculated based on the Mueller matrix show a straight distortion track and an observable pedestal. Numerical comparison to the backscattering coefficients calculated by using planar bottom boundary conditions with or without the incoherent addition of the rough surface effects are also made.

6. Polarimetric Passive Remote Sensing

The concept of polarimetry in active remote sensing is extended to passive remote sensing. The potential use of the third and fourth Stokes parameters U and V , which play an important role in polarimetric active remote sensing, is demonstrated for passive remote sensing. It is shown that, by the use of the reciprocity principle, the polarimetric parameters of passive remote sensing can be obtained through the solution of the associated direct scattering problem. In particular, the full polarimetric information, including the corresponding brightness temperatures of U and V , can be obtained from the solution of the direct scattering problem for four different polarizations of the incident wave. These ideas are applied to study polarimetric passive remote sensing of periodic surfaces. The solution of the direct scattering problem is obtained by an integral equation formulation. Incidence on a penetrable, lossy, medium is considered. Since the kernels of the integral equations are the periodic Green's functions and their normal derivatives on the surface,

rapid evaluation of the slowly convergent series associated with these functions is observed to be critical for the feasibility of the method. The study has shown that the brightness temperature of the Stokes parameter U can be significant in passive remote sensing. Values as high as 50 K are observed for certain configurations.

To demonstrate the use of polarimetry in passive remote sensing of azimuthally asymmetric features on a terrain surface, an experiment was designed and implemented. A triangular corrugation pattern was made on the sandy soil surface. Polarimetric brightness temperatures are measured with horizontal, vertical, and 45° polarization orientations for various observation angles. From the measured temperatures, absolute values as high as 30–40 K of the third Stokes brightness temperatures are observed. A theoretical analysis of the data indicates that the high values of U are caused by the azimuthal asymmetry on the remotely sensed soil surface. It is also observed from the experiment that the brightness temperatures for all three Stokes parameters vary as the observation direction varies from being parallel to the surface row structure to being perpendicular to the row structure. The significant implication of this experiment is that the surface asymmetry can be detected with a measurement of U at a single azimuthal angle.

PUBLICATIONS SPONSORED BY THE ONR CONTRACT:

Polarimetric passive remote sensing of periodic surfaces (M. E. Veysoglu, H. A. Yueh, R. T. Shin, and J. A. Kong), *J. Electromag. Waves Applic.*, Vol. 5, No. 3, 267-280, 1991.

Polarimetric passive remote sensing of a periodic soil surface: Microwave measurements and analysis (S. V. Nghiem, M. E. Veysoglu, J. A. Kong, R. T. Shin, K. O'Neill, and A. W. Lohanick), accepted for publication in *J. Electromag. Waves Applic.*, 1991.

Application of neural network to polarimetric SAR image classification (Y. Hara, R. G. Atkins, S. H. Yueh, R. T. Shin, J. A. Kong, and R. Kwok), *Progress in Electromag. Research Symposium*, Cambridge, Massachusetts, July 1-5, 1991.

Multiple ellipsoidal species in layer random medium model for polarimetric remote sensing (S. V. Nghiem, J. A. Kong, R. T. Shin, and T. Le Toan), *Progress in Electromag. Research Symposium*, Cambridge, Massachusetts, July 1-5, 1991.

Polarimetric passive remote sensing of an azimuthally asymmetric periodic soil surface (S. V. Nghiem, M. E. Veysoglu, J. A. Kong, R. T. Shin, K. O'Neill, and A. Lohanick), *Progress in Electromag. Research Symposium*, Cambridge, Massachusetts, July 1-5, 1991.

Polarimetric passive remote sensing of periodic surfaces (M. E. Veysoglu, H. A. Yueh, R. T. Shin, and J. A. Kong), *Progress in Electromag. Research Symposium*, Cambridge, Massachusetts, July 1-5, 1991.

Analytical solution of the vector radiative transfer equation with rough surface boundary condition (H. C. Han, J. A. Kong, S. V. Nghiem, and T. Le Toan), *Progress in Electromag. Research Symposium*, Cambridge, Massachusetts, July 1-5, 1991.

External calibration of polarimetric radars using point and distributed targets (S. H. Yueh, J. A. Kong, and R. T. Shin), *Second Annual JPL Airborne Geoscience Workshop*, JPL, Pasadena, CA, May 20-24, 1991

Application of neural networks to radar image classification (Y. Hara, R. G. Atkins, S. H. Yueh, R. T. Shin, and J. A. Kong), submitted for publication in *IEEE Trans. Geoscience Remote Sensing*, 1991.

K-distribution and multi-frequency polarimetric terrain radar clutter (H. A. Yueh, J. A. Kong, R. T. Shin, H. A. Zebker, and T. Le Toan), *J. Electromag. Waves Applic.*, Vol. 5, No. 1, 1-15, 1991.

Calibration of polarimetric radars using in-scene reflectors (S. H. Yueh, J. A. Kong, and R. T. Shin), *Progress In Electromag. Research*, edited by J. A. Kong, Chapter 9, Vol. 3, 451-510, Elsevier, New York, 1990.

Classification and maximum contrast of earth terrain using polarimetric synthetic aperture radar images (J. A. Kong, S. H. Yueh, H. H. Lim, R. T. Shin, and J. J. van Zyl), *Progress*

In Electromag. Research, edited by J. A. Kong, Chapter 6, Vol. 3, 327-370, Elsevier, New York, 1990.

Scattering from randomly oriented scatterers with strong permittivity fluctuations (H. A. Yueh, R. T. Shin, and J. A. Kong), *J. Electromag. Waves Applic.*, Vol. 4, No. 10, 983-1004, 1990.

Polarimetric remote sensing of geophysical media with layer random medium model (S. V. Nghiem, M. Borgeaud, J. A. Kong, and R. T. Shin), *Progress in Electromag. Research*, edited by J. A. Kong, Chapter 1, Vol. 3, 1-73, Elsevier, 1990.

Theoretical models and experimental measurements for polarimetric remote sensing of snow and sea ice (S. V. Nghiem, J. A. Kong, R. T. Shin, H. A. Yueh, and R. Onstott), *URSI International Commission F meeting*, Hyannis, Massachusetts, May 1st-18, 1990.

Calibration of polarimetric radars using in-scene reflectors (S. H. Yueh, J. A. Kong, and R. T. Shin), *10th International Geoscience & Remote Sensing Symposium*, College Park, Maryland, May 20-24, 1990.

Correlation function for a random collection of discrete scatterers (H. H. Lim, S. H. Yueh, R. T. Shin, and J. A. Kong), *10th International Geoscience & Remote Sensing Symposium*, College Park, Maryland, May 20-24, 1990.

Statistical modeling for polarimetric remote sensing of earth terrain (S. H. Yueh, J. A. Kong, R. T. Shin, and H. A. Zebker), *10th International Geoscience & Remote Sensing Symposium*, College Park, Maryland, May 20-24, 1990.

Study of polarimetric response of sea ice with layered random medium model (S. V. Nghiem, J. A. Kong, and R. T. Shin), *10th International Geoscience & Remote Sensing Symposium*,

Electromagnetic wave modeling for remote sensing (S. V. Nghiem, J. A. Kong, and T. Le Toan), *International Conference on Directions in Electromagnetic Wave Modeling*, New York, October 22-24, 1990.

K-distribution and polarimetric terrain radar clutter (S. H. Yueh, J. A. Kong, J. K. Jao, R. T. Shin, H. A. Zebker, T. Le Toan, and H. Öttl), *Progress in Electromag. Research*, edited by J. A. Kong, Chapter 4, Vol. 3, 237-275, Elsevier, 1990.

Calibration of polarimetric radar using in-scene reflectors (H. A. Yueh, J. A. Kong, R. M. Barnes, and R. T. Shin), *J. Electromag. Waves Applic.*, Vol. 4, No. 1, 27-48, 1990.

Application of three-layer random medium model for microwave remote sensing of snow-covered sea ice (F. C. Lin, J. A. Kong, and R. T. Shin), *J. Geophysical Research*, 1989.

Classification of earth terrain using synthetic aperture radar images (H. H. Lim, A. A. Swartz, H. A. Yueh, J. A. Kong, R. T. Shin, and J. J. van Zyl), *J. Geophysical Research*, Vol. 94, No. B6, 7049-7057, June 10, 1989.

Radiative transfer theory for active remote sensing of two-layer random medium (R. T. Shin and J. A. Kong), *Progress In Electromag. Research*, Elsevier, New York, Vol. 1, Chapter 5, 359-417, 1989.

Scattering from randomly perturbed periodic and quasiperiodic surfaces (H. A. Yueh, R. T. Shin, and J. A. Kong), *Progress In Electromag. Research*, Elsevier, New York, Vol. 1, Chapter 4, 297-358, 1989.

Contrast and classification studies of polarimetric SAR images for remote sensing of earth terrain (H. H. Lim, H. A. Yueh, J. A. Kong, R. T. Shin, and J. J. van Zyl), *Progress in Electromag. Research Symposium*, Boston, Massachusetts, July 25-27, 1989.

K-distribution and polarimetric terrain radar clutter (H. A. Yueh, J. A. Kong, J. K. Jao, R. T. Shin, and L. M. Novak), *Progress in Electromag. Research Symposium*, Boston, Massachusetts, July 25-26, 1989.

Calibration of polarimetric radars using in-scene reflectors (H. A. Yueh, J. A. Kong, R. M. Barnes, and R. T. Shin), *Progress in Electromag. Research Symposium*, Boston, Massachusetts, July 25-26, 1989.

Three-layer random medium model for fully polarimetric remote sensing of geophysical media (S. V. Nghiem, F. C. Lin, J. A. Kong, R. T. Shin, and H. A. Yueh), *Progress in Electromag. Research Symposium*, Boston, Massachusetts, July 25-26, 1989.

Correlation function study for random media with multiphase mixtures (F. C. Lin, H. A. Yueh, J. A. Kong and R. T. Shin), *Progress in Electromag. Research Symposium*, Boston, Massachusetts, July 25-26, 1989.

Polarimetric remote sensing of earth terrain with two-layer random medium model (M. Borgeaud, J. A. Kong, R. T. Shin, and S. V. Nghiem), *Progress in Electromag. Research Symposium*, Boston, Massachusetts, July 25-26, 1989.

Application of three-layer random medium model to polarimetric remote sensing of snow and sea ice (S. V. Nghiem, J. A. Kong, R. T. Shin, and H. A. Yueh), *North American Sea Ice Work Shop*, Amherst, Massachusetts, June 26-28, 1989.

Theoretical models for polarimetric microwave remote sensing of earth terrain (M. Borgeaud, S. V. Nghiem, R. T. Shin, and J. A. Kong), *J. Electromag. Waves and Application*, Vol. 3, No. 1, 61-81, 1988.

The optimal polarizations for achieving maximum contrast in radar polarimetry (A. A. Swartz, H. A. Yueh, J. A. Kong, L. M. Novak, and R. T. Shin), *J. Geophysical Research*, Vol. 93, No. B12, 15235-15260, 1988.

Bayes classification of terrain cover using normalized polarimetric data (H. A. Yueh, A. A. Swartz, J. A. Kong, R. T. Shin, and L. M. Novak), *J. Geophysical Research*, Vol. 93, No. B12, 15261-15267, 1988.

Correlation function study for sea ice (F. C. Lin, J. A. Kong, R. T. Shin, A. J. Gow, and S. A. Arcone), *J. Geophysical Research*, Vol. 93, No. C11, 14055-14063, November 1988.

Polarimetric remote sensing of earth terrain with three-layer random medium model (S. V. Nghiem, F. C. Lin, J. A. Kong, R. T. Shin, and H. A. Yueh), MIT Research Lab. of Electronics, EWT-RS124-8810, 1988.

Theoretical models for polarimetric microwave remote sensing of earth terrain (M. Borgeaud, J. A. Kong, R. T. Shin, and S. V. Nghiem), *Proceedings of the 1988 NATO Advanced Research Workshop*, Nuremberg, Germany, 1988.

Three-layer random medium model for polarimetric remote sensing of earth terrain (H. A. Yueh, S. V. Nghiem, F. C. Lin, J. A. Kong, and R. T. Shin), *IEEE AP-S International Symposium and URSI Radio Science Meeting*, Syracuse, June 6-10, 1988.

The optimal polarizations for achieving maximum contrast in radar polarimetry (A. A. Swartz, L. M. Novak, R. T. Shin, H. A. Yueh, and J. A. Kong), *IEEE AP-S International Symposium and URSI Radio Science Meeting*, Syracuse, June 6-10, 1988.

Theoretical model for snow-covered sea ice (F. C. Lin, J. A. Kong, R. T. Shin, A. J. Gow, and D. Perovich), *IEEE AP-S International Symposium and URSI Radio Science Meeting*, Syracuse, June 6-10, 1988.

K-distribution and polarimetric terrain radar clutter (H. A. Yueh, J. A. Kong, J. K. Jao, and R. T. Shin), *IEEE AP-S International Symposium and URSI Radio Science Meeting*, Syracuse, June 6-10, 1988.

Effective permittivity of dielectric mixtures (A. Sihvola and J. A. Kong), *IEEE Trans. Geosci. Remote Sensing*, Vol. 26, No. 4, 420-429, July 1988.

Classification of earth terrain using polarimetric synthetic aperture radar imagery (H. H. Lim, A. A. Swartz, H. A. Yueh, J. A. Kong, and J. J. van Zyl), *IEEE AP-S International Symposium and URSI Radio Science Meeting*, Syracuse, June 6-10, 1988.

Scattering of electromagnetic waves from a periodic surface with random roughness (H. A. Yueh, R. T. Shin, and J. A. Kong), *J. Appl. Phys.*, Vol. 64, No. 4, 1657-1670, 1988.

Scattering of electromagnetic waves from a periodic surface with random roughness (H. A. Yueh, R. T. Shin, and J. A. Kong), *SPIE Proceedings*, Vol. 927, Florida, April 6-8, 1988.

Identification of terrain cover using the optimum polarimetric classifier (J. A. Kong, A. A. Swartz, H. A. Yueh, L. M. Novak, and R. T. Shin), *J. Electromag. Waves Applic.*, Vol. 2, No. 2, 171-194, 1987.

Polarimetric microwave remote sensing of anisotropic earth terrain with strong fluctuation theory (M. Borgeaud, J. A. Kong, and R. T. Shin), *IGARSS 87 and URSI Meeting*, University of Michigan, Ann Arbor, MI, May 18-21, 1987.

Theoretical models for active and passive microwave remote sensing of snow-covered sea ice (F. C. Lin, J. A. Kong, and R. T. Shin), *IGARSS 87 and URSI Meeting*, University of Michigan, Ann Arbor, MI, May 18-21, 1987.

Theoretical models for polarimetric radar clutter (M. Borgeaud, R. T. Shin, and J. A. Kong), *J. Electromag. Waves Applic.*, Vol. 1, No. 1, 73-89, 1987.

Electromagnetic Wave Theory (J. A. Kong), Wiley-Interscience, New York, 696 pages, 1986.

Microwave remote sensing of snow-covered sea ice (M. Borgeaud, J. A. Kong, and F. C. Lin), *1986 International Geosci. Remote Sensing Symposium*, Zürich, Switzerland, 8-11, September, 1986.

Polarimetric radar clutter modeling with a two-layered anisotropic random medium (M. Borgeaud, J. A. Kong, and R. T. Shin), *International Union of Radio Science Commission F Open Symposium*, University of New Hampshire, Durham, New Hampshire, July 28-August 1, 1986.

Remote sensing of snow-covered sea ice (F. C. Lin and J. A. Kong), *International Union of Radio Science Commission F Open Symposium*, University of New Hampshire, Durham, New Hampshire, July 28-August 1, 1986.

Effective permittivity of dielectric mixtures (A. Sihvola and J. A. Kong), *International Union of Radio Science Commission F Open Symposium*, University of New Hampshire, Durham, New Hampshire, July 28-August 1, 1986.

Modified radiative transfer theory for a two-layer anisotropic random medium (J. K. Lee and J. A. Kong), *National Radio Science Meeting*, Philadelphia, Pennsylvania, June 9-13, 1986.

Theoretical modeling of polarimetric radar clutter (M. Borgeaud, R. T. Shin, and J. A. Kong), *National Radio Science Meeting*, Philadelphia, Pennsylvania, June 9-13, 1986.

Backscattering and propagation of radar pulses in earth terrain media (F. C. Lin, J. A. Kong, R. T. Shin, and Y. E. Yang), *IEEE IMTC/86 Meeting*, Boulder, Colorado, March 24-27, 1986.

Theory of Microwave Remote Sensing (L. Tsang, J. A. Kong, and R. T. Shin), Wiley-Interscience, New York, 613 pages, 1985.

Electromagnetic wave scattering in a two-layer anisotropic random medium (J. K. Lee and J. A. Kong), *J. Optical Society of America*, Vol. 2, No. 12, 2171-2186, December 1985.

Passive microwave remote sensing of an anisotropic random medium layer (J. K. Lee and J. A. Kong), *IEEE Trans. Geosci. Remote Sensing*, Vol. GE-23, No. 6, 924-932, November 1985.

Active microwave remote sensing of an anisotropic random medium layer (J. K. Lee and J. A. Kong), *IEEE Trans. Geosci. Remote Sensing*, Vol. GE-23, No. 6, 910-923, November 1985

Electromagnetic wave scattering by a two-layer anisotropic random medium (J. K. Lee and J. A. Kong), *IGARSS 85 and URSI Meeting*, University of Massachusetts, Amherst, MA, October 7-9, 1985.

Strong fluctuation theory for scattering, attenuation, and transmission of microwave through snowfall (Y. Q. Jin and J. A. Kong), *IEEE Trans. Geosci. Remote Sensing*, Vol. GE-23, No. 5, 754-760, September 1985.

Electromagnetic characterization of snow and ice for active and passive remote sensing (J. A. Kong), *AGU meeting*, San Francisco, CA, September 1985.

Strong fluctuation theory of random medium and applications in remote sensing (Y. Q. Jin and J. A. Kong), *International Symposium on Antennas and EM Theory (ISAE)*, Beijing, China, August 26-28, 1985.

Mean dyadic Green's function for a two-layer anisotropic random medium: nonlinear approximation to the Dyson equation (J. K. Lee and J. A. Kong), *International Symposium on Antennas and Propagation*, Kyoto, Japan, August 20-22, 1985.

Radar backscattering from snow-covered ice (F. C. Lin, J. K. Lee, J. A. Kong, and R. T. Shin), *Proceedings Snow Symposium V*, Cold Regions Research and Engineering Laboratory, Hanover, New Hampshire, August 13-15, 1985.

Electromagnetic characterization of inhomogeneous media exhibiting volume scattering effects (J. A. Kong), *Workshop on Waves in Inhomogeneous Media*, Schlumberger Doll Research, Ridgefield, Connecticut, August 8-9, 1985.

Ladder and cross terms in second-order distorted Born approximation (Y. Q. Jin and J. A. Kong), *J. Mathematical Physics*, Vol. 26, No. 5, 994-1011, May 1985.

Wave approach to brightness temperature from a bounded layer of random discrete scatterers (Y. Q. Jin), *Electromagnetics*, Vol. 4, 323-341, 1984.

Active and passive microwave remote sensing of layered anisotropic random medium (J. K. Lee and J. A. Kong), *National Radio Science Meeting*, Boston, Massachusetts, June 25-28, 1984.

Modified radiative transfer equation in strong fluctuation approach (Y. Q. Jin and J. A. Kong), *National Radio Science Meeting*, Boston, Massachusetts, June 25-28, 1984.

Scattering of electromagnetic waves by a randomly perturbed quasi-periodic surface (R. T. Shin and J. A. Kong), *National Radio Science Meeting*, Boston, Massachusetts, June 25-28, 1984.

Wave scattering by a bounded layer of random discrete scatterers (Y. Q. Jin and J. A. Kong), *National Radio Science Meeting*, Boulder, Colorado, January 11-13, 1984.

Applied Electromagnetism (L. C. Shen and J. A. Kong), Brooks/Cole, California, 507 pages, 1983.

Dyadic Green's functions for layered anisotropic medium (J. K. Lee and J. A. Kong), *Electromagnetics*, Vol. 3, 111-130, 1983.

Polarimetric Passive Remote Sensing of Periodic Surfaces

M. E. Veysoglu, H. A. Yueh, R. T. Shin, and J. A. Kong

Department of Electrical Engineering and Computer Science
and Research Laboratory of Electronics
Massachusetts Institute of Technology
Cambridge, MA 02139, USA

Abstract— The concept of polarimetry in active remote sensing is extended to passive remote sensing. The potential use of the third and fourth Stokes parameters U and V , which play an important role in polarimetric active remote sensing, is demonstrated for passive remote sensing. It is shown that, by the use of the reciprocity principle, the polarimetric parameters of passive remote sensing can be obtained through the solution of the associated direct scattering problem. These ideas are applied to study polarimetric passive remote sensing of periodic surfaces. The solution of the direct scattering problem is obtained by an integral equation formulation which involves evaluation of periodic Green's functions and normal derivative of those on the surface. Rapid evaluation of the slowly convergent series associated with these functions is observed to be critical for the feasibility of the method. New formulas, which are rapidly convergent, are derived for the calculation of these series. The study has shown that the brightness temperature of the Stokes parameter U can be significant in passive remote sensing. Values as high as 50 K are observed for certain configurations.

I. INTRODUCTION

Although the use of polarimetry is well understood in active remote sensing [1-4], little attention has been given to it in passive remote sensing. In active remote sensing, additional polarimetric information is obtained from the third and fourth Stokes parameters U and V . They are defined as $2 \text{Re}\langle E_v E_h^* \rangle$ and $2 \text{Im}\langle E_v E_h^* \rangle$ respectively, where the brackets denote ensemble averaging. Therefore, U and V are the measure of correlation between the horizontal and vertical components (E_h and E_v) of the electric field and thereby carry further information. Tsang [5] extended the concept of polarimetry to passive remote sensing and considered scattering by discrete scatters and rough surfaces when the thermal emission of third and fourth Stokes parameters are nonzero. Passive polarimetric measurements have been extensively used in radio astronomy to study planets and stars [6]. In this paper, we discuss polarimetric passive remote sensing of periodic rough surfaces. In particular, we calculate the brightness temperatures of U and V as can be obtained by passive measurements.

The reciprocity principle is used to relate active remote sensing parameters to polarimetric passive remote sensing. The emissivity of the surface for a particular polarization can be obtained as one minus the reflectivity [7,8]. In order to be able to get the full polarimetric information, including the corresponding brightness temperatures of U and V , we need the emissivities of four different polarizations:

However, with the use of the field periodicity, it is possible to reduce the integrals over a single period, P , [11]. After this is done, the form of (2) remains exactly as before with the limits of integration modified to cover a single period. The Green's function is also modified and takes the form

$$g_P(\vec{r}, \vec{r}') = \frac{i}{4} \sum_{m=-\infty}^{\infty} H_0^{(1)} \left(k_{1\perp} \sqrt{[z - (z' + mp)]^2 + (z - z')^2} \right) \exp(ik_{1s}mp) \quad (5)$$

Spectral representation of this periodic Green's function is

$$g_P(\vec{r}, \vec{r}') = \frac{i}{2p} \sum_{n=-\infty}^{\infty} \frac{1}{k_{2n}} \exp[ik_{2n}(z - z') + ik_{2n}|z - z'|] \quad (6)$$

where

$$k_{2n} = k_{1s} + n \frac{2\pi}{p} \quad (7)$$

and

$$k_{2n} = \sqrt{k_{1\perp}^2 - k_{2n}^2} \quad (8)$$

These functions together with their normal derivatives on the surface need to be evaluated for the solution of the integral equations given by (2). In their present form, they converge slowly especially for small values of $|z - z'|$. A transformation is used to speed up the convergence (see Appendix).

Now, we concentrate on the numerical solution of the coupled integral equations (2). As it appears, (2) has eight unknown functions to be determined. However, the number of unknown functions can be reduced to four by using the boundary conditions. For a dielectric surface, tangential electric and magnetic fields should be continuous and we are led to the following equations [9]

$$E_{1y} = E_{2y} \quad (9a)$$

$$H_{1y} = H_{2y} \quad (9b)$$

$$\hat{y}(\hat{n} \cdot \nabla_s E_{1y}) = c_0 \hat{n} \times \nabla_s H_{2y} + c_2 \hat{y}(\hat{n} \cdot \nabla_s E_{2y}) \quad (9c)$$

$$\hat{y}(\hat{n} \cdot \nabla_s H_{1y}) = -d_0 \hat{n} \times \nabla_s E_{2y} + d_2 \hat{y}(\hat{n} \cdot \nabla_s H_{2y}) \quad (9d)$$

where

$$c_0 = \left(\frac{k_{1\perp}^2}{k_{2\perp}^2} - 1 \right) \frac{k_{1y}}{\omega \epsilon_1} \quad (10a)$$

$$c_2 = \frac{\epsilon_2 k_{1\perp}^2}{\epsilon_1 k_{2\perp}^2} \quad (10b)$$

$$d_0 = \left(\frac{k_{1\perp}^2}{k_{2\perp}^2} - 1 \right) \frac{k_{1y}}{\omega \mu_1} \quad (10c)$$

$$d_2 = \frac{\mu_2 k_{1\perp}^2}{\mu_1 k_{2\perp}^2} \quad (10d)$$

Here $\nabla_s = \hat{z}(\partial/\partial z)$, ϵ is the permittivity, and μ is the permeability. After the number of unknowns is reduced to four, the method of moments is used to solve the coupled integral equations. Rectangular basis functions are used to expand the four unknown functions on the surface. The basis functions are "tested" by delta functions at their mid-points. This is usually called the point matching technique [12]. Hence the integral equations (2) are converted to matrix equations. In this process, integrals of Green's function need to be evaluated over subintervals of one period. When the testing point is not within the limits of integration, the singularity of the Green's function is avoided and numerical integration is used. Otherwise, for the "self terms", asymptotic expression for the integrand is used and the integral is evaluated analytically. This is relatively standard [13] and the details are not repeated here. Hence, the integral equations are transformed to the following matrix equations

$$\begin{bmatrix} A & c_2 B & c_0 C & 0 \\ D & E & 0 & 0 \\ -d_0 C & 0 & A & d_2 B \\ 0 & 0 & D & E \end{bmatrix} \begin{bmatrix} \gamma \\ \delta \\ \zeta \\ \xi \end{bmatrix} = \begin{bmatrix} E_{1y} \\ 0 \\ H_{1y} \\ 0 \end{bmatrix} \quad (11)$$

$\gamma, \delta, \zeta, \xi$ are the field quantities to be solved; they represent $E_{2y}, \hat{n} \cdot \nabla_s E_{2y}, H_{2y}$, and $\hat{n} \cdot \nabla_s H_{2y}$, respectively, evaluated at designated testing points. A, B, C, D, E are square matrices of order N , which is the number of basis functions used. The elements of these matrices are given as

$$A_{mn} = \frac{\delta_{mn}}{2} + \int_{z_{n-1}}^{z_n} [\hat{n} \cdot \nabla_s g_{p1}(t_m, z)] dz \quad (12a)$$

$$B_{mn} = \int_{z_{n-1}}^{z_n} g_{p1}(t_m, z) dz \quad (12b)$$

$$C_{mn} = g_{p1}(t_m, z_n) - g_{p1}(t_m, z_{n-1}) \quad (12c)$$

$$D_{mn} = \frac{\delta_{mn}}{2} - \int_{z_{n-1}}^{z_n} [\hat{n} \cdot \nabla_s g_{p2}(t_m, z)] dz \quad (12d)$$

$$E_{mn} = - \int_{z_{n-1}}^{z_n} g_{p2}(t_m, z) dz \quad (12e)$$

Here, one period of the surface is divided into N sections defined by z_n . The midpoint between z_n and z_{n-1} , designated as t_n , is the testing point of the point matching algorithm.

After the surface fields are determined, the coefficients of the reflected Floquet modes can be calculated. When the reflected fields for $z > f(z)$ are written as

$$E_{1y}^r = \sum_n b_n e^{i\tilde{x}_{1n} \cdot \vec{r}} \quad (13a)$$

$$H_{1y}^r = \sum_n b_n^h e^{i\tilde{x}_{1n} \cdot \vec{r}} \quad (13b)$$

the coefficients b_n and b_n^h are given in terms of the surface fields as

$$b_n = \frac{1}{2ik_{1L}p} \int d\phi \left[\frac{e^{-i\vec{k}_{1L} \cdot \vec{p}}}{\beta_n} \hat{n} \cdot \nabla_\phi E_{1y}(\vec{p}) - E_{1y}(\vec{p}) \hat{n} \cdot \nabla_\phi \frac{e^{-i\vec{k}_{1L} \cdot \vec{p}}}{\beta_n} \right] \quad (14a)$$

$$b_n^h = \frac{1}{2ik_{1L}p} \int d\phi \left[\frac{e^{-i\vec{k}_{1L} \cdot \vec{p}}}{\beta_n} \hat{n} \cdot \nabla_\phi H_{1y}(\vec{p}) - H_{1y}(\vec{p}) \hat{n} \cdot \nabla_\phi \frac{e^{-i\vec{k}_{1L} \cdot \vec{p}}}{\beta_n} \right] \quad (14b)$$

where

$$\alpha_n = (k_{1s} + n \frac{2\pi}{p}) / k_{1L} \quad (15a)$$

$$\beta_n = \sqrt{1 - \alpha_n^2} \quad (15b)$$

$$\vec{k}_{1n} = k_{1L}(\alpha_n \hat{z} + \beta_n \hat{z}) \quad (15c)$$

Similar expressions are valid for transmitted fields [9].

III. POLARIMETRIC BRIGHTNESS TEMPERATURES

In this section, we will discuss the evaluation of polarimetric brightness temperatures using the solution of the direct scattering problem outlined in Section II. As it was pointed out in the introduction, polarimetric parameters U and V defined as $2\text{Re}(E_y E_y^*)$ and $2\text{Im}(E_y E_y^*)$ are the measure of correlation between the horizontal and vertical components of the electric field. They carry information about the relative phase of the two components. One way to get this phase information is to calculate the emissivities of four different polarizations; horizontal, vertical, 45° linear, and right-hand circular. While horizontal and vertical emissivities give individual brightness temperatures, 45° linear, and right-hand circular emissivities can be used to obtain the brightness temperatures of U and V . Consider

$$2\text{Re}(E_y E_y^*) = (E_h E_h^*) + (E_v E_v^*) - 2 \left\langle \left(\frac{E_h - E_v}{\sqrt{2}} \right) \left(\frac{E_h^* - E_v^*}{\sqrt{2}} \right) \right\rangle \quad (16a)$$

$$2\text{Im}(E_y E_y^*) = (E_h E_h^*) + (E_v E_v^*) - 2 \left\langle \left(\frac{E_h + iE_v}{\sqrt{2}} \right) \left(\frac{E_h^* - iE_v^*}{\sqrt{2}} \right) \right\rangle \quad (16b)$$

where, E_h and E_v are the horizontal and vertical components of the electric field of the thermal emission from the surface. These quantities can be determined by passive measurements. The left-hand side of (16a) is the Stokes parameter U , while the terms on the right-hand side can be recognized as the emissivities of horizontal, vertical, and 45° linear polarizations. Equation (16b) gives the relation between the Stokes parameter V and the relevant emissivities. In terms of brightness temperatures we can write

$$U = T_h + T_v - 2T_p \quad (17a)$$

$$V = T_h + T_v - 2T_r \quad (17b)$$

since brightness temperatures are linearly related to the emissivities with the proportionality constant being the physical temperature of the surface. That is

$$T_a = \epsilon_a T_0 \quad (18)$$

where $a = h, v, p, r$ for the polarizations horizontal, vertical, 45° linear, and right-hand circular, respectively. T_0 is the physical temperature in Kelvins, ϵ_a the emissivity and T_a the brightness temperature. Therefore, all of the four Stokes parameters can be obtained from the passive measurements of the four emissivities corresponding to the polarizations mentioned above. On the other hand, the emissivity of a certain polarization can be calculated from the reflectivity of that particular polarization using the relation (13)

$$\epsilon_a = 1 - r_a \quad (19)$$

where the reflectivity r_a can be evaluated from the solution of the direct scattering problem as described below.

In Section II, we have given the formulas to calculate the field amplitudes of the reflected Floquet modes for an incident plane wave of any polarization. Now, consider a plane wave which has an arbitrary angle of incidence. Its wave vector is given by $\vec{k}_1 = k_{1x}\hat{x} + k_{1y}\hat{y} + k_{1z}\hat{z}$. We define two unit vectors \hat{h} and \hat{v} for the vertical and horizontal components of the electric field as follows:

$$\hat{h} = \frac{\vec{k}_1 \times \hat{z}}{|\vec{k}_1 \times \hat{z}|} = \frac{1}{\sqrt{k_{1x}^2 + k_{1y}^2}} (k_{1y}\hat{x} - k_{1x}\hat{y}) \quad (20)$$

$$\hat{v} = \hat{h} \times \hat{k}_1 = \frac{-1}{k_1 \sqrt{k_{1x}^2 + k_{1y}^2}} [k_{1x}k_{1z}\hat{x} + k_{1y}k_{1z}\hat{y} - (k_{1x}^2 + k_{1y}^2)\hat{z}] \quad (21)$$

With these definitions, we can express the incident wave as

$$\vec{E} = (E_h \hat{h} + E_v \hat{v}) e^{i\vec{k}_1 \cdot \vec{r}} \quad (22)$$

where E_h and E_v are the amplitudes of the vertical and horizontal components of the electric field. E_h and E_v are equal for 45° linear polarization and for circular polarization they are equal in magnitude but phase shifted by 90°.

For incident waves of different polarizations, the distribution of power among the reflected and transmitted Floquet modes will be different. Therefore, each polarization will have a different reflectivity associated with it. Calculating the power of reflected propagating modes along z direction, we obtain reflectivities as

$$r_a = \sum \sqrt{\beta_0} \frac{|b_n|^2 + |\gamma_1 b_n^h|^2}{|E_{1y}|^2 + |\gamma_1 H_{1y}|^2} \quad (23)$$

The summation is over the propagating modes. The variables b_n , b_n^h , E_{1y} , H_{1y} are as defined in Section II and different for each polarization. Having obtained the reflectivities, emissivities, brightness temperatures for four polarizations and the Stokes parameters can be evaluated using (17), (18) and (19).

The geometry of the problem is depicted in Fig. 1 and the results are presented in Section IV.

IV. RESULTS

In this section, polarimetric brightness temperatures are illustrated for the radiation from a sinusoidal surface (Fig. 1). Figures 2-5 show the dependence of the temperatures on different parameters. For all of the cases, the frequency is fixed at 1 GHz and the period at 50 cm. The first region is free space and the physical temperature of the periodic surface, T_0 , is fixed at 300 K. The relative permeability of the second region is also taken as unity.

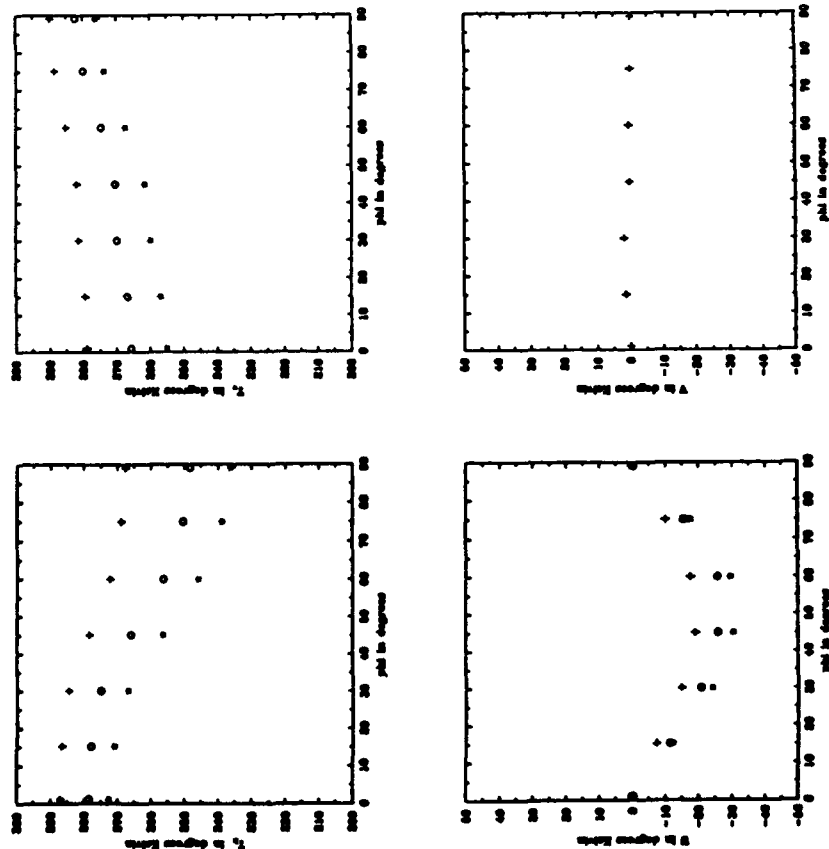


Figure 2. Brightness temperatures vs. ϕ .

+ : $\epsilon_{r2} = 6$, o : $\epsilon_{r2} = 9$, * : $\epsilon_{r2} = 12$.

Figure 2 plots the brightness temperatures versus the azimuth angle ϕ . For these plots, the height is 15 cm and the incident angle θ is 20° . Runs are made for three different values of ϵ_{r2} . It is seen that T_h and T_v tend to be higher for smaller ϵ_{r2} while $|U|$ increases with increasing ϵ_{r2} . No significant change is observed in V . With increasing ϕ , T_h decreases and T_v increases. The brightness

temperature of U is zero when $\phi = 0^\circ$ or $\phi = 90^\circ$ as expected. This is a check point of the numerical results. In between, it decreases to about -30 K. Values of V are small for the whole range of ϕ .

Figure 3 shows the variation with respect to θ with ϕ fixed at 45° and height kept at 15 cm. Again, the plots are given for three different values of ϵ_{r2} and we observe the same behavior. There is more than a 30 K difference in T_h for different ϵ_{r2} values at $\theta = 60^\circ$. We also observe a change in V with increasing θ .

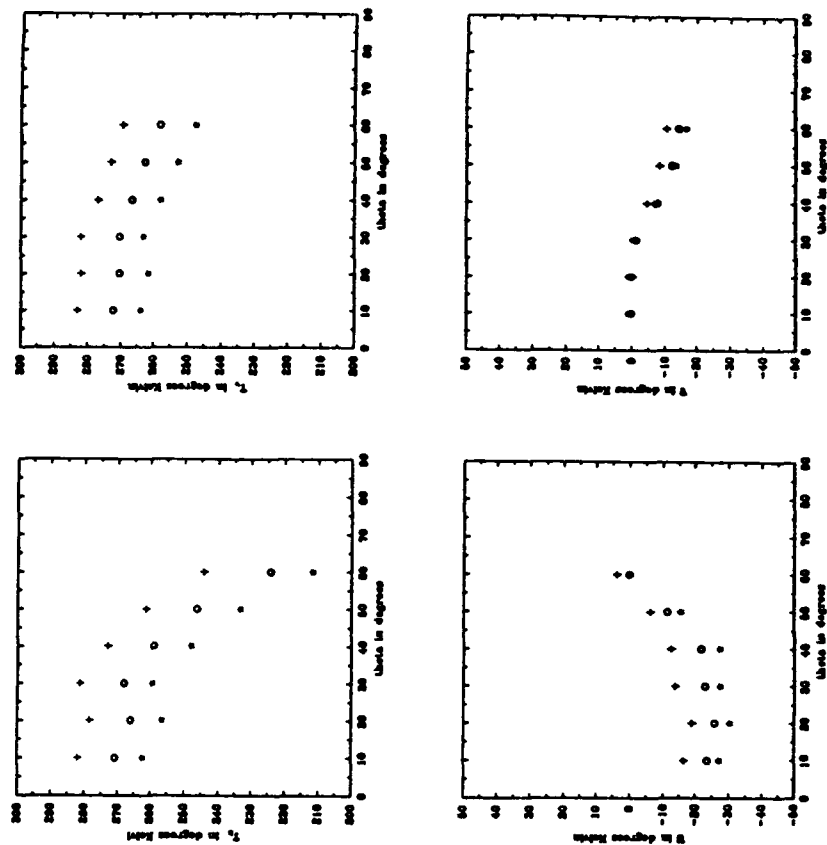


Figure 3. Brightness temperatures vs. θ .

+ : $\epsilon_{r2} = 6$, o : $\epsilon_{r2} = 9$, * : $\epsilon_{r2} = 12$.

Dependence of brightness temperatures on the surface height is given in Fig. 4. For this case, $\epsilon_{r2} = 12$, $\theta = 20^\circ$, and $\phi = 30^\circ$. We see a general tendency of increasing T_h and T_v . V does not change much but U varies significantly with height. We note that when the height is 10 cm, $|U|$ is as high as 48 K.

Finally, we analyse the effect of complex ϵ_{r2} on the brightness temperatures in Fig. 5, when θ is 20° , ϕ is 45° , and height is 15 cm. The real part of ϵ_{r2} is fixed at 12 and the imaginary part is varied from 0 to 8. Real ϵ_{r2} is taken as a base and the difference in temperatures is plotted. It is seen that variations in T_h and T_v are almost identical while the decrease in U is less. There is a slight increase in V .

Note also that the plots are not given as continuous curves. We merely show the results of some runs and linear interpolation between these values may be misleading. This is due to the presence of links in actual continuous curves [8].

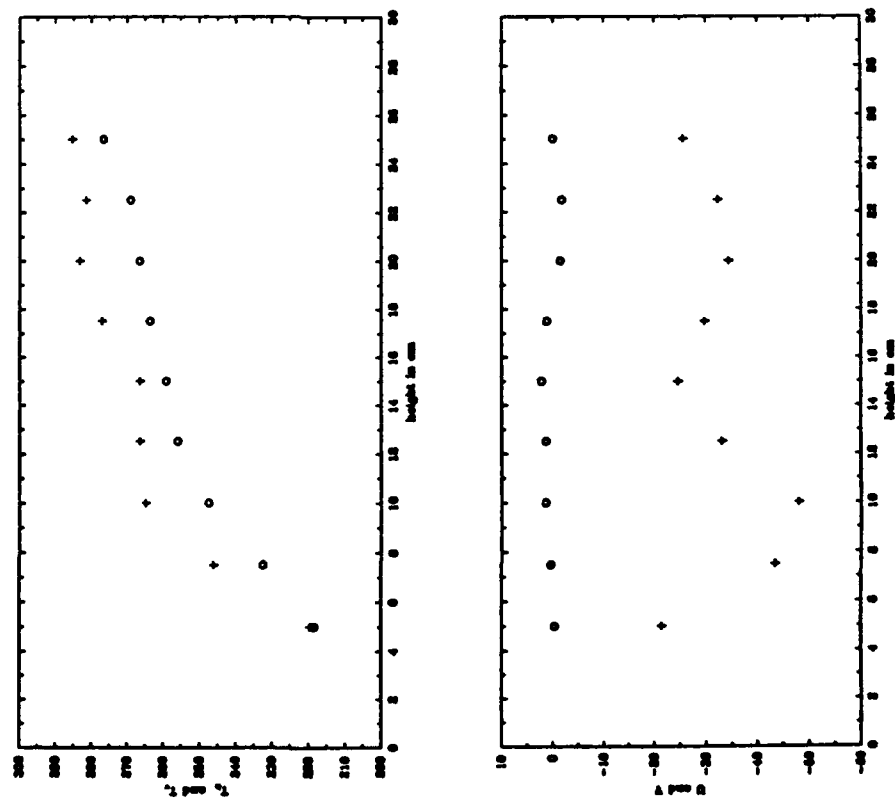


Figure 4. Brightness temperatures vs. height.
+; T_h , o; T_v , +; U , o; V .

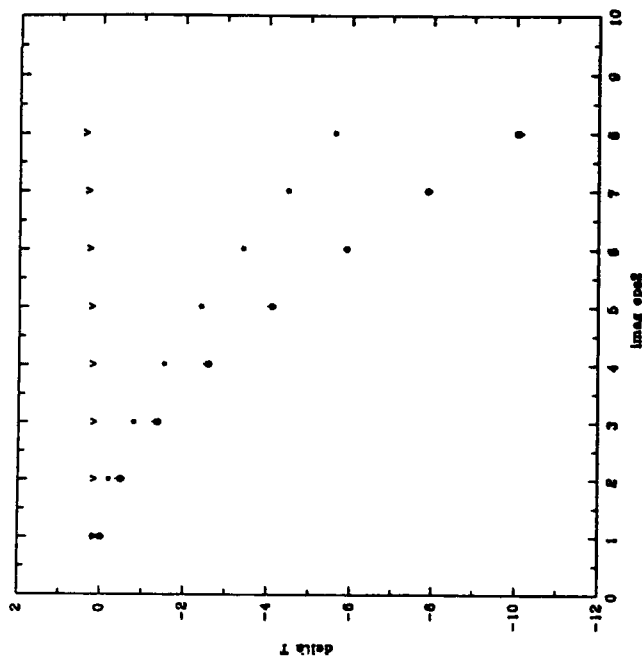


Figure 5. Brightness temperatures vs. ϵ_{r2} .
+; T_h , o; T_v , +; U , o; V .

V. SUMMARY AND CONCLUSIONS

The concept of polarimetry in active remote sensing is extended to passive remote sensing. It is shown that additional polarimetric information can be obtained by passive measurements through the use of the third and fourth Stokes parameters U and V . Brightness temperatures of these parameters are obtained from the solution of the direct scattering problem by the use of the reciprocity principle. Polarimetric passive remote sensing of periodic surfaces is studied in some detail. Numerical results are obtained for the brightness temperatures of a sinusoidal surface for different geometrical configurations. It is observed that the brightness temperature of U can be as high as 50 K for certain configurations. It is concluded that U can be an important parameter in passive remote sensing. Numerical results are compared with other methods like Extended Boundary Condition [9] where are applicable and good agreement is observed. For the presented results, power convergence checks are made and shown to be within two percent.

Scattering of waves from periodic surfaces is analysed by an integral equation formalism. It is shown that this method can successfully be used to determine

be scattering characteristics of periodic surfaces of deep corrugations and various profile shapes. The formulation given is kept general to handle general angles of incidence on a periodic dielectric surface with no restrictions on the polarization. It is shown that the slowly convergent series associated with the kernels of the integrals can be transformed into rapidly convergent integrals which can easily be evaluated by Romberg integration.

APPENDIX

In this section, we present the technique we used to transform the slowly convergent series associated with the periodic Green's functions to rapidly convergent integrals. The periodic Green's functions were given as infinite sums in Section I. These expressions are repeated below for convenience

$$g_p(\vec{p}, \vec{p}') = \frac{i}{4} \sum_{m=-\infty}^{\infty} H_0^{(1)} \left(k_{1\perp} \sqrt{[z - (z' + mp)]^2 + (z - z')^2} \right) \exp(ik_{1z}mp) \quad (1)$$

or alternatively

$$g_p(\vec{p}, \vec{p}') = \frac{i}{2p} \sum_{n=-\infty}^{\infty} \frac{1}{k_{zn}} \exp \left[ik_{zn}(z - z') + ik_{zn}|z - z'| \right] \quad (2)$$

These summations converge slowly. The second form, (2), does converge rapidly for large values of $|z - z'|$ due to exponential decay but we often need to evaluate this function for small values of $|z - z'|$ in which case the summation is slowly convergent. Here, we present a general transformation to speed up the convergence of summations and apply this method to the summation of (1). We start from the expansion

$$(e^s - e^{-s})^{-1} = e^{-s} \sum_{n=1}^{\infty} e^{ns} e^{-ns} \quad (3)$$

Then we multiply both sides by $h(z)$ and integrate from 0 to ∞ . If we denote the Laplace transform of the function $h(z)$ by $H(n)$ we get [14]

$$\sum_{n=1}^{\infty} e^{ns} H(n) = e^s \int_0^{\infty} (e^s - e^{-s})^{-1} h(z) dz \quad (4)$$

Now, in order to be able to use this formula, we must be able to identify the function we want to sum as the Laplace transform of some other function. For our case, the useful Laplace transform pair is [15]

$$i\sqrt{\frac{2}{\pi}} \frac{1}{\alpha^{\nu-1/2}} (z^2 + 2iz)^{\nu/2-1/4} J_{\nu-1/2} \left[\alpha (z^2 + 2iz)^{1/2} \right] \Leftrightarrow \frac{e^{is} H_{\nu}^{(2)} \left[(\alpha^2 + \alpha^2)^{1/2} \right]}{(\alpha^2 + \alpha^2)^{\nu/2}} \quad (5)$$

The case we are interested in is $\nu = 0$. For this case, $J_{\nu-1/2}(u)$ simplifies to elementary functions and we do not have to evaluate Bessel functions. Using (4), (5) and the general properties of Laplace transforms, we obtain

$$\begin{aligned} \frac{i}{4} \sum_{m=1}^{\infty} H_0^{(1)} \left(k_{1\perp} \sqrt{[z - (z' + mp)]^2 + (z - z')^2} \right) \exp(ik_{1z}mp) \\ = \frac{e^{ibz}}{\pi} \int_0^{\infty} \frac{e^{-a(b+1)u^2} e^{-it} \cos(au\sqrt{u^2 - 2i})}{(1 - e^{-vu^2} e^{-it}) \sqrt{u^2 - 2i}} du \quad (6) \end{aligned}$$

where

$$\begin{aligned} a &= k_{1\perp}(z - z') \\ b &= -(z - z')/p \\ s &= k_{1\perp}p \\ t &= -p(k_{1\perp} + k_{1z}) \end{aligned}$$

This integral is rapidly convergent due to exponential decay and can easily be evaluated by using Romberg integration. Having this formula for the periodic Green's function, we can easily compute the normal derivative along the surface by partial differentiation.

ACKNOWLEDGMENTS

This work was supported by the NASA Contract 958461, the NASA Contract NAGW-1617, the ARMY Corps of Engineers Contract DACA39-87-K-0022, the ONR Contract N00014-89-J-1107, and the U.S. Army/Cold Regions Research and Engineering Laboratory Contract DACA89-90-K-0016.

The Editor thanks S. V. Nghiem, K. O'Neill, P. Pampaloni, and L. Tsang for reviewing the paper.

REFERENCES

1. Borgeaud, M., S. V. Nghiem, R. T. Shin, and J. A. Kong, "Theoretical models for polarimetric microwave remote sensing of earth terrain," *J. Electro. Waves Applic.*, Vol. 3, No. 1, 61-81, 1989.
2. Zebker, H. A., J. J. van Zyl, and D. N. Hald, "Imaging radar polarimetry from wave synthesis," *J. Geophys. Res.*, Vol. 92, No. B1, 683-701, 1987.
3. Evans, D. L., T. G. Farr, J. J. Van Zyl, and H. A. Zebker, "Radar polarimetry analysis tools and applications," *IEEE Trans. Geosci. Remote Sensing*, Vol. GE-26, 774-789, 1988.
4. Lim, H., A. A. Swartz, H. A. Yueh, J. A. Kong, R. T. Shin, and J. J. van Zyl, "Classification of earth terrain using polarimetric synthetic aperture radar images," *J. Geophys. Res.*, Vol. 94, No. B6, 7049-7057, 1989.
5. Tsang, L., "Polarimetric passive microwave remote sensing of random discrete scatterers and rough surfaces," *J. Electro. Waves Applic.*, Vol. 5, No. 1, 41-57, 1991.
6. Gehrels, T., ed., *Planets, Stars and Nebulae Studied with Photopolarimetry*, The University of Arizona Press, Tucson, 1974.
7. Tsang, L., J. A. Kong, and R. T. Shin, *Theory of Microwave Remote Sensing*, John Wiley, New York, 1985.
8. Kong, J. A., S. L. Lin, and S. L. Chuang, "Microwave thermal emission from periodic surfaces," *IEEE Trans. Geosci. Remote Sensing*, Vol. GE-22, No. 4, 377-382, 1984.
9. Chuang, S. L., and J. A. Kong, "Wave scattering from a periodic dielectric surface for a general angle of incidence," *Radio Science*, Vol. 17, No. 3, 545-557, 1982.

10. Garcia, N., V. Celli, N. R. Hill, and N. Cabrera, "Til-conditioned matrices in the scattering of waves from hard corrugated surfaces," *Phys. Rev. B*, Vol. 18, No. 10, 5184-89, 1978.
11. Kong, J. A., *Electromagnetic Wave Theory*, John Wiley, New York, 1990.
12. Harrington, R. F., *Field Computation by Moment Method*, Macmillan, New York, 1968.
13. Zaki, K. A., and A. R. Neureuther, "Scattering from a perfectly conducting surface with a sinusoidal height profile: TE polarization," *IEEE Trans. Antennas Propagat.*, Vol. AP-19, No. 2, 208-214, 1971.
14. Glasser, M. L., "The summation of series," *SIAM J. Math. Anal.*, Vol. 2, No. 4, 595-600, 1971.
15. Oberhettinger, F., and L. Badii, *Tables of Laplace Transforms*, Springer-Verlag, New York, 1973.

Murat Emre Veysoglu was born in Ankara, Turkey in 1968. He received the B.Sc. degree summa cum laude in electrical engineering and computer science from Middle East Technical University in 1989. He is currently pursuing the degree of Master of Science at the Massachusetts Institute of Technology. His research interests include remote sensing, electromagnetic wave propagation and scattering.

S. H. Yueh received the SB (1982) and SM (1984) from the Electrical Engineering Department of National Taiwan University, Taiwan, and is currently working on the Ph.D. degree in electrical engineering at the Massachusetts Institute of Technology, Cambridge. His fields of interest are electromagnetic field theory and remote sensing.

R. T. Shin received his SB (1977), SM (1980), and Ph.D. (1984) in electrical engineering from the Massachusetts Institute of Technology. Since 1984 he has been on the Research Staff in the Air Defense Techniques Group at the MIT Lincoln Laboratory. His research interest is the areas of electromagnetic wave scattering and propagation and theoretical model development and data interpretation for microwave remote sensing. He is the coauthor of *Theory of Microwave Remote Sensing* (Wiley, 1985). Dr. Shin is a senior member of the IEEE, American Geophysical Union, Tau Beta Pi, Eta Kappa Nu, and commission F of the International Union of Radio Science.

J. A. Kong is Professor of Electrical Engineering and Chairman of Area IV on Energy and Electromagnetic Systems in the Department of Electrical Engineering and Computer Science at the Massachusetts Institute of Technology in Cambridge, Massachusetts. His research interest is in the field of electromagnetic wave theory and applications. He has published 7 books and over 300 refereed journal and conference papers, and is the Editor of the Wiley Series in Remote Sensing, and Chief Editor of the Elsevier book series of Progress In Electromagnetics Research (PIER).

Application of Neural Networks to Polarimetric SAR Image Classification

Y. Hara, R. G. Atkins, S. H. Yueh, R. T. Shin, and J. A. Kong
Department of Electrical Engineering and Computer Science
and Research Laboratory of Electronics
Massachusetts Institute of Technology
Cambridge, MA 02139, USA

R. Kwok
Jet Propulsion Laboratory
California Institute Technology
Pasadena, CA 91109, USA

Classification of terrain cover using polarimetric radar is an area of considerable current interest and research. A number of methods have been developed to classify ground terrain types from fully polarimetric synthetic aperture radar (SAR) images, and these techniques are often grouped into supervised and unsupervised approaches. Supervised methods, including both conventional Maximum Likelihood (ML) and more recent Multi-layer Perceptron classifiers, have yielded higher accuracy than unsupervised techniques, but suffer from the need for human interaction to predetermine classes and training regions. In contrast, unsupervised methods determine classes automatically, but generally show limited ability to accurately divide terrain into natural classes. In this paper, a new terrain classification technique is introduced, utilizing unsupervised neural networks to provide automatic classification, but employing an iterative algorithm which overcomes the poor accuracy of other unsupervised techniques.

Several types of unsupervised neural networks are first applied to the classification of SAR images, and the results are compared with those of more conventional unsupervised methods. Neural Network approaches include Adaptive Resonance theory (ART), Learning Vector Quantization (LVQ), and Kohonen's self-organizing feature map. Conventional classifiers utilized are the migrating means clustering algorithm and the K-means clustering method. With both neural network and conventional classifiers, preprocessing is performed to reduce speckle noise and to stabilize the training process. Results show that LVQ is the best of the neural network techniques, and that this method outperforms all of the conventional unsupervised classifiers. The accuracy of even the LVQ technique, however, is seen to remain below that of supervised methods.

To overcome this poor accuracy, an iterative algorithm is proposed in which the SAR image is reclassified using a Maximum Likelihood (ML) classifier. Training of the ML classifier is performed using a training data set first classified by the above unsupervised method, thus, requiring no human intervention, and preserving the unsupervised nature of the overall classification scheme. The process is then repeated iteratively, training a second ML classifier using data classified by the first. It is shown that as applied to polarimetric SAR images of San Francisco and Beaufort sea ice, acquired by the Jet Propulsion Laboratory, this algorithm converges rapidly, and significantly improves classification accuracy. Performance after convergence is seen to be comparable to that obtained with a supervised ML classifier, while maintaining the advantages of an unsupervised technique.

Multiple Ellipsoidal Species in Layer Random Medium Model for Polarimetric Remote Sensing

S. V. Nghiem, J. A. Kong, and R. T. Shin
Department of Electrical Engineering and Computer Science
and Research Laboratory of Electronics
Massachusetts Institute of Technology
Cambridge, MA 02139, USA

T. Le Toan
Centre d'Etude Spatiale des Rayonnements
CNRS, Université Paul Sabatier
9, Avenue du Colonel Roche
31029 Toulouse Cedex, France

For polarimetric remote sensing, geophysical media are modeled as layers containing randomly embedded scatterers. In a medium such as vegetation canopy, the scatterers can have various shapes, sizes, and permittivities that are significantly distinct from the background medium. The model presented in this paper will consider each type of the scatterers as a species which can take on a shape, size, and complex permittivity different from other species. The effective permittivity of the random medium is derived under the strong permittivity fluctuation theory and the polarimetric scattering coefficients are calculated for the layer configuration with the distorted Born approximation in the analytical wave theory which preserves the phase information.

The multiple species in the random medium are considered as randomly oriented ellipsoids and described by multiple three-dimensional ellipsoidal correlation functions. The variances and correlation lengths of the correlation functions characterize the fluctuation strengths and the physical geometry of the scatterers, respectively. The strong permittivity fluctuation theory is extended to account for the multiple species of ellipsoidal shape. In the random medium, a coincidence of an observation point with a source point gives rise to the singularity of the dyadic Green's function which is properly taken into account with exclusion volumes of the scatterers.

Polarimetric scattering properties of a remotely sensed medium are depicted with a covariance matrix whose elements are polarimetric scattering coefficients. The medium has a layer configuration: the top layer such as air is considered as homogeneous, the middle layer such as a vegetation canopy is random, and the underlying layer such as soil is a homogeneous half space. More random medium layers can also be introduced in the configuration to account for weather effect such as fog cover. The distorted Born approximation is then used with the effective permittivity to obtain the polarimetric covariance matrix. The result for the cross-polarized return σ_{hv} is non-zero even in the first order approximation. Due to the non-spherical shape and the random orientation of the scatterers, the correlation coefficient between the HH and VV returns has a magnitude different from unity and a small phase. The scattering coefficients are also used to calculate the Mueller matrix for synthesis of polarization signatures. The copolarized signature of the random medium has a rather straight distortion track and a recognizable pedestal.

Polarimetric Passive Remote Sensing of an Azimuthally Asymmetric Periodic Soil Surface

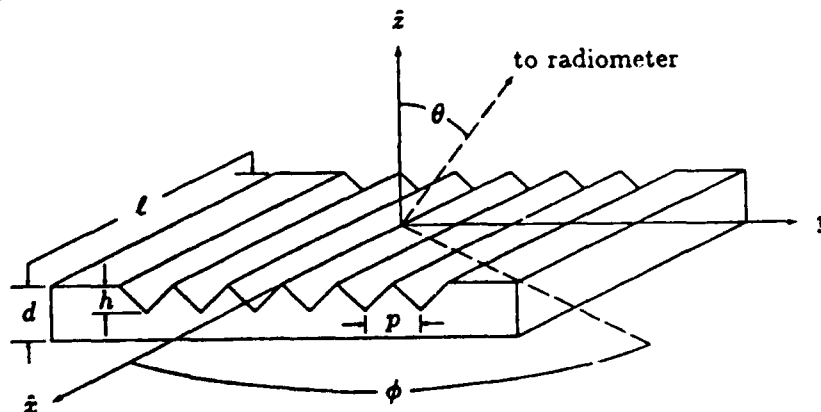
S. V. Nghiem, M. E. Veysoglu, J. A. Kong, and R. T. Shin
Department of Electrical Engineering and Computer Science
and Research Laboratory of Electronics
Massachusetts Institute of Technology
Cambridge, MA 02139, USA

K. O'Neill and A. W. Lohanick
U.S. Army Cold Regions Research and Engineering Laboratory
Hanover, NH 03755, USA

To demonstrate the use of polarimetry in passive remote sensing of azimuthal asymmetric features on a terrain surface, an experiment is designed, implemented, and presented in this paper.

The experiment setup is illustrated in the figure below. A triangular corrugation pattern with height $h = 2.5$ cm and period $p = 5$ cm is made on the sandy soil surface covering 23 periods by length $\ell = 160$ cm and thickness $d = 12.7$ cm. A radiometer of 15° beam width operating at 10 GHz is used in the experiment. The radiometer is mounted on a tripod at an elevation of 1.8 m height and directed toward the soil surface along the look direction determined by azimuthal angle ϕ and polar angle θ . Polarimetric brightness temperatures T_{Bh} , T_{Bv} , and T_{Bp} are measured respectively with horizontal, vertical, and 45° polarization orientations for $\theta = 20^\circ, 30^\circ$ and ϕ from 0° to 90° . From the measured temperatures, the third Stokes brightness temperatures U_B are obtained.

Absolute values as high as 30–40 K of the third Stokes brightness temperatures are observed. A theoretical analysis of the data indicates that the high values of U_B are caused by the azimuthal asymmetry on the remotely sensed soil surface. It is also observed from the experiment that T_{Bh} decreases, T_{Bv} increases, T_{Bp} decreases to a minimum at $\phi = 45^\circ$ and then increases as ϕ takes on the increased values. For U_B , the trend is similar to that of T_{Bp} . These general trends are supported by our theoretical predictions of the polarimetric brightness temperatures. The significant observation from this experiment is that the surface asymmetry can be detected with a measurement of U_B at a single azimuthal angle.



Analytical Solution of the Vector Radiative Transfer Equation with Rough Surface Boundary Condition

H. C. Han, J. A. Kong, and S. V. Nghiem
Department of Electrical Engineering and Computer Science
and Research Laboratory of Electronics
Massachusetts Institute of Technology
Cambridge, MA 02139 USA

T. Le Toan
Centre d'Etude Spatiale des Rayonnements
CNRS-Universite Paul Sabatier
Toulouse Cedex, France

Among the various theoretical models applied to the study of electromagnetic wave scatterings from geophysical terrain, such as snow, ice, and vegetation canopy, the radiative transfer theory has drawn intensive attention in the microwave remote sensing society during the past years. In most of the scattering models, the volume scattering and the surface scattering effects have been investigated separately. Recently, there has been a growing interest in the construction of composite models which can take into account both types of scattering.

In this research, we present the first order iterative solution to the vector radiative transfer equations for a two-layer medium with a diffuse top boundary and an irregular bottom boundary of Gaussian roughness. The Kirchhoff approximation and the geometrical optics approach with shadowing correction are used in formulating the boundary conditions. To demonstrate the utilities of this theory, we apply our formula with a phase matrix for randomly distributed and oriented spheroidal discrete scatterers to calculate the backscattering coefficients from soybean field at different growing stages and compare the results with experimental measurements. Good agreement has been achieved for both the co-polarized and the cross-polarized data. It is observed that the presence of the rough surface can significantly enhance the backscattering at small incident angles and the levels of the cross-polarized return. The polarization signatures calculated based on the Mueller matrix shows a straight distortion track and an observable pedestal. Numerical comparison to the backscattering coefficients calculated by using planar bottom boundary conditions with or without the incoherent addition of the rough surface effects are also made in this work.

EXTERNAL CALIBRATION OF POLARIMETRIC RADARS USING POINT AND DISTRIBUTED TARGETS

S. H. Yueh, J. A. Kong, and R. T. Shin

Department of Electrical Engineering and Computer Science
and Research Laboratory of Electronics
Massachusetts Institute of Technology
Cambridge, Massachusetts

ABSTRACT. Polarimetric calibration algorithms using combinations of point targets and reciprocal distributed targets are developed. From the reciprocity relations of distributed targets, an equivalent point target response is derived. Then the problem of polarimetric calibration using two point targets and one distributed target reduces to that using three point targets, which has been solved before. For calibration using one point target and one reciprocal distributed target, two cases are analyzed with the point target being a trihedral reflector or a polarimetric active radar calibrator (PARC). For both cases, the general solutions of the system distortion matrices are written as a product of a particular solution and a matrix with one free parameter. For the trihedral-reflector case, this free parameter is determined by assuming azimuthal symmetry for the distributed target. For the PARC case, knowledge of one ratio of two covariance matrix elements of the distributed target is required to solve for the free parameter. Numerical results are simulated to demonstrate the usefulness of the algorithms developed in this paper.

I. Introduction

In this paper the measured scattering matrix corresponding to a target with scattering matrix S is assumed to be [1]

$$X = cRST \quad (1)$$

The matrices T and R account for the channel imbalance and cross-polarization coupling of the transmitting and receiving ports, respectively. Propagation delay and loss between the radar and the target is accounted for by parameter c . The objective of polarimetric calibration is to solve for the R and T matrices using responses from targets with known polarization scattering parameters.

For general polarimetric systems, six parameters need to be estimated for relative polarimetric calibration: three for each of the transmitting and receiving ports including one for channel imbalance and two for cross-talk. To calibrate a general polarimetric system, algorithms using three point targets (in-scene reflectors) have been developed in [1-5] and a calibration algorithm using one distributed target and two point targets was presented in [6,7].

For polarimetric radars with a specific form, the number of calibration targets can be reduced. For example, a commonly adopted model is the reciprocal radar (R being the transpose of T). In this case, a calibration technique using natural distributed targets with azimuthal symmetry and trihedral corner reflectors was developed [8].

In this paper, we will investigate algorithms for calibrating a general polarimetric system using combinations of point and distributed targets.

II. Equivalent Point Target Response Using Reciprocity

In this section, we derive an equivalent point target from the response of reciprocal distributed targets, utilizing the model of polarimetric radars defined by Equation (1). Let us define a mapping between the scattering matrix X and a column vector \mathcal{X} as

$$X = \begin{bmatrix} X_{11} & X_{12} \\ X_{21} & X_{22} \end{bmatrix} \longleftrightarrow \mathcal{X} = [X_{11} \quad X_{12} \quad X_{21} \quad X_{22}]^t \quad (2)$$

where the superscript t signifies transpose. Likewise, we can map the matrix S into the column vector S . Thereafter, Equation (1) can be converted into a matrix equation

$$X = AS \quad (3)$$

where A is the direct product of R and T^t

$$A = R \otimes T^t \quad (4)$$

For the case that S is the response from a distributed target, it is more appropriate to describe the distributed target by its covariance matrix, C_s . From Equation (3), the measured covariance matrices C_x of X is related to C_s by

$$C_x = AC_s A^+ \quad (5)$$

where '+' signifies conjugate transpose.

By assuming the distributed target is reciprocal ($S_{12} = S_{21}$) and its covariance matrix C_s has rank 3, Klein and Freeman [6,7] derived the following equation

$$Q_x = c' A^{+^{-1}} Q_s \quad (6)$$

where Q_x and Q_s are, respectively, the eigenvectors of C_x and C_s with zero eigenvalue. In addition, $S_{12} = S_{21}$ means that columns 2 and 3 of C_s are equal. Hence,

$$Q_s = [0 \quad -1 \quad 1 \quad 0]^t \quad (7)$$

Note that c' is an appropriate scaling constant, taking into account the arbitrary absolute magnitudes of eigenvectors.

Equation (6) is an important observation made by Klein and Freeman [6,7] using the reciprocity relations satisfied by the distributed targets. Subsequently, they carried out the matrix inversion and multiplication in Equation (6) and obtained three nonlinear equations for matrix elements of R and T [Ref. 6, Eqs. (19)-(21)]. Further supplementing these three equations with the response from two point targets, they solved for the normalized matrix elements of R and T explicitly.

A. Equivalent Point Target Response

In this paper, we recast Equation (6) into another form to allow for a general application. After realizing that the mapping from Equation (1) to Equation (3) is one to one in nature, we can convert Equation (6) into the following form

$$Q_x^{+^{-1}} = \frac{1}{c'^*} R Q_s^{+^{-1}} T \quad (8)$$

where Q_s and Q_x are 2 by 2 matrices corresponding to vectors Q_s and Q_x , respectively, through the mapping defined by Equation (2). '*' denotes complex conjugate. Comparing Equation (8) with Equation (1), we can identify that $Q_x^{+^{-1}}$ is the response from a point target with scattering matrix $Q_s^{+^{-1}}$.

B. Reciprocation of Polarimetric Radar

As we know that a polarimetric radar is in general not reciprocal ($R \neq T^t$), therefore the measured scattering matrix X is not symmetric when S is symmetric. As to be shown in the following, Equation (8) can be utilized to symmetrize the measured scattering matrix.

From Equation (8), it can be shown that

$$T = R^t (Q_z^+ Q_z^t)^{-1} \quad (9)$$

For convenience, all the proportional constants like c' will not be written out explicitly from now on. Then substituting Equations (9) into (1), it is easy to show that

$$Y \stackrel{\text{def}}{=} X Q_z^+ Q_z^t = R S R^t \quad (10)$$

Note that if S is symmetric, so is Y . After comparing Equations (10) with (1), we can readily interpret Y as the response observed by a reciprocal polarimetric radar with T being the transpose of R .

If X is the backscatter from a reciprocal distributed target, then we can derive from C_z a reciprocated covariance matrix C_y of Y which is given by

$$C_y = A_y C_z A_y^+ \quad (11)$$

where

$$A_y = I \otimes (Q_z Q_z^*) \quad (12)$$

The results of this section show that the target reciprocity can be utilized to derive an equivalent target response and makes a polarimetric radar reciprocal.

III. Calibration Using Two Point Targets and One Reciprocal Distributed Target

This section discusses how to use two general point targets and one reciprocal distributed target for polarimetric calibration. Note that a general class of problems where these two point targets are two reciprocal reflectors have been solved explicitly by Klein and Freeman and verified with the Jet Propulsion Laboratory polarimetric sensors [7]. Here, we will show how the equivalent target can be used to solve the problem.

As shown in the previous section, we obtain an equivalent target from the reciprocity. Hence, by combining this equivalent target with another two point targets, the problem of calibration using two point targets and one distributed target is converted to that using three point targets, which has already been solved [3].

IV. One Trihedral Reflector and One Reciprocal Distributed Target

This section discusses how to calibrate a polarimetric radar using the responses from a trihedral reflector and one distributed target. Note that van Zyl [8] has already provided a scheme for calibrating a reciprocal polarimetric radar ($T = R^t$) using one trihedral reflector and one distributed target with azimuthal symmetry. Also in the previous section we have shown that a general polarimetric radar ($R \neq T^t$) can be made symmetric by using the reciprocity, indicating that van Zyl's approach can be directly applied. However, we will take a different approach in solving the problem so that partial calibration can be carried out without assuming the azimuthal symmetry for distributed targets.

Suppose that the measured response from a trihedral is given by

$$X_c = R T \quad (13)$$

Hence,

$$Y_c = X_c Q_z^+ Q_z^t = R R^t \quad (14)$$

and T can be expressed as

$$T = R^{-1}X_c \quad (15)$$

The general solution of R can be written as the product of a particular solution R_p and a matrix M

$$R = R_p M^{-1} \quad (16)$$

where the particular solution R_p has the following form:

$$R_p = \begin{bmatrix} R_{p11} & 0 \\ R_{p21} & R_{p22} \end{bmatrix} \quad (17)$$

and

$$M = \begin{bmatrix} \cos \theta & \sin \theta \\ -\sin \theta & \cos \theta \end{bmatrix} \quad (18)$$

Note that θ is allowed to be complex. After substituting Equation (16) into Equation (14), we can solve for the following quantities from the resulting equation

$$\frac{R_{p21}}{R_{p11}} = \frac{Y_{c12}}{Y_{c11}} = \frac{Y_{c21}}{Y_{c11}} \quad (19a)$$

$$\frac{R_{p22}}{R_{p11}} = \pm \sqrt{\frac{Y_{c22}}{Y_{c11}} - \left(\frac{R_{p21}}{R_{p11}}\right)^2} \quad (19b)$$

Then from Equation (15), we obtain the particular solution of $T_p (= R_p^{-1}X_c)$ and the general solution of $T (= MT_p)$. Hence, the general forms of R and T have been deduced and only one parameter $\alpha (= \tan \theta)$ remains to be determined. In the following, we assume the azimuthal symmetry for the distributed target to determine α . Azimuthal symmetry of the distributed target implies that

$$C_{s12} = C_{s13} = C_{s24} = C_{s34} = 0 \quad (20)$$

By substituting the general form of R and T into Equation (1), it can be shown that

$$X_p = R_p^{-1}XT_p^{-1} = M^{-1}SM \quad (21)$$

Note that $M^{-1} = M^t$. Therefore, matrix X_p is symmetric.

Representing X_p by a vector χ_p according to Equation (2), we can define the covariance matrix $C_p = E[\chi_p \chi_p^+]$ which is related to C_x and C_s by

$$C_p = A_p C_x A_p^+ \quad (22a)$$

$$= A_m C_s A_m^+ \quad (22b)$$

where

$$A_p = R_p^{-1} \otimes T_p^{-1t} \quad (23a)$$

$$A_m = M^{-1} \otimes M^t \quad (23b)$$

Multiplying both sides of Equation (21) by M , then calculating the ensemble average of the products of matrix elements, and using the fact that $C_{p12} = C_{p13}$ and $C_{p34} = C_{p24}$, we obtain the following equations for α

$$\alpha(C_{p32} + C_{s22} - C_{p22} - C_{s32}) + \alpha^*(C_{p14} - C_{s11} + C_{p44} - C_{s41}) = -(C_{p12} + C_{p42}) \quad (24)$$

$$\alpha(C_{p33} + C_{s23} - C_{p23} - C_{s33}) + \alpha^*(-C_{p11} + C_{s14} - C_{p41} + C_{s44}) = -(C_{p13} + C_{p43}) \quad (25)$$

Note that α can be obtained by utilizing the solution of the following equation

$$a\alpha + b\alpha^* = c \quad (26)$$

which has the following solution

$$\alpha = \frac{ca^* - c^*b}{|a|^2 - |b|^2}, \quad \text{provided } |a| \neq |b|. \quad (27)$$

The criterion $|a| \neq |b|$ can be satisfied for a large class of distributed targets as observed from Equations (24) and (25).

If we start with a polarimetric radar having good channel isolation (small α), we can use the following iterative scheme to determine the value of α :

Step 1. Initialize α as zero.

Step 2. Evaluate A_m from Equation (23b) with the current value of α and calculate

$$C'_s = A_m^{-1} C_p A_m^{-1+} \text{ from Equation (22b) as the current estimate of } C_s.$$

Step 3. Solve α from either Equations (24) or (25) by using the current value of C'_s .

Step 4. Repeat Steps 2 and 3 until C'_{s12} , C'_{s13} , C'_{s24} , and C'_{s34} are smaller than a selected threshold, which in our case is set to be 10^{-6} times C'_{s11} .

Once α is solved, the solution for R and T is complete except for their absolute magnitudes.

V. One Polarimetric Active Radar Calibrator and One Reciprocal Distributed Target

This section discusses how to use a PARC and a distributed target for calibration. Suppose that there is a PARC with the following scattering matrix [2],

$$S_c = \begin{bmatrix} 0 & 1 \\ 0 & 0 \end{bmatrix} \quad (28)$$

Subsequently, substituting Equation (28) into (10) results in a equation for the transformed scattering matrix Y_c . Then it is straightforward to show that the general solution of R has the following form

$$R = R_\mu M_\mu^{-1} \quad (29)$$

where the particular solution R_μ is

$$R_\mu = R_{11} \begin{bmatrix} 1 & Y_{c11}/Y_{c12} \\ Y_{c22}/Y_{c12} & 1 \end{bmatrix} \quad (30)$$

and

$$M_\mu = \begin{bmatrix} 1 & 0 \\ 0 & 1/\beta \end{bmatrix}. \quad (31)$$

Here β is a free parameter. In addition, the particular solution of T is obtained from Equation (8) and is given by

$$T_\mu = Q_s^t R_\mu^{-1} Q_z^{-1+} \quad (32)$$

It can be shown that the general solution of T can be written as

$$T = \frac{1}{\beta} M_\mu^{-1} T_\mu \quad (33)$$

Substituting Equations (29) and (33) into Equation (1) results in

$$M_{\mu}^{-1} S M_{\mu}^{-1} = R_{\mu}^{-1} X T_{\mu}^{-1} \quad (34)$$

Let $X_{\mu} = R_{\mu}^{-1} X T_{\mu}^{-1}$ and vectorize it as χ_{μ} by Equation (2). We can relate the covariance matrix $C_{\mu} = E[\chi_{\mu} \chi_{\mu}^+]$ to C_z by

$$C_{\mu} = A_{\mu} C_z A_{\mu}^+ \quad (35)$$

where

$$A_{\mu} = R_{\mu}^{-1} \otimes T_{\mu}^{-1} \quad (36)$$

Multiplying X_{μ} by R_{μ} from the left-hand side of (34) and carrying out the ensemble average of products of matrix elements, we can obtain the following equations

$$\beta = \left(\frac{C_{s11} C_{\mu12}}{C_{s12} C_{\mu11}} \right)^* = \left(\frac{C_{s11} C_{\mu13}}{C_{s13} C_{\mu11}} \right)^* \quad (37a)$$

$$= \frac{C_{s12} C_{\mu22}}{C_{s22} C_{\mu12}} = \frac{C_{s13} C_{\mu23}}{C_{s23} C_{\mu13}} \quad (37b)$$

$$= \left(\frac{C_{s22} C_{\mu24}}{C_{s24} C_{\mu22}} \right)^* = \left(\frac{C_{s23} C_{\mu34}}{C_{s34} C_{\mu23}} \right)^* \quad (37c)$$

and

$$\beta = \pm \sqrt{\left(\frac{C_{s11} C_{\mu14}}{C_{s14} C_{\mu11}} \right)^*} = \pm \sqrt{\frac{C_{s14} C_{\mu44}}{C_{s44} C_{\mu14}}} \quad (38)$$

Here we can see that in order to solve the parameter β , it is necessary to know one of the ratios of matrix elements of C_s beforehand. Also notice that Equation (37) is not applicable to distributed targets with azimuthal symmetry which will result in the case of zero divided by zero.

VI. Numerical Simulation and Discussion

In this section numerical simulation of algorithms discussed in the previous two sections will be presented. The polarization transfer matrices of the polarimetric radar are assumed to be

$$R = \begin{bmatrix} 1 & 0.0426\angle -169.5^\circ \\ 0.0532\angle 113.6^\circ & 1.0638\angle -86.3^\circ \end{bmatrix} \quad (39)$$

$$T = \begin{bmatrix} 1 & 0.1042\angle -77.8^\circ \\ 0.0625\angle 30^\circ & 1.0417\angle -57.9^\circ \end{bmatrix} \quad (40)$$

This set of system matrices corresponds to the distortion matrices of the Jet Propulsion Laboratory L-band radar estimated by a three-point-target approach [9]. Note that the cross-talk errors are smaller than -20 dB and the channel imbalances are around 0.5 dB. The most severe errors are the differences in phases between channels, which will significantly distort the co-polarization signature [10] of trihedral reflectors and make it look like that of a dihedral reflector.

In this paper, we denote channels 1 and 2 as horizontal (h) and vertical (v) polarizations, respectively. Therefore, the parameters of a covariance matrix C_s are defined as

$$C_s = \sigma_{hh} \begin{bmatrix} 1 & \sqrt{\epsilon_{hv}} \rho_{hhh v} & \sqrt{\epsilon_{vh}} \rho_{hh v h} & \sqrt{\gamma} \rho_{hh v v} \\ \sqrt{\epsilon_{hv}} \rho_{hhh v}^* & \epsilon_{hv} & \sqrt{\epsilon_{vh} \epsilon_{vh}} \rho_{h v v h} & \sqrt{\epsilon_{hv} \gamma} \rho_{h v v v} \\ \sqrt{\epsilon_{vh}} \rho_{hh v h}^* & \sqrt{\epsilon_{hv} \epsilon_{vh}} \rho_{h v v h}^* & \epsilon_{vh} & \sqrt{\epsilon_{vh} \gamma} \rho_{v h v v} \\ \sqrt{\gamma} \rho_{hh v v}^* & \sqrt{\epsilon_{hv} \gamma} \rho_{h v v v}^* & \sqrt{\epsilon_{vh} \gamma} \rho_{v h v v}^* & \gamma \end{bmatrix} \quad (41)$$

Here, $\rho_{\alpha\beta\gamma\delta}$ represents the correlation coefficient of ' $\alpha\beta$ ' and ' $\gamma\delta$ ' polarizations. For distributed targets with azimuthal symmetry, $\rho_{hhh v} = \rho_{hh v h} = \rho_{h v v v} = \rho_{v h v v} = 0$.

Listed in column 1, Table 1 are the covariance parameters of the distributed target to be used for the simulation of calibration algorithms, and its co-polarization signature is shown in Figure 1(a). Due to the channel imbalance and cross-talk for the radar defined by Equations (39) and (40), the observed co-polarization signature would be that shown in Figure 1(b). After the reciprocity is applied, the co-polarization signature corresponding to the reciprocated covariance matrix C_y is illustrated in Figure 1(c), which becomes symmetric with respect to the 90-degree orientation angle.

A. One Trihedral Reflector and One Reciprocal Distributed Target

Considered below is the trihedral-reflector approach (see Section III). Two solutions were obtained. One produces the correct R and T and the other is related to the correct one by

$$R' = R \begin{bmatrix} 1 & 0 \\ 0 & -1 \end{bmatrix}, \quad T' = \begin{bmatrix} 1 & 0 \\ 0 & -1 \end{bmatrix} T. \quad (42)$$

Using these two solutions to calibrate the radar, the calibrated covariance parameters of the distributed target are the same as those given in column 2 of Table 1. This is due to the fact the sign difference does not affect the responses from trihedral reflectors and azimuthally symmetric distributed targets.

Particular solutions for the case considered are given by

$$R_{p1} = \begin{bmatrix} 1 & 0 \\ 0.098 \angle 109.24^\circ & 1.06 \angle -86.40^\circ \end{bmatrix}, \quad T_{p1} = \begin{bmatrix} 1 & 0.0698 \angle -96.51^\circ \\ 0.1038 \angle 22.21^\circ & 1.0482 \angle -57.84^\circ \end{bmatrix}$$

and

$$R_{p2} = \begin{bmatrix} 1 & 0 \\ 0.098 \angle 109.24^\circ & 1.06 \angle 93.6^\circ \end{bmatrix}, \quad T_{p2} = \begin{bmatrix} 1 & 0.0698 \angle -96.51^\circ \\ 0.1038 \angle -157.79^\circ & 1.0482 \angle 122.16^\circ \end{bmatrix}$$

Note that the first solution is very close to the correct system parameters, in particular, the channel imbalance. If the system is calibrated by the particular solution, the calibrated distributed target parameters are given in columns 4 and 5 of Table 1, and the corresponding polarization signatures are shown in Figures 1(d) and 1(e), respectively, which are not visibly distinguishable from the correct signature shown in Figure 1(a).

B. One Polarimetric Active Radar Calibrator and One Reciprocal Distributed Target

The PARC approach outlined in Section IV is considered next. The particular solution is given by

$$R_\mu = \begin{bmatrix} 1 & 0.400 \angle -83.2^\circ \\ 0.0532 \angle 113.6^\circ & 1.0 \end{bmatrix}, \quad T_\mu = \begin{bmatrix} 1 & 0.1042 \angle -77.8^\circ \\ 0.0588 \angle 116.3^\circ & 0.9792 \angle 28.4^\circ \end{bmatrix}$$

We can see that $R_{\mu 21}$ and $T_{\mu 12}$ match correctly with R_{21} and T_{12} [see (29) and (33)]. Calibration by the particular solution alone yields the parameters of C_μ which are shown

in Table 2. Note that all the correlation coefficients are well calibrated except the phase of ρ_{hhvv} . Hence, if we have a system with an ideal phase balance between h and v channels, then all the correlation coefficients can be well calibrated by the particular solution, R_μ and T_μ .

Further assuming that two of the distributed target parameters γ and ρ_{hhvv} are known, we can apply Equation (38) for the calculation of β and to obtain two solutions. One correctly produces the system parameters, whereas the other is related to it by Equation (42). By calibrating the system using these two solutions, the calibrated covariance matrix parameters are given in column 2, Table 2, which correctly match the original parameters. It should be noted that if correlation coefficients, ρ_{hhvv} , ρ_{hhvh} , ρ_{hvvv} , and ρ_{vhvv} are not zeros, then the correlation parameters after calibration by the wrong solution will carry an opposite sign.

C. Comparison of Trihedral Reflector and PARC Approaches

The results of the above two sub-sections indicate that when the particular solution is applied for calibration, the trihedral-reflector approach is quite robust in calibrating the channel imbalance and weak at detecting the cross-polarization couplings. In contrast, the PARC approach is poor at removing the channel imbalance and useful in estimating the cross-talk. In other words, the trihedral-reflector approach is useful when the system has relatively small cross-talk, and the PARC approach is useful when the system has good channel balance, if no further assumption about the distributed targets is made.

We should also note that the alignment of point target is less critical in the trihedral-reflector approach than the PARC approach, since the PARCs need to be carefully oriented in order to avoid artificial cross-talks. However, the PARC approach can provide a larger signal to noise ratio than the trihedral-reflector approach.

REFERENCES

- [1] R. M. Barnes, "Antenna Polarization Calibration Using In-scene Reflectors," Proceedings of the Tenth DARPA/Tri-Service Millimeter Wave Symposium, U. S. Army Harry Diamond Lab., Adelphi, MD, April 8-10, 1986.
- [2] A. Freeman, Y. Shen, and C. Werner, "Polarimetric SAR Calibration Experiment Using Active Radar Calibrators," *IEEE Trans. Geosci. Remote Sensing*, Vol. 28, No. 2, pp. 224-240, 1990.
- [3] S. H. Yueh, J. A. Kong, and R. T. Shin, "Calibration of Polarimetric Radars Using In-Scene Reflectors," *Progress In Electromagnetics Research*, Elsevier, New York, Vol. 3, Chapter 9, 1990.
- [4] S. H. Yueh, J. A. Kong, R. M. Barnes, and R. T. Shin, "Calibration of Polarimetric Radars Using In-scene Reflectors," *J. Electromagnetic Waves and Appl.*, Vol. 4, No. 1, 27-49, 1990.
- [5] M. W. Whitt and F. Ulaby, "A Polarimetric Radar Calibration Technique with Insensitivity to Target Orientation," *Radio Science*, Vol. 25, No. 6, pp. 1137-1143, 1990.
- [6] J. D. Klein, "Polarimetric SAR Calibration Using Two Targets and Reciprocity," *Proc. IGRASS '90 Symposium*, pp. 1105-1108, Washington, D.C., May 20-24, 1990.
- [7] J. D. Klein and A. Freeman, "Quadpolarization SAR Calibration Using Target Reciprocity," *J. Electromagnetic Waves and Appl.*, in press, 1991.
- [8] J. J. van Zyl, "Calibration of Polarimetric Radar Images Using Only Image Parameters and Trihedral Corner Reflectors Responses," *IEEE Trans. Geoscience and Remote Sensing*, Vol. 28, No. 3, 337-348, 1990.
- [9] M. Zink, F. Heel, and H. Kietzmann, "Airborne SAR Calibration," submitted for publication in *J. Electromagnetic Waves and Appl.*, 1990.
- [10] J. J. van Zyl, H. A. Zebker and C. Elachi, "Imaging Radar Polarization Signature:

Acknowledgments

This work was supported by the NASA Contract NAGW-1272, the ARMY Corp of Engineers Contract DACA39-87-K-0022, the NASA Grant NAG5-270, and the ONR Contract N00014-83-K-0258.

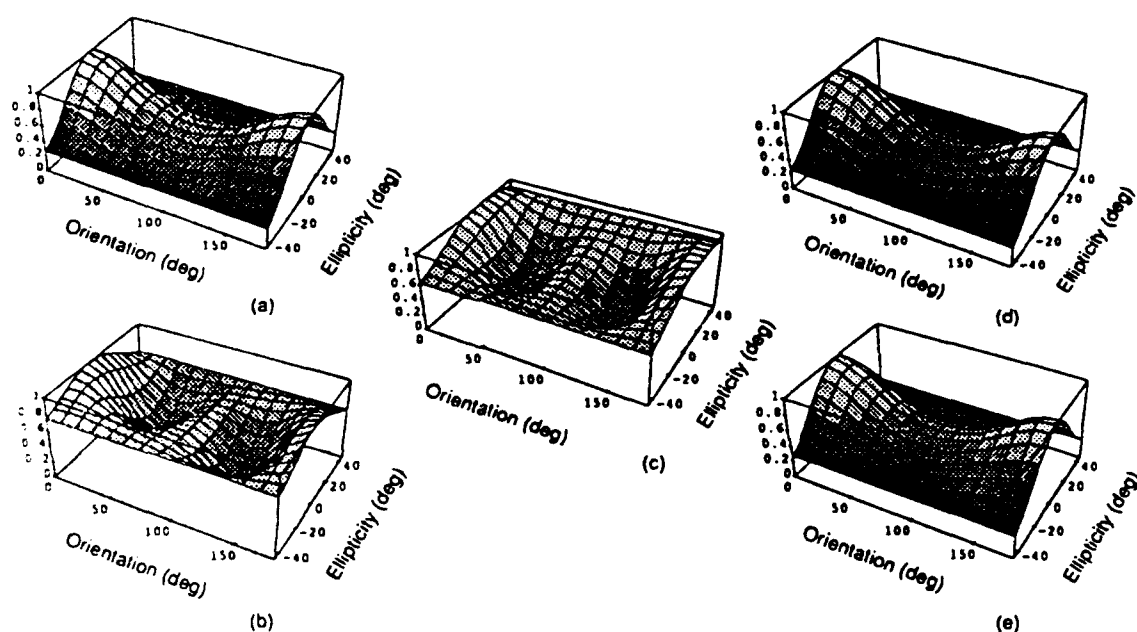


Figure 1. Co-polarization signatures of a distributed target with azimuthal symmetry: (a) original, (b) distorted (C_x), (c) reciprocated (C_y), (d) calibrated by the particular solution, R_{p1} and T_{p1} , and (e) calibrated by the particular solution, R_{p2} and T_{p2} .

| Covariance Matrix Parameters | Original and Fully Calibrated | Observed (distorted) | Calibrated by R_{p1} and T_{p1} | Calibrated by R_{p2} and T_{p2} |
|------------------------------|-------------------------------|-----------------------------|-------------------------------------|-------------------------------------|
| ϵ_{hv} | 0.1 | 0.1162 | 0.1006 | 0.1006 |
| ϵ_{vh} | 0.1 | 0.1150 | 0.1006 | 0.1006 |
| γ | 0.5 | 0.6104 | 0.5011 | 0.5011 |
| ρ_{hhvv} | 0.6 | $0.594 \angle 144^\circ$ | $0.601 \angle -0.044^\circ$ | $0.601 \angle -0.044^\circ$ |
| ρ_{hhhv} | 0 | $0.266 \angle 84.97^\circ$ | $0.053 \angle -20.9^\circ$ | $0.053 \angle 159.1^\circ$ |
| ρ_{hhvh} | 0 | $0.074 \angle -108.7^\circ$ | $0.053 \angle -20.9^\circ$ | $0.053 \angle 159.1^\circ$ |
| ρ_{vvvh} | 1 | $0.93 \angle 29.45^\circ$ | 1.0 | 1.0 |
| ρ_{vvvv} | 0 | $0.116 \angle 57.03^\circ$ | $0.0251 \angle -22.35^\circ$ | $0.0251 \angle 157.7^\circ$ |
| ρ_{vhvv} | 0 | $0.08 \angle 106.42^\circ$ | $0.0251 \angle -22.35^\circ$ | $0.0251 \angle 157.7^\circ$ |

Table 1. Original, observed, and calibrated covariance matrix parameters by using the responses from a trihedral reflector and azimuthal symmetric distributed targets.

| Covariance Matrix Parameters | Original and Fully Calibrated | Observed (distorted) | Calibrated by R_μ and T_μ |
|------------------------------|-------------------------------|-----------------------------|-----------------------------------|
| ϵ_{hv} | 0.1 | 0.1162 | 0.1132 |
| ϵ_{vh} | 0.1 | 0.1150 | 0.1132 |
| γ | 0.5 | 0.6104 | 0.6404 |
| ρ_{hhvv} | 0.6 | $0.594 \angle 144^\circ$ | $0.6 \angle 172.6^\circ$ |
| ρ_{hhhv} | 0 | $0.266 \angle 84.97^\circ$ | 0 |
| ρ_{hhvh} | 0 | $0.074 \angle -108.7^\circ$ | 0 |
| ρ_{vvvh} | 1 | $0.93 \angle 29.45^\circ$ | 1.0 |
| ρ_{vvvv} | 0 | $0.116 \angle 57.03^\circ$ | 0 |
| ρ_{vhvv} | 0 | $0.08 \angle 106.42^\circ$ | 0 |

Table 2. Original, observed, and calibrated covariance matrix parameters by using the responses from a PARC and azimuthal symmetric distributed targets with known γ and ρ_{hhvv} .

K-Distribution and Multi-Frequency Polarimetric Terrain Radar Clutter

S. H. Yueh and J. A. Kong

Department of Electrical Engineering and Computer Science
and Research Laboratory of Electronics
Massachusetts Institute of Technology
Cambridge, MA 02139, USA

J. K. Jao and R. T. Shin

MIT Lincoln Laboratory
Lexington, MA 02173, USA

H. A. Zebker

Jet Propulsion Laboratory
California Institute of Technology
Pasadena, CA 91109, USA

T. Le Toan

Centre d'Etudes Spatiales des Rayonnements
31029 Toulouse Cedex, France

Abstract— A multivariate K -distribution, well supported by experimental data, is proposed to model the statistics of fully polarimetric radar clutter of earth terrain. In this approach, correlated polarizations of backscattered radar returns are characterized by a covariance matrix and homogeneity of terrain scatterers is characterized by a parameter α . As compared with C-, L- and P-band polarimetric SAR image simultaneously measured by Jet Propulsion Laboratory (JPL) on Mt. Shasta, it is found that α appears to decrease from C- to P-band for both the forest and burned areas.

1. INTRODUCTION

Polarimetric terrain backscatter data observed with satellite and airborne synthetic aperture radars (SAR) have demonstrated potential applications in geologic mapping and terrain cover classification [1-7]. In previous publications on this subject, Gaussian statistics have been frequently assumed for the radar return signals to build the Bayes terrain classifier [1-3]. However, abundant experimental evidence shows that terrain radar clutter is non-Gaussian, i.e., non-Rayleigh in amplitude distribution [8-10].

Among many non-Gaussian statistics, the K -distribution has proven to be useful in characterizing the amplitude distribution of electromagnetic echoes from various objects [9-15], including diverse ground surfaces [9], sea surface [10] and

wave propagation through atmospheric turbulence [12,13,15].

Recently, a multivariate K -distribution has been developed to model the non-Gaussian statistics of fully polarimetric terrain clutter [16]. The multivariate K -distribution is characterized by a parameter α and a covariance matrix for the returns from multi-polarization channels. The correlations among polarizations are properly taken into account by a covariance matrix, whereas the parameter α characterizes homogeneity of terrain radar scatterers. When α becomes large, the intensity fluctuation of clutter decreases. If α approaches infinity, the multivariate K -distribution reduces to the Gaussian distribution. The multivariate K -distribution has been validated by two sets of polarimetric radar measurements [16]: JAWS polarimetric data obtained from MIT Lincoln Laboratory and polarimetric Synthetic Aperture Radar (SAR) images of a region near Traverse City obtained from JPL.

In this paper, measured C-, L- and P-band polarimetric SAR images of Mt. Shasta in northern California, simultaneously obtained by JPL, are analyzed against the multivariate K -distribution to lend support to the above model.

Section II derives the multivariate K -distribution. In Section III, the JPL data in the form of averaged Stokes matrices are outlined and the effects of averaging on the probability distribution of clutter are discussed. In Section IV, the measured cumulative density functions (CDF) of JPL data at C-, L-, and P-bands are compared with theoretical values of the K -distribution.

II. MULTIVARIATE K -DISTRIBUTION

We consider a discrete scatterer model for the polarimetric terrain radar clutter in this section. The polarimetric scattering data are shown to be multivariately K -distributed, if the number of scatterers within the region of electromagnetic illumination obeys a negative binomial distribution [16]. An alternative derivation of the multivariate K -distribution is given in Appendix A.

The received polarimetric data \bar{X} can be written as the sum of the polarimetric return from each of N independent scatterers inside the illuminated region. For terrain and sea clutter, the cross section is normalized with respect to the area A illuminated by the radar. Thus the polarimetric data are given as

$$\bar{X} = \frac{1}{\sqrt{A}} \sum_{j=1}^N \bar{X}_j \quad (1)$$

where \bar{X}_j corresponds to the scattered polarimetric data from the j th scatterer and all \bar{X}_j are independent identically distributed n -dimensional random vectors with zero mean, i.e., $E(\bar{X}_j) = 0$. The dimension of \bar{X} corresponds to the number of radar channels. For the polarimetric backscattering from a reciprocal medium, where HV equals to VH, the dimension of \bar{X} is taken to be six, considering the I (in-phase) and Q (quadrature) components of HH, HV, and VV separately.

The characteristic function of \bar{X} , given the number of scatterers N , is the N th power of the characteristic function of \bar{X}_j with argument scaled by \sqrt{A} .

Now let N be a negative binomial random variable such that

$$P(N) = \frac{\Gamma(N + \alpha)}{\Gamma(N + 1)\Gamma(\alpha)} \frac{(N\alpha/\alpha)^N}{(1 + N\alpha/\alpha)^{N+\alpha}} \quad (2)$$

where $N\alpha$ can be interpreted as the average number of scatterers observed within the illuminated region. Then, averaging the characteristic function of (1) over N , and as the illuminated area A approaching infinity with $N\alpha/A$ kept constant, we have a unconditioned characteristic function of \bar{X}

$$\Phi_{N\alpha}(\bar{k}) \cong \left[1 + \frac{1}{2\alpha} \bar{k}^T \cdot \bar{C} \cdot \bar{k} \right]^{-\alpha} \quad (3)$$

In (3),

$$\bar{C} = \frac{N\alpha \bar{C}_s}{A} \quad (4)$$

is the fully polarimetric covariance matrix [17] measured by the radar system and \bar{C}_s can be attributed to the fundamental scattering properties of a single scatterer:

$$\bar{C}_s = E(\bar{X}_j \bar{X}_j^T) \quad (5)$$

In general, \bar{C}_s , which contains information regarding the geometry and the constituents of each single scatterer, is a function of the probing radar frequency and look angle. For example, \bar{C}_s for leaves or branches of vegetation will be influenced by their distributions of shape, tilt angle, and permittivity.

The corresponding limiting distribution of \bar{X} , obtained by carrying out the inverse Fourier transform of (3), is the multivariate K -distribution [16],

$$P(\bar{X}) = \frac{1}{(2\pi)^{n/2} |\bar{C}|^{1/2}} \frac{(2\alpha)^{n/4 + \alpha/2} \bar{X}^T \cdot \bar{C}^{-1} \cdot \bar{X})^{\alpha/2 - n/4}}{2^{\alpha-1} \Gamma(\alpha)} \times K_{n/2 - \alpha} \left[\sqrt{2\alpha} \bar{X}^T \cdot \bar{C}^{-1} \cdot \bar{X} \right]^{1/2} \quad (6)$$

As the parameter α goes to infinity, (3) and (6) approach the characteristic function and probability density function, respectively, of the Gaussian distribution.

If the in-phase and quadrature components of each polarization are of equal variance and uncorrelated, the intensity distribution for the return at each polarization reduces to [9,11]

$$p(I) = \frac{2\alpha}{\sigma^2 \Gamma(\alpha)} \left(\frac{\alpha I}{\sigma^2} \right)^{\alpha-1/2} K_{\alpha-1} \left(2\sqrt{\frac{\alpha I}{\sigma^2}} \right) \quad (7)$$

where the variable I represents the intensity of each polarization and σ^2 corresponds to the average intensity. If α approaches infinity, (7) reduces to the exponential distribution:

$$p(I) = \left(\frac{1}{\sigma^2} \right) \exp \left[-I/\sigma^2 \right] \quad (8)$$

corresponding to the intensity distribution for a complex Gaussian random variable.

III. EXPERIMENTAL DATA FORMAT AND ITS PROBABILITY DISTRIBUTION

Mt. Shasta data recorded with two different formats, the scattering matrix and the four-look averaged Stokes matrix, have been obtained from JPL. The averaged Stokes matrix format was developed to reduce the speckle effects from the observed polarization signatures [7]. Because of the averaging process, it is shown in this section that the statistical distribution of averaged Stokes matrix is distinctly different from that of scattering matrix data; whereas the next section shows that the scattering matrix data for two clutter classes on Mt. Shasta area have a K -distribution which is a closed form expression, being a very desirable feature for the purpose of fully polarimetric classification [1,4]. However, no closed form expression is available yet for the probability distribution of the averaged Stokes matrix.

The Stokes matrix is a linear combination of the squared quantities of the measured scattering matrix

$$[M] = [R^t]^{-1} \begin{bmatrix} S_{hh}S_{hh}^* & S_{hv}S_{hv}^* & S_{hh}S_{hv}^* & S_{hh}S_{hh}^* & S_{hv}S_{hv}^* & S_{hh}S_{hv}^* \\ S_{vh}S_{vh}^* & S_{vv}S_{vv}^* & S_{vh}S_{vv}^* & S_{vh}S_{vv}^* & S_{vv}S_{vv}^* & S_{vh}S_{vv}^* \\ S_{hh}S_{vh}^* & S_{hv}S_{vh}^* & S_{hh}S_{vv}^* & S_{hh}S_{vh}^* & S_{hv}S_{vh}^* & S_{hh}S_{vv}^* \\ S_{vh}S_{hh}^* & S_{vv}S_{hh}^* & S_{vh}S_{hv}^* & S_{vv}S_{hv}^* & S_{vh}S_{vv}^* & S_{vv}S_{vv}^* \end{bmatrix} [R]^{-1} \quad (9)$$

where

$$[R] = \begin{bmatrix} 1 & 1 & 0 & 0 \\ 1 & -1 & 0 & 0 \\ 0 & 0 & 1 & 1 \\ 0 & 0 & -i & i \end{bmatrix} \quad (10)$$

and superscript t represents transpose. $S_{\mu\nu}$ is the element of scattering matrix corresponding to μ received and ν transmitted polarizations. The subscripts h and v represent the horizontal and vertical polarizations of the transmitted or received electric field, respectively. Note that in the backscattering direction $S_{vh} = S_{hv}$ for a reciprocal medium [17].

In order to reduce the statistical variations of the power measurements, the Stokes matrix has been averaged over L individual measurements at the expense of spatial resolution ($L = 4$ for standard JPL data).

$$[M]_L = \sum_{n=1}^L \frac{[M_n]}{L} \quad (11)$$

where $[M_n]$ is the Stokes matrix of n th measurement.

The effects of averaging on the probability distribution are demonstrated for the following example, Fig. 1. If I_n (e.g., $|S_{hh}|^2$) is exponentially distributed (8) or $\sqrt{I_n}$ is Rayleigh, the L -look averaged intensity I has a Gamma distribution

$$p(I) = \frac{1}{\Gamma(L)} \left(\frac{L}{\sigma^2} \right) \left(\frac{LI}{\sigma^2} \right)^{L-1} \exp \left[-\left(\frac{LI}{\sigma^2} \right) \right] \quad (12)$$

where

$$I = \frac{\sum_{n=1}^L I_n}{L} \quad (13)$$

Also included in Fig. 1 are the curves for the K -distribution (7) and the 4-look averaged K -distributed intensities. The averaged K -distributed quantities are obtained by Monte Carlo simulation: K -distributed random vectors are generated, and the corresponding Stokes matrices are formed and averaged over every four samples to simulate the 4-look averaged Stokes matrix. It is seen that the averaged quantities have a smaller standard deviation than the unaveraged quantities.

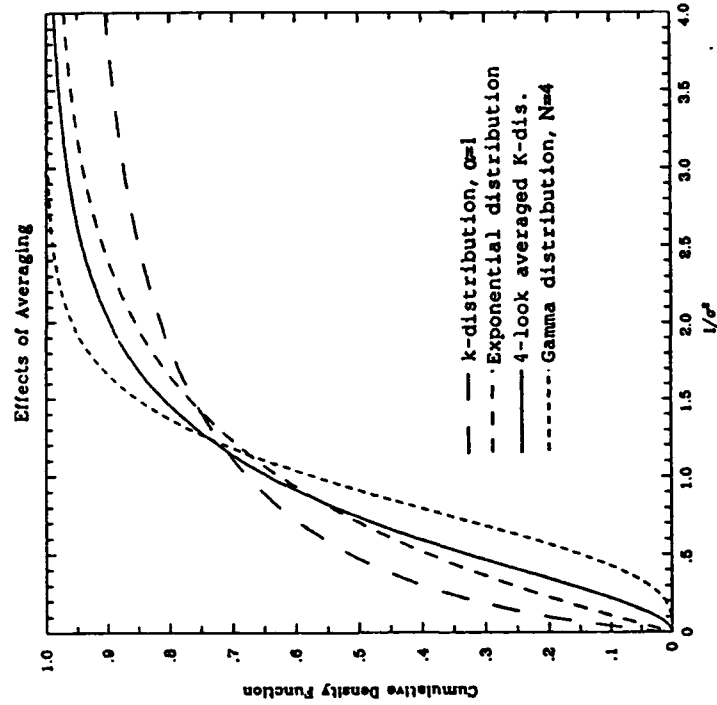


Figure 1. Comparison for cumulative density functions between 4-look averaged and unaveraged data.

IV. RESULTS AND DISCUSSIONS

The SAR images of areas on Mt. Shasta obtained from JPL are analyzed in this section. Mt. Shasta data contain simultaneously measured C-, L- and P-band polarimetric SAR images of an area on Mt. Shasta in northern California [19]. The images cover an area of about 12 km by 5 km and each pixel represents 6.662 m in slant range and 3.03 m in azimuth on the ground. The imaged Mt. Shasta site contains some forested areas with conifers and some hardwoods and a burned region having smaller trees (35 meters versus 45 meters for the the undamaged

area) [19]. Data are plotted and compared with K -distribution for two clutter classes: the forested area and the burned area.

To compare K -distribution with the experimental data, analyzed are the following quantities derived from the scattering matrix data at each frequency band:

$$A_{hh} = |S_{hh}| \quad (14a)$$

$$A_{hv} = |S_{hv}| \quad (14b)$$

$$A_{vv} = |S_{vv}| \quad (14c)$$

$$\phi_{hhvv} = \angle \left(\frac{S_{hh} S_{vv}^*}{(S_{hh} S_{vv}^*)} \right) \quad (14d)$$

$$\phi_{hhvv} = \angle \left(\frac{S_{hh} S_{vv}^*}{(S_{hh} S_{vv}^*)} \right) \quad (14e)$$

$$r_{hhvv} = \frac{A_{vv}}{A_{hh}} \quad (14f)$$

$$r_{hhvv} = \frac{A_{hv}}{A_{hh}} \quad (14g)$$

where $\langle \cdot \rangle$ represents the ensemble average of the averaged data over the sample areas. $\angle \cdot$ denotes the phase angle of the argument.

In order to estimate the parameter α from the experimental data, it is useful to define the following normalized intensity moments,

$$I_{HH}^{(2)} = \frac{\langle A_{hh}^4 \rangle}{\langle A_{hh}^2 \rangle^2} \quad (15a)$$

$$I_{HV}^{(2)} = \frac{\langle A_{hv}^4 \rangle}{\langle A_{hv}^2 \rangle^2} \quad (15b)$$

$$I_{VV}^{(2)} = \frac{\langle A_{vv}^4 \rangle}{\langle A_{vv}^2 \rangle^2} \quad (15c)$$

After the scattering matrix data are analyzed, it is found that the in-phase and quadrature components of the experimental data are approximately zero mean, uncorrelated, and of equal variance. This enables us to completely specify the real covariance matrix \bar{C} in (6) in terms of the measured complex covariance matrix of S_{hh} , S_{hv} , and S_{vv} , and provides the following formula [11,16]

$$I^{(2)} = 2 \left(1 + \frac{1}{\alpha} \right) \quad (16)$$

Note that $\alpha = \infty$ for Gaussian distribution.

Figure 2 illustrates the averaged normalized intensity moment $I^{(2)}$ and the estimated α versus wavelength for these two selected clutter classes. The parameter α is estimated to be 2.49 at C-band, 2.47 at L-band, and 2.46 at P-band for the undamaged forest; whereas α is estimated to be 3.2, 2.3, and 1.9 for C-, L-, and P-bands, respectively, for the burned forest area. It appears that the clutter power variation, $I^{(2)}$, is larger toward the lower frequency band for the clutter region, whereas it remains essentially constant for the healthy forested area at all frequency bands. This can be due to the differing penetration effects between

these two regions.

Larger clutter fluctuation $I^{(2)}$ at the lower frequency band could be due to the fact that electromagnetic waves at different frequencies experience different penetration depths, and therefore the resulting scattering effects differ. At the burned forest area, waves at C-band may remain within the upper crown region, while the P-band waves may penetrate into the lower crown region and probably reach the trunk and underlying soil regions where the scatterers are in general less homogeneously distributed. As a result, the clutter fluctuation at the lower frequency band increases. However, the healthy forest may be so dense that the waves at all frequency bands remain within the upper crown region. Hence the same scattering effects are observed for the healthy forest area. The other possible reason is that the physical resolution area of JPL instrument is essentially kept constant for all frequency bands, but if scaled by the wavelength, the effective number of scatterers in a resolution cell for P-band is the smallest among all. This will also results in more clutter variation (smaller α) in P-band. Because of insufficient ground truth, the frequency dependence of α needs to be further studied.

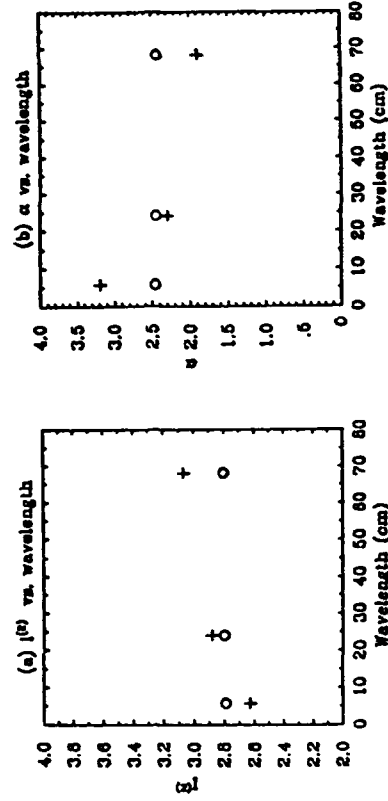


Figure 2. Measured (a) $I^{(2)}$ and (b) α versus wavelength at C-, L-, and P-bands. o represents forested area and + for burned area.

The measured CDFs of amplitude, phase difference, and amplitude ratios have been computed for both clutter classes and are all in very good agreement with the expected K -distribution at all frequency bands. The corresponding curves for the K -distribution were computed from (12) and (32) in [16] by selecting a parameter α and a covariance matrix \bar{C} that match the experimental data at each frequency band. Figs. 3-6 illustrate the C-band data from the selected areas. The measured CDFs of A_{hh} , A_{hv} , and A_{vv} are shown in Figs. 3 and 5 where σ represents the measured standard deviation of signal amplitudes over the selected area. The Rayleigh distribution is also included for comparison. The calculated and measured CDFs of amplitude ratios A_{vv}/A_{hh} and A_{hv}/A_{hh} , and

phases ϕ_{hhvv} and ϕ_{hhhh} are shown in Figs. 4 and 6 for both clutter classes. It can be seen that the experimental data are in good agreement with the expected K -distribution.

In the following, the effects of polarimetric radar miscalibration and radar characteristics at different frequencies will be addressed for the statistics of the polarimetric radar clutter. For the polarimetric miscalibration, the presence of the cross-talk and channel imbalance makes the measured scattering (covariance) matrix elements become the linear combination of the true scattering (covariance) matrix elements. Hence, just like the measured polarimetric data shown in this paper having a K -distribution, the original polarimetric data will also be K -distributed except having a different covariance matrix.

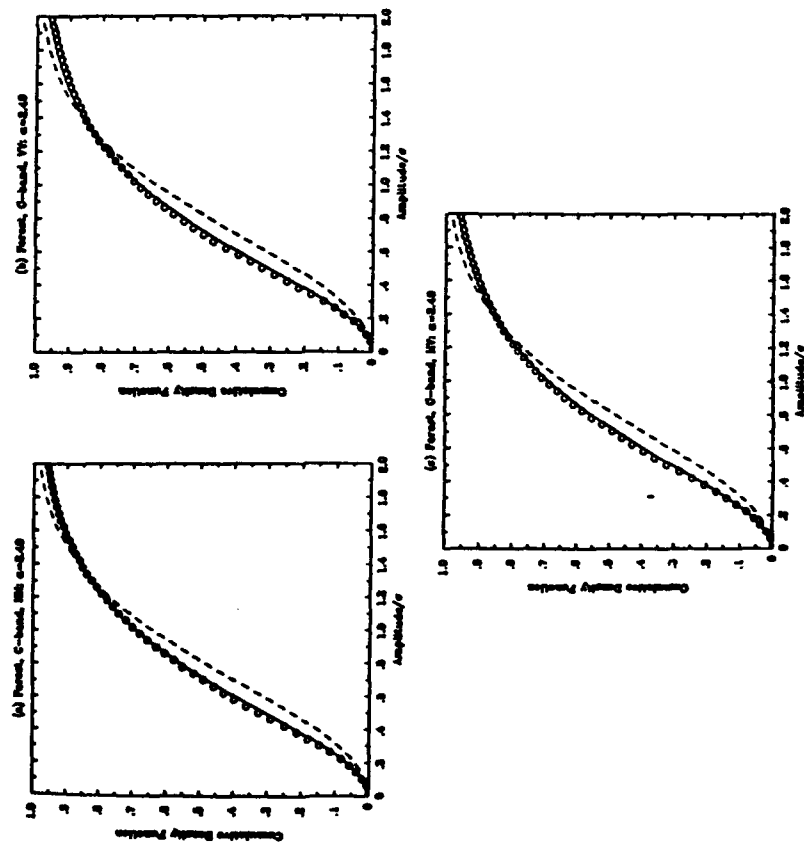


Figure 3. Cumulative density function versus (a) A_{hh} , (b) A_{vv} , and (c) A_{hv} for C-band SAR image of Mt. Shasta forests. \circ represents experimental data. The dashed line represents Rayleigh distribution and the solid curve K -distribution with $\alpha = 2.49$.

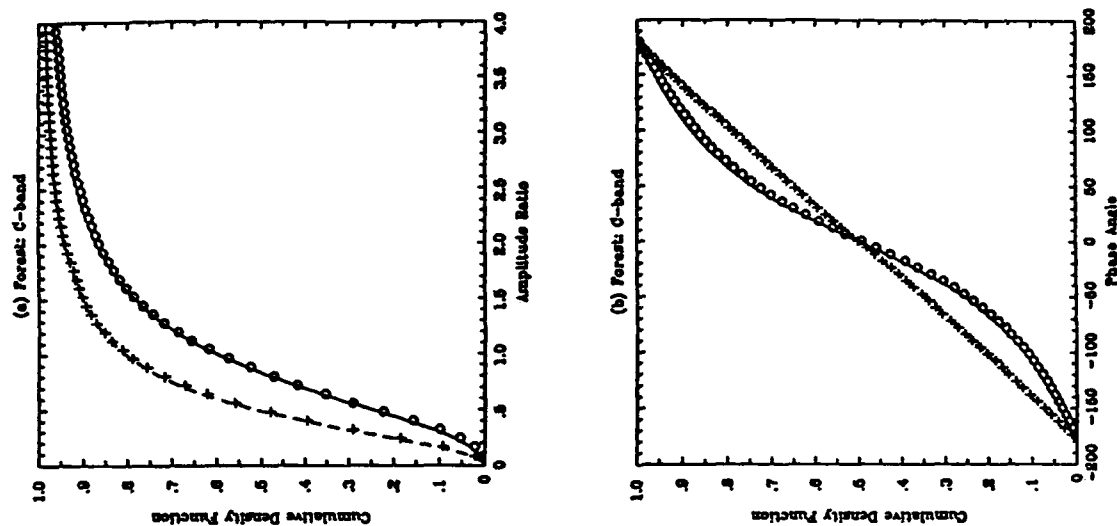


Figure 4. Cumulative density function versus (a) A_{vv}/A_{hh} and A_{hv}/A_{hh} , and (b) ϕ_{hhvv} and ϕ_{hhhv} for C-band SAR image of Mt. Shasta forests. \circ represents measured A_{vv}/A_{hh} or ϕ_{hhvv} . $+$ represents measured A_{hv}/A_{hh} or ϕ_{hhhv} . Solid and dashed curves correspond to the expected K -distribution.

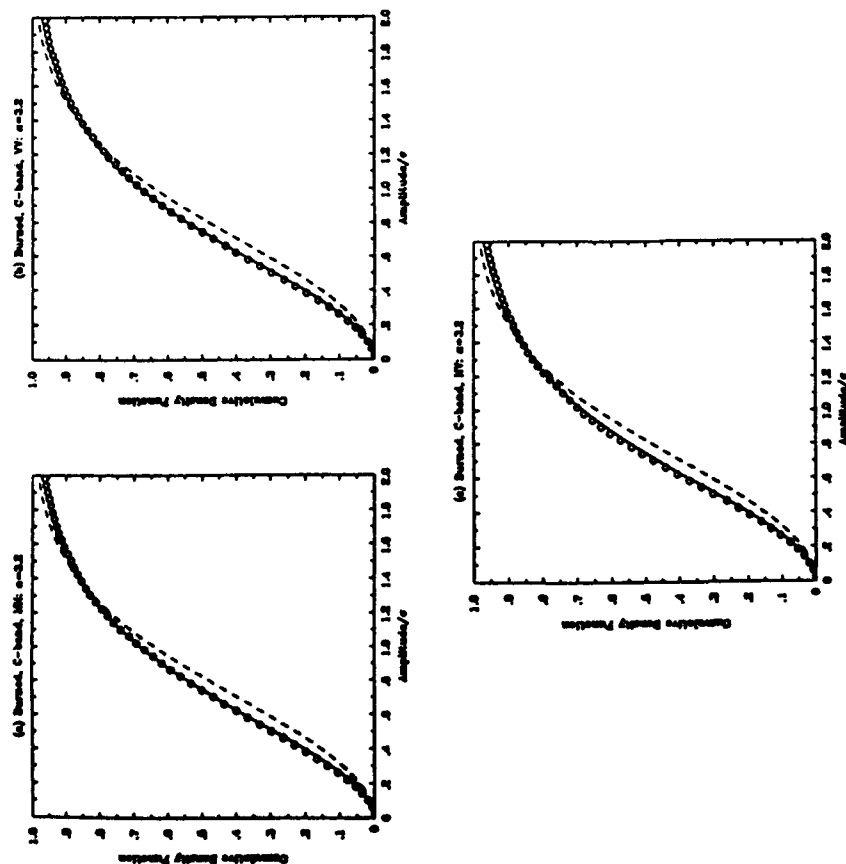


Figure 5. Cumulative density function versus (a) A_{HH} , (b) A_{VV} , and (c) A_{HV} for C-band SAR image of Mt. Shasta burned area. \circ represents experimental data. The dashed line represents Rayleigh distribution and the solid curve K -distribution with $\alpha = 3.2$.

Another common concern is whether the observed statistics for the cross-polarization HV is due to the polarization cross-talk. We can expect that if HV is due to the cross-coupling from HH or VV channels, then HV should be highly correlated with HH and VV. However, the experimental data show that the measured correlation coefficient is small between HV and HH or VV ranging from 0.03 to 0.2 except for the L-band images of the undamaged forest (≈ 0.3). Note that the correlation coefficient, defined as the magnitude of the covariance normalized by the standard deviation, is one for complete correlation and zero for no correlation. The fact that the correlation coefficient is small indicates that the

effect of cross-talk was small in measured HV. As seen in Fig. 4(b) the fairly small correlation between HH and HV (0.05) results in an almost uniform distribution for the measured ϕ_{HHV} as compared with the measured distribution for ϕ_{HHV} (0.4 correlation between HH and VV).

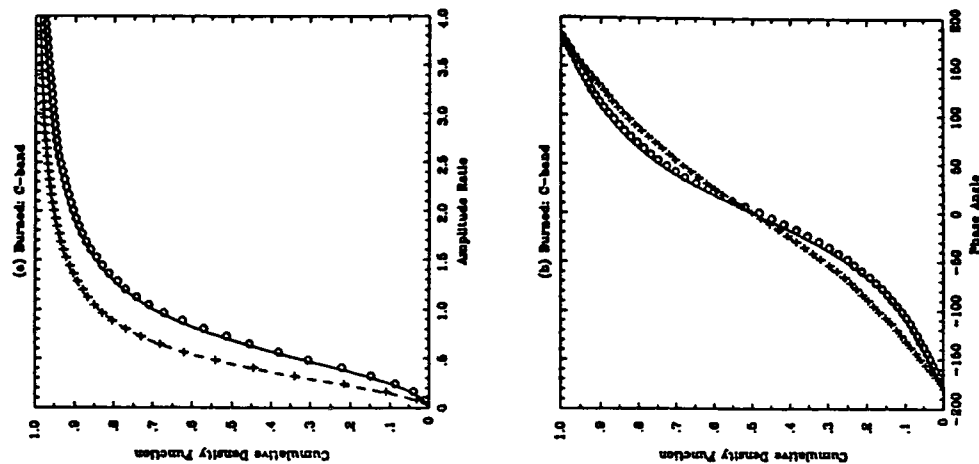


Figure 6. Cumulative density function versus (a) A_{VV}/A_{HH} and A_{HV}/A_{HH} , and (b) ϕ_{HHV} and ϕ_{HHh} for C-band SAR image of Mt. Shasta burned area. \circ represents measured A_{VV}/A_{HH} or ϕ_{HHV} . $+$ represents measured A_{HV}/A_{HH} or ϕ_{HHh} . Solid and dashed curves correspond to the expected K -distribution.

The remaining issue is whether the observed frequency behavior of α is due to the radar characteristics at different frequency bands. As indicated before, α inverted from the normalized intensity moment $I^{(2)}$ characterizes the spatial variation of the power. Hence, fluctuations of both terrain clutter and variations due to the system misfunction will contribute to the measured power variation. However, it is reasonable to believe that the radar system parameters, including the radar transmitted power, the antenna gains, and the platform motions at each frequency band remain essentially constant within a short time period while the radar is imaging over each sample area. Therefore, the observed K -distribution in this paper should be the result of terrain clutter fluctuations.

The multivariate K -distribution for polarimetric scattering from terrain cover is confirmed by the simultaneous multi-frequency experimental data obtained from the Jet Propulsion Laboratory. This suggests that the K -distribution (6) with a parameter α and a covariance matrix can be used to characterize the statistics of fully polarimetric backscatter returns from vegetation covers at each frequency band.

APPENDIX A: ALTERNATIVE DERIVATION OF MULTIVARIATE K -DISTRIBUTION

By assuming the Gaussian statistics for \bar{X} and a large N_a , an alternative derivation of the multivariate K -distribution will be given in this appendix. The final result will provide a useful simulation model for the multivariate K -distributed random vector.

Using the asymptotic expansion of gamma function for large argument,

$$\Gamma(z) \approx z^{z-1/2} e^{-z} \sqrt{2\pi} \quad (A1)$$

it can be shown that for large N_a and N the negative binomial distribution (2) can be approximated by

$$P(N)\Delta N \approx \frac{1}{\Gamma(\alpha)} e^{1-\alpha} \alpha^\alpha \left(\frac{N}{N_a}\right)^\alpha \frac{(1+\alpha/N)^N}{(1+\alpha/N_a)^N} \frac{(1+\alpha/N)^\alpha}{(1+\alpha/N_a)^\alpha} \times (1+1/N)^{-N} \sqrt{\frac{N+1}{N+\alpha N+1}} \frac{\Delta N}{\Delta N} \quad (A2)$$

where $\Delta N = 1$. Thus

$$P(N)\Delta N \approx \frac{1}{\Gamma(\alpha)} \alpha^\alpha \left(\frac{N}{N_a}\right)^\alpha \exp\left(-\frac{\alpha N}{N_a}\right) \frac{N_a}{N} \Delta\left(\frac{N}{N_a}\right) \quad (A3)$$

Introducing the variable

$$\mu = N/N_a \quad (A4)$$

then (A3) can be written as

$$P(N)\Delta N = P(\mu)d\mu = \frac{\alpha^\alpha \mu^{\alpha-1}}{\Gamma(\alpha)} \exp(-\alpha\mu)d\mu \quad (A5)$$

It can be readily identified that $P(\mu)$ is a gamma probability density function for the continuous random variable μ , which may also be regarded as the continuum limit of the corresponding negative binomial distribution with large N_a and N .

At this moment, let the number N be fixed and approaches infinity. Then, by the central limit theorem, the statistics of the polarimetric return (1) can be approximated as Gaussian

$$P(\bar{X}|N) = \frac{1}{(2\pi)^{n/2} |\mu\bar{C}|^{1/2}} \exp\left[-\frac{\bar{X}^t \cdot (\mu\bar{C})^{-1} \cdot \bar{X}}{2}\right] \quad (A6)$$

where \bar{C} is given in (4) and μ is defined by (A4).

Averaging the above conditional Gaussian distribution over the negative binomial distribution at large N and N_a

$$\sum_N P(\bar{X}|N)P(N) \approx \int_0^\infty d\mu P(\bar{X}|N)P(\mu) \quad (A7)$$

the integration of the last integral can be carried out exactly [14] and gives rise to the multivariate K -distribution (6).

The above result indicates that the K -distributed random vector \bar{X} can be considered as a conditional Gaussian random vector with the absolute radar cross section varying as a Gamma random variable. This model has been termed as the product model [18]. This interpretation helps to generate the K -distribution in the following way: First generate a gamma random number μ with a given parameter α and then generate a Gaussian random vector \bar{X} according to the covariance matrix $\mu\bar{C}$.

ACKNOWLEDGMENTS

This work was supported by the ONR Contract N00014-89-J-1107, the ARMY Corp of Engineers Contract DACA39-87-K-0022, the NASA Contract NAGW-1617, and the NASA Contract 958461.

This work was also sponsored by the U.S. Air Force under Contract F19628-C-85-0002. The views expressed are those of the authors and do not reflect the official policy or position of the U.S. Government.

The Editor thanks M. Borgeaud, L. M. Novak, C. J. Oliver, J. van Zyl, and two anonymous Reviewers for reviewing the paper.

REFERENCES

1. Kong, J. A., A. A. Swartz, H. A. Yueh, L. M. Novak, and R. T. Shin, "Identification of terrain cover using the optimum polarimetric classifier," *J. Electro. Waves Applic.*, Vol. 2, No. 2, 171-194, 1988.
2. Yueh, H. A., A. A. Swartz, J. A. Kong, R. T. Shin, and L. M. Novak, "Bayes classification of terrain cover using normalised polarimetric data," *J. Geophys. Res.*, Vol. 93, No. B12, 15261-15267, 1988.
3. Swartz, A. A., H. A. Yueh, J. A. Kong, L. M. Novak, and R. T. Shin, "Optimal polarizations for achieving maximum contrast in radar images," *J. Geophys. Res.*, Vol. 93, No. B12, 15252-15260, 1988.

4. Lim, H., A. A. Swartz, H. A. Yueh, J. A. Kong, R. T. Shin, and J. J. van Zyl, "Classification of earth terrain using synthetic aperture radar images," *J. Geophys. Res.*, Vol. 93, No. B12, 15253-15260, 1988.
5. Durden, S. L., J. J. van Zyl, and H. A. Zebker, "Modelling and observation of the radar polarization signature of forested areas," *IEEE Trans. Geosci. Remote Sensing*, Vol. GE-27, 1989.
6. Zebker, H. A., J. J. van Zyl, and D. N. Held, "Imaging radar polarimetry from wave synthesis," *J. Geophys. Res.*, Vol. 92, No. B1, 683-701, 1987.
7. Van Zyl, J. J., H. A. Zebker, and C. Elachi, "Imaging radar polarization signature: theory and observation," *Radio Science*, Vol. 22, No. 4, 529-543, 1987.
8. Trunk, G. V., "Non-Rayleigh sea-clutter: properties and detection of targets," *Automatic Detection and Radar Data Processing*, D. C. Schleher Ed., Artch House, 1988.
9. Jao, J. K., "Amplitude distribution of composite terrain radar clutter and the K -distribution," *IEEE Trans. Antennas Propagat.*, Vol. AP-32, No. 10, 1049-1062, 1984.
10. Jakeman, E., and P. N. Pusey, "A model for non-Rayleigh sea echo," *IEEE Trans. Antennas Propagat.*, Vol. AP-24, No. 6, 806-814, 1976.
11. Jakeman, E., "On the statistics of K -distributed noise," *J. Phys. A: Math. Gen.*, 13, 31-48, 1980.
12. Schütz, K., "K-distributed phase differences in turbulent random phase screens," *J. Opt. Soc. Am.*, Vol. 73, No. 3, 269-276, 1983.
13. Barakat, R., "Weak-scatterer generalization of the K -density function with application to laser scattering in atmospheric turbulence," *J. Opt. Soc. Am. A.*, Vol. 3, No. 4, 401-409, 1986.
14. Jakeman, E., and R. J. A. Tough, "Generalised K distribution: a statistical model for weak scattering," *J. Opt. Soc. Am. A.*, Vol. 4, No. 9, 1764-1772, 1987.
15. Andrews, L. C., and R. L. Phillips, "I - K distribution as a universal propagation model of laser beams in atmospheric turbulence," *J. Opt. Soc. Am. A.*, Vol. 2, No. 2, 160-163, 1985.
16. Yueh, H. A., J. A. Kong, J. K. Jao, R. T. Shin, and L. M. Novak, "K-distribution and polarimetric terrain radar clutter," *J. Electro. Waves Applic.*, Vol. 3, No. 8, 747-768, 1989.
17. Borgesand, M., R. T. Shin, and J. A. Kong, "Theoretical models for polarimetric radar clutter," *J. Electro. Waves Applic.*, Vol. 1, No. 1, 67-86, 1987.
18. Novak, L. M., M. B. Sechin, and M. J. Cardullo, "Studies on target detection algorithms which use polarimetric radar data," *IEEE Trans. on Aerospace Electronic Systems*, Vol. AES-25, No. 2, 1989.
19. Durden, S. L., J. J. van Zyl, and H. A. Zebker, "The unpolarised component in polarimetric radar observations of forested areas," *IEEE Trans. Geosci. Remote Sensing*, 28(2), 268-271, 1990.

S. H. Yueh received the SB (1982) and SM (1984) from the Electrical Engineering Department of National Taiwan University, Taiwan, and is currently working on the Ph.D. degree in electrical engineering at Massachusetts Institute of Technology, Cambridge. His fields of interest are electromagnetic field theory and remote sensing.

J. A. Kong is Professor of Electrical Engineering and Chairman of Area IV on Energy and Electromagnetic Systems in the Department of Electrical Engineering and Computer Science at the Massachusetts Institute of Technology in Cambridge, Massachusetts. His research interest is in the field of electromagnetic wave theory and applications. He has published 7 books and over 300 refereed journal and conference papers, and is the Editor of the Wiley Series in Remote Sensing, and Chief Editor of the Elsevier book series of Progress in Electromagnetics Research (PIER).

Jen King Jao received the B.Sc. degree in electrophysics from National Chiao-Tung University, Hsinchu, Taiwan, in 1988, and the Ph.D. degree in electrical engineering from the Massachusetts Institute of Technology, Cambridge, Massachusetts, in 1976. While in MIT, he did his thesis studies on microwave and optical wave interactions in solid state materials. From 1975 to 1978, he was with Riverside Research Institute working on laser radars, electro-optical systems, and measurements. From 1978 to 1979, he was employed by Raytheon Co. performing coherent CO₂ laser radar sensor design. Since 1979, he has been with MIT Lincoln Laboratory working in the general area of air defense radar phenomenology including analyses and modeling of radar clutter. In recent years, his activities concentrated on the development, measurement, and evaluation of advanced airborne pulse-Doppler radars. Dr. Jao is a member of the American Physical Society, the Institute of Electrical and Electronic Engineers, and the American Association for the Advancement of Science.

R. T. Shin received his SB (1977), SM (1980), and Ph.D. (1984) in electrical engineering from the Massachusetts Institute of Technology. Since 1984 he has been on the Research Staff in the Air Defense Techniques Group at the MIT Lincoln Laboratory. His research interest is the areas of electromagnetic wave scattering and propagation and theoretical model development and data interpretation for microwave remote sensing. He is the coauthor of *Theory of Microwave Remote Sensing* (Wiley, 1985). Dr. Shin is a member of the IEEE, American Geophysical Union, Tau Beta Pi, Eta Kappa Nu, and Commission F of the International Union of Radio Science.

Howard A. Zebker received the B.S., M.S., and Ph.D. degrees from the California Institute of Technology, University of California at Los Angeles, and Stanford University, respectively. His dissertation was on the solution of particle size distribution functions for Saturn's rings, as derived from Voyager radio occultation data. At present he is supervisor of the Radar System Science and Engineering Group at the NASA Jet Propulsion Laboratory, where he is involved in the development of new techniques such as radar polarimetry and radar interferometry. His current research interests include planetary exploration, EM scattering theory and measurement, and radar system design and calibration.

Thuy Le Toan received the Engineer degree and the Ph.D. degree in physics from the Paul Sabatier University, Toulouse, France. In 1973, she joined the Centre d'Etude Spatiale des Rayonnements where she is presently leader of the Remote Sensing Group. Since 1973, her research activity has been in the area of microwave remote sensing applied to vegetation. Her research interests include experimentation and modeling of microwave interaction with agricultural and forested media, and analysis of SAR images. She has served as the Project Coordinator and Principal Investigator of several Microwave Airborne experiments in Europe and is the Principal Investigator of ERS-1 and SIR-C projects. Dr. Le Toan is member of the Land Application Working Group (European Space Agency), the SAR expert team (ESA), the Space SAR Adhoc team (Centre National d'Etude Spatiale). She is member of the Electromagnetics Academy. She is the recipient of the 1988 Symposium Prize Paper Award of the IEEE Geoscience and Remote Sensing Society.

9

CALIBRATION OF POLARIMETRIC RADARS USING IN-SCENE REFLECTORS

S. H. Yuch, J. A. Kong, and R. T. Shin

- 9.1 Introduction
- 9.2 Polarimetric Calibration Using Three In-Scene Reflectors
 - a. S_1 and S_2 are Singular
 - b. S_1 and S_2 are Nonsingular
 - c. S_1 is Singular and S_2 is Nonsingular
- 9.3 Uniqueness
- 9.4 Polarimetric Calibration Using Three Simple In-Scene Reflectors
 - a. Two Dipoles and One General Target
 - b. One Trihedral Reflector, One Target with Diagonal Scattering Matrix, and One General Target
 - c. One Dipole, One Trihedral Reflector, and One General Reflector
- 9.5 Misalignment
 - a. Uniform Misalignment
 - b. Relative Misalignment
- 9.6 Effect of Noise
- 9.7 Polarimetric Compensation
- 9.8 Summary
- Acknowledgments
- Appendices
- References

9.1 Introduction

Polarimetric radar backscatter data observed with satellite and airborne synthetic aperture radars (SAR) have demonstrated potential applications in geologic mapping and terrain cover classification [1-8]. Accurate calibration of such polarimetric radar systems is essential for polarimetric remote sensing of earth terrain. In this chapter, we will investigate the polarimetric calibration using three in-scene reflectors and provide a calibration algorithm which will be a useful tool in radar image interpretation.

The concept and formulation of polarimetric calibration using in-scene reflectors were developed by Barnes [9]. The transmitting and receiving ports of the polarimetric radar are modeled by two unknown polarisation transfer matrices. The measured polarimetric scattering matrix is then expressed as the product of the transfer matrix of the receiving port, the scattering matrix of the illuminated target, the transfer matrix of the transmitting port, and a common factor. These two unknown polarisation transfer matrices are determined by using the measured scattering matrices from targets with known polarisation scattering parameters.

Two sets of simple targets, screened corner reflectors (SCRs) and top-hats with a trihedral, have been investigated [9]. The SCR approach uses three SCRs (wire grids in front of trihedral corner reflectors) oriented at 0° , 45° , and 90° , respectively. The top hats are dihedral-like reflectors oriented at 0° and 45° . The SCR approach solved for all unknowns exactly while the top-hat approach solved approximately for cross-talk and imbalance by assuming the cross-polarisation coupling to be small. The top-hat approach was concluded to be superior to the SCR approach on the achievable polarimetric purity and broad angular pattern of targets, sensitivity on misalignment, and effect of noise.

Besides the passive corner reflectors, a set of Polarimetric Active Radar Calibrators (PARCs) is also used to calibrate the L-band and C-band airborne imaging radar images [10]. The advantage of the PARCs approach is that a very high signal-to-background-noise ratio (S/B) can be achieved. Initial results indicate that in some polarizations the S/B is as high as 60 dB, which will totally eliminate the effects of background noise. The tradeoff is that PARCs are more expensive, and the scattering characteristics may be more sensitive to the change of environmental temperature than the passive reflectors.

A polarimetric calibration algorithm using three reciprocal reflectors has been developed for the case where at least two of the scattering matrices can be simultaneously diagonalized [11]. The algorithm allows more degrees of freedom in the choice of calibration devices and makes it possible to analyze the sensitivities on noise and misalignment for each set of calibration targets.

All of the calibration procedures outlined above are based on the deployed point targets. When the point targets are not available, natural distributed targets (clutter) have good potential in polarimetric calibration. A technique to calibrate compressed polarimetric radar images using natural targets and trihedral corner reflectors was introduced by van Zyl [12]. The method is based on the theoretical results that the co- and cross-polarized components of the scattering matrix are uncorrelated for natural targets with azimuthal symmetry [13,14].

The objectives of this chapter are to generalize the polarimetric calibration algorithm developed in [11] for nonreciprocal calibrators, such as PARCs, and provide the performance analysis and comparison for several typical target sets. In section 9.2, a Polarisation-basis Transformation technique (PT) is introduced to convert the scattering matrices into one of six sets of targets with simpler scattering matrices. The solution to the original problem then can be expressed in terms of the solution for simple scattering matrices. In section 9.3, the uniqueness of polarimetric calibration using three targets is addressed for all possible combinations of scattering parameters. Section 9.4 presents the polarimetric calibration solution for three sets of targets which correspond to the case where the scattering matrices of at least two of the calibration targets can be simultaneously diagonalized. Section 9.5 illustrates the effects of misalignment for six sets of calibration targets. In section 9.6, the effect of noise is illustrated for those six target sets and the PARCs [10]. Explicit polarimetric compensation formulas, which can be used to remove the effect of the radar distortion matrices from measured data, are given in section 9.7.

9.2 Polarimetric Calibration Using Three In-Scene Reflectors

The polarimetric calibration using three in-scene reflectors is formulated in this section. A set of coupled nonlinear equations is derived for the unknown system parameters including channel imbalance and

polarization cross-talk errors (isolation) for both transmitter and receiver.

The model of the polarimetric radar system defined in [9,11] is employed to formulate the problem. Assume that the measured polarization scattering matrices corresponding to three in-scene reflectors are

$$X = \begin{bmatrix} X_{11} & X_{12} \\ X_{21} & X_{22} \end{bmatrix} = e^{i\phi_1} R S_1 T \quad (1a)$$

$$Y = \begin{bmatrix} Y_{11} & Y_{12} \\ Y_{21} & Y_{22} \end{bmatrix} = e^{i\phi_2} R S_2 T \quad (1b)$$

$$Z = \begin{bmatrix} Z_{11} & Z_{12} \\ Z_{21} & Z_{22} \end{bmatrix} = e^{i\phi_3} R S_3 T \quad (1c)$$

where S_1 , S_2 , and S_3 are the (undistorted) polarization scattering matrices of the calibration targets, and the matrices T and R account for the mismatch and cross-polarization coupling of the transmitting and receiving ports, respectively.

$$R = \begin{bmatrix} R_{11} & R_{12} \\ R_{21} & R_{22} \end{bmatrix}, \quad T = \begin{bmatrix} T_{11} & T_{12} \\ T_{21} & T_{22} \end{bmatrix} \quad (2)$$

Note that the matrix R equals the transpose of the matrix B in [9]. The factor $\exp(i\phi_k)$ accounts for the phase delay and attenuation due to atmospheric effects and the path length between the radar and the target. This is treated as a nuisance parameter, and the objective of the polarimetric calibration is to solve for the normalized quantities of R and T matrices in terms of the normalized quantities of the X , Y , and Z matrices.

The normalized quantities, t_{12} , t_{21} , t_{22} , r_{12} , r_{21} , and r_{22} are defined by

$$t_{12} = T_{12}/T_{11} \quad (3a)$$

$$t_{21} = T_{21}/T_{11} \quad (3b)$$

$$t_{22} = T_{22}/T_{11} \quad (3c)$$

$$r_{12} = R_{12}/R_{11} \quad (3d)$$

$$r_{21} = R_{21}/R_{11} \quad (3e)$$

$$r_{22} = R_{22}/R_{11} \quad (3f)$$

r_{22} and t_{22} are the parameters describing channel imbalance, whereas r_{12} , r_{21} , t_{12} , and t_{21} are the parameters for polarization cross-talk. Note that (1) gives a set of coupled nonlinear equations for the system parameters.

In general, it is difficult to solve the unknowns directly from these nonlinear equations for three calibration targets with arbitrary scattering parameters. Another difficulty is in determining how many sets of solutions exist for a given set of targets. The latter issue involves whether it is sufficient to use only three targets. The Polarization-basis Transformation technique (PT) is presented to simplify the complexity of the problem and resolve these issues. The method will simultaneously diagonalize two matrices, or diagonalize one and transform the other one into a Jordan Canonical form.

The physical interpretation of the transformation scheme, PT, is that instead of working on the original polarization basis (e.g., linear basis) yielding complicated scattering matrices, we find a particular polarization basis so that the scattering matrices turn out to have a simpler form like $(A)-(F)$ to be discussed below. Hence the transformation method is in effect performing a polarization basis transformation. There are three positive features associated with this transformation scheme:

- (i) It enables us to solve the calibration problem using only some simple targets. The polarimetric calibration using general targets can be obtained from these simple target cases by straightforward matrix inversion and multiplication.
- (ii) The transformation method helps us to determine the number of solutions associated with any given set of calibration targets.
- (iii) If there are multiple sets of solutions, the relationship between all the solutions can be clearly identified. Once we obtain a particular solution, the other solutions can be obtained by using the transformation relation.

The essence of PT is to find two nonsingular matrices A and B so that the scattering matrices of calibration targets can be transformed into one of the following cases:

$$(A) \begin{bmatrix} 1 & 0 \\ 0 & 0 \end{bmatrix}, \begin{bmatrix} 0 & 0 \\ 0 & 1 \end{bmatrix}, \begin{bmatrix} c & d_1 \\ d_2 & e \end{bmatrix}$$

$$(B) \begin{bmatrix} 1 & 0 \\ 0 & 1 \end{bmatrix}, \begin{bmatrix} a & 0 \\ 0 & b \end{bmatrix}, \begin{bmatrix} c & d_1 \\ d_2 & e \end{bmatrix}$$

$$(C) \begin{bmatrix} a & 0 \\ 0 & 0 \end{bmatrix}, \begin{bmatrix} 1 & 0 \\ 0 & 1 \end{bmatrix}, \begin{bmatrix} c & d_1 \\ d_2 & e \end{bmatrix}$$

$$(D) \begin{bmatrix} 1 & 0 \\ 0 & 1 \end{bmatrix}, \begin{bmatrix} a & 1 \\ 0 & a \end{bmatrix}, \begin{bmatrix} c & d_1 \\ d_2 & e \end{bmatrix}$$

$$(E) \begin{bmatrix} 1 & 0 \\ 0 & 0 \end{bmatrix}, \begin{bmatrix} 0 & 1 \\ 0 & 0 \end{bmatrix}, \begin{bmatrix} c & d_1 \\ d_2 & e \end{bmatrix}$$

$$(F) \begin{bmatrix} 1 & 0 \\ 0 & 0 \end{bmatrix}, \begin{bmatrix} 0 & 0 \\ 1 & 0 \end{bmatrix}, \begin{bmatrix} c & d_1 \\ d_2 & e \end{bmatrix}$$

(A)-(C) correspond to the cases where S_1 and S_2 can be simultaneously diagonalized. (D)-(F) represent the cases where S_1 and S_2 cannot be simultaneously diagonalized. If it is possible to obtain the calibration solution using the targets with the above scattering matrices, then the solution for the general case can be obtained by an inverse transformation. The PT scheme will be described in detail in the remainder of this section.

a. S_1 and S_2 are Singular

Assuming that S_1 and S_2 are both singular, two nonsingular matrices A and B can be obtained such that S_1 and S_2 can be written into one of the following forms:

$$S_1 = A \begin{bmatrix} 1 & 0 \\ 0 & 0 \end{bmatrix} B \quad (4a)$$

$$S_2 = A \begin{bmatrix} 0 & 0 \\ 0 & 1 \end{bmatrix} B \quad (4b)$$

or

$$S_1 = A \begin{bmatrix} 1 & 0 \\ 0 & 0 \end{bmatrix} B \quad (5a)$$

$$S_2 = A \begin{bmatrix} 0 & 1 \\ 0 & 0 \end{bmatrix} B \quad (5b)$$

or

$$S_1 = A \begin{bmatrix} 1 & 0 \\ 0 & 0 \end{bmatrix} B \quad (6a)$$

$$S_2 = A \begin{bmatrix} 0 & 0 \\ 1 & 0 \end{bmatrix} B \quad (6b)$$

Equation (4) corresponding to case (A) represents the situation where S_1 and S_2 can be simultaneously diagonalized. Equations (5) and (6) correspond to cases (E) and (F), respectively.

Because of the particularly simple equations (4)-(6), it is easy to solve for nonsingular matrices A and B in terms of the scattering parameters of S_1 and S_2 by explicitly multiplying out the right-hand-side of the equations and equating the results term-by-term with S_1 and S_2 . After A and B are found, the scattering matrix of the third target is also transformed accordingly as follows

$$S_3 = A \begin{bmatrix} c & d_1 \\ d_2 & e \end{bmatrix} B \quad (7)$$

or

$$\begin{bmatrix} c & d_1 \\ d_2 & e \end{bmatrix} = A^{-1} S_3 B^{-1} \quad (7')$$

We will describe how PT helps to reduce the complexity of the problem for case (A) in detail. The same idea applies to all other cases. For case (A), we can pre and postmultiply (1) by A^{-1} and B^{-1} , respectively, and substitute (4) and (7) into the resulting equations. Thus, (1) becomes

$$X' = A^{-1} X B^{-1} = e^{i\phi_1} R' \begin{bmatrix} 1 & 0 \\ 0 & 0 \end{bmatrix} T' \quad (8a)$$

$$Y' = A^{-1} Y B^{-1} = e^{i\phi_2} R' \begin{bmatrix} 0 & 0 \\ 0 & 1 \end{bmatrix} T' \quad (8b)$$

$$Z' = A^{-1} Z B^{-1} = e^{i\phi_3} R' \begin{bmatrix} c & d_1 \\ d_2 & e \end{bmatrix} T' \quad (8c)$$

where

$$R' = A^{-1} \begin{bmatrix} R_{11} & R_{12} \\ R_{21} & R_{22} \end{bmatrix} A \quad (9a)$$

$$T' = B \begin{bmatrix} T_{11} & T_{12} \\ T_{21} & T_{22} \end{bmatrix} B^{-1} \quad (9b)$$

Note that if the polarimetric calibration can be solved for the calibration targets with the scattering matrices given by cases (A)-(F), then it is straightforward to obtain the solution to the original problem by inverting (9a) and (9b).

It should also be noted that case (F) can be solved by taking advantage of similarity between case (E) and case (F). Taking the transpose of (1) results in

$$X^t = e^{i\phi_1} T^t S_1^t R^t \quad (10a)$$

$$Y^t = e^{i\phi_2} T^t S_2^t R^t \quad (10b)$$

$$Z^t = e^{i\phi_3} T^t S_3^t R^t \quad (10c)$$

where superscript t represents transpose. When S_1 and S_2 have the form of case (F), S_1^t and S_2^t become the form of case (E). If we know how to determine the solution for case (E), then it is straightforward to determine the solution for case (F).

b. S_1 and S_2 are Nonsingular

If both S_1 and S_2 are nonsingular, based on the same idea discussed above, we would like to transform the scattering matrices of these targets into the form of case (B) or (D). That is, to find the transformation matrices A and B such that

$$S_1 = A \begin{bmatrix} 1 & 0 \\ 0 & 1 \end{bmatrix} B \quad (11a)$$

$$S_2 = A \begin{bmatrix} a & 0 \\ 0 & b \end{bmatrix} B \quad (11b)$$

if S_1 and S_2 can be diagonalized simultaneously (case B), otherwise

$$S_1 = A \begin{bmatrix} 1 & 0 \\ 0 & 1 \end{bmatrix} B \quad (12a)$$

$$S_2 = A \begin{bmatrix} a & 1 \\ 0 & a \end{bmatrix} B \quad (12b)$$

which corresponds to case (D) with $a \neq 0$.

Inverting (11a) or (12a), we obtain

$$B = A^{-1} S_1. \quad (13)$$

If $S_2 S_1^{-1}$ has distinct eigenvalues, substituting (13) into (11b) gives

$$S_2 S_1^{-1} A = A \begin{bmatrix} a & 0 \\ 0 & b \end{bmatrix} \quad (14)$$

This is a typical eigenvalue problem. a and b corresponding to eigenvalues and A can be obtained by solving for the eigenvectors of the corresponding eigenvalues.

If $S_2 S_1^{-1}$ has double-order eigenvalues ($a = b$), we should perform the transformation (12b) yielding

$$S_2 S_1^{-1} A = A \begin{bmatrix} a & 1 \\ 0 & a \end{bmatrix} \quad (15)$$

This corresponds to transforming $S_2 S_1^{-1}$ into the Jordan canonical form.

Like the transformation method resulting in (8), the scattering matrix of the third target is also transformed according to (7). Hence, the polarimetric calibration using general targets can be transformed into the calibration problem using the simple targets: cases (B) or (D). The transformed and original R and T matrices are related to each other by (9).

c. S_1 is Singular and S_2 is Nonsingular

When S_1 is singular and S_2 is nonsingular, the transformation matrix A can be found so that

$$S_1 = A \begin{bmatrix} a & 0 \\ 0 & 0 \end{bmatrix} B \quad (16a)$$

$$S_2 = A \begin{bmatrix} 1 & 0 \\ 0 & 1 \end{bmatrix} B \quad (16b)$$

when S_1 and S_2 can be simultaneously diagonalized, otherwise

$$S_1 = A \begin{bmatrix} 0 & 1 \\ 0 & 0 \end{bmatrix} B \quad (17a)$$

$$S_2 = A \begin{bmatrix} 1 & 0 \\ 0 & 1 \end{bmatrix} B \quad (17b)$$

By inverting (16b) or (17b), matrix B is given as

$$B = A^{-1} S_2 \quad (18)$$

whereas A is obtained by solving the following eigenvalue problem:

$$S_1 S_2^{-1} A = A \begin{bmatrix} a & 0 \\ 0 & 0 \end{bmatrix} \quad \text{for case (C),} \quad (19)$$

or

$$S_1 S_2^{-1} A = A \begin{bmatrix} 0 & 1 \\ 0 & 0 \end{bmatrix} \quad \text{for case (D) with } a = 0. \quad (20)$$

Again (19) and (20) become the typical eigenvalue and eigenvector problem for matrix diagonalization and Jordan canonical form transformation, respectively. Subsequently, the third scattering matrix is transformed into the form of (7). Like the approach used in arriving at (8) and (9), once the normalized quantities of R' and T' are solved, the normalized quantities of R and T are obtained through (9).

In this section, we presented how the problem of polarimetric calibration using a general set of targets can be transformed into one of the simple target sets in (A)-(F). The transformation method enables us to work on the simple cases and also obtain the solution for more complicated cases. In general, there may be $3! (= 6)$ ways to arrange the order of the targets such that the transformed problem reduces to the cases shown in (A)-(F). It is always better to choose the order which makes the solution less sensitive to additive noise and misalignment of targets. This can be done by computer simulation of each possible order of calibration targets. Thus, the polarimetric radar calibration with three general targets can be completely solved using the method of PT if the polarimetric calibration using the simple targets (A)-(F) is solved.

9.3 Uniqueness

In this section, the uniqueness problems associated with each case are discussed. The method of PT is used to find out the number of solutions and the transformation relation between multiple solutions for each set of targets outlined in (A)-(F), section 9.2.

Suppose that the scattering matrices of three targets are S_1 , S_2 , and S_3 . The method is to find all the possible A and B matrices such that

$$S_i = c_i A S_i B, \quad i = 1, 2, 3 \quad (21)$$

where c_i 's are the appropriate scaling constant, which do not affect the solution of the normalized quantities (3). It is easy to see that the identity matrix is a trivial solution for both A and B in (21).

Substituting (21) into (1), we obtain

$$X = c_1 e^{i\phi_1} R A S_1 B T \quad (22a)$$

$$Y = c_2 e^{i\phi_2} R A S_2 B T \quad (22b)$$

$$Z = c_3 e^{i\phi_3} R A S_3 B T \quad (22c)$$

Comparing (1) and (22) indicates that if there are any solutions for A and B other than identity matrix, then the normalized quantities of

$$\begin{aligned} R' &= R A \\ T' &= B T \end{aligned} \quad (23)$$

are also solutions to the original problem. If a particular solution is solved from (1), (23) can be used to generate the other solutions.

Tables 9.1 through 9.5 list the solutions of A and B for cases (A)-(E) in section 9.2. In those tables, I denotes the identity matrix, and matrices A_1 - A_6 , B_1 , D_1 , and D_2 are defined as follows:

$$\begin{aligned} A_1 &= \begin{bmatrix} A_{11} & 0 \\ 0 & A_{22} \end{bmatrix} \\ A_2 &= \begin{bmatrix} A_{22} & 0 \\ 0 & A_{11} \end{bmatrix} \\ A_3 &= \begin{bmatrix} A_{11} & A_{12} \\ 0 & A_{11} \end{bmatrix} \\ A_4 &= \begin{bmatrix} A_{11} & (A_{22} - A_{11})c/d_2 \\ 0 & A_{22} \end{bmatrix} \\ A_5 &= \begin{bmatrix} A_{11} & (A_{11} - A_{22})d_1/(c - e) \\ 0 & A_{22} \end{bmatrix} \\ A_6 &= \begin{bmatrix} A_{11} & (A_{22} - A_{11})d_1/e \\ 0 & A_{22} \end{bmatrix} \\ B_1 &= \begin{bmatrix} B_{11} & 0 \\ 0 & B_{22} \end{bmatrix} \\ D_1 &= \begin{bmatrix} 0 & d_1 \\ d_2 & 0 \end{bmatrix} \\ D_2 &= \begin{bmatrix} 0 & d_1 \\ -d_2 & 0 \end{bmatrix} \end{aligned}$$

| No. | Parameters | Solution of A and B |
|-----|-------------------------------|---------------------|
| 1 | $d_1 d_3 c \neq 0$ | $A = B = I$ |
| 2 | $d_1 d_3 e \neq 0$ | $A = B = I$ |
| 3 | $d_1 c e \neq 0$ | $A = B = I$ |
| 4 | $d_3 c e \neq 0$ | $A = B = I$ |
| 5 | $d_1 c \neq 0, d_3 = e = 0$ | $A = A_1, B = I$ |
| 6 | $d_1 e \neq 0, d_3 = c = 0$ | $A = I, B = B_1$ |
| 7 | $d_3 c \neq 0, d_1 = e = 0$ | $A = I, B = B_1$ |
| 8 | $d_3 e \neq 0, d_1 = c = 0$ | $A = A_1, B = I$ |
| 9 | $d_1 d_3 \neq 0, c = e = 0$ | $A = B = A_1$ |
| 10 | $c e \neq 0, d_1 = d_3 = 0$ | $A = A_1, B = A_3$ |
| 11 | $d_1 \neq 0, d_3 = c = e = 0$ | $A = A_1, B = B_1$ |
| 12 | $d_3 \neq 0, d_1 = c = e = 0$ | $A = A_1, B = B_1$ |
| 13 | $c \neq 0, d_1 = d_3 = e = 0$ | $A = A_1, B = B_1$ |
| 14 | $e \neq 0, d_1 = d_3 = c = 0$ | $A = A_1, B = B_1$ |

Table 9.1 All possible solutions of A and B matrices that may transform the scattering matrices of three calibration targets into themselves for case A with $\begin{bmatrix} 1 & 0 \\ 0 & 0 \end{bmatrix}, \begin{bmatrix} 0 & 0 \\ 0 & 1 \end{bmatrix}, \begin{bmatrix} c & d_1 \\ d_2 & e \end{bmatrix}$.

If the elements of A_i , B_1 , and D_i are not assigned a definite number, then they are considered arbitrary as long as A_i , B_1 , and D_i remain nonsingular. As can be seen from Tables 9.1-9.5, many cases do not provide a finite set of solutions for the polarimetric calibration using three targets. Note that case (F) is not shown separately because of the one to one correspondence between case (F) and case (E) (see the discussion given at the end of section 9.2.a).

9.4 Polarimetric Calibration Using Three Simple In-Scene Reflectors

Solutions of polarimetric calibration using three sets of simple cal-

ibrators are presented in this section. These three cases correspond to the situation that at least two of the scattering matrices can be simultaneously diagonalized. The solutions to the following cases are presented separately in the remainder of this section: (A) two dipoles and one general target, (B) one trihedral, one target with diagonal

| No. | Parameters | Solution of A |
|-----|--|---|
| 1 | $d_1 = d_3 = 0, c = \pm e$ | $A_1, \begin{bmatrix} 0 & A_{12} \\ A_{21} & 0 \end{bmatrix}$ |
| 2 | $d_1 = d_3 = 0, c \neq \pm e$ | A_1 |
| 3 | $d_3 \neq 0, d_1 = c = e = 0$ | A_1 |
| 4 | $d_1 \neq 0, d_3 = c = e = 0$ | A_1 |
| 5 | $c \neq 0, d_1 \neq 0, a \neq -b \text{ or } c \neq \pm e$ | I |
| 6 | $c \neq 0, d_3 \neq 0, a \neq -b \text{ or } c \neq \pm e$ | I |
| 7 | $e \neq 0, d_1 \neq 0, a \neq -b \text{ or } c \neq \pm e$ | I |
| 8 | $e \neq 0, d_3 \neq 0, a \neq -b \text{ or } c \neq \pm e$ | I |
| 9 | $d_1 d_3 \neq 0, c = e \neq 0, a = -b$ | I, D_1 |
| 10 | $d_1 d_3 \neq 0, c = -e \neq 0, a = -b$ | I, D_2 |
| 11 | $d_1 d_3 \neq 0, c = e = 0, a \neq -b$ | $I, \begin{bmatrix} 1 & 0 \\ 0 & -1 \end{bmatrix}$ |
| 12 | $d_1 d_3 \neq 0, c = e = 0, a = -b$ | $I, \begin{bmatrix} 1 & 0 \\ 0 & -1 \end{bmatrix}, D_1, D_2$ |
| 13 | $d_1 \neq 0, d_3 = 0, c = \pm e \neq 0, a = -b$ | I |
| 14 | $d_3 \neq 0, d_1 = 0, c = \pm e \neq 0, a = -b$ | I |

Table 9.2 $B = A^{-1}$ and all possible solutions of A matrix that may transform the scattering matrices of three calibration targets into themselves for case B with $\begin{bmatrix} 1 & 0 \\ 0 & 1 \end{bmatrix}, \begin{bmatrix} a & 0 \\ 0 & b \end{bmatrix}, \begin{bmatrix} c & d_1 \\ d_2 & e \end{bmatrix}$.

| No. | Parameters | Solution of A |
|-----|-----------------------------------|--|
| 1 | $cd_1 \neq 0$ | I |
| 2 | $cd_2 \neq 0$ | I |
| 3 | $cd_1 \neq 0$ | I |
| 4 | $cd_2 \neq 0$ | I |
| 5 | $d_1 d_2 \neq 0, c = e = 0$ | $I, \begin{bmatrix} 1 & 0 \\ 0 & -1 \end{bmatrix}$ |
| 6 | $c \neq 0, d_1 = d_2 = 0$ | A_1 |
| 7 | $e \neq 0, d_1 = d_2 = 0$ | A_1 |
| 8 | $d_1 = 0$ or $d_2 = 0, c = e = 0$ | A_1 |

Table 9.3 $B = A^{-1}$ and all possible solutions of A matrix that may transform the scattering matrices of three calibration targets into themselves for case C with $\begin{bmatrix} a & 0 \\ 0 & 0 \end{bmatrix}, \begin{bmatrix} 1 & 0 \\ 0 & 1 \end{bmatrix}, \begin{bmatrix} c & d_1 \\ d_2 & e \end{bmatrix}$.

| No. | Parameters | Solution of A |
|-----|--|--|
| 1 | $a \neq 0, d_2 = 0, c \neq e$ | I |
| 2 | $a \neq 0, d_2 = 0, c = e$ | A_3 |
| 3 | $a \neq 0, d_2 \neq 0$ | I |
| 4 | $a = 0, d_2 \neq 0, c \neq -e$ | I |
| 5 | $a = 0, d_2 \neq 0, c = -e, ce = d_1 d_2$ | A_4 |
| 6 | $a = 0, d_2 \neq 0, c = -e, ce \neq d_1 d_2$ | $I, \begin{bmatrix} 1 & -2c/d_2 \\ 0 & -1 \end{bmatrix}$ |
| 7 | $a = 0, d_2 = 0, c \neq e$ | A_5 |
| 8 | $a = 0, d_2 = 0, c = e$ | A_5 |

Table 9.4 $B = A^{-1}$ and all possible solutions of A matrix that may transform the scattering matrices of three calibration targets into themselves for case D with $\begin{bmatrix} 1 & 0 \\ 0 & 1 \end{bmatrix}, \begin{bmatrix} a & 1 \\ 0 & a \end{bmatrix}, \begin{bmatrix} c & d_1 \\ d_2 & e \end{bmatrix}$.

| No. | Parameters | Solution of A and B |
|-----|--------------------------------------|-------------------------|
| 1 | $d_2 \neq 0, d_1 = c = e = 0$ | $A = A_1, B = B_1$ |
| 2 | $d_1 \neq 0, d_2 = c = e = 0$ | $A = A_1, B = B_1$ |
| 3 | $c \neq 0, d_1 = d_2 = e = 0$ | $A = A_1, B = B_1$ |
| 4 | $e \neq 0, d_2 = d_1 = c = 0$ | $A = A_1, B = B_1$ |
| 5 | $d_1 c \neq 0, e = d_2 = 0$ | $A = A_1, B = I$ |
| 6 | $d_2 e \neq 0, c = d_1 = 0$ | $A = A_1, B = I$ |
| 7 | $d_2 c \neq 0, d_1 = e = 0$ | $A = A_4, B = B_1$ |
| 8 | $d_1 d_2 \neq 0, c = e = 0$ | $A = B = A_1$ |
| 9 | $ce \neq 0, d_2 = d_1 = 0$ | $A = A_1, B = A_2$ |
| 10 | $d_1 e \neq 0, d_2 = c = 0$ | $A = A_6, B = B_1$ |
| 11 | $e = 0, d_1 d_2 c \neq 0$ | $A = A_4, B = A_1$ |
| 12 | $d_2 = 0, cd_1 e \neq 0$ | $A = A_6, B = A_2$ |
| 13 | $d_1 = 0, d_2 ec \neq 0$ | $A = B = I$ |
| 14 | $c = 0, d_2 ed_1 \neq 0$ | $A = B = I$ |
| 15 | $d_2 ed_1 c \neq 0, ce \neq d_1 d_2$ | $A = B = I$ |
| 16 | $d_2 ed_1 c \neq 0, ce = d_1 d_2$ | $A = A_6, B = I$ |

Table 9.5 All possible solutions of A and B matrices that may transform the scattering matrices of three calibration targets into themselves for case E with $\begin{bmatrix} 1 & 0 \\ 0 & 0 \end{bmatrix}, \begin{bmatrix} 0 & 1 \\ 0 & 0 \end{bmatrix}, \begin{bmatrix} c & d_1 \\ d_2 & e \end{bmatrix}$.

scattering matrix, and one general reflector, and (C) one dipole, one trihedral, and one general reflector. These cases correspond to the cases (A)-(C) in section 9.2.

a. Two Dipoles and One General Target

The scattering matrices of three calibration targets are given as follows:

$$S_1 = \begin{bmatrix} 1 & 0 \\ 0 & 0 \end{bmatrix}, \quad S_2 = \begin{bmatrix} 0 & 0 \\ 0 & 1 \end{bmatrix}, \quad S_3 = \begin{bmatrix} c & d_1 \\ d_2 & e \end{bmatrix} \quad (24)$$

where the first two targets correspond to horizontal and vertical dipoles, respectively. The third target is a some other general reflector.

By substituting (24) into (1) and taking the ratio of the measurements, it can be easily shown that

$$t_{12} = \frac{X_{12}}{X_{11}} \quad (25a)$$

$$r_{21} = \frac{X_{21}}{X_{11}} \quad (25b)$$

$$r_{21}t_{12} = \frac{X_{22}}{X_{11}} \quad (25c)$$

$$\frac{t_{21}}{t_{22}} = \frac{Y_{21}}{Y_{22}} \quad (25d)$$

$$\frac{r_{12}}{r_{22}} = \frac{Y_{12}}{Y_{22}} \quad (25e)$$

$$\frac{r_{12}t_{21}}{r_{22}t_{22}} = \frac{Y_{11}}{Y_{22}} \quad (25f)$$

and

$$\frac{Z_{12}}{Z_{11}} = \frac{t_{12}c + t_{22}d_1 + r_{12}t_{12}d_2 + r_{12}t_{22}e}{c + t_{21}d_1 + r_{12}d_2 + r_{12}t_{21}e} \quad (26a)$$

$$\frac{Z_{21}}{Z_{11}} = \frac{r_{21}c + r_{21}t_{21}d_1 + r_{22}d_2 + r_{22}t_{21}e}{c + t_{21}d_1 + r_{12}d_2 + r_{12}t_{21}e} \quad (26b)$$

$$\frac{Z_{22}}{Z_{11}} = \frac{r_{21}t_{12}c + r_{21}t_{22}d_1 + r_{22}t_{12}d_2 + r_{22}t_{22}e}{c + t_{21}d_1 + r_{12}d_2 + r_{12}t_{21}e} \quad (26c)$$

In (26), Z_{11} is used to normalize the measurements of the other polarization channels. This is justified if the magnitude of c is not small. In cases where c is small, we can also use Z_{22} , Z_{12} , or Z_{21} to normalize the other quantities when e or d_1 or d_2 is not small.

In the following, the solutions for the normalized quantities of the R and T matrices given in (3) are presented for the following subcases (A.1) $cd_1d_2 \neq 0$, (A.2) $ed_1d_2 \neq 0$, (A.3) $d_1ce \neq 0$, (A.4) $d_2ce \neq 0$, and (A.5) $d_1d_2 = ce$ and $cd_1d_2e \neq 0$. Note that (A.1)-(A.4) correspond to the first four rows in Table 9.1. Case (A.5) can actually be covered by the cases (A.1)-(A.4). The reason the solution of this case is included is because of its particular simplicity. Also note that the cases (A.1) to (A.5) are not mutually exclusive to each other. For the parameters of S_2 in the common regime of validity, each formula can be applied.

9.4.1 H-dipole, V-dipole, and another reflector with $cd_1d_2 \neq 0$

3. For this case, the parameter e is arbitrary. By substituting (25) into (26), three linear equations are obtained with unknowns t_{22} , r_{22} , and $r_{21}t_{22}$. It is straightforward to solve for these unknowns. The solutions are given as

$$t_{22} = \frac{c}{d_1} \frac{Y_{22}}{X_{11}} \frac{\Delta_{11}}{\Delta_1} \quad (27a)$$

$$t_{21} = \frac{Y_{21}}{Y_{22}} t_{22} \quad (27b)$$

$$r_{22} = \frac{c}{d_2} \frac{Y_{22}}{X_{11}} \frac{\Delta_{1r}}{\Delta_1} \quad (27c)$$

$$r_{12} = \frac{Y_{12}}{Y_{22}} r_{22} \quad (27d)$$

where Δ_1 , Δ_{1r} , and Δ_{1r} are given by (A1) in appendix A.

If c is close to zero, it is impractical to apply the above solution to targets within a noisy background; if c is small, the determinant Δ_1 will also be small, and any additive noise will cause a large error in Δ_1 .

9.4.2 H-dipole, V-dipole, and another reflector with $ed_1d_2 \neq 0$

When $e \neq 0$, we can use Z_{22} to normalize the other elements of the Z matrix and obtain three equations. Like the derivation of the previous case, three linear equations are obtained for the unknowns $1/t_{21}$, $1/r_{22}$, and $1/r_{22}t_{22}$, by substituting (25a), (25b), (25d), and (25e) into these equations. The solutions are given by,

$$t_{22} = \frac{-d_2}{e} \frac{Y_{22}}{X_{11}} \frac{\Delta_2}{\Delta_{2r}} \quad (28a)$$

$$t_{21} = \frac{Y_{21}}{Y_{22}} t_{22} \quad (28b)$$

$$r_{22} = \frac{-d_1}{e} \frac{Y_{22}}{X_{11}} \frac{\Delta_2}{\Delta_{2r}} \quad (28c)$$

$$r_{12} = \frac{Y_{12}}{Y_{22}} r_{22} \quad (28d)$$

where Δ_2 , Δ_{2r} , and Δ_{2r} are given by (B1) in appendix B.

a.3 H-dipole, V-dipole, and another reflector with $d_{1ce} \neq 0$

When $d_1 \neq 0$, we use Z_{12} to normalize the other elements of the Z matrix and obtain three equations. Substituting (25a), (25b), (25d), and (25e) into these equations gives three linear equations for the unknowns $1/r_{22}$, r_{21} , and r_{22}/t_{22} . The solutions are given by,

$$t_{22} = \frac{c}{d_1} \frac{Y_{22}}{X_{11}} \frac{\Delta_3}{\Delta_{3r}} \quad (29a)$$

$$t_{21} = \frac{Y_{21}}{Y_{22}} t_{22} \quad (29b)$$

$$r_{22} = \frac{d_1}{c} \frac{Y_{22}}{X_{11}} \frac{\Delta_3}{\Delta_3} \quad (29c)$$

$$r_{12} = \frac{Y_{12}}{Y_{22}} r_{22} \quad (29d)$$

where Δ_3 , Δ_{3r} , and Δ_3 are given by (C1) in appendix C.

a.4 H-dipole, V-dipole, and another reflector with $d_{2ce} \neq 0$

When $d_2 \neq 0$, we use Z_{21} to normalize the other elements of the Z matrix and obtain three equations. By substituting (25a), (25b), (25d), and (25e) into these equations, three linear equations are obtained for the unknowns $1/r_{22}$, t_{22} , and t_{22}/r_{22} . The solution is given by,

$$t_{22} = \frac{d_2}{c} \frac{Y_{22}}{X_{11}} \frac{\Delta_4}{\Delta_4} \quad (30a)$$

$$t_{21} = \frac{Y_{21}}{Y_{22}} t_{22} \quad (30b)$$

$$r_{22} = \frac{c}{d_2} \frac{Y_{22}}{X_{11}} \frac{\Delta_4}{\Delta_{4r}} \quad (30c)$$

$$r_{12} = \frac{Y_{12}}{Y_{22}} r_{22} \quad (30d)$$

where Δ_4 , Δ_{4r} , and Δ_4 are given by (D1) in appendix D.

a.5 H-dipole, V-dipole, and inclined dipole with $d_1 d_2 = ce$ and $cd_1 d_2 e \neq 0$

The special case with $c = d_1 = d_2 = e = 1$ has been solved for the screened reflector approach in [9]. In this case the third target has a

singular matrix (i.e., $d_1 d_2 = ce$). When $d_1 d_2 = ce$, (26) will reduce to

$$\frac{Z_{12}}{Z_{11}} = \frac{t_{22} d_1 + t_{12} c}{t_{21} d_1 + c} \quad (31a)$$

$$\frac{Z_{21}}{Z_{11}} = \frac{r_{22} d_2 + r_{21} c}{r_{12} d_2 + c} \quad (31b)$$

$$Z_{22} Z_{11} = Z_{12} Z_{21} \quad (31c)$$

Then, the solution can be obtained from (25) and (31) and is given as

$$r_{22} = \frac{c}{d_2} \frac{Y_{22}}{X_{11}} \frac{X_{11} Z_{21} - X_{21} Z_{11}}{Y_{22} Z_{11} - Y_{12} Z_{21}} \quad (32a)$$

$$r_{12} = \frac{Y_{12}}{Y_{22}} r_{22} \quad (32b)$$

$$t_{22} = \frac{c}{d_1} \frac{Y_{22}}{X_{11}} \frac{X_{11} Z_{12} - X_{12} Z_{11}}{Y_{22} Z_{11} - Y_{21} Z_{12}} \quad (32c)$$

$$t_{21} = \frac{Y_{21}}{Y_{22}} t_{22} \quad (32d)$$

or

$$r_{22} = \frac{d_1}{c} \frac{Y_{22}}{X_{11}} \frac{X_{11} Z_{22} - X_{21} Z_{12}}{Y_{22} Z_{12} - Y_{12} Z_{22}} \quad (33a)$$

$$r_{12} = \frac{Y_{12}}{Y_{22}} r_{22} \quad (33b)$$

$$t_{22} = \frac{d_2}{c} \frac{Y_{22}}{X_{11}} \frac{X_{11} Z_{22} - X_{12} Z_{21}}{Y_{22} Z_{21} - Y_{21} Z_{22}} \quad (33c)$$

$$t_{21} = \frac{Y_{21}}{Y_{22}} t_{22} \quad (33d)$$

b. One Trihedral Reflector, One Target with Diagonal Scattering Matrix, and One General Target

For this case, the scattering matrices of the calibration targets are given as follows

$$S_1 = \begin{bmatrix} 1 & 0 \\ 0 & 1 \end{bmatrix}, \quad S_2 = \begin{bmatrix} a & 0 \\ 0 & b \end{bmatrix}, \quad S_3 = \begin{bmatrix} c & d_1 \\ d_2 & e \end{bmatrix} \quad (34)$$

where

$$ab \neq 0 \quad (35a)$$

$$a \neq b \quad (35b)$$

For this set of scattering matrices, the solutions are presented for the following subcases

(B.1) $c \neq e$, $d_1 \neq 0$ or $d_2 \neq 0$, and $ae \neq bc$,

(B.2) $a = -b$, $c = e \neq 0$, and $d_1 d_2 \neq 0$,

(B.3) $a \neq -b$, $c = e = 0$, and $d_1 d_2 \neq 0$,

(B.4) $a = -b$, $c = e = 0$, and $d_1 d_2 \neq 0$,

(B.5) $a \neq -b$, $c = e \neq 0$, and $d_1 \neq 0$ or $d_2 \neq 0$,

(B.6) $a = -b$, $c = e \neq 0$, $d_1 \neq 0$, and $d_2 = 0$,

(B.7) $a = -b$, $c = e \neq 0$, $d_2 \neq 0$, and $d_1 = 0$.

It will be shown in the following sections that the number of solutions is one for case (B.1), two for case (B.2), two for case (B.3), four for case (B.4), one for case (B.5), one for case (B.6), and one for case (B.7).

Note that the case with $c \neq e$, $d_1 \neq 0$ or $d_2 \neq 0$, and $ae = bc$ is not covered in (B.1)-(B.7). Under these circumstances, we should exchange the order of the first two targets and apply the method of PT [see (11)]. For example, we can select

$$A = \begin{bmatrix} 1 & 0 \\ 0 & 1 \end{bmatrix}, \quad B = \begin{bmatrix} a & 0 \\ 0 & b \end{bmatrix} \quad (36)$$

such that

$$S_2 = \begin{bmatrix} a & 0 \\ 0 & b \end{bmatrix} = A \begin{bmatrix} 1 & 0 \\ 0 & 1 \end{bmatrix} B \quad (37a)$$

$$S_1 = \begin{bmatrix} 1 & 0 \\ 0 & 1 \end{bmatrix} = A \begin{bmatrix} 1/a & 0 \\ 0 & 1/b \end{bmatrix} B \quad (37b)$$

$$S_3 = \begin{bmatrix} c & d_1 \\ d_2 & e \end{bmatrix} = A \begin{bmatrix} c/a & d_1/b \\ d_2/a & e/b \end{bmatrix} B \quad (37c)$$

It is easy to see that the new transformed matrices will become one of the cases, (B.2), (B.5), (B.6) and (B.7) presented in this section. It should also be noted that other cases not presented in this section do not provide a finite number of solutions (see Table 9.2).

By substituting (34) into (1a) and (1b), we first obtain the following equalities

$$t_{12} = \frac{\lambda X_{12} Y_{11} + X_{11} Y_{12} + \lambda (X_{12} Y_{11} - X_{11} Y_{12}) r_{12} t_{21}}{(1 + \lambda) X_{11} Y_{11}} \quad (38a)$$

$$r_{12} t_{22} = \frac{X_{12} Y_{11} - X_{11} Y_{12} + (X_{12} Y_{11} + \lambda X_{11} Y_{12}) r_{12} t_{21}}{(1 + \lambda) X_{11} Y_{11}} \quad (38b)$$

$$r_{21} = \frac{\lambda X_{21} Y_{11} + X_{11} Y_{21} + \lambda (X_{21} Y_{11} - X_{11} Y_{21}) r_{12} t_{21}}{(1 + \lambda) X_{11} Y_{11}} \quad (38c)$$

$$r_{22} t_{21} = \frac{X_{21} Y_{11} - X_{11} Y_{21} + (X_{21} Y_{11} + \lambda X_{11} Y_{21}) r_{12} t_{21}}{(1 + \lambda) X_{11} Y_{11}} \quad (38d)$$

$$r_{21} t_{12} = \frac{\lambda X_{22} Y_{11} + X_{11} Y_{22} + \lambda (X_{22} Y_{11} - X_{11} Y_{22}) r_{12} t_{21}}{(1 + \lambda) X_{11} Y_{11}} \quad (38e)$$

$$r_{22} t_{22} = \frac{X_{22} Y_{11} - X_{11} Y_{22} + (X_{22} Y_{11} + \lambda X_{11} Y_{22}) r_{12} t_{21}}{(1 + \lambda) X_{11} Y_{11}} \quad (38f)$$

where

$$\lambda = -\frac{b}{a} \quad (39)$$

The quantities on the left-hand-side of the above equations are expressed in terms of the measurements of the first two targets and the unknown quantity $r_{12} t_{21}$. After $r_{12} t_{21}$ is solved using the measured Z matrix, all the normalized quantities (3) can be solved subsequently.

b.1 $c \neq e$, $d_1 \neq 0$ or $d_2 \neq 0$, and $ae \neq bc$

The solution for $r_{12} t_{21}$ shown below is valid only for $c \neq e$ and $ae \neq bc$. To solve for $r_{12} t_{21}$, firstly, two equations for r_{22} and t_{22} are obtained by substituting (46a) and (46b) into (26a) and (26b). Then r_{22} and t_{22} are solved which are given by (42a) and (43a). Thereafter using (38) to express (42a) and (43a) in terms of the unknown $r_{12} t_{21}$ and substituting the final expressions of r_{22} , t_{22} , and (38) into (26c) gives one equation for $r_{12} t_{21}$. After some algebraic manipulation, $r_{12} t_{21}$ can be solved and is given as

$$r_{12} t_{21} = \frac{\Delta r_i}{\Delta} \quad (40)$$

where Δ and Δr_i are given by (E1) in appendix E. The products t_{12} , $r_{12} t_{22}$, r_{21} , $r_{22} t_{21}$, $r_{21} t_{12}$, and $r_{22} t_{22}$ can then be calculated from (38). Let

$$y'_{21} \equiv \frac{t_{21}}{t_{22}} = \frac{r_{22} t_{21}}{r_{22} t_{22}} \quad (41a)$$

$$y'_{12} \equiv \frac{r_{12}}{r_{22}} = \frac{r_{12} t_{22}}{r_{22} t_{22}} \quad (41b)$$

The following formulas are used to solve for r_{22} and t_{22} . When $c \neq 0$ and $d_1 \neq 0$

$$t_{22} = \frac{\Delta_{5t}}{\Delta_5} \quad (42a)$$

$$r_{22} = \frac{r_{22}t_{22}}{t_{22}} \quad (42b)$$

When $c \neq 0$ and $d_2 \neq 0$

$$r_{22} = \frac{\Delta_{5r}}{\Delta_5} \quad (43a)$$

$$t_{22} = \frac{r_{22}t_{22}}{r_{22}} \quad (43b)$$

When $c \neq 0$ and $d_1 \neq 0$,

$$t_{22} = \frac{\Delta_{6t}}{\Delta_6} \quad (44a)$$

$$r_{22} = \frac{r_{22}t_{22}}{t_{22}} \quad (44b)$$

When $c \neq 0$ and $d_2 \neq 0$,

$$r_{22} = \frac{\Delta_{6r}}{\Delta_6} \quad (45a)$$

$$t_{22} = \frac{r_{22}t_{22}}{r_{22}} \quad (45b)$$

where Δ_5 , Δ_{5t} , Δ_6 , Δ_{6t} , and Δ_{6r} are given in appendix F. After t_{22} and r_{22} are determined, t_{21} and r_{12} can be solved from (41) and given as

$$t_{21} = y'_{21}t_{22} \quad (46a)$$

$$r_{12} = y'_{12}r_{22} \quad (46b)$$

b.2 $a = -b$, $c = e \neq 0$, and $d_1d_2 \neq 0$

There are two sets of solutions for this case (No. 9, Table 9.2). Note that case No. 10 in Table 9.2 can be transformed into this case by exchanging the order of the first two targets and reapplying the

method of PT as discussed in section 9.2.b. From (38a), (38c), and (38e), the following quadratic equation for $r_{12}t_{21}$ can be obtained

$$a_1(r_{12}t_{21})^2 + 2a_2r_{12}t_{21} + a_3 = 0 \quad (47)$$

where

$$a_1 = (X_{12}Y_{11} - X_{11}Y_{12})(X_{21}Y_{11} - X_{11}Y_{21})$$

$$a_2 = (X_{12}X_{21}Y_{11}^2 - X_{11}^2Y_{12}Y_{21} - X_{11}X_{22}Y_{11}^2 + X_{11}^2Y_{11}Y_{22})$$

$$a_3 = (X_{12}Y_{11} + X_{11}Y_{12})(X_{21}Y_{11} + X_{11}Y_{21}) - 2X_{11}Y_{11}(X_{22}Y_{11} + X_{11}Y_{22})$$

After expressing a_1 and a_3 in terms of the elements of transfer matrices R and T and the scattering matrix elements a and b , it can be shown that

$$a_1 = a_3 \quad (48)$$

This means that these two roots of (47) are reciprocal to each other, i.e., if $r_{12}t_{21}$ is a solution, then $1/r_{12}t_{21}$ is the other solution. This obviously raises a problem in cases for which either r_{12} or t_{21} is zero.

In calculating the solutions for these cases, we find a root of (47) whose magnitude is smaller than one. For this root, we can employ (42)-(46) to solve for the corresponding t_{22} , r_{22} , t_{21} , and r_{12} . The second solution of (47) gives $r_{12}t_{21}$ with a magnitude greater than one and approaches infinity as r_{12} or t_{21} approaches zero. The relation between the solutions is discussed next, and an alternative way of obtaining the second solution is given.

The relation between two sets of solutions can be understood easily by exploring the symmetry property of this set of scattering matrices. Let the matrices A and B be

$$A = \begin{bmatrix} 0 & d_1 \\ d_2 & 0 \end{bmatrix}, \quad B = \begin{bmatrix} 0 & d_1 \\ d_2 & 0 \end{bmatrix} \quad (49)$$

By inserting the identity matrix between the scattering matrices and the transfer matrices in (1), it can be seen that

$$X = e^{i\phi_1} R A^{-1} A \begin{bmatrix} 1 & 0 \\ 0 & 1 \end{bmatrix} B B^{-1} T \quad (50a)$$

$$Y = e^{i\phi_2} R A^{-1} A \begin{bmatrix} a & 0 \\ 0 & -a \end{bmatrix} B B^{-1} T \quad (50b)$$

$$Z = e^{i\phi_3} R A^{-1} A \begin{bmatrix} c & d_1 \\ d_3 & c \end{bmatrix} B B^{-1} T \quad (50c)$$

Define

$$R' = RA^{-1} = \frac{1}{d_1 d_2} \begin{bmatrix} d_2 R_{12} & d_1 R_{11} \\ d_2 R_{22} & d_1 R_{21} \end{bmatrix} \quad (51a)$$

$$T' = B^{-1}T = \frac{1}{d_1 d_2} \begin{bmatrix} d_1 T_{21} & d_1 T_{22} \\ d_2 T_{11} & d_2 T_{12} \end{bmatrix} \quad (51b)$$

After straightforward multiplication, (50) becomes

$$X = e^{i\phi_1} R' \begin{bmatrix} 1 & 0 \\ 0 & 1 \end{bmatrix} T' \quad (52a)$$

$$Y = e^{i\phi_2 + i\pi} R' \begin{bmatrix} a & 0 \\ 0 & -a \end{bmatrix} T' \quad (52b)$$

$$Z = e^{i\phi_3} R' \begin{bmatrix} c & d_1 \\ d_2 & c \end{bmatrix} T' \quad (52c)$$

Comparing (52) with (1) indicates that if the normalized quantities of R and T are the solutions of (1), then the normalized quantities of R' and T' are also the solutions of (1). These two sets of solutions are related by (51). Therefore, after the solution with smaller $r_{12}'t_{21}$ is found, the other solution can be obtained by using the transformation relation given by (51).

b.3 $a \neq -b$, $c = e = 0$, and $d_1 d_2 \neq 0$

There are two sets of solutions for this case (No. 11, Table 9.2). By equating the product of (38a) and (38c) with (38e), a quadratic equation for $r_{12}'t_{21}$ is given in (47). The other quadratic equation can be obtained by multiplying (38f) with $r_{12}'t_{21}$ and equating the result with the product of (38b) and (38d). If $a \neq -b$ ($\lambda \neq 1$), these two second-order polynomial equations will be independent of each other. Thus, by canceling the second-order term from these two equations, $r_{12}'t_{21}$ can be solved and is given as

$$r_{12}'t_{21} = \frac{(1-\lambda)(X_{12}Y_{11} - X_{11}Y_{12})(X_{21}Y_{11} - X_{11}Y_{21})}{\left[\frac{\lambda(X_{12}Y_{11} - X_{11}Y_{12})(X_{21}Y_{11} - X_{11}Y_{21})}{\lambda(X_{12}Y_{11} - X_{11}Y_{12})(X_{21}Y_{11} - X_{11}Y_{21})} - (X_{12}Y_{11} + \lambda X_{11}Y_{12})(X_{21}Y_{11} + \lambda X_{11}Y_{21}) + (1+\lambda)X_{11}Y_{11}(X_{22}Y_{11} + \lambda X_{11}Y_{22}) \right]} \quad (53)$$

Then, t_{12} , $r_{12}'t_{22}$, r_{21} , $r_{22}'t_{21}$, $r_{21}'t_{12}$, and $r_{22}'t_{22}$ can be determined uniquely by (38).

There are two possible sets of solutions in this case for r_{12} , t_{21} , r_{22} , and t_{22} ,

$$r_{22} = \pm \sqrt{\frac{r_{22}'t_{22}(Z_{21} - r_{21}'y_{21}'Z_{12})}{Z_{12} - Z_{21}'y_{12}'t_{12}}} \frac{d_1}{d_2} \quad (54a)$$

$$t_{22} = \frac{r_{22}'t_{22}}{r_{22}} \quad (54b)$$

$$r_{12} = y_{12}'r_{22} \quad (54c)$$

$$t_{21} = y_{21}'t_{22} \quad (54d)$$

If the real parts of t_{22} or r_{22} can be required to be either greater or smaller than zero, then a unique solution can be chosen.

The relation between these two sets of solutions can also be understood by looking at the symmetry property of this set of targets. Let matrix A be

$$A = \begin{bmatrix} 1 & 0 \\ 0 & -1 \end{bmatrix} \quad (55)$$

By inserting the identity matrix between the scattering matrices and the transfer matrices in (1), it can be shown that

$$X = e^{i\phi_1} RA^{-1}A \begin{bmatrix} 1 & 0 \\ 0 & 1 \end{bmatrix} AA^{-1}T \quad (56a)$$

$$Y = e^{i\phi_2} RA^{-1}A \begin{bmatrix} a & 0 \\ 0 & b \end{bmatrix} AA^{-1}T \quad (56b)$$

$$Z = e^{i\phi_3} RA^{-1}A \begin{bmatrix} 0 & d_1 \\ d_2 & 0 \end{bmatrix} AA^{-1}T \quad (56c)$$

After straightforward multiplication, the above equations become

$$X = e^{i\phi_1} R' \begin{bmatrix} 1 & 0 \\ 0 & 1 \end{bmatrix} T' \quad (57a)$$

$$Y = e^{i\phi_2} R' \begin{bmatrix} a & 0 \\ 0 & b \end{bmatrix} T' \quad (57b)$$

$$Z = e^{i\phi_3 + i\pi} R' \begin{bmatrix} 0 & d_1 \\ d_2 & 0 \end{bmatrix} T' \quad (57c)$$

where

$$R' = \begin{bmatrix} R_{11} & R_{12} \\ R_{21} & R_{22} \end{bmatrix} A^{-1} = \begin{bmatrix} R_{11} & -R_{12} \\ R_{21} & -R_{22} \end{bmatrix} \quad (58a)$$

$$T' = A^{-1} \begin{bmatrix} T_{11} & T_{12} \\ T_{21} & T_{22} \end{bmatrix} = \begin{bmatrix} T_{11} & T_{12} \\ -T_{21} & -T_{22} \end{bmatrix} \quad (58b)$$

By comparing (57) with (1), it can be seen that if the normalized quantities of R and T are the solution of (1), then the normalized quantities of R' and T' are also a solution of (1). These two sets of solutions are related by (58).

b.4 $a = -b$, $c = e = 0$, and $d_1 d_2 \neq 0$

This case corresponds to case No. 12, Table 9.2. When $a = -b$ or $\lambda = 1$, there are two possible roots for $r_{12} t_{21}$ given by (47). For each root, there are two sets of solutions for r_{22} , t_{22} , r_{12} , and t_{21} which can be obtained by using (54). Therefore, there are four sets of solutions in this case. This case, $a = -b$ and $c = e = 0$, has both of the symmetry properties of cases B.2 and B.3. Therefore, these four sets of solutions can be related to each other by (51) or (58). This particular case ($d_1 = d_2$) has been solved approximately in [9] by assuming that the cross-polarization coupling is small, and the real parts of r_{22} and t_{22} are positive. With those assumptions, a particular set of solutions can be chosen.

b.5 $a \neq -b$, $c = e \neq 0$, and $d_1 \neq 0$ or $d_2 \neq 0$

This case can be solved by using (53) to determine $r_{12} t_{21}$ and then applying (38) and (42)-(46) for the unique solution of the normalized quantities defined in (3).

b.6 $a = -b$, $c = e \neq 0$, $d_1 \neq 0$, and $d_2 = 0$

This case corresponds to case No. 13 in Table 9.2. From the measurement of the first and second targets, the following equation is obtained

$$\frac{2t_{12}}{1 + t_{12}(t_{21}/t_{22})} = \frac{Y_{12}X_{22} - Y_{22}X_{12}}{Y_{11}X_{22} - Y_{21}X_{12}} \quad (59)$$

and from the measurement of the first and third targets, two equations are obtained

$$\frac{t_{21}}{t_{22}} = \frac{X_{22}Z_{11} - X_{12}Z_{21} + X_{21}Z_{12} - X_{11}Z_{22}}{2(X_{22}Z_{12} - X_{12}Z_{22})} \quad (60)$$

$$\frac{c}{d_1} \frac{1}{t_{22}} (1 - t_{12} \frac{t_{21}}{t_{22}}) = \frac{X_{22}Z_{11} - X_{12}Z_{21} - X_{21}Z_{12} + X_{11}Z_{22}}{2(X_{22}Z_{12} - X_{12}Z_{22})} \quad (61)$$

Again let

$$y'_{21} = \frac{t'_{21}}{t'_{22}} \quad (62)$$

Solving t_{12} from (59) gives us

$$t_{12} = \frac{Y_{12}X_{22} - Y_{22}X_{12}}{2(Y_{11}X_{22} - Y_{21}X_{12}) - y'_{21}(Y_{12}X_{22} - Y_{22}X_{12})} \quad (63)$$

Hence, we can solve t_{22} from (61) in terms of t_{12} and y'_{21} .

$$t_{22} = \frac{c}{d_1} (1 - t_{12} y'_{21}) \frac{2(X_{22}Z_{12} - X_{12}Z_{22})}{X_{22}Z_{11} - X_{12}Z_{21} - X_{21}Z_{12} + X_{11}Z_{22}} \quad (64)$$

Therefore,

$$t'_{21} = t_{22} y'_{21} \quad (65)$$

Once the normalized quantities of matrix T are all solved, the normalized quantities of matrix R can be obtained from any one of the following relations

$$R = e^{-i\phi_1} X T^{-1} \quad (66a)$$

$$R = e^{-i\phi_2} Y T^{-1} \begin{bmatrix} 1/a & 0 \\ 0 & -1/a \end{bmatrix} \quad (66b)$$

$$R = e^{-i\phi_3} Z T^{-1} \begin{bmatrix} 1/c & -d_1/c^2 \\ 0 & 1/c \end{bmatrix} \quad (66c)$$

which are obtained by inverting (1).

b.7 $a = -b$, $c = e \neq 0$, $d_1 = 0$, and $d_2 \neq 0$

This case is similar to case 6 (No. 14 in Table 9.2). As a matter of fact, after we take the transpose of the measured polarisation matrices,

$$X^t = e^{i\phi_1} T^t \begin{bmatrix} 1 & 0 \\ 0 & 1 \end{bmatrix} R^t \quad (67a)$$

$$Y^t = e^{i\phi_2} T^t \begin{bmatrix} 1 & 0 \\ 0 & -1 \end{bmatrix} R^t \quad (67b)$$

$$Z^t = e^{i\phi_3} T^t \begin{bmatrix} c & d_2 \\ 0 & c \end{bmatrix} R^t \quad (67c)$$

we can use the following mapping

$$\begin{aligned} X &\rightarrow X^t & (68a) \\ Y &\rightarrow Y^t & (68b) \\ Z &\rightarrow Z^t & (68c) \\ R &\rightarrow T^t & (68d) \\ T &\rightarrow R^t & (68e) \end{aligned}$$

to obtain the solution of this case from those of case B.6.

c. One Dipole, One Trihedral Reflector, and One General Reflector

The scattering matrices of the calibration targets are given as follows

$$S_1 = \begin{bmatrix} a & 0 \\ 0 & 0 \end{bmatrix}, \quad S_2 = \begin{bmatrix} 1 & 0 \\ 0 & 1 \end{bmatrix}, \quad S_3 = \begin{bmatrix} c & d_1 \\ d_2 & e \end{bmatrix} \quad (69)$$

By substituting (69) into (1a) and (1b), the following equalities can be obtained

$$t_{12} = \frac{X_{12}}{X_{11}} \quad (70a)$$

$$r_{21} = \frac{X_{21}}{X_{11}} \quad (70b)$$

$$y'_{21} \equiv \frac{t_{21}}{t_{22}} = \frac{Y_{21}X_{11} - Y_{11}X_{21}}{Y_{22}X_{11} - Y_{12}X_{21}} \quad (70c)$$

$$y'_{12} \equiv \frac{r_{12}}{r_{22}} = \frac{Y_{12}X_{11} - Y_{11}X_{12}}{Y_{22}X_{11} - Y_{21}X_{12}} \quad (70d)$$

and

$$r_{22}t_{22} = \frac{Y_{22}X_{11}^2 - Y_{11}X_{21}X_{12}}{X_{11}^2(Y_{11} - y'_{12}y'_{21}Y_{21})} \quad (71)$$

Hence, we can obtain

$$r_{22}t'_{21} = r_{22}t_{22}y'_{21} \quad (72a)$$

$$r_{12}t'_{21} = r_{22}t_{22}y'_{12} \quad (72b)$$

$$r_{12}t'_{21} = r_{22}t_{22}y'_{21}y'_{12} \quad (72c)$$

by multiplying (71) with (70c) or (70d). Thus, all of the quantities appearing in (38) are obtained.

9.5 Misalignment

Discussed below are five subcases (C.1) $c \neq 0$ and $d_1 \neq 0$ (No. 1, Table 9.3), (C.2) $c \neq 0$ and $d_2 \neq 0$ (No. 2, Table 9.3), (C.3) $e \neq 0$ and $d_1 \neq 0$ (No. 3, Table 9.3), (C.4) $e \neq 0$ and $d_2 \neq 0$ (No. 4, Table 9.3), and (C.5) $c = e = 0$ (No. 5, Table 9.3).

For cases (C.1)–(C.4), we can use (42)–(45), respectively, to solve for r_{22} and t_{22} , and then apply (46) for r_{12} and t_{21} . Note that t_{12} and r_{21} are given in (70). Thus, all the normalized quantities are uniquely determined.

For case (C.5), when both c and e are zero, there are two sets of solutions (see No. 5, Table 9.3). Note that this set of targets has exactly the same kind of symmetry as case B.3. Equation (58) gives the relation of these two solutions. The solutions are solved in the following manner. Taking the ratio of Z_{12} and Z_{21} and making use of (41), we obtain

$$r_{22} = \frac{X_{11}Z_{21} - X_{21}Z_{12}y'_{21}d_1}{X_{11}Z_{12} - X_{12}Z_{21}y'_{12}d_2}t_{22} \quad (73)$$

where y'_{12} and y'_{21} denote r_{12}/r_{22} and t_{21}/t_{22} , respectively. Then, from the ratio of Y_{22} and Y_{11} , we obtain the solution of t_{22} as

$$t_{22} = \pm \sqrt{\frac{(X_{11}Z_{12} - X_{12}Z_{21}y'_{12})(Y_{22}X_{11}^2 - Y_{11}X_{12}X_{21})d_2}{(X_{11}Z_{21} - X_{21}Z_{12}y'_{21})(Y_{11}X_{11}^2 - Y_{22}X_{11}y'_{12}y'_{21})d_1}} \quad (74)$$

The rest of the quantities can be obtained from (70).

9.5 Misalignment

Effects of misalignment between calibration targets and the polarimetric radar are considered in this section. When the calibration reflectors are not aligned correctly relative to the radar system, the misalignment will manifest its effects in the estimated normalized quantities of R and T matrices. The misalignment may be due to the misplaced roll or yaw angles during the deployment of the calibration targets or the uncertain pitch and roll angles of the platform which carries the radar system.

The effect of misalignment in the pointing direction (parallel to the line-of-sight) is determined by the angular scattering pattern of the target. Calibration targets with broad angular beam width are desired to reduce this error. The above misalignment will not be discussed

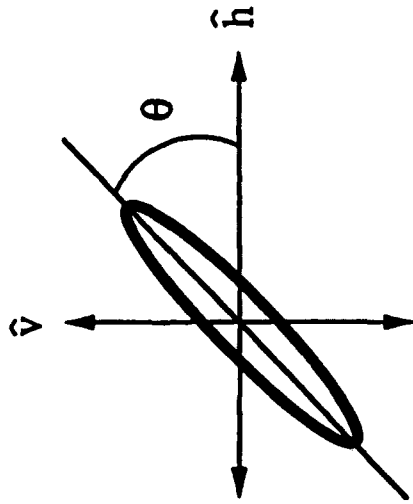


Figure 9.1 Configuration of rolling a target by θ .

further. In the remainder of this section, we will focus on the effects of misalignment in roll angles.

Let S be the scattering matrix of a calibration target. Thus, if the target is rolled by an angle θ on the plane perpendicular the line-of-sight (Fig. 9.1) the scattering matrix S_θ of the rolled target becomes

$$S_\theta = A S A^{-1} \quad (75)$$

where

$$A = \begin{bmatrix} \cos \theta & -\sin \theta \\ \sin \theta & \cos \theta \end{bmatrix} \quad (76)$$

is the coordinate rotation matrix.

Note that a linear combination of the following two matrices is invariant under arbitrary rolling angle (roll-invariant)

$$\begin{bmatrix} 1 & 0 \\ 0 & 1 \end{bmatrix}, \begin{bmatrix} 0 & 1 \\ -1 & 0 \end{bmatrix}$$

The former corresponds to a sphere or trihedral reflector. The latter represents a non-reciprocal target which always rotates the polarization of the electric field by 90° and could be simulated by a polarimetric active calibrator or manufactured by use of the Faraday rotation phenomena exhibited in some passive gyrotropic materials. It can be

shown that there are only two linear independent roll-invariant targets. All other roll-invariant targets must be a linear combination of these two roll-invariant targets.

a. Uniform Misalignment

To illustrate the effects of misalignment, let us consider a simple case that the first two targets are roll-invariant and the third target has a general scattering matrix S_3 . Hence, the rolling angles of the first two targets need not be concerned. If the third target is misaligned by a roll angle θ , it is equivalent to say that all the targets are off by the same roll angle. Thus the corresponding measurements become

$$X = e^{i\phi_1} R A S_1 A^{-1} T \quad (77a)$$

$$Y = e^{i\phi_2} R A S_2 A^{-1} T \quad (77b)$$

$$Z = e^{i\phi_3} R A S_3 A^{-1} T \quad (77c)$$

Assume that there is no knowledge of the roll angle θ . The estimated R and T matrices will be

$$R' = R A, \quad T' = A^{-1} T \quad (78)$$

for the given measurements X , Y , and Z . Expressing (78) explicitly gives

$$R' = R A = \begin{bmatrix} R_{11} \cos \theta + R_{12} \sin \theta & -R_{11} \sin \theta + R_{12} \cos \theta \\ R_{21} \cos \theta + R_{22} \sin \theta & -R_{21} \sin \theta + R_{22} \cos \theta \end{bmatrix} \quad (79a)$$

$$T' = A^{-1} T = \begin{bmatrix} T_{11} \cos \theta + T_{21} \sin \theta & T_{12} \cos \theta + T_{22} \sin \theta \\ -T_{11} \sin \theta + T_{21} \cos \theta & -T_{12} \sin \theta + T_{22} \cos \theta \end{bmatrix} \quad (79b)$$

If the cross-polarization coupling of the polarimetric radar is relatively small and the misaligned roll angle θ is no more than a few degrees, the normalized quantities of estimated matrices R' and T' are

$$\frac{R'_{12}}{R'_{11}} \approx \frac{R_{12}}{R_{11}} - \tan \theta \quad (80a)$$

$$\frac{R'_{21}}{R'_{11}} \approx \frac{R_{21}}{R_{11}} + \frac{R_{22}}{R_{11}} \tan \theta \quad (80b)$$

$$\frac{R'_{22}}{R'_{11}} \approx \frac{R_{22}}{R_{11}} - \left(\frac{R_{22}R_{12}}{R_{11}^2} + \frac{R_{21}}{R_{11}} \right) \tan \theta \quad (80c)$$

$$\frac{T'_{12}}{T'_{11}} \approx \frac{T_{12}}{T_{11}} + \frac{T_{22}}{T_{11}} \tan \theta \quad (80d)$$

$$\frac{T'_{21}}{T'_{11}} \approx \frac{T_{21}}{T_{11}} - \tan \theta \quad (80e)$$

$$\frac{T'_{22}}{T'_{11}} \approx \frac{T_{22}}{T_{11}} - \left(\frac{T_{22}T_{21}}{T_{11}^2} + \frac{T_{12}}{T_{11}} \right) \tan \theta \quad (80f)$$

Note that the terms describing the channel imbalance, (80c) and (80f), are not sensitive to the misalignment when the cross-polarization coupling of the radar is small. However, the errors in the estimated cross-polarization couplings (80a), (80b), (80d), and (80e) are of the order of $\tan \theta$. For a perfect polarimetric system without cross-polarization coupling and mismatch ($R = T = \text{Identity Matrix}$), the effect of misalignment appears purely as a pseudo cross-polarization coupling $\tan \theta$. If the error in the estimated cross-talk is to be smaller than -30 dB, the roll angle of the target must be within $\pm 1.8^\circ$ accuracy.

The above conclusion also holds for arbitrary sets of calibration targets uniformly misplaced by the same roll angle (uniform misalignment). Nevertheless, if the previous system parameters for the radar are available, we can always check to see whether the newly estimated system parameters are related to the previous parameters by the simple coordinate transformation (79). If that is the case, we can remove the errors by an inverse rotation transformation.

b. Relative Misalignment

Next to be considered is the case that each calibration reflector may be misaligned by a different roll angle (nonuniform misalignment). This nonuniform misalignment problem can be thought of as a uniform misalignment problem plus a relative misalignment problem where the first calibrator is aligned correctly, and all the other calibrators are misaligned relative to the first one. As discussed before, a uniform misalignment simply introduces a rotation-transformed error and could be corrected by an inverse rotation. Hence, we may restrict the discussion to the case that the first target is in alignment with the radar and the other calibration targets may be misplaced by some other angles.

The effect of relative misalignment will be analyzed in the following manner. The measurements from these misaligned targets are simu-

9.5 Misalignment

lated, and the normalized quantities of R and T matrices are estimated by assuming all the targets are aligned. Comparing the estimated solution for t'_{mn} and r'_{mn} with the true system parameters, t_{mn} and r_{mn} , gives the square error defined as

$$E_\theta = \sum_{m,n=1}^2 |t'_{mn} - t_{mn}|^2 + \sum_{m,n=1}^2 |r'_{mn} - r_{mn}|^2 \quad (81)$$

In general, if we substitute the estimated quantities t'_{mn} and r'_{mn} back to calculate the corresponding measurements X' , Y' , and Z' for perfectly aligned targets

$$X' = R' S_1 T' \quad (82a)$$

$$Y' = R' S_2 T' \quad (82b)$$

$$Z' = R' S_3 T' \quad (82c)$$

The calculated normalized quantities of X' , Y' , and Z' may not be consistent with the true normalized quantities of X , Y , and Z . It is, therefore, necessary to check whether the solutions are consistent with the measurements or not. Let us define $D(M)$ as the distance between the true and calculated normalized measurements

$$D(M) = \sum_{m,n=1}^2 |x'_{mn} - x_{mn}|^2 + |y'_{mn} - y_{mn}|^2 + |z'_{mn} - z_{mn}|^2 \quad (83)$$

where

$$x_{mn} = \frac{X_{mn}}{\sqrt{\sum_{m,n} |X_{mn}|^2 \exp(i\theta_{ij})}} \quad (84a)$$

$$x'_{mn} = \frac{X'_{mn}}{\sqrt{\sum_{m,n} |X'_{mn}|^2 \exp(i\theta'_{ij})}} \quad (84b)$$

and θ_{ij} is the phase angle of X_{ij} which has the largest magnitude among the elements of X . Note that θ'_{ij} , the phase angle of X'_{ij} (not necessarily the largest element of X'), is used for the phase reference of X' . Likewise, $Y(Z)$ and $Y'(Z')$ are normalized in the same manner.

Under the situation that the radar is perfect ($R = T = I$), Figs. 9.2-9.7 illustrate E_θ and $D(M)$ for the following sets of calibration

targets (i)-(vi) where the first target is assumed to be in perfect alignment with the radar (relative misalignment). θ_2 and θ_3 represent, respectively, the actual roll angle of the second and third targets.

(i) Trihedral and two nonreciprocal reflectors

$$\begin{bmatrix} 1 & 0 \\ 0 & 1 \end{bmatrix}, \begin{bmatrix} 0 & 1 \\ -1 & 0 \end{bmatrix}, \begin{bmatrix} 3.2 & -1 \\ 1 & -1 \end{bmatrix}$$

(ii) Horizontal (0°), Vertical (90°) and 45° dipoles

$$\begin{bmatrix} 1 & 0 \\ 0 & 0 \end{bmatrix}, \begin{bmatrix} 0 & 0 \\ 0 & 1 \end{bmatrix}, \begin{bmatrix} 1 & 1 \\ 1 & 1 \end{bmatrix}$$

(iii) Horizontal dipole, Vertical dipole, and 22.5° dihedral

$$\begin{bmatrix} 1 & 0 \\ 0 & 0 \end{bmatrix}, \begin{bmatrix} 0 & 0 \\ 0 & 1 \end{bmatrix}, \begin{bmatrix} 1 & 1 \\ 1 & -1 \end{bmatrix}$$

(iv) Trihedral, 0° dihedral, and 22.5° dihedral

$$\begin{bmatrix} 1 & 0 \\ 0 & 1 \end{bmatrix}, \begin{bmatrix} 1 & 0 \\ 0 & -1 \end{bmatrix}, \begin{bmatrix} 1 & 1 \\ 1 & -1 \end{bmatrix}$$

(v) Trihedral, 0° dihedral, and 45° dihedral

$$\begin{bmatrix} 1 & 0 \\ 0 & 1 \end{bmatrix}, \begin{bmatrix} 1 & 0 \\ 0 & -1 \end{bmatrix}, \begin{bmatrix} 0 & 1 \\ 1 & 0 \end{bmatrix}$$

(vi) Horizontal dipole, trihedral, and 22.5° dihedral

$$\begin{bmatrix} 1 & 0 \\ 0 & 0 \end{bmatrix}, \begin{bmatrix} 1 & 0 \\ 0 & 1 \end{bmatrix}, \begin{bmatrix} 1 & 1 \\ 1 & -1 \end{bmatrix}$$

Figure 9.2 corresponds to target set (i). Because trihedral and the second reflector are roll-invariant, this case corresponds to the case of uniform misalignment. Hence, the total square error E_θ is independent of θ_2 and equal to $4 \tan^2 \theta_3$ [see (80a,b,d,e)]. Also $D(M)$ is zero for all angles. The performance is the optimum in all cases.

Figure 9.3 for target set (ii) shows larger E_θ than Fig. 9.2. Note that $D(M)$ shown in Fig. 9.3(b) is also zero everywhere. This is because the measurement from each dipole gives two independent equations [see

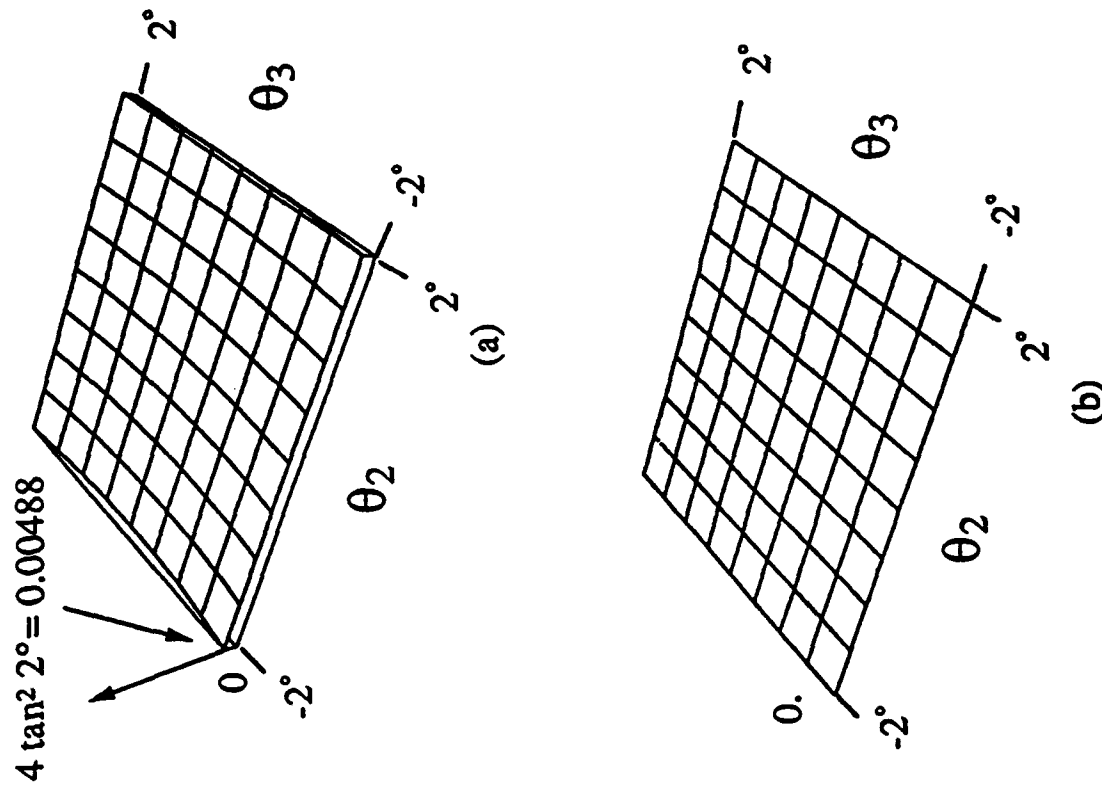


Figure 9.2 Effect of misalignment for target set (i). (a) E_θ and (b) $M(D)$.

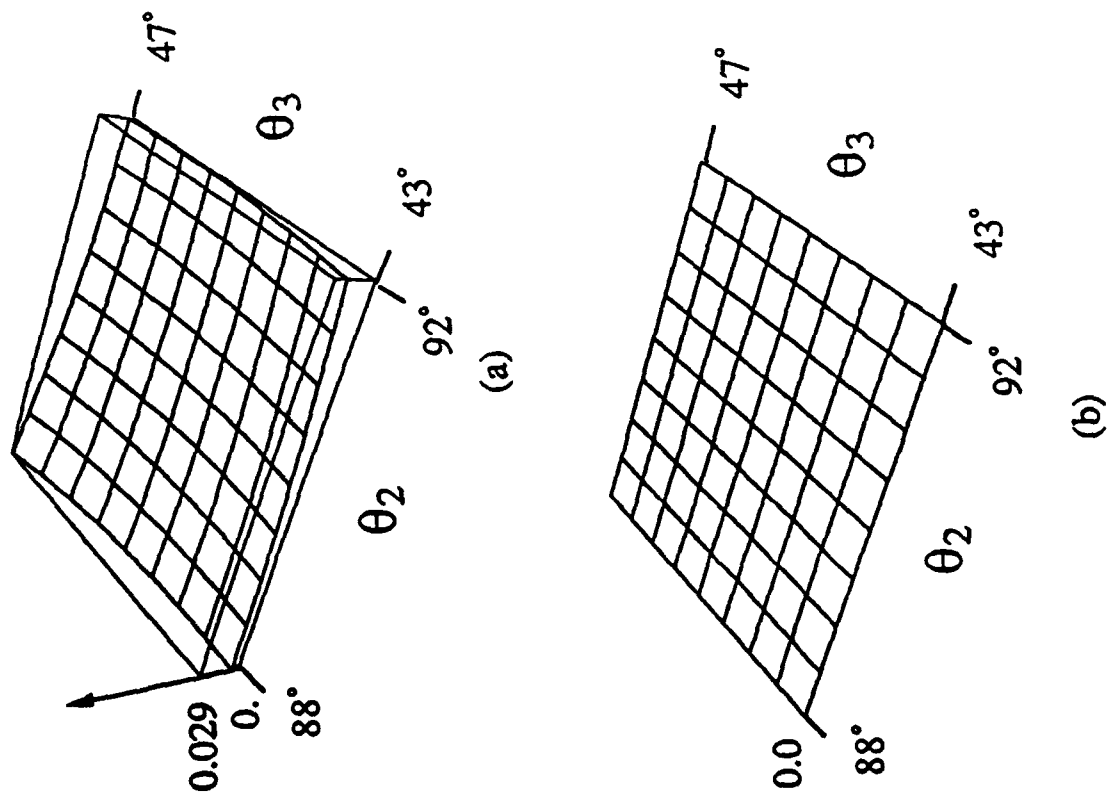


Figure 9.3 Effect of misalignment for target set (ii). (a) E_θ and (b) $M(D)$.

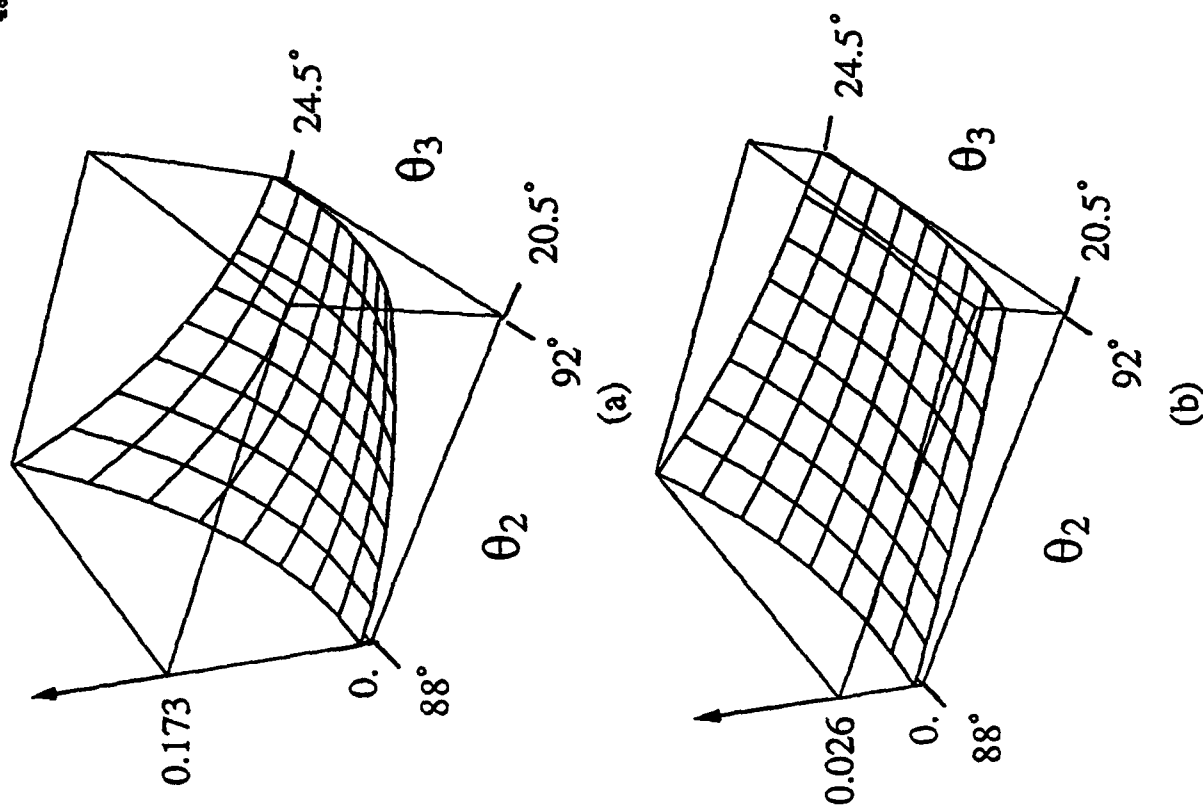
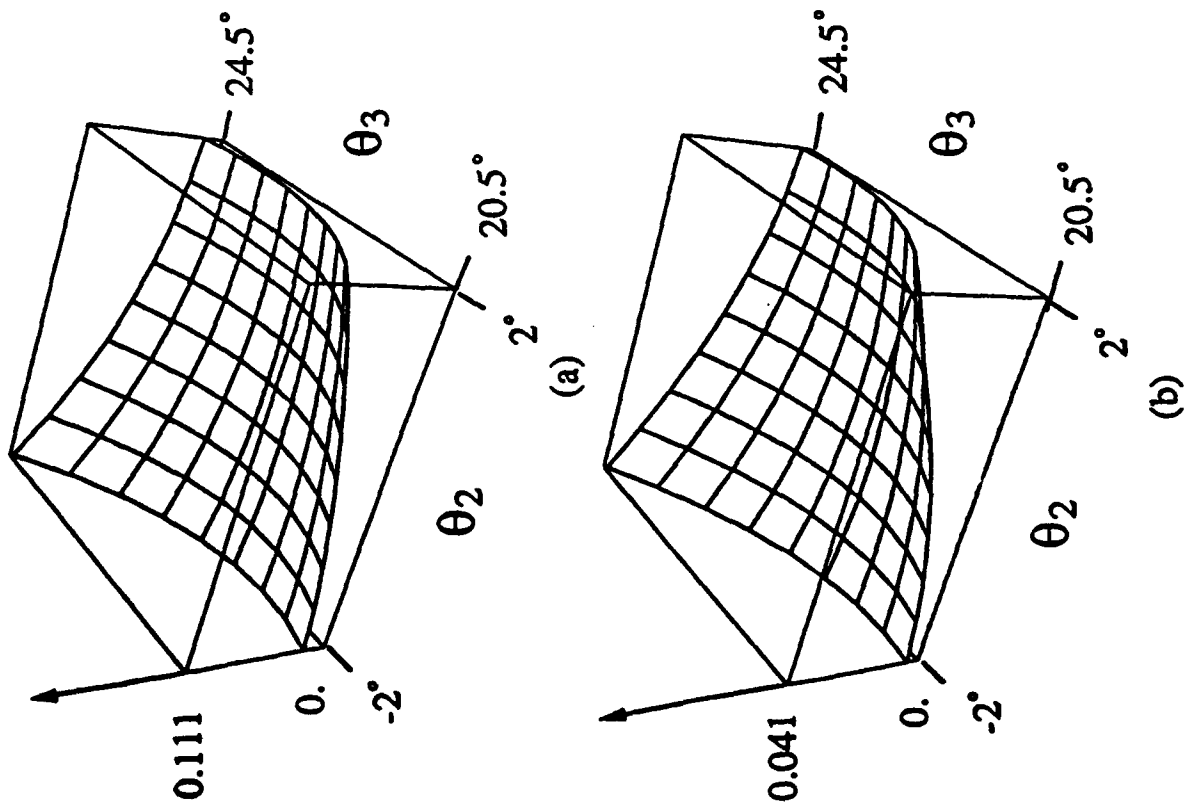
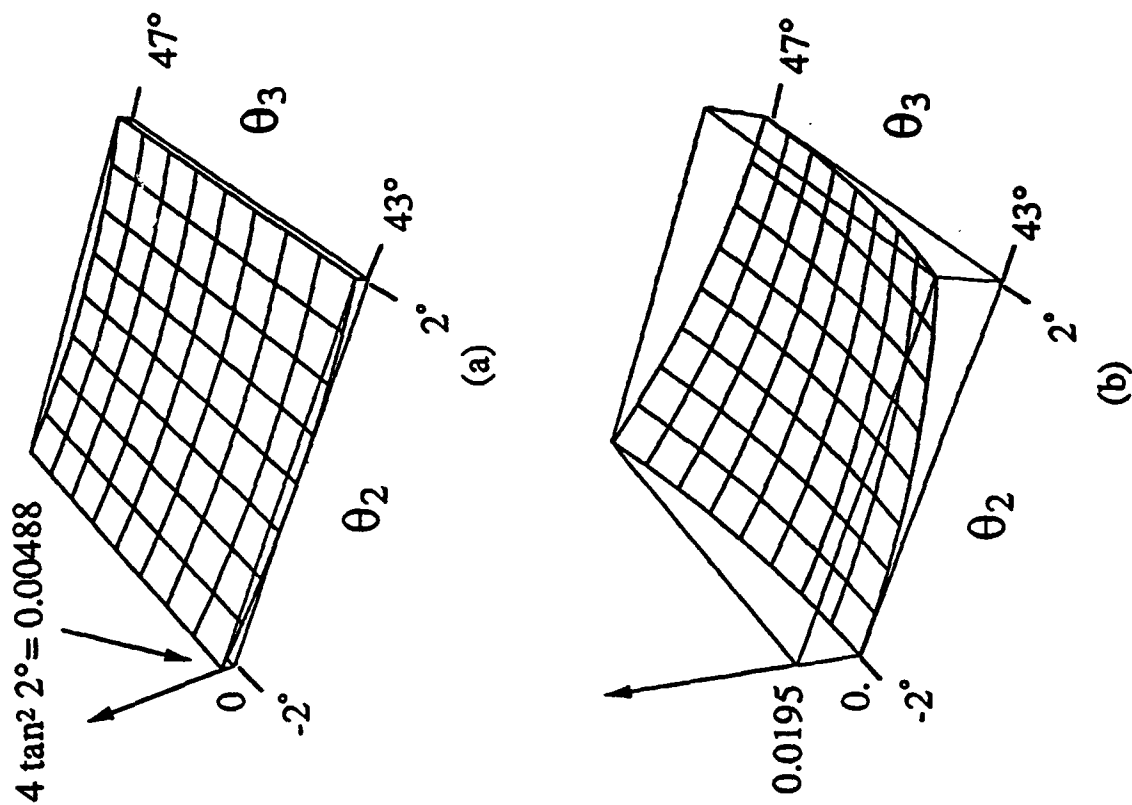


Figure 9.4 Effect of misalignment for target set (iii). (a) E_θ and (b) $M(D)$.

Figure 9.5 Effect of misalignment for target set (iv). (a) E_θ and (b) $M(D)$.Figure 9.6 Effect of misalignment for target set (v). (a) E_θ and (b) $M(D)$.

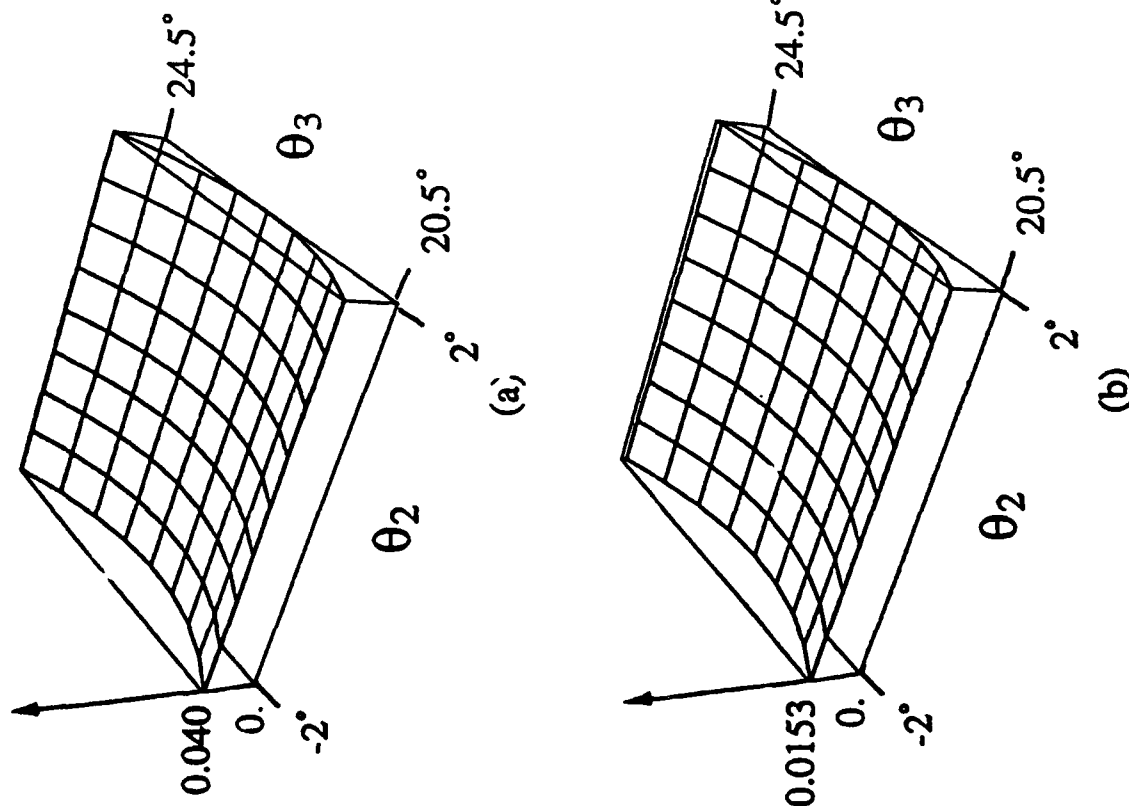


Figure 9.7 Effect of misalignment for target set (vi). (a) E_θ and (b) $M(D)$.

9.5 Misalignment

(31)]. Hence, we have only six equations to determine six unknowns (3a-f). If a set of solutions is found, then it will satisfy all equations even though some targets are misaligned. Thus, $D(M)$ is zero and does not provide us with any information regarding the misalignment of the targets.

Figure 9.4 shows the effect of misalignment for target set (iii). Note that E_θ is the largest among all six cases. Nevertheless, $D(M)$, which is zero only at the center of the figure ($\theta_2 = \theta_3 = 0$), carry the information about the alignment of the targets. This is useful in self-calibrating the roll angles of calibration targets. We can use $D(M)$ to estimate the roll angles of targets two and three relative to the first target even when the first target is not aligned with the radar. After θ_2 and θ_3 are corrected with respect to the first one, the residual error will become that of uniform alignment.

E_θ for target set (iv) shown in Fig. 9.5 is smaller than that in Fig. 9.4. $D(M)$ is not zero when the second or the third targets are misaligned. Note that this case corresponding to case B.2, section 9.4, has two sets of solutions. We select the solution that makes the cross-talk smaller than the one for the results shown in Fig. 9.5.

Figure 9.6 illustrates E_θ and $D(M)$ for target set (v), corresponding to case B.4, section 9.4. One of the four solutions which is closest to the correct solution is selected. Note that E_θ is equal to $4 \tan^2 \theta_2$ as compared with $4 \tan^2 \theta_3$ in Fig. 9.2. It is also interesting to see that E_θ is not a function of θ_3 whereas $D(M)$ is still a function of θ_3 . This is due to the fact that Z_{11} and Z_{22} are not used to calculate the solution [see (54)]. As a matter of fact, if the radar does have some cross-polarization coupling, E_θ will show the dependence on θ_3 .

The results of target case (vi) are illustrated in Fig. 9.7. Because the second target is roll-invariant, neither E_θ nor $D(M)$ is a function of θ_2 . E_θ is larger than those of target sets (i) and (v) and smaller than all the others.

As a summary of the investigation of these six target sets, target sets (i) and (v) provide better performance than the others if $D(M)$ is not used to self-calibrate the relative roll angles. Regarding the disadvantage of these two sets of targets, using set (i) requires a nonreciprocal reflector for one of the roll-invariant targets whereas using set (v) requires extra information in selecting the correct one from four possible solutions. If $D(M)$ is used for self-calibration, E_θ for all the other cases can be corrected to that of the optimum case (i), except

case (ii) using three dipoles.

9.6 Effect of Noise

In general, the measurements cannot be free from noise which will affect the estimated system parameters. In this section the effect of noise will be analyzed for those sets of calibration targets discussed in the previous section. Let us consider the case that the noises are additive to the returns from the targets and are independent complex Gaussian with equal variance for each polarization channel.

When the measurements are contaminated by additive noise,

$$X = e^{i\phi} RST + N \quad (85)$$

where N is a two by two matrix with each element accounting for the noise received by the corresponding polarization channel.

As a result of noise, the estimated normalized quantities of R and T matrix will contain some errors,

$$R' = R'_{11} \begin{bmatrix} 1 & r_{12} + \epsilon_{r12} \\ r_{21} + \epsilon_{r21} & r_{22} + \epsilon_{r22} \end{bmatrix} \quad (86a)$$

$$T' = T'_{11} \begin{bmatrix} 1 & t_{12} + \epsilon_{t12} \\ t_{21} + \epsilon_{t21} & t_{22} + \epsilon_{t22} \end{bmatrix} \quad (86b)$$

where ϵ_{r22} and ϵ_{t22} are the estimated errors in channel imbalance, and ϵ_{r12} , ϵ_{r21} , ϵ_{t12} , and ϵ_{t21} are errors for the estimated cross-talk.

The following mean square errors (MSE) will be evaluated by the Monte Carlo simulation for each set of calibration targets.

$$MSE_{r,ij} = \langle |\epsilon_{r,ij}|^2 \rangle \quad (87)$$

Under the assumption that the radar is perfect ($R = T = I$), Figs. 9.8-9.14 illustrate the MSEs for six sets of calibration targets described in section 9.5 and one additional set of targets composed of three PARCs with the following scattering parameters [10]

$$\begin{bmatrix} 0 & 1 \\ 0 & 0 \end{bmatrix}, \begin{bmatrix} 0 & 0 \\ 1 & 0 \end{bmatrix}, \begin{bmatrix} -1 & -1 \\ 1 & 1 \end{bmatrix}$$

Note that the MSEs are approximately linearly proportional to the power of noise in all cases. It should be noticed that there are actually

four solutions for case (v) and two solutions for case (iv). In plotting Figs. 9.11 and 12, we chose the solution which is closest to the correct solution. This requires extra information about the radar system.

Figure 9.8 illustrates the results for case (i) which is the most robust to the misalignment as discussed in the previous section. The diagonal elements, c and e , of the third target have been varied so that smaller MSEs are achieved. c and e turn out to be 3.2 and -1 , respectively, for minimum MSE. Comparing Figs. 9.8 and 9.12 indicates that the performance of target set (v) is slightly better than set (i). However, unlike case (v), set (i) provides a unique solution. Also the first two targets are roll-invariant, and only the third target needs a special treatment in alignment. The disadvantage for target set (i) is that the second and third targets are not reciprocal reflectors which may be difficult to make.

Figures 9.9 and 9.10 show that the MSEs for cross-talk are equal to the power of noise. However, the MSEs for channel imbalance are 6 dB and 9 dB higher than the power of noise for case (ii) and case (iii), respectively. Comparing Fig. 9.9 and Fig. 9.11 shows that case (iv) is 3 dB better in cross-talk than case (ii), and about the same in channel imbalance.

Figure 9.13 shows the MSEs for case (vi). The results indicate that the targets used in case (vi) are not good for polarimetric calibration purposes.

Figure 9.14 illustrates the approach of the three PARCs [10]. In evaluating the MSEs for this set of targets, they are transformed into (24) in section 9.4.a, according to (4) with the transformation matrices A and B given by

$$A = \begin{bmatrix} 1 & 0 \\ 0 & 1 \end{bmatrix} \quad (88a)$$

$$B = \begin{bmatrix} 0 & 1 \\ 1 & 0 \end{bmatrix} \quad (88b)$$

indicating that the polarization bases of these two polarization channels in the transmitting port are switched, whereas those of receiving port remain unchanged. The performance is shown to be almost identical to the three-dipole case by comparing Fig. 9.9 with 9.14.

Overall, target set (v) gives the best performance. This is due to the fact that Z_{11} and Z_{22} , supposed to be pure noises in case (v), are not used to evaluate the solutions. In contrast, using Z_{11} and Z_{22} degrades

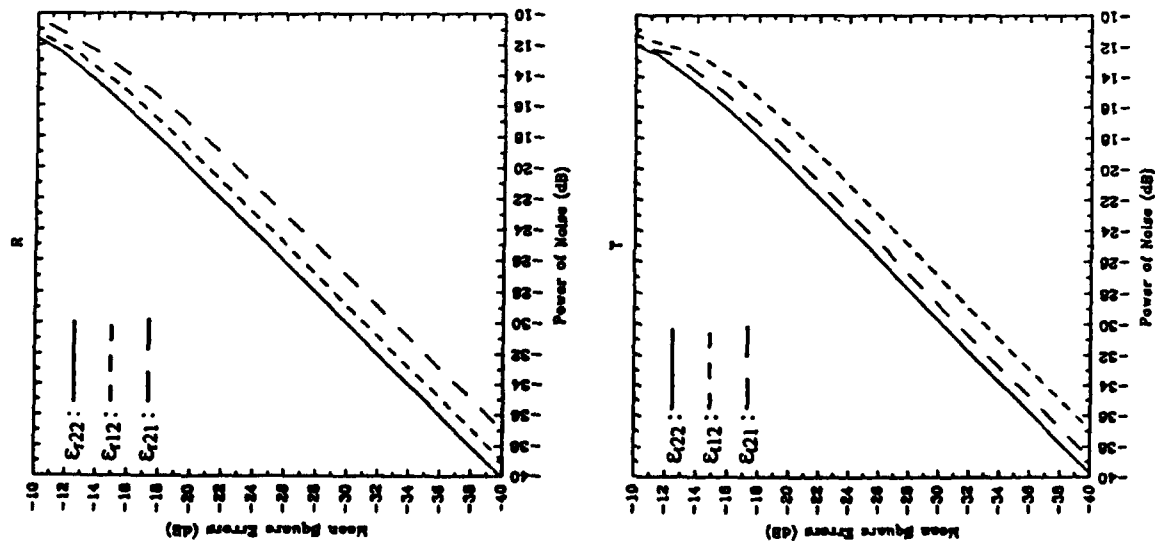


Figure 9.8 Effect of noise for target set (I). (a) MSE for r_{22} , r_{12} , and r_{21} (b) MSE for t_{22} , t_{12} , and t_{21} .

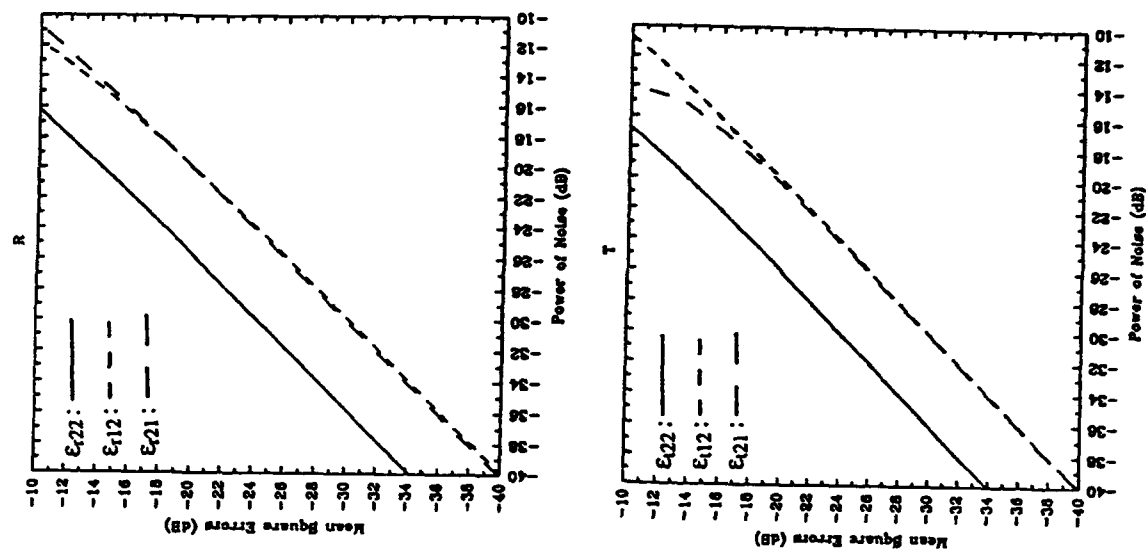


Figure 9.9 Effect of noise for target set (II). (a) MSE for r_{22} , r_{12} , and r_{21} (b) MSE for t_{22} , t_{12} , and t_{21} .

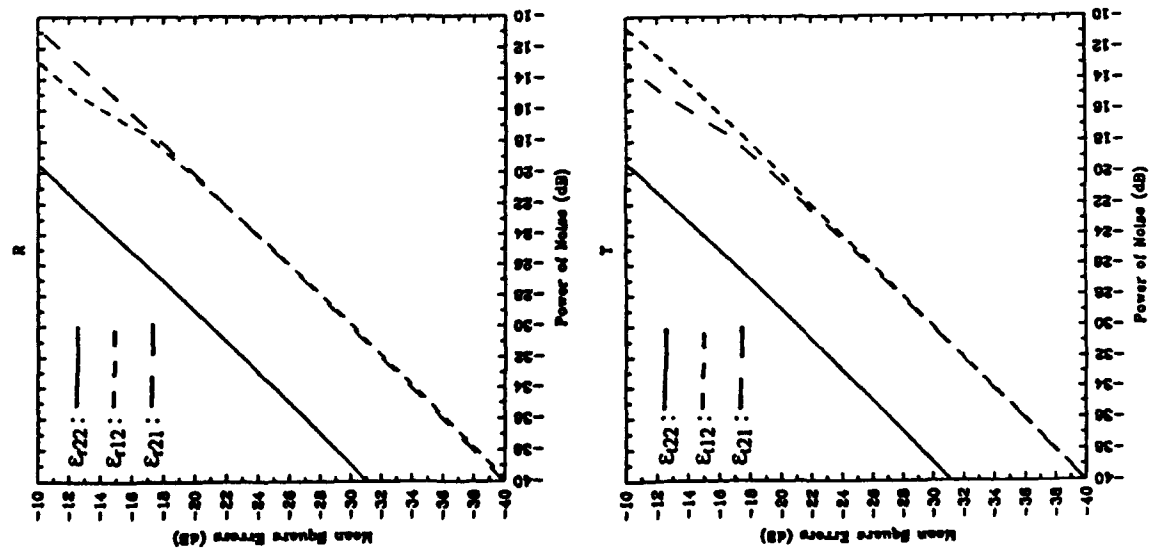


Figure 9.10 Effect of noise for target set (iii). (a) MSE for r_{22} , r_{12} , and r_{21} . (b) MSE for t_{22} , t_{12} , and t_{21} .

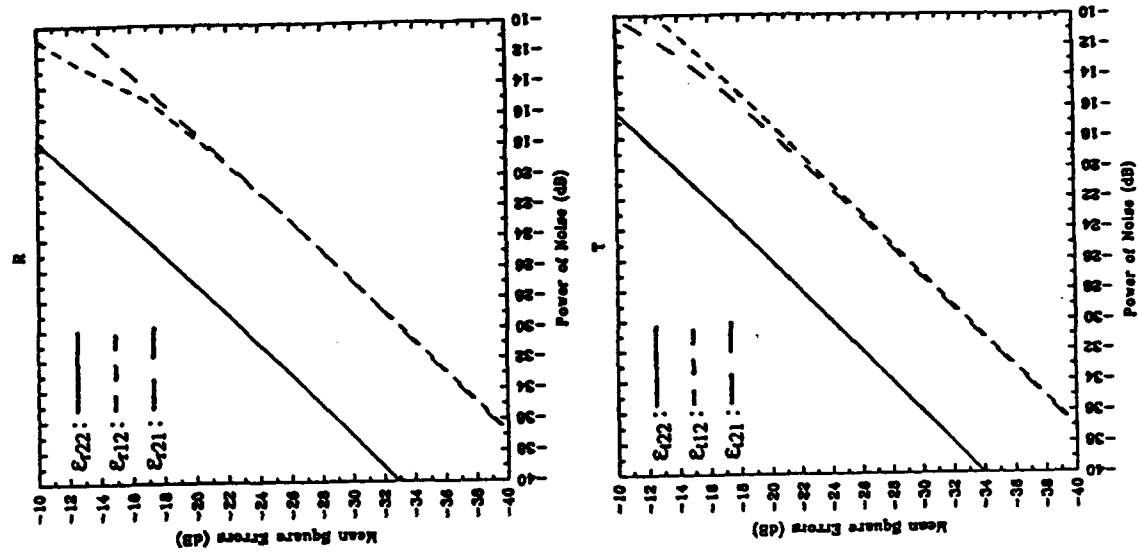


Figure 9.11 Effect of noise for target set (iv). (a) MSE for r_{22} , r_{12} , and r_{21} . (b) MSE for t_{22} , t_{12} , and t_{21} .

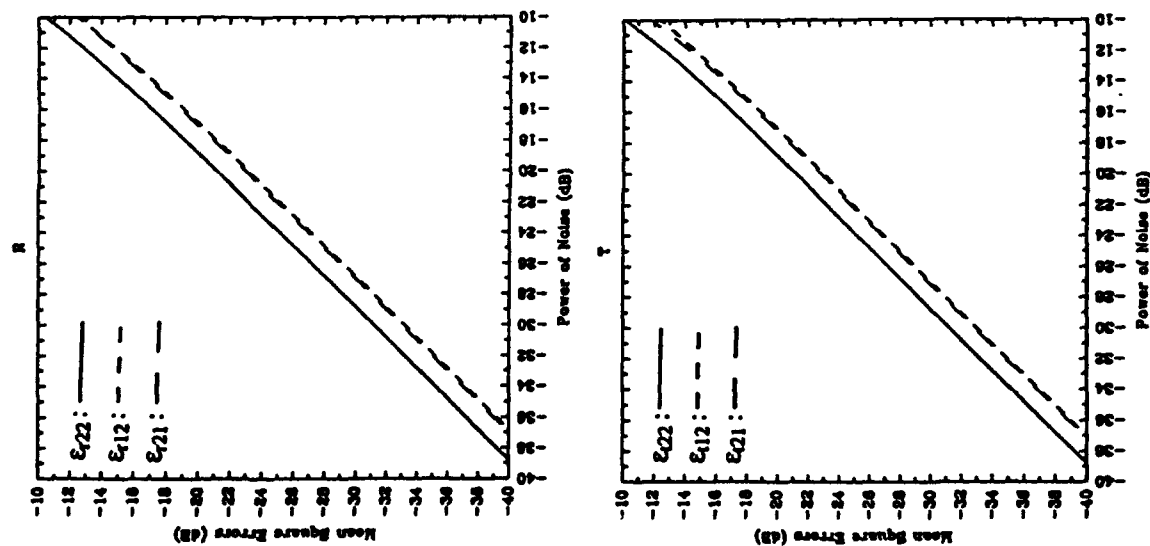


Figure 9.12 Effect of noise for target set (v). (a) MSE for r_{22} , r_{13} , and r_{21} (b) MSE for t_{22} , t_{13} , and t_{21} .

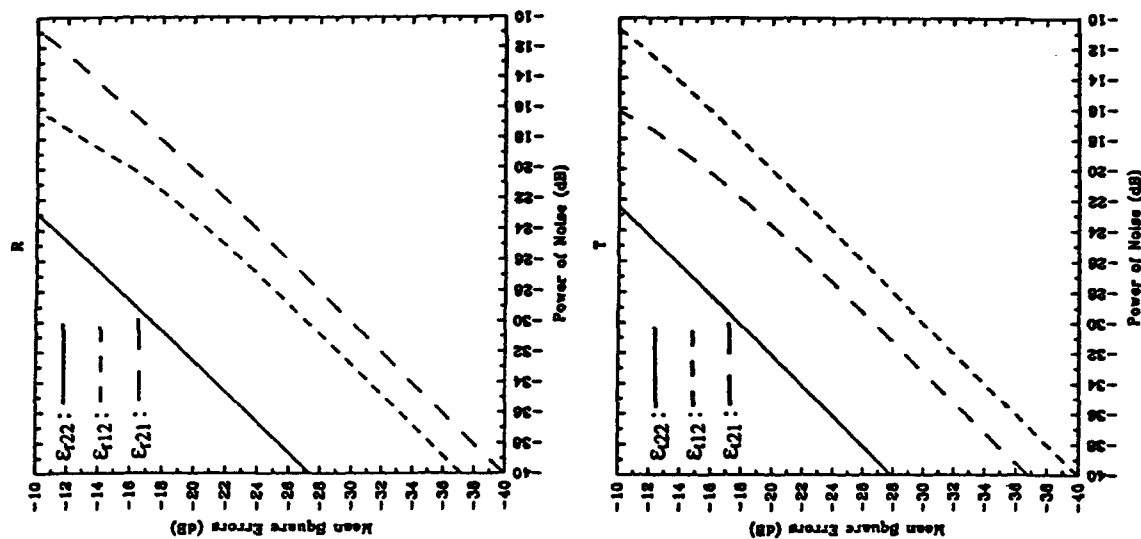


Figure 9.13 Effect of noise for target set (vi). (a) MSE for r_{22} , r_{13} , and r_{21} (b) MSE for t_{22} , t_{13} , and t_{21} .

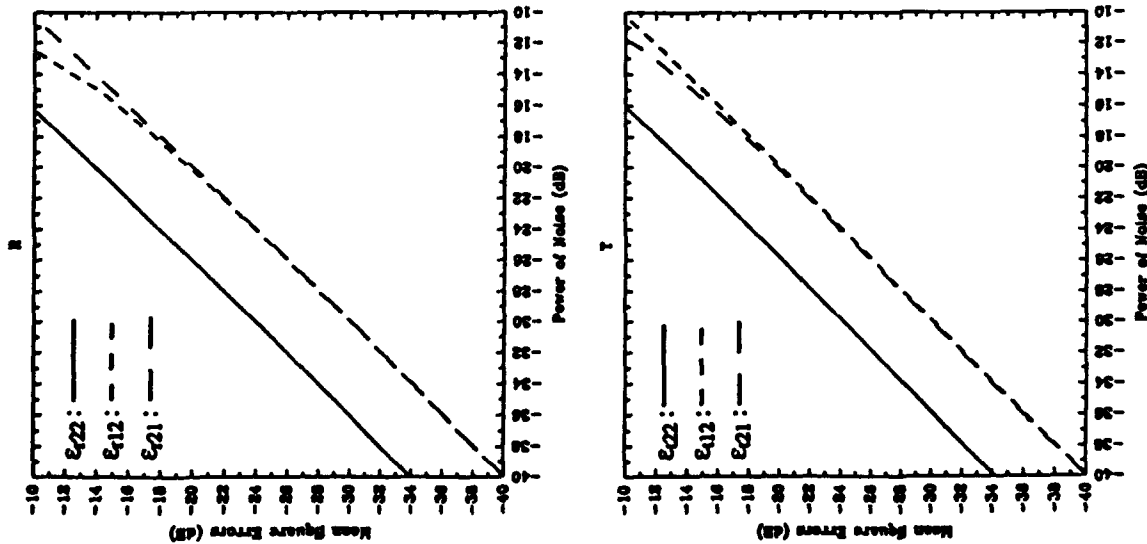


Figure 9.14 Effect of noise for three PARCs [10]. (a) MSE for r_{22} , t_{22} , and r_{21} (b) MSE for t_{22} , t_{12} , and t_{21} .

9.7 Polarimetric Compensation

501

the MSE for channel imbalance as shown in Fig. 9.11 for target set (iv) which offers similar MSEs for cross-talk (3 dB lower than the noise) as compared with Fig. 9.12.

9.7 Polarimetric Compensation

In this section, the explicit polarimetric compensation formula is given. Once radar returns from the three calibration targets have been measured, the polarimetric radar can be calibrated so that only the absolute phase is undetermined. Assuming the measured polarization matrix $[V_{ij}]$ of a target with scattering matrix S is given as

$$\begin{bmatrix} V_{11} & V_{12} \\ V_{21} & V_{22} \end{bmatrix} = \exp(i\phi) \begin{bmatrix} R_{11} & R_{12} \\ R_{21} & R_{22} \end{bmatrix} \begin{bmatrix} S_{hh} & S_{hv} \\ S_{vh} & S_{vv} \end{bmatrix} \begin{bmatrix} T_{11} & T_{12} \\ T_{21} & T_{22} \end{bmatrix} \quad (89)$$

it can be shown that the calibrated scattering matrix elements are given by

$$\begin{bmatrix} S_{hh} \\ S_{hv} \\ S_{vh} \\ S_{vv} \end{bmatrix} = \frac{\exp(-i\phi)}{R_{11}T_{11}(r_{22} - r_{12}r_{21})(t_{22} - t_{12}t_{21})} \times \begin{bmatrix} r_{22}t_{22} & -r_{22}t_{21} & -r_{12}t_{22} & r_{12}t_{21} \\ -r_{22}t_{12} & r_{22} & r_{12}t_{12} & -r_{12} \\ -r_{21}t_{22} & r_{21}t_{21} & t_{22} & -t_{21} \\ r_{21}t_{12} & -r_{21} & -t_{12} & 1 \end{bmatrix} \begin{bmatrix} V_{11} \\ V_{12} \\ V_{21} \\ V_{22} \end{bmatrix} \quad (90)$$

where r_{12} , r_{21} , r_{22} , t_{12} , t_{21} , and t_{22} have been obtained, in terms of the measurements of the calibration targets, in sections 9.2 and 9.3.

The calibration of absolute radar cross section can be carried out by using (1) to solve for the absolute magnitude of the transfer matrices

$$|R_{11}T_{11}| = \frac{|X_{11}|}{|S_{1hh} + (t_{21} + r_{12})S_{1hv} + r_{12}t_{21}S_{1vv}|} \quad (91a)$$

$$= \frac{|X_{12}|}{|r_{21}t_{12}S_{1hh} + (r_{21}t_{22} + r_{22}t_{12})S_{1hv} + r_{22}t_{22}S_{1vv}|} \quad (91b)$$

$$= \frac{|t_{12}S_{1hh} + (t_{22} + r_{12}t_{12})S_{1hv} + r_{12}t_{22}S_{1vv}|}{|X_{12}|} \quad (91c)$$

$$= \frac{|r_{21}S_{1hh} + (r_{21}t_{21} + r_{22})S_{1hv} + r_{22}t_{21}S_{1vv}|}{|X_{21}|} \quad (91d)$$

Equations (91a) and (91b) are useful when the calibration target has large like-like polarized returns HH and VV. Equations (91c) and (91d) are useful when the calibration target can significantly depolarize the radar signal.

9.8 Summary

Polarimetric calibration algorithms have been found for a general choice of three calibration targets. The algorithm presented is not limited to any particular polarization basis although the examples are given on the linear polarization basis. A method of Polarization-basis Transformation technique (PT) is employed to convert the scattering matrices into one of six canonical cases. The uniqueness problem for those six canonical cases is studied in detail. If there are multiple solutions for a given target choice, the relation between these solutions is clearly identified. The solution is presented for three canonical cases which correspond to the general cases that at least two of the scattering matrices of three calibration targets can be simultaneously diagonalized.

Based on the analysis on the effects of noise and misalignment for some typical calibration targets, target sets (i) and (v) show superior performance. However, the implementation of the second and third reflectors in target set (i) needs to be further investigated. Also it should be noted that target set (v) corresponding to case B.4 gives four solutions. Two of these solutions can be rejected if we know that the cross-polarization couplings are not greater than unity. The other two solutions give the same magnitude for the channel imbalance but with a plus or minus sign difference. Extra information is needed to select the correct solution for target set (v) [9]. The evaluation of PARCs [10] shown to be equivalent to the three-dipole approach indicates that PARC having a dipole-like scattering matrix can be used to replace the more complicated design used [10]. The analysis of misalignment also indicates that a possible self-calibration procedure could be used to remove the effects of misalignment based on the distance measure $D(M)$.

•
•
•

Appendix A

Acknowledgments

This work was supported by NASA Contract 958461, NASA Contract NAGW-1617, NASA Contract NAGW-1272, ARMY Corp of Engineers Contract DACA39-87-K-0022, and ONR Contract N00014-89-J-1107.

Appendix A

Δ_1 , Δ_{1c} , and Δ_{1r} are given as

$$\begin{aligned} \Delta_1 &= \begin{vmatrix} p_{11} & p_{12} & p_{13} \\ p_{21} & p_{22} & p_{23} \\ p_{31} & p_{32} & p_{33} \end{vmatrix} \\ \Delta_{1c} &= \begin{vmatrix} q_1 & p_{12} & p_{13} \\ q_2 & p_{22} & p_{23} \\ q_3 & p_{32} & p_{33} \end{vmatrix} \\ \Delta_{1r} &= \begin{vmatrix} p_{11} & q_1 & p_{13} \\ p_{21} & q_2 & p_{23} \\ p_{31} & q_3 & p_{33} \end{vmatrix} \end{aligned} \quad (A1)$$

where

$$\begin{aligned} p_{11} &= X_{11}(Y_{22}Z_{11} - Y_{21}Z_{12}) \\ p_{12} &= Y_{12}(X_{12}Z_{11} - X_{11}Z_{12}) \\ p_{13} &= Y_{12}(Y_{22}Z_{11} - Y_{21}Z_{12}) \\ p_{21} &= Y_{21}(X_{21}Z_{11} - X_{11}Z_{21}) \\ p_{22} &= X_{11}(Y_{22}Z_{11} - Y_{12}Z_{21}) \\ p_{23} &= Y_{21}(Y_{22}Z_{11} - Y_{12}Z_{21}) \\ p_{31} &= X_{21}Y_{22}Z_{11} - X_{11}Y_{21}Z_{22} \\ p_{32} &= X_{12}Y_{22}Z_{11} - X_{11}Y_{12}Z_{22} \\ p_{33} &= Y_{22}^2Z_{11} - Y_{12}Y_{21}Z_{22} \end{aligned}$$

and

$$\begin{aligned} q_1 &= X_{11}(X_{11}Z_{12} - X_{12}Z_{11}) \\ q_2 &= X_{11}(X_{11}Z_{21} - X_{21}Z_{11}) \\ q_3 &= X_{11}^2Z_{22} - X_{21}X_{12}Z_{11} \end{aligned}$$

Appendix B

Δ_3 , Δ_{31} , and Δ_{3r} are given as

$$\begin{aligned}\Delta_3 &= \begin{vmatrix} p_{11} & p_{12} & p_{13} \\ p_{21} & p_{22} & p_{23} \\ p_{31} & p_{32} & p_{33} \end{vmatrix} \\ \Delta_{31} &= \begin{vmatrix} p_{11} & q_1 & p_{13} \\ p_{21} & q_2 & p_{23} \\ p_{31} & q_3 & p_{33} \end{vmatrix} \\ \Delta_{3r} &= \begin{vmatrix} q_1 & p_{12} & p_{13} \\ q_2 & p_{22} & p_{23} \\ q_3 & p_{32} & p_{33} \end{vmatrix}\end{aligned}$$

where

$$\begin{aligned}p_{11} &= Y_{22}(X_{31}Z_{12} - X_{11}Z_{22}) \\ p_{12} &= X_{12}(Y_{22}Z_{12} - Y_{12}Z_{22}) \\ p_{13} &= X_{12}(X_{31}Z_{12} - X_{12}Z_{22}) \\ p_{21} &= X_{31}(Y_{22}Z_{21} - Y_{21}Z_{22}) \\ p_{22} &= Y_{22}(X_{12}Z_{21} - X_{11}Z_{22}) \\ p_{23} &= X_{31}(X_{12}Z_{21} - X_{11}Z_{22}) \\ p_{31} &= X_{31}Y_{22}Z_{11} - X_{11}Y_{21}Z_{22} \\ p_{32} &= X_{12}Y_{22}Z_{11} - X_{11}Y_{12}Z_{22} \\ p_{33} &= X_{12}X_{31}Z_{11} - X_{11}^2Z_{22}\end{aligned}$$

and

$$\begin{aligned}q_1 &= Y_{22}(Y_{22}Z_{12} - Y_{12}Z_{22}) \\ q_2 &= Y_{22}(Y_{22}Z_{21} - Y_{21}Z_{22}) \\ q_3 &= Y_{22}^2Z_{11} - Y_{21}Y_{12}Z_{22}\end{aligned}$$

Appendix C

Appendix C

Δ_3 , Δ_{31} , and Δ_{3r} are given as

$$\begin{aligned}\Delta_3 &= \begin{vmatrix} p_{11} & p_{12} & p_{13} \\ p_{21} & p_{22} & p_{23} \\ p_{31} & p_{32} & p_{33} \end{vmatrix} \\ \Delta_{31} &= \begin{vmatrix} q_1 & p_{12} & p_{13} \\ q_2 & p_{22} & p_{23} \\ q_3 & p_{32} & p_{33} \end{vmatrix} \\ \Delta_{3r} &= \begin{vmatrix} p_{11} & p_{12} & q_1 \\ p_{21} & p_{22} & q_2 \\ p_{31} & p_{32} & q_3 \end{vmatrix}\end{aligned}$$

(B1)

where

$$\begin{aligned}p_{11} &= X_{11}(X_{11}Z_{12} - X_{12}Z_{11}) \\ p_{12} &= Y_{12}(X_{11}Z_{12} - X_{12}Z_{11}) \\ p_{13} &= Y_{12}(Y_{21}Z_{12} - Y_{22}Z_{11}) \\ p_{21} &= X_{11}(X_{21}Z_{12} - X_{12}Z_{21}) \\ p_{22} &= X_{11}Y_{22}Z_{12} - X_{12}Y_{12}Z_{21} \\ p_{23} &= Y_{22}(Y_{21}Z_{12} - Y_{12}Z_{21}) \\ p_{31} &= X_{12}(X_{21}Z_{12} - X_{11}Z_{22}) \\ p_{32} &= X_{12}(Y_{22}Z_{12} - Y_{12}Z_{22}) \\ p_{33} &= Y_{22}(Y_{22}Z_{12} - Y_{12}Z_{22})\end{aligned}$$

and

$$\begin{aligned}q_1 &= X_{11}(Y_{22}Z_{11} - Y_{21}Z_{12}) \\ q_2 &= X_{11}Y_{22}Z_{21} - X_{21}Y_{21}Z_{12} \\ q_3 &= Y_{22}(X_{11}Z_{22} - X_{21}Z_{12})\end{aligned}$$

(C1)

Appendix D

Δ_4 , Δ_{4i} , and Δ_{4r} are given as

$$\Delta_4 = \begin{vmatrix} p_{11} & p_{12} & p_{13} \\ p_{21} & p_{22} & p_{23} \\ p_{31} & p_{32} & p_{33} \end{vmatrix}$$

$$\Delta_{4i} = \begin{vmatrix} q_1 & p_{12} & p_{13} \\ q_2 & p_{22} & p_{23} \\ q_3 & p_{32} & p_{33} \end{vmatrix}$$

$$\Delta_{4r} = \begin{vmatrix} p_{11} & p_{12} & q_1 \\ p_{21} & p_{22} & q_2 \\ p_{31} & p_{32} & q_3 \end{vmatrix}$$

where

$$\begin{aligned} p_{11} &= X_{11}(X_{11}Z_{21} - X_{21}Z_{11}) \\ p_{12} &= Y_{21}(X_{11}Z_{21} - X_{21}Z_{11}) \\ p_{13} &= Y_{21}(Y_{12}Z_{21} - Y_{22}Z_{11}) \\ p_{21} &= X_{11}(X_{12}Z_{21} - X_{21}Z_{12}) \\ p_{22} &= X_{11}Y_{22}Z_{21} - X_{21}Y_{21}Z_{12} \\ p_{23} &= Y_{22}(Y_{12}Z_{21} - Y_{21}Z_{12}) \\ p_{31} &= X_{21}(X_{12}Z_{21} - X_{11}Z_{22}) \\ p_{32} &= X_{21}(Y_{22}Z_{21} - Y_{21}Z_{22}) \\ p_{33} &= Y_{22}(Y_{22}Z_{21} - Y_{21}Z_{22}) \end{aligned}$$

and

$$\begin{aligned} q_1 &= X_{11}(Y_{22}Z_{11} - Y_{12}Z_{21}) \\ q_2 &= X_{11}Y_{22}Z_{12} - X_{12}Y_{12}Z_{21} \\ q_3 &= Y_{22}(X_{11}Z_{22} - X_{12}Z_{21}) \end{aligned}$$

Appendix E

Appendix E

Δ and Δ_{ri} are given as

$$\begin{aligned} \Delta &= p_1r_1 + p_2r_2 + p_3r_3 \\ \Delta_{ri} &= -(p_1q_1 + p_2q_2 + p_3q_3) \end{aligned} \quad (E1)$$

where

$$\begin{aligned} p_1 &= Z_{11}(X_{22}Y_{11} - X_{11}Y_{22}) - Z_{21}(X_{12}Y_{11} - X_{11}Y_{12}) \\ &\quad - Z_{12}(X_{21}Y_{11} - X_{11}Y_{21}) \\ p_2 &= Z_{11}(X_{12}Y_{22} - X_{22}Y_{12}) + Z_{12}(X_{21}Y_{12} - X_{12}Y_{21}) \\ &\quad + Z_{22}(X_{12}Y_{11} - X_{11}Y_{12}) \\ p_3 &= Z_{11}(X_{21}Y_{22} - X_{22}Y_{21}) + Z_{21}(X_{12}Y_{21} - X_{21}Y_{12}) \\ &\quad + Z_{22}(X_{21}Y_{11} - X_{11}Y_{21}) \\ q_1 &= (1 + \lambda)cX_{11}Y_{11}Z_{22} - cZ_{11}(\lambda X_{22}Y_{11} + X_{11}Y_{22}) \\ &\quad - cZ_{11}(X_{22}Y_{11} - X_{11}Y_{22}) \\ q_2 &= (1 + \lambda)cX_{11}Y_{11}Z_{21} - cZ_{11}(\lambda X_{21}Y_{11} + X_{11}Y_{21}) \\ &\quad - cZ_{11}(X_{21}Y_{11} - X_{11}Y_{21}) \\ q_3 &= (1 + \lambda)cX_{11}Y_{11}Z_{12} - cZ_{11}(\lambda X_{12}Y_{11} + X_{11}Y_{12}) \\ &\quad - cZ_{11}(X_{12}Y_{11} - X_{11}Y_{12}) \\ r_1 &= (1 + \lambda)cX_{11}Y_{11}Z_{22} - c\lambda Z_{11}(X_{22}Y_{11} - X_{11}Y_{22}) \\ &\quad - cZ_{11}(X_{22}Y_{11} + \lambda X_{11}Y_{22}) \\ r_2 &= (1 + \lambda)cX_{11}Y_{11}Z_{21} - c\lambda Z_{11}(X_{21}Y_{11} - X_{11}Y_{21}) \\ &\quad - cZ_{11}(X_{21}Y_{11} + \lambda X_{11}Y_{21}) \\ r_3 &= (1 + \lambda)cX_{11}Y_{11}Z_{12} - c\lambda Z_{11}(X_{12}Y_{11} - X_{11}Y_{12}) \\ &\quad - cZ_{11}(X_{12}Y_{11} + \lambda X_{11}Y_{12}) \end{aligned}$$

Appendix F

Δ_s , Δ_u , Δ_v , Δ_e , Δ_{ee} , and Δ_{ev} are given as

$$\Delta_s = (Z_{11} - Z_{12}Y'_{21})(Z_{11} - Z_{21}Y'_{12}) \\ - Y'_{12}(Z_{11}t_{12} - Z_{12})Y'_{21}(Z_{11}r_{21} - Z_{21})$$

$$\Delta_u = (Z_{11} - Z_{21}Y'_{12})\left[\frac{c}{d_1}(Z_{12} - Z_{11}t_{12})\right. \\ \left.+ \frac{c}{d_1}(r_{12}t_{21}Z_{12} - r_{12}t_{22}Z_{11})\right] \\ - Y'_{12}(t_{12}Z_{11} - Z_{12})\left[\frac{c}{d_1}(Z_{21} - r_{21}Z_{11})\right. \\ \left.+ \frac{c}{d_1}(r_{12}t_{21}Z_{21} - r_{22}t_{21}Z_{11})\right]$$

$$\Delta_v = (Z_{11} - Z_{12}Y'_{21})\left[\frac{c}{d_2}(Z_{21} - Z_{11}r_{21})\right. \\ \left.+ \frac{c}{d_2}(r_{12}t_{21}Z_{21} - r_{22}t_{21}Z_{11})\right]$$

$$- Y'_{21}(r_{21}Z_{11} - Z_{21})\left[\frac{c}{d_2}(Z_{12} - t_{12}Z_{11})\right. \\ \left.+ \frac{c}{d_2}(r_{12}t_{21}Z_{12} - r_{12}t_{22}Z_{11})\right]$$

$$\Delta_e = (Z_{21} - Z_{12}Y'_{21}r_{21})(Z_{12} - Z_{22}Y'_{12}t_{12}) \\ - (Z_{22} - Z_{12}r_{21})(Z_{12} - Z_{21}Y'_{12}t_{12})$$

$$\Delta_{ee} = (Z_{12} - Z_{21}t_{12}Y'_{12})\left[\frac{c}{d_1}(Z_{22}t_{12} - Z_{12}r_{21}t_{12})\right. \\ \left.+ \frac{c}{d_1}(Z_{22}r_{12}t_{22} - Z_{12}r_{22}t_{22})\right] \\ - t_{12}(Z_{12} - Z_{22}Y'_{12})\left[\frac{c}{d_1}(Z_{21}t_{12} - Z_{12}r_{21})\right. \\ \left.+ \frac{c}{d_1}(r_{12}t_{22}Z_{21} - r_{22}t_{21}Z_{12})\right]$$

$$\Delta_{ev} = (Z_{21} - Z_{12}r_{21}Y'_{21})\left[\frac{c}{d_2}(Z_{22}t_{12} - Z_{12}r_{21}t_{12})\right. \\ \left.+ \frac{c}{d_2}(Z_{22}r_{12}t_{22} - Z_{12}r_{22}t_{22})\right] \\ - (Z_{22} - Z_{12}r_{21})\left[\frac{c}{d_2}(Z_{21}t_{12} - Z_{12}r_{21})\right. \\ \left.+ \frac{c}{d_2}(r_{12}t_{22}Z_{21} - r_{22}t_{21}Z_{12})\right]$$

References

- [1] Evans, D. L., T. G. Farr, J. P. Ford, T. W. Thompson and C. L. Werner, "Multipolarization Radar Images for Geologic Mapping and Vegetation Discrimination," *IEEE Trans. Geosci. Remote Sens.*, GE-24, 2, 246-256, 1986.
- [2] Wu, S. T., and S. A. Sader, "Multipolarization SAR Data for Surface Feature Delineation and Forest Vegetation Characterization," *IEEE Trans. Geosci. Remote Sens.*, GE-25, 1, 67-76, 1987.
- [3] Zebker, H. A., J. J. van Zyl and D. N. Held, "Imaging Radar Polarimetry from Wave Synthesis," *J. Geophys. Res.*, 92, B1, 683-701, 1987.
- [4] van Zyl, J. J., H. A. Zebker and C. Elachi, "Imaging Radar Polarization Signature: Theory and Observation," *Radio Science*, 22, 4, 529-543, 1987.
- [5] Kong, J. A., A. A. Swartz, H. A. Yueh, L. M. Novak, and R. T. Shin, "Identification of Terrain Cover Using the Optimum Polarimetric Classifier," *J. of Electromagnetic Waves and Appl.*, 2, 2, 171-194, 1988.
- [6] Yueh, H. A., A. A. Swartz, J. A. Kong, R. T. Shin, and L. M. Novak, "Bayes Classification of Terrain Cover Using Normalized Polarimetric Data," *J. Geophys. Res.*, 93, B12, 15261-15267, 1988.
- [7] Lim, H., A. A. Swartz, H. A. Yueh, J. A. Kong, R. T. Shin, and J. J. van Zyl, "Classification of Earth Terrain using Synthetic Aperture Radar Images," *J. Geophys. Res.*, 94, B6, 7049-7057, 1989.
- [8] Swartz, A. A., H. A. Yueh, J. A. Kong, R. T. Shin, and L. M. Novak, "Optimal Polarizations for Achieving Maximum Contrast in Radar Images," *J. Geophys. Res.*, 93, B12, 15252-15260, 1988.
- [9] Barnes, R. M., "Antenna Polarization Calibration Using In-scene Reflectors," Proceedings of the Tenth DARPA/Tri-Service Kilometer Wave Symposium, U.S. Army Harry Diamond Lab., Adelphi, MD, April 8-10, 1986.
- [10] Freeman, A., C. L. Werner, and Y. Shen, "Calibration of Multipolarization Imaging Radar," *Proc. IGARSS'88 Symposium*, pp. 335-339, Edinburgh, Scotland, Sept. 13-16, 1988.

- [11] Yueh, S. H., J. A. Kong, R. M. Barnes, and R. T. Shin, "Calibration of Polarimetric Radars Using In-scene Reflectors," *J. Electromagnetic Waves and Appl.*, 4, 1, 27-49, 1990.
- [12] van Zyl, J. J., "A Technique to Calibrate Polarimetric Radar Images Using Only Image Parameters and Trihedral Corner Reflectors," *Proc. Progress in Electromagnetics Research Symp.*, Boston, MA, July 25-26, 1989.
- [13] Shin, R. T., L. M. Novak, and M. Borgeaud, "Theoretical Models for Polarimetric Radar Clutter," *Tenth DARPA/Tri-Service Millimeter Wave Symposium*, U.S. Army Harry Diamond Laboratories, Adelphi, MD, April 8-10, 1986.
- [14] Borgeaud, M., R. T. Shin, and J. A. Kong, "Theoretical Models for Polarimetric Radar Clutter," *J. of Electromagnetic Waves and Appl.*, 1, 1, 67-86, 1987.

6

CLASSIFICATION OF EARTH TERRAIN USING POLARIMETRIC SYNTHETIC APERTURE RADAR IMAGES

*J. A. Kong, S. H. Yueh, H. H. Lim,
R. T. Shin, and J. J. van Zyl*

- 6.1 Introduction
- 6.2 Supervised and Unsupervised Classifications
 - a. Supervised Classification Procedure
 - b. Unsupervised Classification Procedure
 - c. Classification Error Analysis
 - d. Summary
- 6.3 Maximum Contrast Enhancement
 - a. Polarimetric Matched Filter and Contrast Ratio
 - b. Optimal Polarimetric Matched Filter Required to Obtain Maximum Contrast between Two Scattering Classes
 - c. Optimal Receiving Polarization State for a Fixed Transmitting Polarization
 - d. Results and Discussion
- Acknowledgments
- References

6.1 Introduction

Classification of earth terrain within an image is one of the many important applications of polarimetric data. A systematic classification procedure will place the classification process on a more quantitative level and reduce the amount of photo-interpretation necessary [Evans, 1986]. Single feature and multifrequency classifications have been used in the past, but classification can now be applied to fully polarimetric data which have become available due to recent developments in radar technology. It has been shown that Bayes classification using

fully polarimetric data yields optimal results as compared to classification performance using any subset of the complete polarimetry [Kong *et al.*, 1988; Lim *et al.*, 1989].

In some cases, the absolute magnitude and phase of the radar returns are not reliable features for data classification purposes. This is due to the fact that radar system calibration procedures vary in accuracy as well as the fact that they cannot account for attenuation and phase shifts caused by atmospheric distortions. Normalization schemes [Yueh *et al.*, 1988], which preserve only the relative components of the returns, were applied to radar polarimetry in order to circumvent this problem. Previously, normalized polarimetric classification schemes were implemented by assuming a multivariate Gaussian distribution for normalized data [Kriegler *et al.*, 1971; Smedes *et al.*, 1971]. However, this technique yields inconsistent results since the probability of error, as well as classification performance, becomes a function of the particular normalization scheme selected. Therefore, the optimal normalized classification algorithm will be employed in which the probability density function (PDF) is derived under the same assumption used to derive the PDF for the unnormalized fully polarimetric data. When employing this normalization process, the classification result and the probability of error will be independent of the normalization function [Yueh *et al.*, 1988].

From an alternate point of view, unsupervised classification may also be applied. The polarization state of the received wave may be compared to that of the transmitted wave in order to deduce the properties of the scatterer. This algorithm classifies terrain elements based on the relationship between the orientation angle and handedness of the transmitting and receiving polarization states. Classification is then based solely on the properties of the scatterer and not on any *a priori* training data [van Zyl, 1987].

In section 2 of this chapter, both the supervised and unsupervised classification techniques are applied to San Francisco Bay and Traverse City Synthetic Aperture Radar (SAR) images, supplied by the Jet Propulsion Laboratory. These images were collected at L-band (1.225 GHz) with near range along the upper part of the image. There are 896 pixels in the range and 4096 pixels in the azimuth with approximately 10 m by 3 m resolution per pixel. For supervised classification processing, the Bayes technique is used to classify fully polarimetric and normalized polarimetric SAR data. Simpler polarimetric discrimi-

nates, such as the absolute and normalized magnitude response of the individual receiver channel returns, in addition to the phase difference between the receiver channels, are also considered. An unsupervised technique, based on comparing general properties of the Stokes parameters of the scattered wave to that of simple scattering models, is also discussed [van Zyl, 1987]. It is shown that supervised classification yields the best overall performance when accurate classifier training data are used, whereas unsupervised classification is applicable when training data are not available.

Besides classifying earth terrain into different classes, there is also considerable interest in determining the optimal polarizations that maximize contrast between two scattering classes in polarimetric radar images [Swartz *et al.*, 1988]. Contrast enhancement is a processing technique which modifies the input data structure so that either the human observer, computer, or other hardware devices can extract certain information from the processed data more readily after the change [Huang, 1969]. In the second part of this chapter, the polarimetric properties of the radar returns are utilized to enhance the contrast between two scattering classes. It is assumed that complete *a priori* statistical knowledge of the two scattering classes or types exists and the polarimetric signals backscattered from the two scattering classes are independent. The processing requirement is then to determine the optimal transmitting and receiving polarization state which will maximize the separation of the average power returns between the two classes. Applying such a technique to radar imagery will allow for better discrimination of the two classes.

For two deterministic scatterers, completely characterized by 2×2 complex scattering matrices, Kozlov [1979] introduced a method for computing the optimal polarization state which involves transformation of the scattering matrix of each of the two objects into a preferred polarization basis. Solutions involving scattering matrix co-pol and cross-pol (polarization) nulls have also been presented [Mieras, 1983; Nespor *et al.*, 1984; McCormick and Hendry, 1985]. More recently, Kostinski and Boerner [1987] determined the transmitting and receiving polarization state which produced maximum contrast between two classes represented by their Graves power matrices. This technique involved maximizing the expected power return from one deterministic scattering class with respect to another.

Although these are viable procedures when dealing with deter-

ministic scattering classes, they cannot be utilized in the case of statistically distributed scattering objects, e.g., terrain clutter. A deterministic scatterer can be characterized by a scattering matrix, whereas nondeterministic scatterers must be represented either by an average Mueller matrix or, equivalently, by a polarimetric covariance matrix, which are the second order statistics of the scattering matrix. To enhance the contrast between nondeterministic scatterers, the ratio of the average power returns from the two scattering classes must be maximised.

In the case of distributed scatterers in the clear, observability is limited only by background noise. Since the noise in the receiver channels is statistically independent and usually normalized at the same average power, the background noise is generally unpolarized. This implies that when the target-to-clutter ratio is maximized, under the assumption that the distributed scatterer represents the target, whereas background noise denotes clutter, it will be found that the background noise contribution has essentially a constant expected power level [Giuli, 1985]. Thus, for targets which are assumed to be in the clear, or independent of a clutter background, maximizing this ratio is equivalent to maximizing the target return power only. Target detection improvement which can be attained by such a procedure has been analyzed by resorting to a Gaussian target model [Giuli, 1982] derived from Huynen's target decomposition theorem [Huynen, 1978]. Moreover, van Zyl *et al.* [1987] have determined the optimal copolarisation state for maximum power return from an isolated, distributed scatterer, represented by its average Mueller matrix.

For the case of two scattering classes, both of which were either fully or partially polarised, Ioannidis and Hammers [1979] employed a Lagrange multiplier method to determine the transmitting and receiving polarization state that maximized a target's return in the presence of clutter. The target-to-clutter ratio, expressed in terms of average Mueller matrices, was maximised in order to determine the optimal transmitting and receiving antenna Stokes polarization vectors. Zeber *et al.* [1987] have introduced the polarization signature as a means of displaying polarimetric characteristic of various scatterers. They [Zeber *et al.*, 1987] numerically determined the polarization state which maximised contrast between two classes when the receiving polarization was fixed with respect to that of the transmitter, e.g., co- or cross-polarized returns.

It should be noted that all of the techniques previously discussed for polarimetric enhancement of a target's return in the presence of clutter have maximized the target-to-clutter ratio. However, maximization of the contrast between two classes is not necessarily the same as maximizing the target-to-clutter ratio. For example, the object scattering the most power generally is denoted to signify the target class, whereas the other scattering class is referred to as clutter, although this may not always be the case. If a target in severe clutter is considered, the clutter class may actually scatter more power than the target for some transmitting and receiving polarization states. Moreover, the classes can exhibit different polarimetric correlation coefficients between the receiver channels while having comparable radar cross sections. Thus, the notion of a target and clutter class, in some instances, is not well defined. Note also that, in general, maximisation of the target-to-clutter ratio does not provide the same contrast between classes as maximization of the clutter-to-target ratio. Therefore, the problem addressed here is to select the larger of these two values and determine its corresponding polarization state. For this reason, the term contrast ratio will be adopted as opposed to using either the target-to-clutter or clutter-to-target ratios.

Consequently, the procedure implemented in section 3 will determine the transmitting and receiving polarization state which produces maximum contrast, or separation in the average intensity, between the two scattering classes. To realize this objective, the contrast ratio will be maximised, i.e., the *maximum contrast ratio* is computed in order to obtain the optimal linear weighting vector or optimal polarimetric matched filter [Cadsow, 1980; Swartz, 1988]. Processing polarimetric synthetic aperture radar (SAR) images with this filter performs a polarization synthesis on the data which yields maximum contrast between classes.

6.2 Supervised and Unsupervised Classifications

Supervised and unsupervised classification procedures are developed and applied to SAR polarimetric images in order to identify their various earth terrain components. First, the supervised Bayes classification is presented in section 6.2a where the Bayes Classifier is briefly reviewed. Then the polarimetric Bayes classification procedure is discussed where the distance measures for both unnormalised and nor-

malised data will be used to classify the SAR images into different terrain types. Covariance matrices are computed for each terrain class from selected portions within the image where ground truth is available, under the assumption that the polarimetric data have a multivariate Gaussian distribution. These matrices are then used to train the optimal classifier, which in turn is used to classify the entire image. Simple feature classification, which includes magnitude responses $|HH|$, $|HV|$, and $|VV|$, normalised magnitude responses $|HV|/|HH|$ and $|VV|/|HH|$, and phase differences between channels $\phi_{hh} - \phi_{vv}$, $\phi_{hv} - \phi_{vh}$, and $\phi_{hh} - \phi_{hh}$, will also be discussed. The unsupervised classification procedure, which is based on comparing the general properties of the Stokes parameters to those of some simple scattering models, will be described in section 6.2b where it will be applied to the same images analyzed in section 6.2a.

In addition to the classification based on the high resolution data, four-look classification is performed. It has been shown that the probability of error for the problem of terrain classification can be reduced when multiple independent measurements are possible [Kong et al., 1988]. In this section, the four-look classification is achieved by treating the data from every four consecutive pixels in azimuth as four independent looks of one pixel. For the supervised classification, the distance measure of the combined pixel is the average of those of the original four pixels, whereas the unsupervised four-look classification is achieved by averaging the Mueller matrix over every four pixels in azimuth. It is found that this four-look classification greatly improves the probability of classification. The performances of the various supervised and unsupervised classification schemes for both single-look and four-look classification will then be compared in section 6.2c, and the results are summarized in section 6.2d.

a Supervised Classification Procedure

a.1 The Bayes classifier

In reviewing the Bayes Classifier, we first define a complex linear vector \bar{X} containing a fully polarimetric radar return and call it the feature vector [Kong et al., 1988].

$$\bar{X} = \begin{bmatrix} HH \\ HV \\ VV \end{bmatrix} = \begin{bmatrix} HH_I + i HH_Q \\ HV_I + i HV_Q \\ VV_I + i VV_Q \end{bmatrix} \quad (1)$$

6.2 Supervised and Unsupervised Classifications

where HH is the horizontally transmitted and received return, HV the cross polarized return, and VV the vertically transmitted and received return. The subscripts I and Q represent the in-phase and quadrature components. According to the Bayes maximum likelihood ratio test, [Fukunaga, 1972] the feature vector \bar{X} will be assigned to the class ω_i if the probability of it being in that class is greater than that of it being in any other class. Mathematically, this can be written in the following form

$$\omega_i, \quad i = 1, 2, \dots, M \text{ classes}$$

$$\bar{X} \in \omega_i \text{ if } P(\omega_i|\bar{X}) > P(\omega_j|\bar{X}) \text{ for all } j \neq i \quad (2)$$

However, if (2) is to be applied to radar data, reformulation of this criterion is necessary since one normally does not have, nor can easily assume the probability distribution over the range of classes for each pixel, $P(\omega_i|\bar{X})$. By using the Bayes theorem, the decision rule can be written in a more useful form as follows

$$\bar{X} \in \omega_i \text{ if } P(\bar{X}|\omega_i)P(\omega_i) > P(\bar{X}|\omega_j)P(\omega_j) \text{ for all } j \neq i \quad (3)$$

Classification can now be implemented with (3) as long as the *a priori* probabilities, $P(\omega_i)$ and the probability distribution of the radar returns for each class, $P(\bar{X}|\omega_i)$ are known. Since a forehand knowledge of the relative occurrence of each of the classes is not available, the *a priori* probabilities for all classes are assumed to be equal in all of the images discussed.

For convenience, the decision rule can be rewritten in terms of a distance measure defined to be the negative logarithm of the total probability.

$$\bar{X} \in \omega_i \text{ if } d_i(\bar{X}) < d_j(\bar{X}) \text{ for all } j \neq i$$

$$d_i(\bar{X}) = -\ln P(\bar{X}|\omega_i)P(\omega_i) \quad (4)$$

The classification is now based on minimum distance rather than maximum probability. This process of computing the distance measure for each class and assigning it to the class that yields the minimum distance is carried out pixel by pixel until all the pixels of the image are classified, resulting in a final false color-coded image. Likewise, the four-look classification is achieved by comparing the averaged distance measures over every four pixels in azimuth and classifying these four pixels into the class with minimum distance.

6.2 Fully polarimetric classification

For the unnormalized data, the polarimetric feature vector recorded by the SAR is defined to be of the form given by (1). As for the probability distribution of the radar returns, it is assumed that the in-phase and quadrature components of the feature vector \bar{X} have equal variance and are independent zero-mean Gaussian distribution. Based upon the assumption made, the joint probability density function for the feature vector \bar{X} is a multivariate complex Gaussian distribution [Urkowitz, 1980]. Therefore, its corresponding conditional PDF for the m -th class will be of the form

$$P(\bar{X}|m) = \frac{1}{\pi^3 |\bar{C}_m|} \exp \left\{ -\bar{X}^+ \cdot \bar{C}_m^{-1} \cdot \bar{X} \right\} \quad (5)$$

where $\bar{C} = \langle \bar{X} \bar{X}^+ \rangle_{A_m}$ is a 3 by 3 complex covariance matrix of the zero-mean polarimetric data, i.e., $\langle \bar{X} \rangle_{A_m} = 0$. A_m represents the training area for the m -th class over which the covariance matrix is spatially averaged, as shown in Fig. 6.1. From the indicated regions the three covariance matrices are obtained which correspond to the three classes: ocean, urban, and park, considered in this image.

From the definition given in (4), the distance measure corresponding to the fully polarimetric classification can easily be obtained from the probability function in (5). Thus, the distance measure for the m -th class can be written as

$$d_m(\bar{X}) = \bar{X}^+ \cdot \bar{C}_m^{-1} \cdot \bar{X} + \ln |\bar{C}_m| - \ln [P_o(m)] \quad (6)$$

Any term of the distance measure that is not a function of m has been dropped since they do not contribute to the classification. In (6), it can be seen that the covariance matrix, which is obtained from the training regions, serves as a linear weighting vector for the polarimetric return power which optimizes classification.

Four-look Classification based on this distance measure (6) for classification is shown in Fig. 6.2, where the three classes: ocean, urban, and park are represented by the colors: blue, red, and green, respectively. Single-look classification is also implemented with the probability of error summarized in Table 6.1. Even with impure training regions for the park and urban classes, as can be seen in Fig. 6.1, classification

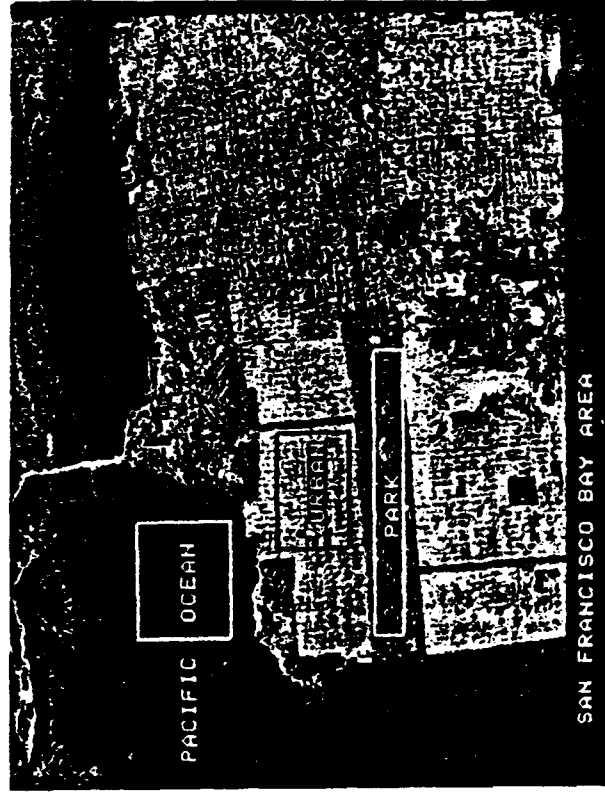


Figure 6.1 Training regions for the three classes: ocean, park, and urban selected from the San Francisco Bay area image to compute covariance matrices for supervised Bayes classification.

using the fully polarimetric information was able to correctly classify a large portion of the terrain components. This classifier was able to identify the tree-lined boulevards of San Francisco and even locate the small lakes within the Golden Gate Park. However, the upper right-hand region of the image was misclassified as urban region, though it should have been classified as ocean. This is due to the higher backscatter from the ocean surface in that region as can be seen in Fig. 6.1. One possible reason for this higher return is a smaller angle of incidence (closer to normal) in this region. This problem can be corrected by implementing a normalization technique which is presented next.



Figure 6.2 Supervised Bayes classification of San Francisco Bay area based on fully polarimetric data [see color plate 6.1].

6.3 Normalized polarimetric classification

When the absolute backscattered power is uncertain, classification can be based on a normalized feature vector given as

$$\frac{\bar{X}}{N} = \frac{1}{N} \begin{bmatrix} HH \\ HV \\ VV \end{bmatrix} \quad (7a)$$

$$N = \sqrt{|HH|^2 + |HV|^2 + |VV|^2} \quad (7b)$$

It has been shown that the classification scheme based on normalized polarimetric data is independent of the normalization function. This holds provided that the PDF of the normalized polarimetric data is derived from the same assumption used to derive the PDF of the unnormalized data [Yueh *et al.*, 1988].

A spherical transformation can be used for the Euclidean norm given in (7b) to derive the PDF of the normalized polarimetric data [Yueh *et al.*, 1988]. Assuming that the probability density for the unnormalized data is a multivariate complex Gaussian distribution, the

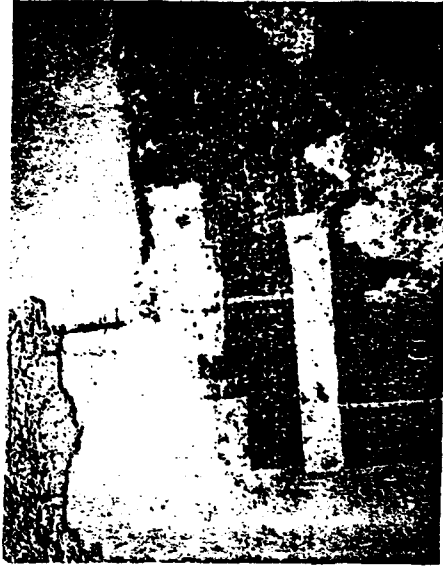


Figure 6.3 Bayes classification of San Francisco Bay area using normalized polarimetric data [see color plate 6.2].

PDF for the normalized data, written in terms of the new normalized quantities θ and ϕ is

$$P(\theta, \phi, \phi_{hh}, \phi_{hv}, \phi_{vv} | m) = \frac{\cos \phi \sin \phi \cos \theta \sin^3 \theta}{\pi^3 |\bar{C}_m|} \left(\frac{\bar{X}^+ \cdot \bar{C}_m^{-1} \cdot \bar{X}}{N^2} \right)^{-3} \quad (8)$$

where

$$\theta = \cos^{-1} \left(\frac{|VV|}{N} \right) \quad (9a)$$

$$\phi = \tan^{-1} \left(\frac{|HV|}{|HH|} \right) \quad (9b)$$

From (8), the new distance measure for the normalized polarimetric case is then easily shown to be as follows

$$d_m = -\ln [P_a(m)] + \ln |\bar{C}_m| + 3 \ln \left(\bar{X}^+ \cdot \bar{C}_m^{-1} \cdot \bar{X} \right) \quad (10)$$

Note that classification performance is independent of the normalization scheme since the normalization factor does not appear in the above expression.

By using the new distance measure given in (10), the same San Francisco Bay SAR image is classified into the ocean, urban, and park regions as shown in Fig. 6.3 for four-look classification. Again, it is assumed that the *a priori* probabilities of each class are equal. Note that the upper right-hand region of the image is now correctly classified as ocean. The result shown in Fig. 6.3 clearly indicates that the normalized polarimetric classification can be quite useful in regions where the absolute return is uncertain. However, it is observed that the performance in the urban-park region has been degraded. This is not surprising since the absolute levels of the radar returns are not used by this classifier.

The classification procedures were applied to another SAR image from a forested region near Traverse City, Michigan. This image was classified into regions consisting of corn fields, forest, lakes, and agricultural fields which are color-coded red, green, blue, and yellow, respectively. The training regions for these four classes are shown in Fig. 6.4, and the classified images for the fully polarimetric and normalized polarimetric classifiers are shown in Figs. 6.5 and 6.6, respectively. Note that these images are obtained using the four-look classification scheme described at the beginning of section 6.2. The classified images clearly indicate that the fully polarimetric result is much better than the normalized classification, unlike the San Francisco images, since there were no large misclassifications due to unusually high returns in the Traverse City fully polarimetric image.

6.1 Simple feature classification

Instead of using the fully polarimetric information, specific features can be isolated for classification by deriving the appropriate probability density functions. The results will then indicate the strong and weak points of each feature in the classification of earth terrain. To derive the classification procedures for simple features, the following

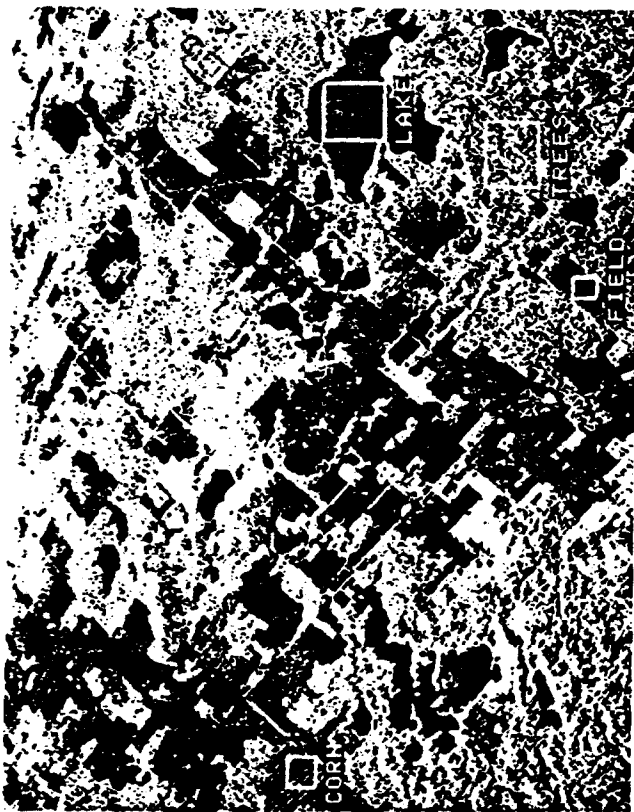


Figure 6.4 Training regions selected for the four classes: corn, fields, lake, and trees selected from the Traverse City, Michigan area image to compute covariance matrices for supervised Bayes classification.

general form of the polarimetric covariance matrix is assumed

$$\bar{C}_m = \sigma_m \begin{bmatrix} 1 & \beta_m \sqrt{\epsilon_m} & \rho_m \sqrt{\gamma_m} \\ \beta_m^* \sqrt{\epsilon} & \epsilon_m & \xi_m \sqrt{\gamma_m \epsilon_m} \\ \rho_m^* \sqrt{\gamma_m} & \xi_m^* \sqrt{\gamma_m \epsilon_m} & \gamma_m \end{bmatrix} \quad (11)$$

where

$$\sigma_m = < |HH|^2 > / A_m \quad (12a)$$

$$\epsilon_m = < |HV|^2 > / A_m / \sigma_m \quad (12b)$$

$$\gamma_m = < |VV|^2 > / A_m / \sigma_m \quad (12c)$$

$$\rho_m = \frac{\langle HH \ VV^* \rangle |A_m|}{\sigma_m \sqrt{\gamma_m}} = |\rho_m| \exp [i\phi_{\rho_m}] \quad (12d)$$

$$\beta_m = \frac{\langle HH \ HV^* \rangle |A_m|}{\sigma_m \sqrt{\epsilon_m}} = |\beta_m| \exp [i\phi_{\beta_m}] \quad (12e)$$

$$\xi_m = \frac{\langle HV \ VV^* \rangle |A_m|}{\sigma_m \sqrt{\epsilon_m \gamma_m}} = |\xi_m| \exp [i\phi_{\xi_m}] \quad (12f)$$

The parameters ρ , β , and ξ are the complex correlation coefficients between the polarimetric channels, γ is the ratio of average VV power to the average HH power, and ϵ is the depolarization ratio within the training region. From the multivariate Gaussian distribution assumption, the probability density functions corresponding to each simple feature can be derived.

For classification based solely on the absolute amplitude such as $|HH|$, $|HV|$, and $|VV|$, the Rayleigh distribution is applied [Kong et al., 1988].

$$P(Y|m) = \frac{2Y}{\sigma_{Ym}^2} \exp \left[-\frac{Y^2}{\sigma_{Ym}^2} \right] \quad (13)$$

where $\sigma_{Ym} = \sigma_m$ for $Y = |HH|$, $\sigma_{Ym} = \sigma_m \epsilon_m$ for $Y = |HV|$, and $\sigma_{Ym} = \sigma_m \gamma_m$ for $Y = |VV|$.

Figure 6.7 illustrates the four-look classification based on the magnitude of the HH return for the San Francisco Bay area image. Although the performance is worse than that of the fully polarimetric classification, this feature yielded the best overall performance among the simple features considered. It should be noted that the same misclassification in the upper right-hand region occurred as was the case for the fully polarimetric image. This problem can be corrected by considering classification schemes based on normalized features such as the phase difference between receiver channels and normalized amplitude ratios.

To examine classification performance using simple normalized features, the PDFs for the magnitude ratios $|VV|/|HH|$ and $|HV|/|HH|$ need to be derived. It can be shown for the ratio $r = |VV|/|HH|$ that the PDF is [Kong et al., 1988; Kriegler et al., 1971]

$$P(r|m) = 2\gamma_m(1 - |\rho_m|^2) \frac{r(\gamma_m + r^2)}{[(\gamma_m + r^2)^2 - 4\gamma_m r^2 |\rho_m|^2]^{3/2}} \quad (14)$$

By replacing $|\rho_m|$ with $|\beta_m|$ and γ_m with ϵ_m , respectively, this expression is transformed into, the probability density for the ratio $r =$

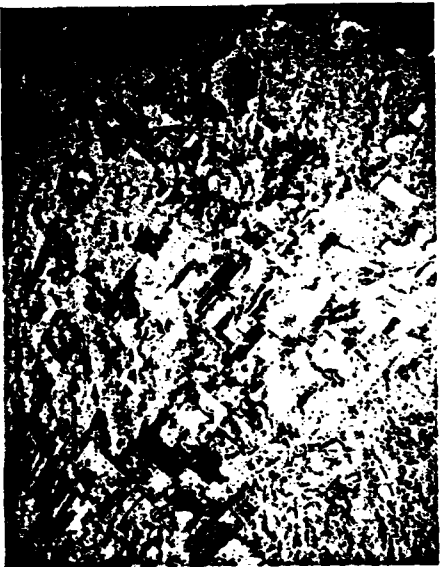


Figure 6.5 Supervised Bayes classification of Traverse City, Michigan using fully polarimetric data [see color plate 6.3].

$|HV|/|HH|$.

The $|HV|/|HH|$ four-look classified image (Fig. 6.8) shows many interesting features. For instance, if observed carefully, the trees lining the large boulevards of San Francisco can be seen. Trees in the other parts of the image are classified well, although the classifier had some difficulty separating the urban and ocean regions. The results indicate that the depolarization ratio is a good discriminate for identifying trees. Also, the essential character of this image resembles the coefficient of variation image [van Zyl et al., 1987] obtained by displaying, in grey-levels, the ratio of the minimum to maximum co-polarized power.

The PDF of the phase difference between HH and VV returns is found by integrating the joint Gaussian PDF for the fully polarimetric data over the amplitudes and the phase of the HV return, ϕ_{hv} . It is given as [Kong et al., 1988]

$$P(\phi|m) = \frac{(1 - |\rho_m|^2)}{2\pi} \left[\frac{(1 - \chi_m^2)^{1/2} + \chi_m(\pi - \cos^{-1} \chi_m)}{(1 - \chi_m^2)^{3/2}} \right] \quad (15)$$



Figure 6.6 Supervised Bayes classification of Traverse City, Michigan using normalized polarimetric data [see color plate 6.4].

where

$$\phi = \phi_{hh} - \phi_{vv} \quad (16a)$$

$$\chi_m = |\rho_m| \cos(\phi - \phi_{\rho_m}) \quad (16b)$$

This PDF can be modified to handle the phase difference between HH and HV , in addition to phase difference between HV and VV returns by using the transformation $|\rho_m| \rightarrow |\beta_m|$, $\phi_{\rho_m} \rightarrow \phi_{\beta_m}$ for $\phi = \phi_{hh} - \phi_{hv}$ and $|\rho_m| \rightarrow |\xi_m|$, $\phi_{\rho_m} \rightarrow \phi_{\xi_m}$ for $\phi = \phi_{hv} - \phi_{vv}$ responses, respectively.

Four-look classification based on the phase difference between the HH and VV channels is shown in Fig. 6.9. The performance in the ocean is very good, whereas the results in the urban-park region are clearly worse than that of the $|HH|$ classified image. Class distinction in this image can be improved, especially in the urban-park region, by preserving the grey-levels of the $|HH|$ image when color coding. The result is shown in Fig. 6.10. The performance is much better now since, in a sense, classification is based on both the magnitude and phase information.



Figure 6.7 Supervised Bayes classification of San Francisco Bay area using $|HH|$ amplitude information only [see color plate 6.5].

b. Unsupervised Classification Procedure

The unsupervised classification procedure utilizes a somewhat simpler approach than the Bayes procedure described previously. This classification technique is based on comparing the general properties of the Stokes parameters of the scattered wave to that of some simple scattering models. The algorithm classifies scatterers based on the relationship between the orientation angles and handedness of the transmit polarization ellipse to the corresponding parameters of the scattered wave for every transmit polarization ellipse.

For example, a slightly rough dielectric surface scattering model [Rice, 1951] predicts that the measured HH and VV signals will be in-phase, and the orientation angle of the scattered wave polarization ellipse increases as the orientation angle of the transmitted wave polarization ellipse increases and decreases as the orientation angle of the transmitted wave polarization ellipse decreases; i.e., the orientation angle of the scattered wave polarization ellipse tracks that of the transmitted wave polarization ellipse. However, the handedness of the scattered wave polarization will be opposite to that of the transmit-



Figure 6.8 Supervised Bayes classification of San Francisco Bay area using magnitude ratio $|HV|/|HH|$ [see color plate 6.6].

ted wave polarization; for example, a left-handed elliptical transmitted polarization will be returned as a right-handed elliptical polarization.

A dihedral corner reflector, on the other hand, exhibits a double bounce geometry [van Zyl *et al.*, 1987], resulting in a 180° phase difference between the measured HH and VV signals. In this case, the orientation angle of the scattered wave polarization ellipse decreases as the orientation angle of the transmitted wave polarization ellipse increases and increases as the orientation angle of the transmitted wave polarization ellipse decreases. The handedness of the scattered wave polarization in this case is the same as that of the transmitted wave polarization.

For areas which exhibit multiple interactions, we have observed a different behavior. As in the case of a slightly rough dielectric surface, the orientation angle of the scattered wave tracks that of the transmitted wave polarization ellipse. The handedness of the scattered wave, however, is the same as that of the transmitted wave polarization which is more consistent with a double bounce mechanism. This behavior can also be generated by a class of vegetation models [Richards *et al.*, 1987;



Figure 6.9 Supervised Bayes classification of San Francisco Bay area using phase difference $\phi_{HH} - \phi_{VV}$ [see color plate 6.7].

van Zyl *et al.*, 1987] or a rough surface partially covered with blocky boulders [van Zyl *et al.*, 1987].

The unsupervised algorithm classifies each pixel of the image by comparing its polarimetric properties to the various models for selected transmitting polarization states. It then assigns the pixel to the class which exhibits similar scattering properties as one of these models. If the pixel does not exhibit polarimetric properties consistent with that predicted by any one of the three models, it is labelled as *unable to be classified*. The classification algorithm produces a false color-coded image as output. The color assignments are as follows: pixels having scattering characteristics consistent with the rough surface model are color-coded blue; those similar to the dihedral corner reflector model are color-coded red; diffusely scattering areas are color-coded green; and pixels that do not exhibit any of the models' scattering characteristics are color-coded yellow. Notice that this classification algorithm does not use training areas, and hence the terminology, unsupervised classification.

For the four-look unsupervised classification, the averaged Mueller



Figure 6.10 Supervised Bayes classification of San Francisco Bay area using phase difference $\phi_{AA} - \phi_v$, color-coded by incorporating grey-levels of the $|HH|$ return power [see color plate 6.8].

matrices of every four pixels are classified based on the single-look classification procedure. Figure 6.11 shows the classified image of the San Francisco Bay area when the four-look unsupervised classification procedure was applied. As was the case in Fig. 6.10 for classification based on the phase difference, the intensity of the HH return power is preserved when color-coding. It is clear that, in general, pixels in the ocean area were correctly classified as being consistent with the rough surface model; while most pixels in the urban, as well as the lighthouse in the ocean (visible off the northwest corner of San Francisco), were correctly classified as being similar to the dihedral corner reflector model. Most of the pixels in Golden Gate park and other tree-covered parts of the city, including the wider tree-lined streets, were classified as being similar to areas with a large amount of diffuse scattering, as predicted by the forested areas model. Notice the urban area which shows up as a green triangle on the right-hand part of the image. Even though there are very few trees in this part of San Francisco, the algorithm classified this urban area as exhibiting a large amount of diffuse scattering. The explanation for this lies in the fact that the streets in this



Figure 6.11 Unsupervised classification based on simple models of San Francisco Bay area incorporating grey-levels of the $|HH|$ return power [see color plate 6.9].

part of the city are at an angle of about 45° with respect to the radar look direction, which leads to a scattering mechanism similar to that described for a rough surface partially covered with blocky boulders.

The unsupervised classification algorithm was also applied to the Traverse City, Michigan data previously discussed. This area consists of forested areas, agricultural fields, and lakes. The results of the four-look unsupervised classification algorithm, when applied to this image, are shown in Fig. 6.12. All the lakes are correctly classified as areas which have polarization characteristics similar to those predicted by slightly rough surface scattering, while the forested areas are classified as exhibiting a large amount of diffuse scattering. Most of the agricultural fields are classified as having polarization characteristics similar to those predicted by the slightly rough surface model. Notice that the far-range shores of the lakes are classified as double bounce reflectors, which is due to scattering off the lake surface into the trees on the shore and back to the radar or vice versa. Also notice that some of the agricultural fields (for example the ones denoted (1) and (2) in Fig. 6.12) are classified as a combination of single and double reflections.) Most



Figure 6.12 Unsupervised classification based on simple models of Traverse City, Michigan incorporating grey-levels of the $|HH|$ return power [see color plate 9.10].

of these fields are corn fields. Corn fields exhibit phase differences between the HH and VV signals which may be appreciably different from the 0° predicted by the slightly rough surface model or the 180° predicted by the dihedral corner reflector model. The area labeled (3) in Fig. 6.12 is classified as exhibiting double reflections. This area consists mostly of trunks of dead trees standing on water-saturated ground resulting in a strong doubly reflected component in the return signal. This example shows that in some cases even this simple classification algorithm is capable of distinguishing between scattering by healthy forests and areas where the trees are dead.

c. Classification Error Analysis

In order to quantitatively assess the relative performance of the classifiers discussed, the probability of error is computed by taking the training regions as absolute ground truth and counting the misclassification within those regions. Table 6.1 shows the results of this analysis for the single-look classification of the fully polarimetric image of the

San Francisco Bay area. The probability of error shown in the last column is obtained by dividing the total number of misclassifications by the total number of pixels in each training region. Then the average probability of error is computed by averaging the three probabilities obtained for each class. In the same way, the results for the four-look classification are shown in Table 6.2 (Note that the total number of pixels is reduced by a factor of four as a result of the four-look averaging.) Carrying out this procedure for each of the features considered, we obtain the numbers compiled in Table 6.3. For the unsupervised technique, two different probabilities of error are computed depending on how the unclassified pixels are accounted for. In case (a), the unclassified pixels were ignored and not included when computing the error; whereas in case (b), the unclassified pixels were counted with the misclassified pixels. The numbers show that the fully polarimetric classification gives the optimal result. The phase difference Bayes classification and the unsupervised classification, which are both two feature classifications, gave similar performance. It should be noted that this may not be the most accurate way of comparing the unsupervised and supervised classifications since the unsupervised technique did not make use of the information contained in the training regions. However, comparison among the supervised classification gives a good measure of the relative performance for each feature; although in the absolute sense, the probability of error may be higher since the training regions may not be pure according to real ground truth. A much better comparison would be to calculate the probability of error over the entire image with respect to the actual pixel by pixel ground truth at the time of the measurement; however, no such information was available.

| Classified Training | Urban | Park | Ocean | P_{error} |
|---------------------|-------|-------|-------|--------------------|
| Urban | 32391 | 29044 | 581 | 0.478 |
| Park | 5150 | 39512 | 2802 | 0.168 |
| Ocean | 43 | 1361 | 60548 | 0.023 |

Avg. $P_{\text{error}} = .223$

Table 6.1 Single-look classification errors and probability of errors obtained for the fully polarimetric San Francisco image by counting the misclassification within each training region assumed to be of a single class.

d. Summary

Two methods for classifying fully polarimetric SAR data, i.e., supervised Bayes classification and an unsupervised classification technique, have been presented and applied to the SAR images of the San Francisco Bay area and a forested area near Traverse City, Michigan. Both techniques can be utilized to full advantage by employing the most appropriate algorithm for a particular application. When accurate training data are available, Bayesian classification will yield optimal results; whereas in the case where ground truth is not well known, unsupervised classification will be useful. In either case, the need for photointerpretation is minimized by employing these polarimetric terrain classification algorithms.

| Classified Training | Urban | Park | Ocean | P_{error} |
|---------------------|-------|-------|-------|--------------------|
| Urban | 9477 | 6027 | 0 | 0.389 |
| Park | 976 | 10823 | 102 | 0.095 |
| Ocean | 24 | 208 | 15256 | 0.015 |

$$\text{Avg. } P_{\text{error}} = .165$$

Table 6.3 Four-look classification errors and probability of errors obtained for the fully polarimetric San Francisco image by counting the misclassification within each training region assumed to be of a single class.

| Feature | Avg. P_{error} (Single-look) | Avg. P_{error} (Four-look) |
|--|--|--|
| Fully Polarimetric | 0.223 | 0.165 |
| Normalised Polarimetric | 0.301 | 0.183 |
| Magnitude of $ HH $ | 0.383 | 0.270 |
| Phase Difference $\phi_{AA} - \phi_{VV}$ | 0.415 | 0.312 |
| Simple Models (a) | 0.437 | 0.342 |
| Magnitude Ratio $ HV / HH $ | 0.529 | 0.366 |
| Simple Models (b) | 0.516 | 0.394 |

Table 6.3 Average Probability of Errors for the supervised and unsupervised classification of San Francisco Images. Fully polarimetric Bayes classification gives the minimum probability of error.

6.3 Maximum Contrast Enhancement

6.3 Maximum Contrast Enhancement

In this section a systematic approach is presented for obtaining the optimal polarimetric matched filter, i.e., that filter which produces maximum contrast between two scattering classes. The contrast ratio is defined as a function of a linear weighting vector (polarization filter) and the polarimetric covariance matrices of the two classes. To exhibit the physical significance of this filter, it is transformed into its associated transmitting and receiving polarization states, written in terms of horizontal and vertical vector components.

In section 6.3a, the polarimetric matched filter and the contrast ratio are defined. The method for achieving maximum contrast between classes, as well as a closed form solution to this problem for the case in which the polarimetric covariance matrices contain four zero elements is considered in section 6.3b. The maximization procedure involves solving an eigenvalue problem where the eigenvector corresponding to the maximum contrast ratio is the optimal polarimetric matched filter. It is then shown how to realize the polarimetric matched filter in terms of an equivalent transmitting and receiving polarization pair. In section 6.3c, for the special case where the transmitting polarization is fixed, the receiving polarization which maximizes the contrast ratio is also obtained. Discussion of the results obtained using optimal polarimetric matched filtering is the scope of section 6.3d. Polarimetric filtering is applied to SAR images obtained from the Jet Propulsion Laboratory. It is shown, both numerically and through the use of radar imagery, that maximum image contrast can be realized when data are processed with the optimal polarimetric matched filter.

a. Polarimetric Matched Filter and Contrast Ratio

Assume that two classes of statistically distributed scattering types exist. Each class is represented by a covariance matrix of the form $\bar{C}_j = E[\bar{X}\bar{X}^H]$, where $j = a, b$ represents class A and class B scatterers, respectively. Here $E[\cdot]$ denotes the expected value and superscript \dagger , the complex conjugate transpose operation. For the case of electromagnetic waves which are backscattered from a reciprocal media, $HV = VH$. Therefore, the polarimetric feature vector, \bar{X} , is expressed in a horizontal-vertical polarization basis as (1) [Kong et al., 1986].

The objective is to find the best linear weighting vector or polarimetric matched filter for processing an observed polarimetric feature vector; that is, the linear combination

$$Y = \bar{W}^T \bar{X} \quad (17)$$

where

$$\bar{W} = \begin{bmatrix} W_{hh} \\ W_{hv} \\ W_{vv} \end{bmatrix} \quad (18)$$

which provides the maximum contrast ratio, r , between the two respective classes (class A and class B). The maximum contrast ratio is defined as

$$r = \text{MAX} \left\{ \text{MAX}_{\bar{W}}(r_{ab}), \text{MAX}_{\bar{W}}(r_{ba}) \right\} \quad (19)$$

where

$$r_{ab} = \frac{\bar{W}^T \bar{C}_a \bar{W}}{\bar{W}^T \bar{C}_b \bar{W}} \quad (20a)$$

$$r_{ba} = \frac{\bar{W}^T \bar{C}_b \bar{W}}{\bar{W}^T \bar{C}_a \bar{W}} \quad (20b)$$

Note that from a physical point of view, the elements of the vector \bar{W} in (17) are linear weighting coefficients which adjust the amplitude and phase of the polarimetric radar measurements. In (20a), the term r_{ab} denotes the contrast ratio of class B with respect to class A scatterers. The contrast ratio of class B with respect to class A scattering elements is expressed in (20b) as r_{ba} . The symbol $\text{MAX}\{\cdot\}$ signifies the maximum value of the argument, i.e., either r_{ab} or r_{ba} in this case, whereas $\text{MAX}_{\bar{W}}(r_{ab})$ indicates that a linear weighting vector \bar{W} has been obtained which maximizes r_{ab} independently of r_{ba} , and $\text{MAX}_{\bar{W}}(r_{ba})$ implies that a different linear weighting vector has been found which maximizes r_{ba} independently of r_{ab} . Also, the numerator and denominator in (20a) and (20b) are obtained from (17) by taking the expected value of the return power from each class.

To demonstrate that the polarimetric matched filter, \bar{W} , directly corresponds to specific transmitting and receiving polarizations, we express (17) in terms of a monostatic reciprocal scattering matrix as

$$Y = [H, V,] \begin{bmatrix} HH & HV \\ HV & VV \end{bmatrix} \begin{bmatrix} H_t \\ V_t \end{bmatrix} \quad (21)$$

6.3 Maximum Contrast Enhancement

in which the values H_t and V_t , H_r and V_r represent the horizontal and vertical vector components of the transmitting and receiving polarization state, respectively. Also, without loss of generality, it is assumed that

$$|H_t|^2 + |V_t|^2 = 1 \quad (22a)$$

$$|H_r|^2 + |V_r|^2 = 1 \quad (22b)$$

Equating (17) and (21) yields

$$H_t H_r = W_{hh}^* \quad (23a)$$

$$H_t V_r + V_t H_r = W_{hv}^* \quad (23b)$$

$$V_t V_r = W_{vv}^* \quad (23c)$$

Thus, given a general linear weighting vector, \bar{W} , its corresponding polarization state components, H_t , V_t , H_r , and V_r , can be completely specified through (23). This will be shown in section 6.3b.

Note that (21) indicates the transmitting and receiving polarization vectors are reciprocal, i.e., the terms H_t and V_t can be interchanged with H_r and V_r without altering the measurement, Y . Therefore, in the case of reciprocal backscattering, the same contrast ratio will be obtained if the transmitting and receiving polarization vectors are exchanged.

b. Optimal Polarimetric Matched Filter Required to Obtain Maximum Contrast Between Two Scattering Classes

b.1 Solution of optimal polarimetric matched filter

In order to compute the optimal polarimetric matched filter, (20a) and (20b) must be maximized. The linear weighting vector which corresponds to the maximum contrast ratio, shown in (19), will be denoted as the optimal polarimetric matched filter. The maximization procedure makes use of the Lagrange multiplier technique. Details of this procedure were outlined by Cadzow [1980], although the steps will be repeated here for completeness. For example, in order to maximize r_{ab} , in (20a),

$$\text{MAX} \left\{ \bar{W}^T \bar{C}_a \bar{W} \right\} \quad (24)$$

is determined under an arbitrary constraint

$$\bar{W}^T \bar{C}_b \bar{W} = 1 \quad (25)$$

This reformulation is possible, without loss of generality, since the linear weighting vector can be multiplied by any arbitrary complex constant without affecting the contrast ratio. The solution to this constrained maximization problem is obtained by making use of the Lagrange multiplier concept, which reflects the constraint shown in (25). Its solution will be a stationary point of the auxiliary functional

$$f(\bar{W}) = \bar{W}^T \bar{C}_s \bar{W} + \lambda [1 - \bar{W}^T \bar{C}_b \bar{W}] \quad (26)$$

in which λ is a scalar valued Lagrange multiplier. Specifically, the stationary points of this auxiliary functional are found first by representing the generally complex vector \bar{W} in terms of its real and imaginary components, as $\bar{W}_R + i\bar{W}_I$. Then, taking the gradient of the auxiliary functional with respect to \bar{W}_R and \bar{W}_I , setting the resulting equations equal to zero, i.e.,

$$\frac{\partial f(\bar{W})}{\partial \bar{W}_R} = 0 \quad (27a)$$

$$\frac{\partial f(\bar{W})}{\partial \bar{W}_I} = 0 \quad (27b)$$

yields the necessary condition for a maxima or minima to occur. Carrying out (27a) and (27b) leads to the eigenvalue equation

$$\bar{C}_s \bar{W} = \lambda \bar{C}_b \bar{W} \quad (28)$$

Note that the eigenvalue (Lagrange multiplier) λ , in (28), is the contrast ratio r_{sb} given by (20a), whereas $1/\lambda$ signifies the contrast ratio r_{bs} shown in (20b). Since the objective is to determine the maximum contrast ratio between classes, the values of the maximum and the reciprocal of the minimum eigenvalue must be compared and the larger of the two selected. The eigenvector which corresponds to this maxima is the optimal polarimetric matched filter that should be employed to process the radar polarimetry. Note that it is not required to maximize both (20a) and (20b). By extremizing (20a) then selecting the largest of either the maximum eigenvalue or the reciprocal of the minimum eigenvalue, both (20a) and (20b) have been simultaneously maximized.

In the event that the eigenvalues of (28) are degenerate, there will exist no preferred polarization basis for which the expected power return of two objects can be separated. Assuming then, that the contrast

ratios are not degenerate, the optimal polarimetric matched filter, \bar{W} , is interpreted to be the equivalent transmitting and receiving polarization state which a radar can utilize in order to detect the maximum contrast, or separation in average intensity, between classes.

The contrast optimization approach used for the case of a monostatic radar also can be applied to a polarimetric bistatic radar. Taking into account the fact that for bistatic scattering $HV \neq VH$ when defining \bar{X} and \bar{W} in (1) and (17), leads to 4×4 polarimetric covariance matrices which characterize the scattering classes. Then applying exactly the same method of solution yields the transmitting and receiving polarization state that maximizes contrast between scattering classes.

Once the optimal polarimetric matched filter is obtained, the corresponding transmitting and receiving polarization state can be calculated. Without loss of generality, the case when W_{hh} is not equal to zero will be shown. From (22) and (23), it is found that

$$H_t = \left[\frac{W_{hv}^* \pm \sqrt{(W_{hv}^*)^2 - 4(W_{hh}W_{vv})^*}}{2W_{hh}^*} \right]^2 + 1 \quad (29a)$$

$$V_t = H_t \cdot \left[\frac{W_{hv}^* \pm \sqrt{(W_{hv}^*)^2 - 4(W_{hh}W_{vv})^*}}{2W_{hh}^*} \right] \quad (29b)$$

$$H_r = \frac{\tau}{H_t} \cdot W_{hh}^* \quad (29c)$$

$$V_r = \frac{\tau}{H_t} \cdot \left[\frac{W_{hv}^* \pm \sqrt{(W_{hv}^*)^2 - 4(W_{hh}W_{vv})^*}}{2} \right] \quad (29d)$$

where

$$\tau = \frac{1}{\sqrt{\tau_1 \cdot \tau_2 \cdot \tau_3}} \quad (30)$$

$$\tau_1 = |W_{hh}^*|^2 \quad (31a)$$

$$\tau_2 = 1 + \left[\frac{W_{hv}^* \pm \sqrt{(W_{hv}^*)^2 - 4(W_{hh}W_{vv})^*}}{2W_{hh}^*} \right]^2 \quad (31b)$$

$$\tau_3 = 1 + \left[\frac{W_{hv}^* \pm \sqrt{(W_{hv}^*)^2 - 4(W_{hh}W_{vv})^*}}{2W_{hh}^*} \right]^2 \quad (31c)$$

The absolute intensity value, I , is given by

$$I = |\tau \bar{W}^1 \bar{X}|^2 \quad (32)$$

where τ is the amplitude normalization constant given in (30).

The observed sign change in (29), i.e., \pm or \mp , indicates the reciprocity of the transmitting and receiving polarization state, as previously mentioned. Also, the resulting transmitting and receiving polarization state is independent of any multiplicative constant effecting the matched filter. This is necessary since the general complex eigenvector solution to (28) can vary by a multiplicative complex constant; however, the resulting polarization state remains unaffected since this constant can be factored out.

Finally, a comparison between the methods for contrast enhancement presented in this chapter versus that originally proposed by Ioannidis and Hammers [1979] is in order. In their method, the target-to-clutter ratio was maximized to determine the optimal transmitting and receiving antenna Stokes polarization vectors. The Ioannidis and Hammers' method requires the use of three constraints in order to solve the maximization problem. One is similar to (25) in that it constrains the denominator of the target-to-clutter ratio to be equal to an arbitrary constant. The other two constrain the transmitting and receiving vectors to be antenna Stokes polarization vectors. This results in complex expressions which specify the optimal transmitting and receiving polarization state. In addition, they do not obtain the matched filter which corresponds to the optimal transmitting and receiving polarization state. When using Cadzow's method, only one constraint (25) is needed to solve for the optimal polarimetric matched filter. In this case, the maximization procedure only requires solving the eigenvalue problem shown in (28). It should be pointed out that both methods yield identical results when polarimetric target and clutter classes are prespecified.

The major difference between these two techniques is that Ioannidis and Hammers' method dealt with the specific problem of maximizing the target-to-clutter ratio by determining the optimal transmitting and receiving antenna Stokes polarization vectors, whereas the matched filtering approach used in this chapter can be applied to a more general class of problems. That is, Cadzow's procedure extends to multichannel, multifrequency sensor data. Polarimetric contrast enhancement is considered here as a special case.

b.2 Solution for the case of a covariance matrix with four zero elements

Thus far, the most general form of the polarimetric covariance matrix has been assumed, which is

$$\bar{C}_j = \sigma_j \begin{bmatrix} 1 & \beta_j \sqrt{\epsilon_j} & \rho_j \sqrt{\gamma_j} \\ \beta_j^* \sqrt{\epsilon_j} & \epsilon_j & \xi_j \sqrt{\epsilon_j \gamma_j} \\ \rho_j^* \sqrt{\gamma_j} & \xi_j^* \sqrt{\epsilon_j \gamma_j} & \gamma_j \end{bmatrix} \quad (33)$$

where $j = a, b$ represents the class A and class B parameters, respectively, and

$$\sigma = \sigma_{hh} \quad (34a)$$

$$c = \sigma_{hv} / \sigma \quad (34b)$$

$$\gamma = \sigma_{vv} / \sigma \quad (34c)$$

$$\rho = \frac{E[HH \cdot VV^*]}{\sigma \sqrt{\gamma}} = |\rho| \exp(i\phi_\rho) \quad (34d)$$

$$\beta = \frac{E[HH \cdot HV^*]}{\sigma \sqrt{\epsilon}} = |\beta| \exp(i\phi_\beta) \quad (34e)$$

$$\xi = \frac{E[HV \cdot VV^*]}{\sigma \sqrt{\epsilon \gamma}} = |\xi| \exp(i\phi_\xi) \quad (34f)$$

Here, the values σ_{hh} , σ_{hv} , and σ_{vv} denote the normalized backscatter cross section per unit area of the HH , HV , and VV returns [Kong et al., 1988].

It has been rigorously shown using the random medium model [Borgeaud et al., 1987], that when each of the two scattering classes can be modeled as a uniform terrain cover, no average correlation exists between HH and HV returns, or between VV and HV returns. Therefore, the variables β and ξ , in (14), are both equal to zero; and the polarimetric covariance matrices contain four zero elements. This implies that the terrain exhibits azimuthal symmetry from a statistical point of view. It should be pointed out that this effect has been experimentally observed at various sites by MIT Lincoln Laboratory in their polarimetric measurements at 35 GHz [Borgeaud et al., 1987] (see Table 6.5). In this case, the polarimetric covariance matrix can be

expressed as

$$\bar{C}_j = \sigma_j \begin{bmatrix} 1 & 0 & \rho_j \sqrt{\gamma_j} \\ 0 & \epsilon_j & 0 \\ \rho_j^* \sqrt{\gamma_j} & 0 & \gamma_j \end{bmatrix} \quad (35)$$

A closed form solution to the general eigenvalue problem in (28), based on the covariance matrix in (35), is presented in the following.

First, the eigenvalues for the matrix $\bar{C}_b^{-1} \bar{C}_a$ are determined. They can be expressed as

$$\lambda_1 = \frac{c_a \sigma_a}{c_b \sigma_b} \quad (36a)$$

$$\lambda_{2,3} = \frac{\sigma_a}{2\sigma_b \gamma_b (1 - |\rho_b|^2)} \left[\gamma_a + \gamma_b - 2\sqrt{\gamma_b \gamma_a} |\rho_a| |\rho_b| \cos(\phi_{\rho_a} - \phi_{\rho_b}) \right. \\ \left. \times \left[\gamma_a + \gamma_b - 2\sqrt{\gamma_b \gamma_a} |\rho_a| |\rho_b| \cos(\phi_{\rho_a} - \phi_{\rho_b}) \right]^2 \right. \\ \left. - 4\gamma_a \gamma_b (1 - |\rho_b|^2) (1 - |\rho_a|^2) \right] \quad (36b)$$

Their corresponding eigenvectors are given as

$$\lambda_1 \rightarrow \bar{W}_1 = \begin{bmatrix} 0 \\ 1 \\ 0 \end{bmatrix} \quad (37a)$$

$$\lambda_{2,3} \rightarrow \bar{W}_{2,3} = \begin{bmatrix} 1 \\ 0 \\ \gamma_{2,3} \end{bmatrix} \quad (37b)$$

where

$$\gamma_{2,3} = \frac{\left[\gamma_a - \gamma_b - i2\sqrt{\gamma_b \gamma_a} |\rho_a| |\rho_b| \sin(\phi_{\rho_a} - \phi_{\rho_b}) \right. \\ \left. \pm \left[\gamma_b + \gamma_a - 2\sqrt{\gamma_b \gamma_a} |\rho_a| |\rho_b| \cos(\phi_{\rho_a} - \phi_{\rho_b}) \right]^2 \right. \\ \left. - 4\gamma_a \gamma_b (1 - |\rho_b|^2) (1 - |\rho_a|^2) \right]}{2(\gamma_b \sqrt{\gamma_a \rho_a} - \gamma_a \sqrt{\gamma_b \rho_b})} \quad (38)$$

As in the case of the generalized solution, the eigenvector corresponding to the maximum of either the largest or the reciprocal of the smallest eigenvalue in (36) will produce maximum contrast between the two classes. Therefore, this eigenvector will be the optimal polarimetric matched filter which should be utilized to process the polarimetric feature vector.

c. The Optimal Receiving Polarization State for a Fixed Transmitting Polarization

If presented with a situation where the radar transmitting polarization state is fixed, an optimal receiving polarization state can be determined which maximizes the contrast between the two classes. This problem arises in the case of radar systems which are not fully polarimetric, i.e., they transmit using only a single polarization, say horizontal, but receive the principle and cross-polarization components of the scattered response, say the horizontal and vertical returns. Applying the following technique will indicate how to coherently combine the horizontal and vertical returns such that the contrast between classes is maximized.

Assume that the values H_i and V_i are known and that the requirement shown in (22a) is satisfied. Thus, from (23), \bar{W} may be written as

$$\bar{W} = \begin{bmatrix} (H_i H_i)^* & 0 \\ (H_i V_i)^* + (V_i H_i)^* & H_i^* \\ (V_i V_i)^* & V_i^* \end{bmatrix} = \begin{bmatrix} H_i^* & 0 \\ V_i^* & H_i^* \\ 0 & V_i^* \end{bmatrix} \begin{bmatrix} H_i^* \\ V_i^* \end{bmatrix} = \zeta \bar{R} \quad (39)$$

Substituting (39) for \bar{W} in (20a) gives

$$r_{ab} = \frac{\bar{R}^t \bar{Z}_a \bar{R}}{\bar{R}^t \bar{Z}_b \bar{R}} \quad (40)$$

where

$$\bar{Z}_a = \zeta^t \bar{C}_a \zeta \quad (41a)$$

$$\bar{Z}_b = \zeta^t \bar{C}_b \zeta \quad (41b)$$

Since \bar{Z}_a and \bar{Z}_b are hermitian symmetric, positive semidefinite matrices, (40) can be extremized as in the previous section to obtain the generalized eigenvalue problem

$$\bar{Z}_a \bar{R} = \lambda \bar{Z}_b \bar{R} \quad (42)$$

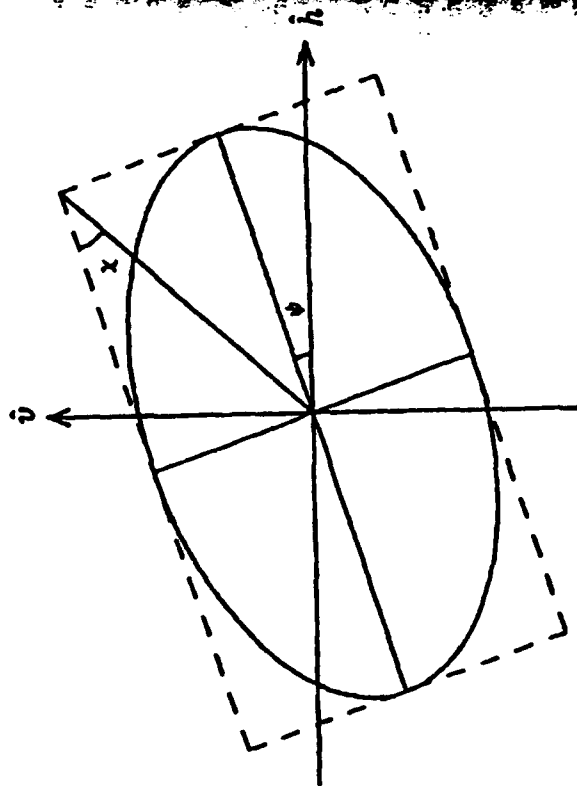


Figure 6.13 Generalized elliptic polarization state.

Once \bar{E} is obtained, it should be normalized so that (22b) holds. Application of the transform given in (39) will yield \bar{W} .

d. Results and Discussion

In order to present the optimal polarimetric matched filtering results in a compact format, orientation (ψ) and ellipticity (χ) angles (Fig. 6.13) are utilized to express the transmitting and receiving polarization states. Here, the definitions from Kong [1986] are adopted. Therefore, horizontal (H) and vertical (V) polarization states will have zero degree ellipticity angles, with orientation angles of 0° and 90° . Right (R) and left (L) polarization states are orientation independent with ellipticity angles of 45° and -45° , respectively. In addition, $0^\circ \leq \psi \leq 180^\circ$ and $-45^\circ \leq \chi \leq 45^\circ$.

A general polarization vector,

$$\bar{P} = \begin{bmatrix} P_h \\ P_v \end{bmatrix} = \begin{bmatrix} |P_h| \exp(i\phi_h) \\ |P_v| \exp(i\phi_v) \end{bmatrix} \quad (45)$$

written in terms of horizontal (\hat{h}) and vertical (\hat{v}) vector components,

can be transformed into a normalized Stokes vector as follows

$$\begin{bmatrix} S_0 \\ S_1 \\ S_2 \\ S_3 \end{bmatrix} = \begin{bmatrix} |P_h|^2 + |P_v|^2 \\ |P_h|^2 - |P_v|^2 \\ 2|P_h||P_v|\cos\phi \\ 2|P_h||P_v|\sin\phi \end{bmatrix} = (|P_h|^2 + |P_v|^2) \begin{bmatrix} 1 \\ \cos 2\chi \cos 2\psi \\ \cos 2\chi \sin 2\psi \\ \sin 2\chi \end{bmatrix} \quad (44)$$

where $\phi = \phi_v - \phi_h$. Using this equation, the angles ψ and χ are obtained.

Two data bases were utilized to study the contrast problem, utilizing the techniques outlined in the previous sections. Table 6.4 gives polarimetric covariance statistics extracted from the San Francisco Bay area, L-band (1.225 GHz) SAR data, collected by the Jet Propulsion Laboratory's airborne polarimeter [Zebker et al., 1987]. These covariance statistics were obtained from the urban and park areas shown in Fig. 6.1 and were utilized to generate the results shown in Tables 6.7, 6.8, and 6.10. Similarly, the experimental polarimetric covariance data, shown in Table 6.5, were supplied by the MIT Lincoln Laboratory [Borgeaud et al., 1987; Kong et al., 1988]. This data, collected at 35 GHz, were used to generate the results presented in Table 6.9. The MIT Lincoln Laboratory radar imaged a vegetation field consisting of grass or trees at a range of approximately 2 kilometers. Studies using this database indicate that essentially no correlation exists between the HH and HV , and between the HV and VV polarimetric returns, i.e., the terrain clutter exhibits azimuthal symmetry.

| | $\sigma(dB)$ | ϵ | γ | $ \rho $ | ϕ_ρ | $ \beta $ | ψ_β | $ \xi $ | ϕ_ξ |
|-------|--------------|------------|----------|----------|-------------|-----------|--------------|---------|------------|
| Urban | -41.7 | 0.043 | 0.882 | 0.281 | -179 | 0.640 | -169 | 0.356 | 18.2 |
| Park | -49.5 | 0.166 | 1.427 | 0.145 | -21.8 | 0.082 | -131 | 0.061 | 96.2 |

Table 6.4 Covariance matrix elements for park and urban (city) regions. Phase angles are given in degrees.

| | $\sigma(dB)$ | ϵ | γ | $ \rho $ | ϕ_ρ |
|-------|--------------|------------|----------|----------|-------------|
| Trees | -13.0 | 0.06 | 1.1 | 0.74 | 0.0 |
| Grass | -15.0 | 0.15 | 1.2 | 0.56 | 0.0 |

Table 6.5 Covariance matrix elements for a uniform terrain cover consisting of grass and tree regions.

Next, a comparison is made which evaluates the performance obtained by processing polarimetric radar data using the optimal polarimetric matched filter versus other commonly used polarization states. Linear weighting vectors which correspond to commonly used transmitting and receiving polarization states are given in Table 6.6. The weighting vectors presented in this table were generated using (23a) through (23c), (43) and (44). These linear weighting vectors are expressed in a horizontal-vertical polarization basis.

Table 6.7 presents theoretical contrast ratios r_{ab} and r_{ba} obtained when utilizing the above-mentioned transmitting and receiving polarization states (Table 6.6) as well as the optimal solution. Here, class A and B scatterers have been defined to denote the park and urban (city) regions, which were represented by their corresponding covariance matrices, \bar{C}_a and \bar{C}_b , respectively. As previously discussed, for reciprocal backscattering the transmitting and receiving polarization state may be interchanged while maintaining the same contrast ratio. This is clearly indicated by the HV and VH results and the LR and RL results. The values r_{ab} and r_{ba} , which denote the maximum and reciprocal of the minimum eigenvalues found after solving (28), are expressed in terms of their corresponding orientation and ellipticity angles, ψ and χ . From Table 6.7 it is seen that the maximum contrast ratio between the two selected classes is 9.12 dB. Note that had only r_{ab} been maximized, a contrast ratio of 0.97 dB would have been realized. In some cases, though, this may be what is required. If the problem was only to make the park processed pixel intensity as large as possible with respect to that of the city, the transmitting and receiving polarization state corresponding to the average power ratio of 0.97 dB would be the appropriate matched filter which should be used to process data.

Table 6.8 shows the actual polarimetric contrast enhancement achieved when processing the radar measurements using the optimal polarimetric matched filter and various other polarization filters. Since the contrast ratios for r_{ba} , given in Table 6.7, are larger than those for r_{ab} , the linear weighting vectors which correspond to the contrast ratios for r_{ba} have been used to generate the results shown in Table 6.8. Thus, Table 6.8 contains the actual average processed pixel intensity realized for each of the two classes (urban and park areas) for both suboptimal polarization filters, i.e., transmitting and receiving polarization states which do not provide maximum contrast between classes, and

6.3 Maximum Contrast Enhancement

the optimal polarimetric matched filter. In comparing the data in this table, it is seen that the quantitative measure of attainable contrast is the contrast ratio, which is the linear ratio of (or the logarithmic distance between) the average pixel intensity for the two respective classes. In the case of processing data with the optimal polarimetric matched filter, this distance is maximum. Thus after optimal processing, it is possible to more readily separate the two classes than prior to it, since the distance between the average value of pixel intensity

| Transmitting Polarization | Receiving Polarization | Linear Weighting Vector: \bar{W} |
|---------------------------|------------------------|---|
| H | H | $\begin{bmatrix} 1.0 \\ 0.0 \\ 0.0 \end{bmatrix}$ |
| H | V | $\begin{bmatrix} 0.0 \\ 1.0 \\ 0.0 \end{bmatrix}$ |
| V | H | $\begin{bmatrix} 0.0 \\ 1.0 \\ 0.0 \end{bmatrix}$ |
| V | V | $\begin{bmatrix} 0.0 \\ 0.0 \\ 1.0 \end{bmatrix}$ |
| L | L | $\begin{bmatrix} 0.5 \\ i \\ -0.5 \end{bmatrix}$ |
| L | R | $\begin{bmatrix} 0.5 \\ 0.0 \\ 0.5 \end{bmatrix}$ |
| R | L | $\begin{bmatrix} 0.5 \\ 0.0 \\ 0.5 \end{bmatrix}$ |
| R | R | $\begin{bmatrix} 0.5 \\ -i \\ -0.5 \end{bmatrix}$ |

Table 6.6 Commonly utilized transmitting and receiving polarization states versus their corresponding linear weighting vectors (expressed in a horizontal-vertical polarization basis).

| Transmitting Polarisation | Receiving Polarisation | Contrast Ratio r_{ab} (dB) | Contrast Ratio r_{ba} (dB) |
|---------------------------|------------------------|------------------------------|------------------------------|
| H | H | -7.86 | 7.86 |
| H | V | -2.00 | 2.00 |
| V | H | -2.00 | 2.00 |
| V | V | -5.77 | 5.77 |
| L | L | -7.62 | 7.62 |
| L | R | -4.78 | 4.78 |
| R | L | -4.78 | 4.78 |
| R | R | -7.51 | 7.51 |
| $\psi = 82.4$ | $\psi = 177.6$ | 0.97 | -0.97 |
| $\chi = 2.25$ | $\chi = -2.43$ | | |
| $\psi = 23.5$ | $\psi = 129.5$ | -9.12 | 9.12 |
| $\chi = -2.45$ | $\chi = 1.92$ | | |

Table 6.7 Theoretical contrast ratios between classes when $\bar{C}_a = \text{Park}$ and $\bar{C}_b = \text{Urban San Francisco Bay regions}$, respectively. Orientation and ellipticity angles are given in degrees. $\text{MAX}_{\bar{W}}(r_{ab}) = 0.97$ dB, $\text{MAX}_{\bar{W}}(r_{ba}) = 9.12$ dB, therefore $r = 9.12$ dB.

| Transmitting Polarisation | Receiving Polarisation | Urban Class (dB) | Park Class (dB) | Contrast Ratio (dB) |
|---------------------------|------------------------|------------------|-----------------|---------------------|
| H | H | -41.7 | -49.5 | 7.8 |
| H | V | -55.3 | -57.3 | 2.0 |
| V | V | -42.2 | -48.0 | 5.8 |
| L | L | -43.5 | -51.2 | 7.7 |
| L | R | -46.4 | -51.2 | 4.8 |
| R | R | -43.6 | -51.1 | 7.5 |
| $\psi = 23.5$ | $\psi = 129.5$ | | | |
| $\chi = -2.45$ | $\chi = 1.92$ | -43.8 | -52.9 | 9.1 |

Table 6.8 Actual average pixel intensities and the contrast ratios between the park and urban San Francisco Bay regions when data were processed using commonly employed polarisation filters and the optimal polarimetric matched filter.

| Transmitting Polarisation | Receiving Polarisation | Contrast Ratio r_{ab} (dB) | Contrast Ratio r_{ba} (dB) |
|---------------------------|------------------------|------------------------------|------------------------------|
| H | H | 2.00 | -2.00 |
| H | V | -1.98 | 1.98 |
| V | H | -1.98 | 1.98 |
| V | V | 1.62 | -1.62 |
| L | L | -1.00 | 1.00 |
| L | R | 2.28 | -2.28 |
| R | L | 2.28 | -2.28 |
| R | R | -1.00 | 1.00 |
| $\psi = 0$ | $\psi = 90$ | | |
| $\chi = 0$ | $\chi = 0$ | -1.98 | 1.98 |
| $\psi \approx 0$ | $\psi \approx 0$ | | |
| $\chi = -38.3$ | $\chi = 38.3$ | 2.31 | -2.31 |

Table 6.9 Theoretical contrast ratios between classes when trees = a and grass = b for class A and B scatterers, respectively. Orientation and ellipticity angles are given in degrees. $\text{MAX}_{\bar{W}}(r_{ab}) = 2.30$ dB, $\text{MAX}_{\bar{W}}(r_{ba}) = 1.99$ dB, therefore $r = 2.30$ dB.

| Transmitting Polarisation | Receiving Polarisation | Contrast Ratio (dB) |
|---------------------------|------------------------|---------------------|
| H | $\psi = 142.1$ | 8.21 |
| | $\chi = 0.51$ | |
| V | $\psi = 44.8$ | 6.10 |
| | $\chi = 0.75$ | |
| R | $\psi = 27.5$ | 7.87 |
| | $\chi = 23.1$ | |
| L | $\psi = 169.5$ | 7.98 |
| | $\chi = -23.6$ | |
| $\psi = 23.5$ | $\psi = 129.5$ | 9.12 |
| $\chi = -2.45$ | $\chi = 1.92$ | |

Table 6.10 Optimal receiving polarisation state for a fixed transmitting polarisation state when $\bar{C}_a = \text{Park}$ and $\bar{C}_b = \text{Urban San Francisco Bay regions}$. Orientation and ellipticity angles are given in degrees.

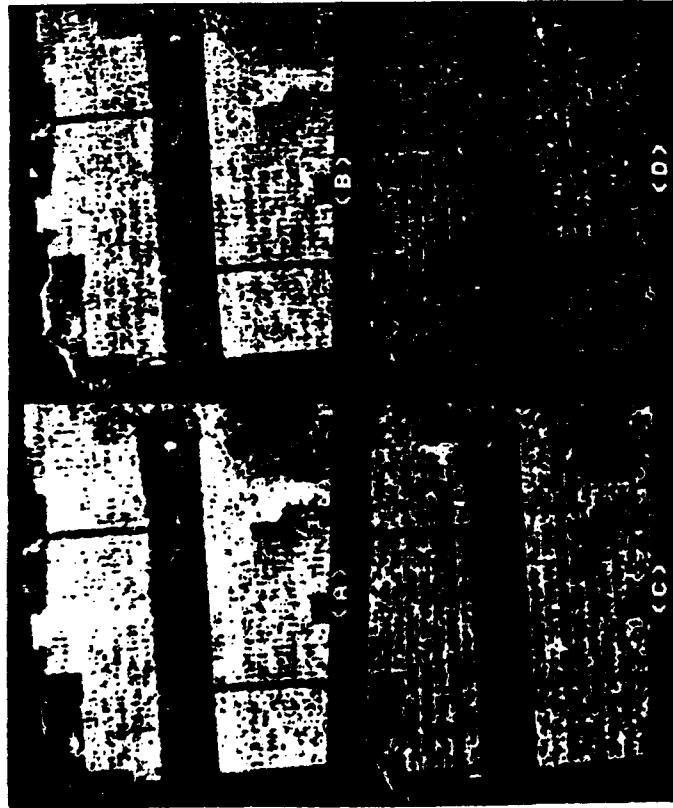


Figure 6.14 San Francisco Bay area images synthesized using the optimal polarimetric matched filter (A), HH (B), VV (C), and HV (D) polarization filters. The corresponding contrast ratios between the city and park region were 9.1, 7.8, 5.8, and 2.0 dB, respectively.

has increased between the two classes. Also note that the contrast ratios, shown in Table 6.8, and those given in Table 6.7 for r_{ba} , are similar indicating a good match between the theoretical predictions and the processed results.

A further demonstration of contrast enhancement can be seen visually by comparing Figs. 6.14A through 6.14D which show San Francisco Bay area images. This imagery has been synthesized utilizing some commonly employed linear polarization states, in addition to the transmitting and receiving polarization state required to produce maximum contrast between the park and urban regions. In all four of these

6.3 Maximum Contrast Enhancement

images, the average processed pixel intensity of the park region was set to the baseline value, i.e., the minimum quantization level of the imaging system display, which was -20 dB. The maximum quantized intensity was -10 dB. By utilizing these quantization limits, some clipping of the higher and lower intensity levels has occurred. This procedure was implemented to compare more easily the contrast between images. Figure 6.14A illustrates the result of processing the San Francisco Bay polarimetry using the optimal polarimetric matched filter. The contrast ratio obtained between the city and park area, as previously indicated in Table 6.8, was 9.1 dB. Contrast ratios achieved using HH (Fig. 6.14B), VV (Fig. 6.14C), and HV (Fig. 6.14D) polarization filters were only 7.8, 5.8, and 2.0 dB, respectively. As indicated in Table 6.8, utilizing the optimal transmitting and receiving polarization state, i.e., the optimal polarimetric matched filter, to process data yields the maximum contrast ratio. Figure 6.14 also shows that the optimal and HH synthesized images appear somewhat similar; this is due to the fact that there is only a 1.2 dB difference between their contrast ratios. However, the optimal polarimetric matched filter always yields a larger contrast ratio between classes than when any other transmitting and receiving polarization states are utilized.

Contrast ratio results, obtained using the MIT Lincoln Laboratory data are presented in Table 6.9. As was the case in Table 6.7, theoretical contrast ratios are given for frequently employed polarization states as well as for the optimal solution. In this table, the tree and grass regions have been arbitrarily selected to denote class a and b scatterers, respectively. The optimal solution again is represented by its corresponding orientation and ellipticity angles ψ and χ , in which case the values presented for r_{ab} and r_{ba} , shown in Table 6.9, signify the maximum and reciprocal of the minimum eigenvalues found when employing the equations shown in (36a) and (36b).

In Table 6.10, the optimal receiving polarization states required to produce the maximum contrast ratio between classes for various fixed transmitting polarization states are presented. These results show that by employing the optimal receiving polarization state, all contrast ratios have increased relative to those shown in Table 6.7 or 6.8. Thus, for a given transmitting polarization state, synthesizing imagery using the optimal receiving polarization state always yields a larger contrast ratio than when any other polarization state is used. However, the

formulation," *IEEE Ant. Prop. Society, International Symposium Digest*, 37-40, 1984.

- [20] Rice, S. O., "Reflection of electromagnetic waves from slightly rough surfaces," *Commun. Pure Appl. Math.*, 4, 351-378, 1951.
- [21] Richards, J. A., G. Sun, and D. Simonett, "L-band radar backscatter modeling of forest stands," *IEEE Trans. Geosci. Remote Sens.* GE-25, 487-498, 1987.
- [22] Smedes, H. W., M. M. Spencer, and F. J. Thomson, "Preprocessing of multispectral data and simulation of ERTS data channels to make computer terrain maps of a Yellowstone National Park test site," *Proc. Seventh International Symposium on Remote Sensing of Environment*, 3, Ann Arbor, Michigan, 2073-2094, 1971.
- [23] Swartz, A. A., H. A. Yueh, J. A. Kong, L. M. Novak, and R. T. Shin, "Optimal polarizations for achieving maximum contrast in radar images," *J. Geophys. Res.*, 93, B12, 15252-15260, 1988.
- [24] Urickovitz, H., *Signal Theory and Random Processes*, Artech House, Inc., 293, 1983.
- [25] van Zyl, J. J., C. H. Papas, and C. Elachi, "On the optimal polarizations of incoherently reflected waves," *IEEE Trans. Ant. Prop.* AP-35, 7, 818-826, July 1987.
- [26] van Zyl, J. J., H. A. Zebker, and C. Elachi, "Imaging radar polarization signature: Theory and observation," *Radio Science*, 22, 4, 529-543, July-Aug., 1987.
- [27] van Zyl, J. J., "Unsupervised classification of scattering behavior using radar polarimetry data," *IEEE Trans. Geosci. Remote Sens.* GE-27, 1, 36-45, 1989.
- [28] Wu, S. T., and S. A. Sader, "Multipolarization SAR data for surface feature delineation and forest vegetation characterization," *IEEE Trans. Geosci. Remote Sens.*, GE-25, 1, 67-76, 1987.
- [29] Yueh, H. A., A. A. Swartz, J. A. Kong, R. T. Shin, and L. M. Novak, "Optimal classification of terrain cover using normalized polarimetric data," *J. Geophys. Res.*, 93, B12, 15261-15267, 1988.
- [30] Zebker, H. A., J. J. van Zyl, and D. N. Held, "Imaging radar polarimetry from wave synthesis," *J. Geophys. Res.*, 92, B1, 683-701, 1987.

Plate 6.1



Plate 6.2

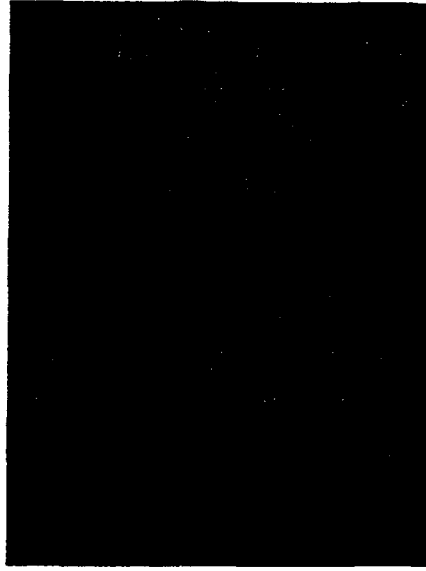


Plate 6.3



Plate 6.7

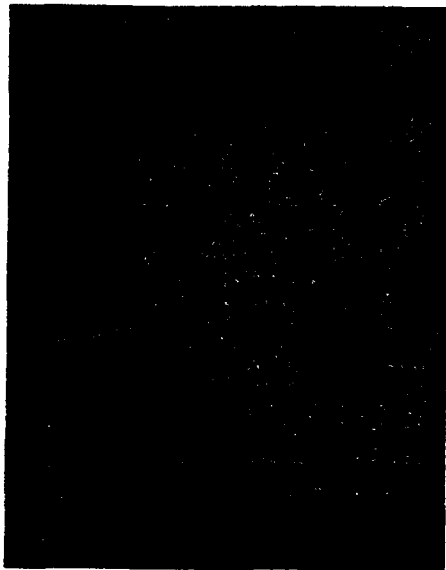


Plate 6.8



Plate 6.9



Plate 6.4

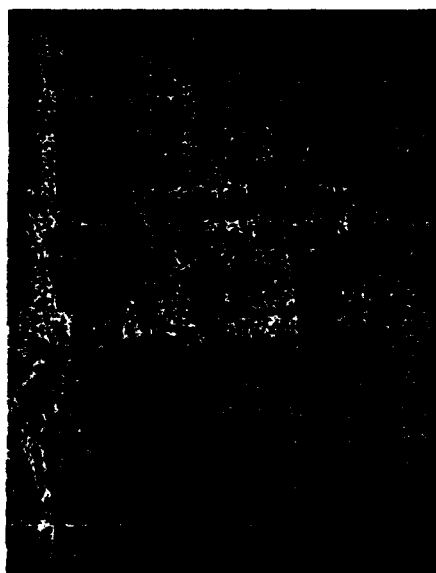


Plate 6.5

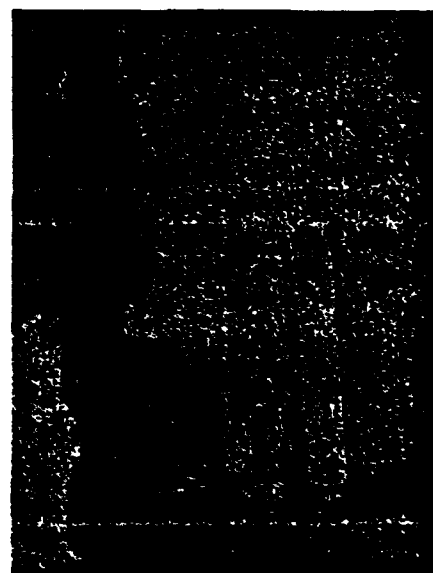


Plate 6.6

Plate 6.10



(a)



(b)



(c)



Plate 7.1

Scattering from Randomly Oriented Scatterers with Strong Permittivity Fluctuations

S. H. Yueh and J. A. Kong

Department of Electrical Engineering
and Computer Science
and Research Laboratory of Electronics
Massachusetts Institute of Technology
Cambridge, MA 02139, USA

R. T. Shin

MIT Lincoln Laboratory
Lexington, MA 02173, USA

Abstract— Strong permittivity fluctuation theory is used to solve the problem of scattering from a medium composed of completely randomly oriented scatterers under the low frequency limit. Based on Finkel'berg's approach [2,3], Gaussian statistics is not assumed for the renormalized scattering sources. The effective permittivity is obtained under the low frequency limit and the result is shown to be isotropic due to no preferred direction in the orientation of the scatterers. Numerical results of the effective permittivity are illustrated for oblate and prolate spheroidal scatterers and compared with the results for spherical scatterers. The results derived are shown to be consistent with the discrete scatterer theory. The effective permittivity of random medium embedded with nonspherical scatterers shows a higher imaginary part than that of spherical scatterer case with equal correlation volume. Under the distorted Born approximation, the polarimetric covariance matrix for the backscattered electric field is calculated for the half-space randomly oriented scatterers. The nonspherical geometry of the scatterers shows significant effects on the cross-polarized backscattering returns $\sigma_{\lambda\lambda}$, and the correlation coefficient ρ between HH and VV returns. The polarimetric backscattering scattering coefficients can provide useful information in distinguishing the geometry of scatterers.

I. INTRODUCTION

There has been a continually growing interest in scattering from random media embedded with nonspherical particles because the particles in rain, ice crystals, fog, snow, leaves, etc., are nonspherical. The radiative transfer theory has been used to study a layer of randomly positioned and oriented nonspherical particles overlying a homogeneous dielectric half space [17,15]. A second approach based on wave theory and Foldy's approximation [6], which is valid only for sparse concentrations of scatterers [5] has also been developed. For nonsparse concentrations of scatterers, incorporating the correlation of scatterer positions, the quasicrystalline approximation and distorted Born approximation have been used to calculate the mean field and the incoherent field [12,14].

For a medium with large spatial permittivity variations, such as water mois-

ture in vegetation and brine inclusions sea ice, strong fluctuation theory has been developed for uniformly aligned spheroidal scatterers [11,13,16]. Because the singularity of the dyadic Green's function is properly taken into account in the renormalization method, the theory is applicable to both small and large variances of permittivity function. However, the orientations of scatterers for natural terrain media are in general random, and, in this paper, we extend the theory to take into account the effect of random orientations.

In the derivation of strong fluctuation theory, a Gaussian random process is usually assumed for the renormalized scattering sources [9,10,11,16]. The Gaussian statistics assumption is employed to factor the higher order moments of the fluctuations in terms of the products of second moments, and a Feynman diagrammatic representation of Dyson's equation for the mean field is derived. Called the bilocal approximation, the mass operator in the form of an infinite series is approximated by the first term. The effective permittivity is derived through the constitutive relation between the mean electric field and the mean dielectric displacement. In the case of non-Gaussian fluctuations, Finkel'berg [2,3,4] introduced the one-group approximation for the mass operator. When the fluctuations are Gaussian, the one-group approximation reduces to the Gaussian case. In this paper, Finkel'berg's approach is generalized to randomly oriented nonspherical scatterers. The polarizability operator is also in the form of an infinite series. The first term of the series is the same for either Gaussian or non-Gaussian fluctuations. This indicates that if the series is approximated by the first term, the bilocal approximation for the effective permittivity gives rise to the same result for Gaussian and non-Gaussian fluctuations.

In Section II, the effective permittivity for an unbounded medium embedded with isotropically oriented nonspherical scatterers is derived using the strong fluctuation theory. The effective permittivity tensor is expressed in terms of an infinite series. The mean field is shown to propagate inside a medium with the effective permittivity. The series is truncated to the lowest-order correction term under the bilocal approximation. An analytical expression for the effective permittivity is given for a specific correlation function under the low frequency approximation. In Section III, numerical results for the effective permittivities for spheroidal scatterers are compared with the discrete scatterer theory in the common regime of validity. In Section IV, under the distorted Born approximation, the scattering from a half-space with ellipsoidal scatterers is solved. The covariance matrix of the polarimetric backscattering coefficients is obtained. Because of the azimuthal symmetry of the orientation, four out of nine elements of the covariance matrix are shown to be zero [1]. In Section V, the polarimetric backscattering coefficients are illustrated for spheroidal scatterers with different axial lengths.

II. STRONG FLUCTUATION THEORY

Consider an unbounded space filled with randomly distributed and oriented scatterers. Assuming the medium is characterized by the permittivity $\epsilon(\vec{r})$, the wave equation for a time harmonic electric field $\vec{E}(\vec{r})$ is

$$\nabla \times \nabla \times \bar{E}(\bar{r}) - k_0^2 \frac{\epsilon(\bar{r})}{\epsilon_0} \bar{E}(\bar{r}) = 0 \quad (1)$$

where

$$\epsilon(\bar{r}) = \begin{cases} \epsilon_s, & \bar{r} \in \text{scatterer} \\ \epsilon_b, & \bar{r} \in \text{background} \end{cases} \quad (2)$$

Introducing ϵ_g which will turn out to be the lowest order term of the effective permittivity by solving (18), we can recast (1) into

$$\nabla \times \nabla \times \bar{E}(\bar{r}) - k_0^2 \frac{\epsilon_g}{\epsilon_0} \bar{E}(\bar{r}) = k_0^2 \frac{\epsilon(\bar{r}) - \epsilon_g}{\epsilon_0} \bar{E}(\bar{r}) \quad (3)$$

By introducing the dyadic Green's function

$$\nabla \times \nabla \times \bar{G}_g(\bar{r}, \bar{r}') - k_0^2 \frac{\epsilon_g}{\epsilon_0} \bar{G}_g(\bar{r}, \bar{r}') = \bar{I} \delta(\bar{r} - \bar{r}') \quad (4)$$

(3) is transformed into the following integral equation:

$$\bar{E}(\bar{r}) = \bar{E}_0 + k_0^2 \int d\bar{r}' \bar{G}_g(\bar{r}, \bar{r}') \cdot \left(\frac{\epsilon(\bar{r}') - \epsilon_g}{\epsilon_0} \right) \cdot \bar{E}(\bar{r}') \quad (5)$$

\bar{E}_0 is the applied electric field. In consideration of the singularity at the source point, the dyadic Green's function is decomposed into two parts:

$$\bar{G}_g(\bar{r}, \bar{r}') = PS \bar{G}_g(\bar{r}, \bar{r}') - \frac{\bar{S}(\bar{r})}{k_0^2} \delta(\bar{r} - \bar{r}') \quad (6)$$

where PS denotes the principal value and $\bar{S}(\bar{r})$ takes into account the shape of exclusion volume at \bar{r} [16].

By substituting (6) into (5), the following equation is obtained:

$$\bar{F}(\bar{r}) = \bar{E}_0 + k_0^2 \int d\bar{r}' PS \bar{G}_g(\bar{r}, \bar{r}') \cdot \bar{\xi}(\bar{r}') \cdot \bar{F}(\bar{r}') \quad (7)$$

where $\bar{F}(\bar{r})$ is the external field and $\epsilon_0 \bar{\xi}(\bar{r}) \cdot \bar{F}(\bar{r})$ corresponds to the induced polarization density:

$$\bar{F}(\bar{r}) = \left[\bar{I} + \bar{S}(\bar{r}) \left(\frac{\epsilon(\bar{r}) - \epsilon_g}{\epsilon_0} \right) \right] \bar{E}(\bar{r}) \quad (8a)$$

$$\bar{\xi}(\bar{r}) = \left(\frac{\epsilon(\bar{r}) - \epsilon_g}{\epsilon_0} \right) \left[\bar{I} + \bar{S}(\bar{r}) \left(\frac{\epsilon(\bar{r}) - \epsilon_g}{\epsilon_0} \right) \right]^{-1} \quad (8b)$$

Expand the solution of the integral equation (7) in terms of infinite series,

$$\begin{aligned} \bar{F}(\bar{r}) = & \bar{E}_0 + k_0^2 \int d\bar{r}_1 PS \bar{G}_g(\bar{r}, \bar{r}_1) \cdot \bar{\xi}(\bar{r}_1) \cdot \bar{E}_0(\bar{r}_1) \\ & + k_0^4 \int d\bar{r}_1 \int d\bar{r}_2 PS \bar{G}_g(\bar{r}, \bar{r}_1) \cdot \bar{\xi}(\bar{r}_1) \cdot PS \bar{G}_g(\bar{r}_1, \bar{r}_2) \cdot \bar{\xi}(\bar{r}_2) \cdot \bar{E}_0(\bar{r}_2) \end{aligned}$$

$$\begin{aligned}
& + k_0^6 \int d\bar{r}_1 \int d\bar{r}_2 \int d\bar{r}_3 PS \bar{G}_g(\bar{r}, \bar{r}_1) \cdot \bar{\xi}(\bar{r}_1) \cdot PS \bar{G}_g(\bar{r}_1, \bar{r}_2) \cdot \bar{\xi}(\bar{r}_2) \\
& \cdot PS \bar{G}_g(\bar{r}_2, \bar{r}_3) \cdot \bar{\xi}(\bar{r}_3) \cdot \bar{E}_0(\bar{r}_3) \\
& + \dots
\end{aligned} \tag{9}$$

The above equation can be represented in an operator form

$$\begin{aligned}
\bar{F}(\bar{r}) = & \bar{E}_0 + PS \bar{G}_g(\bar{r}, \bar{r}_1) \cdot \bar{\xi}(\bar{r}_1) \bar{E}_0(\bar{r}_1) \\
& + PS \bar{G}_g(\bar{r}, \bar{r}_1) \cdot \bar{\xi}(\bar{r}_1) \cdot PS \bar{G}_g(\bar{r}_1, \bar{r}_2) \cdot \bar{\xi}(\bar{r}_2) \\
& + PS \bar{G}_g(\bar{r}, \bar{r}_1) \cdot \bar{\xi}(\bar{r}_1) \cdot PS \bar{G}_g(\bar{r}_1, \bar{r}_2) \cdot \bar{\xi}(\bar{r}_2) \cdot PS \bar{G}_g(\bar{r}_2, \bar{r}_3) \cdot \bar{\xi}(\bar{r}_3) \cdot \bar{E}_0(\bar{r}_3) \\
& + \dots
\end{aligned} \tag{10}$$

Taking the ensemble average of (10), we obtain

$$\begin{aligned}
\langle \bar{F} \rangle = & \langle \bar{I} + \langle PS \bar{G}_g \cdot \bar{\xi} \rangle + \langle PS \bar{G}_g \cdot \bar{\xi} \cdot PS \bar{G}_g \cdot \bar{\xi} \rangle \\
& + \langle PS \bar{G}_g \cdot \bar{\xi} \cdot PS \bar{G}_g \cdot \bar{\xi} \cdot PS \bar{G}_g \cdot \bar{\xi} \rangle + \dots \rangle \cdot \bar{E}_0
\end{aligned} \tag{11}$$

Multiplying (10) by $\bar{\xi}(\bar{r})$ and taking the ensemble average,

$$\begin{aligned}
\langle \bar{\xi} \cdot \bar{F} \rangle = & \langle \bar{\xi} \rangle + \langle \bar{\xi} \cdot PS \bar{G}_g \cdot \bar{\xi} \rangle + \langle \bar{\xi} \cdot PS \bar{G}_g \cdot \bar{\xi} \cdot PS \bar{G}_g \cdot \bar{\xi} \rangle \\
& + \langle \bar{\xi} \cdot PS \bar{G}_g \cdot \bar{\xi} \cdot PS \bar{G}_g \cdot \bar{\xi} \cdot PS \bar{G}_g \cdot \bar{\xi} \rangle + \dots \rangle \cdot \bar{E}_0
\end{aligned} \tag{12}$$

Through cancelling \bar{E}_0 from (12) by using (11), the following equation is obtained:

$$\epsilon_0 \langle \bar{\xi} \cdot \bar{F} \rangle = \epsilon_0 \bar{\xi}_{eff} \langle \bar{F} \rangle \tag{13}$$

where

$$\begin{aligned}
\bar{\xi}_{eff} = & \langle \bar{\xi} \rangle + \left(\langle \bar{\xi} \cdot PS \bar{G}_g \cdot \bar{\xi} \rangle - \langle \bar{\xi} \rangle \cdot \langle PS \bar{G}_g \cdot \bar{\xi} \rangle \right) \\
& + \left(\langle \bar{\xi} \cdot PS \bar{G}_g \cdot \bar{\xi} \cdot PS \bar{G}_g \cdot \bar{\xi} \rangle - \langle \bar{\xi} \cdot PS \bar{G}_g \cdot \bar{\xi} \rangle \cdot \langle PS \bar{G}_g \cdot \bar{\xi} \rangle \right) \\
& - \langle \bar{\xi} \rangle \cdot \langle PS \bar{G}_g \cdot \bar{\xi} \cdot PS \bar{G}_g \cdot \bar{\xi} \rangle + \langle \bar{\xi} \rangle \cdot \langle PS \bar{G}_g \cdot \bar{\xi} \rangle \cdot \langle PS \bar{G}_g \cdot \bar{\xi} \rangle \\
& + \dots
\end{aligned} \tag{14}$$

Note that (13) relates the mean induced polarization density to the mean external field. Making use of (8), we can relate the mean induced polarization density and the mean external field to the mean dielectric displacement $\langle \bar{D} \rangle$ and the mean electric field $\langle \bar{E} \rangle$. Thus the following constitutive relation can be obtained:

$$\langle \bar{D}(\bar{r}) \rangle = \bar{\xi}_{eff} \langle \bar{E}(\bar{r}) \rangle \tag{15}$$

where

$$\bar{\xi}_{eff} = \epsilon_g \bar{I} + \epsilon_0 \left(\bar{I} - \bar{\xi}_{eff} \langle \bar{S} \rangle \right)^{-1} \bar{\xi}_{eff} \tag{16}$$

is the effective permittivity tensor of the random medium. Note that in the derivation of (15) and (16), the fact that the \bar{D} and \bar{E} are independent of \bar{S} or the shape of exclusion volume has been used [18].

By taking the ensemble average of (3) and making use of (15), the mean field can be shown to satisfy the following wave equation:

$$\nabla \times \nabla \times \langle \bar{E} \rangle - k_0^2 \frac{\bar{\epsilon}_{eff}}{\epsilon_0} \langle \bar{E} \rangle = 0 \quad (17)$$

This indicates that the mean field inside the random medium propagates in a homogeneous medium with the effective permittivity tensor $\bar{\epsilon}_{eff}$.

Effective Permittivity Under Low Frequency Approximation

In evaluating the effective permittivity (16), ϵ_g and $\bar{\epsilon}_{eff}$ need to be computed. Note that $\langle \bar{\xi} \rangle$ gives the lowest order correction to the effective permittivity as indicated by (14) and (16). In this paper, ϵ_g will be adjusted so that the first term of $\bar{\epsilon}_{eff}$, (14), is zero, i.e.,

$$\langle \bar{\xi} \rangle = 0 \quad (18)$$

Also, the infinite series (14) will be approximated by the lowest-order term

$$\bar{\epsilon}_{eff} \simeq \langle \bar{\xi} \cdot PS \bar{G}_g \cdot \bar{\xi} \rangle \quad (19)$$

The above approximations correspond to the bilocal approximation for strong fluctuation theory [17].

Assuming

$$|(\bar{\epsilon}_{eff})_{ij}| \ll 1 \quad (20)$$

the effective permittivity of the medium under the low frequency approximation is given by [Appendix A]

$$\bar{\epsilon}_{eff} \simeq \epsilon_g \bar{I} + \epsilon_0 \bar{\xi}_{eff}^{(0)} \quad (21)$$

where $\bar{\xi}_{eff}^{(0)}$ is given in (A6). Explicitly,

$$\bar{\xi}_{eff}^{(0)} = \int d\theta d\phi P(\theta(\bar{r}), \phi(\bar{r})) \left\langle k_0^2 \int \bar{\xi}(\bar{r}) \cdot \bar{G}_g(\bar{r}, \bar{r}') \cdot \bar{\xi}(\bar{r}') d\bar{r}' + \bar{\xi}(\bar{r}) \cdot \bar{S}(\bar{r}) \cdot \bar{\xi}(\bar{r}) \middle| \theta(\bar{r}), \phi(\bar{r}) \right\rangle \quad (22)$$

where $\theta(\bar{r})$ and $\phi(\bar{r})$ represent the corresponding orientation angle of the scatterer at \bar{r} and $P(\theta, \phi)$ corresponds to the probability density function of the orientation.

Let

$$\left\langle \left[\bar{\xi}(\bar{r}) \right]_{il} \left[\bar{\xi}(\bar{r}') \right]_{mj} \middle| \theta(\bar{r}), \phi(\bar{r}) \right\rangle = \Gamma_{ilmj; \theta, \phi}(\bar{r}, \bar{r}') \quad (23)$$

and assume the normalized correlation function for the cross-correlation between the components of $\bar{\xi}(\bar{r})$ and $\bar{\xi}(\bar{r}')$ to be

$$R_{\theta,\phi}(\bar{r}, \bar{r}') = \frac{\Gamma_{ilmj;\theta,\phi}(\bar{r}, \bar{r}')}{\Gamma_{ilmj;\theta,\phi}(\bar{r}, \bar{r})} \quad (24)$$

Using Einstein's convention

$$\begin{aligned} & \left\langle k_0^2 \int \bar{\xi}(\bar{r}) \cdot \bar{G}_g(\bar{r}, \bar{r}') \cdot \bar{\xi}(\bar{r}') d\bar{r}' + \bar{\xi}(\bar{r}) \cdot \bar{S}(\bar{r}) \cdot \bar{\xi}(\bar{r}) \middle| \theta(\bar{r}), \phi(\bar{r}) \right\rangle_{ij} \\ &= \Gamma_{ilmj;\theta,\phi}(\bar{r}, \bar{r}) \left\{ k_0^2 \int R_{\theta,\phi}(\bar{r}, \bar{r}') [\bar{G}_g(\bar{r}, \bar{r}')]_{lm} d\bar{r}' + [\bar{S}]_{lm} \right\} \end{aligned} \quad (25)$$

\bar{S} will be chosen in such a way that $\bar{\xi}_{eff}^{(0)}$ approaches zero when the frequency goes to zero.

$$[\bar{S}(\bar{r})]_{lm} = - \lim_{\omega \rightarrow 0} k_0^2 \int R_{\theta,\phi}(\bar{r}, \bar{r}') [\bar{G}_g(\bar{r}, \bar{r}')]_{lm} d\bar{r}' \quad (26)$$

In this manner ϵ_g corresponds to the effective permittivity at very low frequency. Assuming the scatterers are of spheroidal shape, let

$$k_0^2 \int R_{\theta=0,\phi=0}(\bar{r}, \bar{r}') [\bar{G}_g(\bar{r}, \bar{r}')]_{lm} d\bar{r}' = \begin{bmatrix} I_\rho & 0 & 0 \\ 0 & I_\rho & 0 \\ 0 & 0 & I_z \end{bmatrix} \quad (27)$$

and

$$\bar{S}_l = \begin{bmatrix} S_\rho & 0 & 0 \\ 0 & S_\rho & 0 \\ 0 & 0 & S_z \end{bmatrix} = - \lim_{\omega \rightarrow 0} \begin{bmatrix} I_\rho & 0 & 0 \\ 0 & I_\rho & 0 \\ 0 & 0 & I_z \end{bmatrix} \quad (28)$$

Defining the local coordinates with the following transformation [Fig. 1]

$$\hat{e}_3 = \hat{x} \sin \theta \cos \phi + \hat{y} \sin \theta \sin \phi + \hat{z} \cos \theta \quad (29a)$$

$$\hat{e}_1 = \hat{x} \sin \phi - \hat{y} \cos \phi \quad (29b)$$

$$\hat{e}_2 = \hat{x} \cos \theta \cos \phi + \hat{y} \cos \theta \sin \phi - \hat{z} \sin \theta \quad (29c)$$

such that \hat{e}_3 is in the direction of the axis of the scatterer. Therefore,

$$\bar{\xi} = \bar{T}^{-1} \cdot \bar{\xi}_l \cdot \bar{T} \quad (30a)$$

$$\bar{S} = \bar{T}^{-1} \cdot \bar{S}_l \cdot \bar{T} \quad (30b)$$

where the effective scattering source in the scatterer coordinates is

$$\begin{aligned} \bar{\xi}_l(\bar{r}) &= \left(\frac{\epsilon(\bar{r}) - \epsilon_g}{\epsilon_0} \right) \left[\bar{T} + \bar{S}_l(\bar{r}) \left(\frac{\epsilon(\bar{r}) - \epsilon_g}{\epsilon_0} \right) \right]^{-1} \\ &= \begin{bmatrix} \frac{\epsilon - \epsilon_g}{\epsilon_0 + S_\rho(\epsilon - \epsilon_g)} & 0 & 0 \\ 0 & \frac{\epsilon - \epsilon_g}{\epsilon_0 + S_\rho(\epsilon - \epsilon_g)} & 0 \\ 0 & 0 & \frac{\epsilon - \epsilon_g}{\epsilon_0 + S_z(\epsilon - \epsilon_g)} \end{bmatrix} \end{aligned} \quad (31)$$

and the coordinate transformation matrix is given by

$$\bar{T} = \begin{bmatrix} \sin \phi & -\cos \phi & 0 \\ \cos \theta \cos \phi & \cos \theta \sin \phi & -\sin \theta \\ \sin \theta \cos \phi & \sin \theta \sin \phi & \cos \theta \end{bmatrix} \quad (32)$$

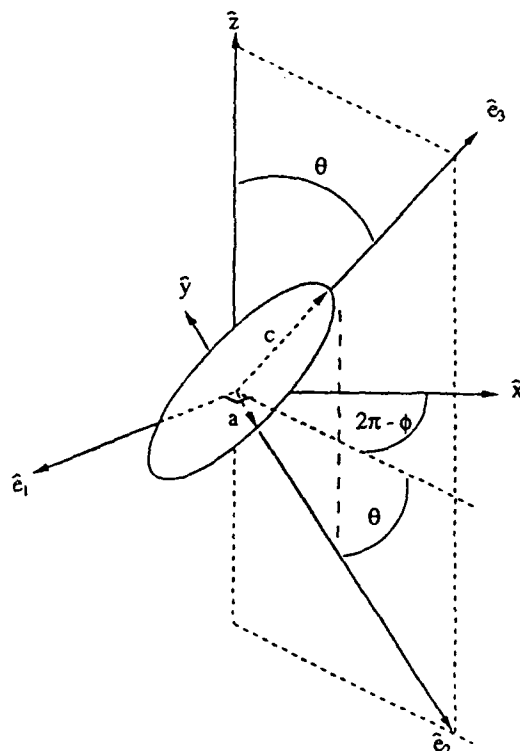


Figure 1. Coordinate system and scatterer geometry.

Because the scatterers are assumed to be isotropically oriented, the probability density function of the orientation is

$$P(\theta, \phi) = \frac{\sin \theta}{4\pi} \quad (33)$$

After straightforward algebraic manipulation, the following result is obtained:

$$\begin{aligned} \langle \bar{\xi}(\bar{r}) \rangle &= \int d\theta d\phi P(\theta, \phi) \bar{\xi}(\theta, \phi) \\ &= \left[f \left(\frac{2}{3} \xi_{sp} + \frac{1}{3} \xi_{sz} \right) + (1-f) \left(\frac{2}{3} \xi_{bp} + \frac{1}{3} \xi_{bz} \right) \right] \bar{I} \end{aligned} \quad (34)$$

and

$$\bar{\xi}_{eff}^{(0)} = \left\{ f \left[\frac{2}{3} \xi_{s\rho}^2 (I_\rho + S_\rho) + \frac{1}{3} \xi_{sz}^2 (I_z + S_z) \right] + (1-f) \left[\frac{2}{3} \xi_{b\rho}^2 (I_\rho + S_\rho) + \frac{1}{3} \xi_{bz}^2 (I_z + S_z) \right] \right\} \bar{I} \quad (35)$$

where

$$\xi_{s\rho} = \frac{\epsilon_s - \epsilon_g}{\epsilon_0 + S_\rho(\epsilon_s - \epsilon_g)} \quad (36a)$$

$$\xi_{sz} = \frac{\epsilon_s - \epsilon_g}{\epsilon_0 + S_z(\epsilon_s - \epsilon_g)} \quad (36b)$$

$$\xi_{b\rho} = \frac{\epsilon_b - \epsilon_g}{\epsilon_0 + S_\rho(\epsilon_b - \epsilon_g)} \quad (36c)$$

$$\xi_{bz} = \frac{\epsilon_b - \epsilon_g}{\epsilon_0 + S_z(\epsilon_b - \epsilon_g)} \quad (36d)$$

and f is the fractional volume of the scatterers. The subscripts s and b represent scatterer and background, respectively.

For a given correlation function (24), e.g., (37), S_ρ and S_z are related to ϵ_g by (28). The equation for ϵ_g is obtained by letting (34) equal to zero [see (18)] for given S_ρ and S_z . These three coupled equations constitute the basis for the solution of ϵ_g , S_ρ , and S_z .

In this paper the correlation function in the local coordinates ($\hat{e}_1, \hat{e}_2, \hat{e}_3$) is chosen to be

$$R_{\theta=0, \phi=0}(\bar{r}) = \exp \left(-\sqrt{\frac{x^2 + y^2}{l_\rho^2} + \frac{z^2}{l_z^2}} \right) \quad (37)$$

For this correlation function, analytical expressions of S_ρ , S_z , I_ρ , and I_z are given in Appendix B.

III. NUMERICAL RESULTS OF EFFECTIVE PERMITTIVITY

In this section, we compare the effective permittivities obtained using strong fluctuation theory (21) and discrete scatterer theory (C1) for randomly oriented spheroids under the low frequency and small fractional volume limits. The effective permittivity obtained with the discrete scatterer theory is given in Appendix C. The effective permittivities are plotted as a function of frequency. The parameters of the correlation function (37) are related to the discrete scatterer parameters in the following manner. The correlation volume is selected to be the volume of the discrete scatterers, i.e.,

$$\frac{4\pi}{3} 6l_\rho^2 l_z = \frac{4\pi}{3} a^2 c \quad (38)$$

and the equi-correlation surface is chosen according to the shape of the scatterer

$$\frac{l_\rho}{l_z} = \frac{a}{c} \quad (39)$$

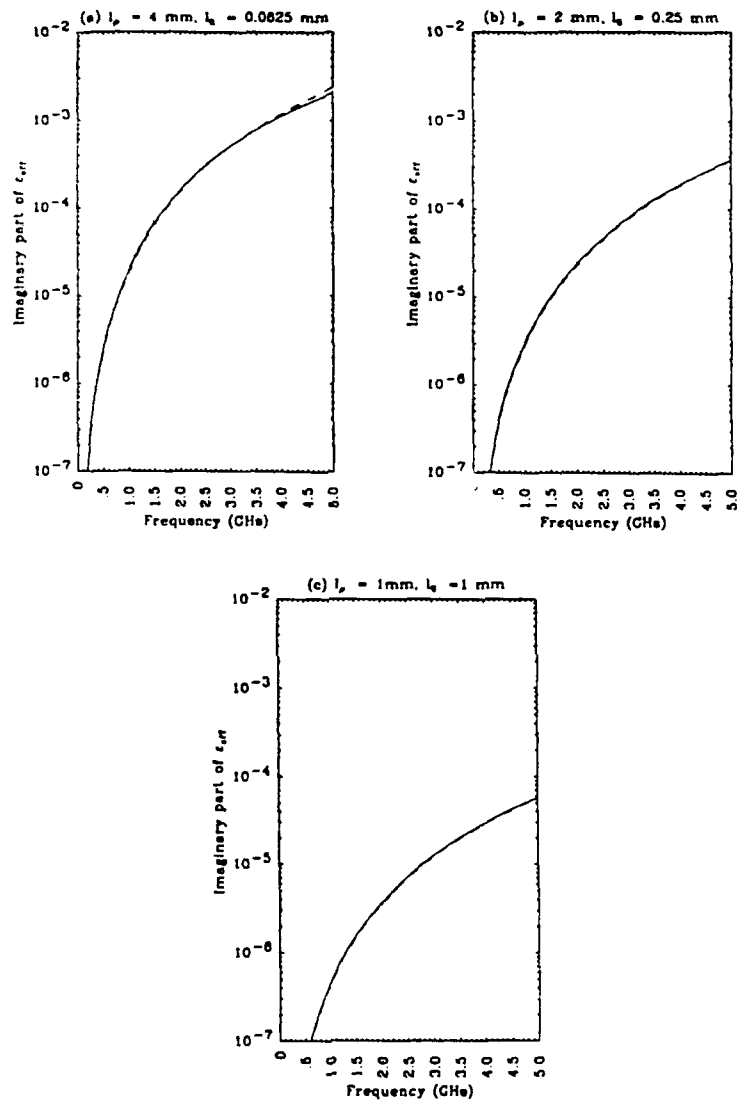


Figure 2. Imaginary part of ϵ_{eff} as a function of frequency. (a) $l_p = 4$ mm and $l_z = 0.0625$ mm, (b) $l_p = 2$ mm and $l_z = 0.25$ mm, (c) $l_p = 1$ mm and $l_z = 1$ mm, (d) $l_p = 0.5$ mm and $l_z = 4$ mm, and (e) $l_p = 0.25$ mm and $l_z = 16$ mm. The dashed line corresponds to discrete scatterer theory. The solid curve corresponds to strong fluctuation theory.

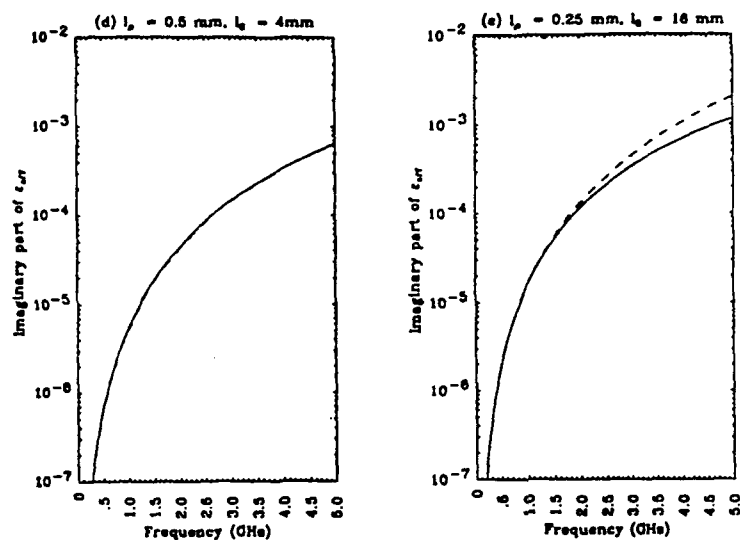


Figure 2. Continued.

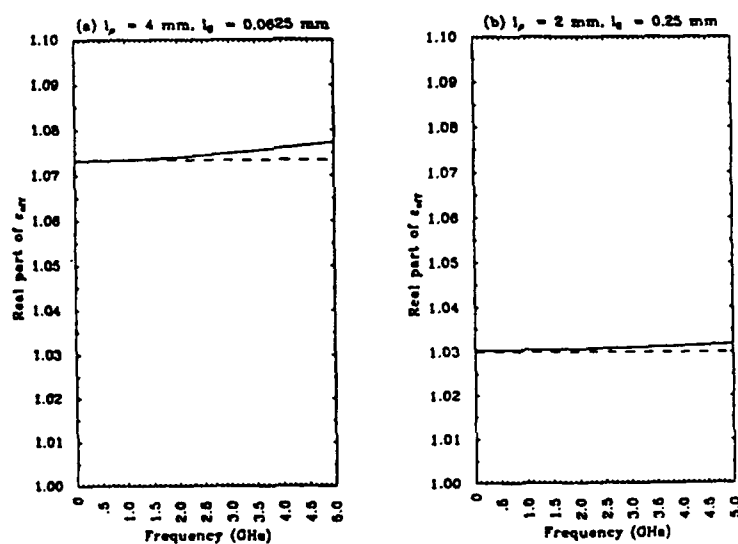


Figure 3. Real part of ϵ_{eff} as a function of frequency. (a) $l_p = 4 \text{ mm}$ and $l_z = 0.0625 \text{ mm}$, (b) $l_p = 2 \text{ mm}$ and $l_z = 0.25 \text{ mm}$, (c) $l_p = 1 \text{ mm}$ and $l_z = 1 \text{ mm}$, (d) $l_p = 0.5 \text{ mm}$ and $l_z = 4 \text{ mm}$, and (e) $l_p = 0.25 \text{ mm}$ and $l_z = 16 \text{ mm}$. The dashed line corresponds to discrete scatterer theory. The solid curve corresponds to strong fluctuation theory.

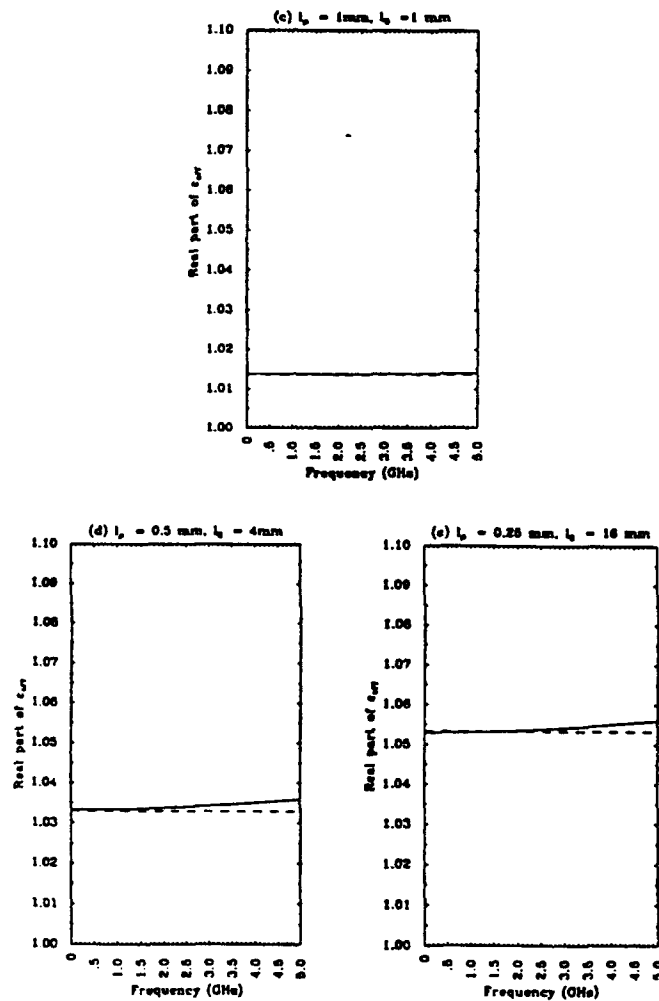


Figure 3. Continued.

The imaginary and real parts of the effective permittivities are shown in Figs. 2 and 3, respectively. The permittivities of the scatterers and background are assumed to be real so that the scattering will be the dominant effect compared to the absorption effect. The fractional volume of the scatterers is 0.5%. The correlation volume (38) is kept a constant for all cases. Figures 2(a) and 2(b) correspond to disk-like scatterers with correlation lengths ($l_p = 4.0 \text{ mm}$ and $l_z = 0.0625 \text{ mm}$) and ($l_p = 2.0 \text{ mm}$ and $l_z = 0.25 \text{ mm}$), respectively. Figures 2(d) and 2(e) are for needle-like scatterers with correlation lengths ($l_p = 0.5 \text{ mm}$ and $l_z = 4.0 \text{ mm}$), and ($l_p = 0.25 \text{ mm}$ and $l_z = 16 \text{ mm}$), respectively. Figure 2(c) is for spherical

scatterers ($l_\rho = 1.0$ mm and $l_z = 1.0$ mm). The corresponding cases for the real parts of ϵ_{eff} are shown in Figs. 3(a) through 3(e). Note that the real and imaginary parts of ϵ_{eff} for the nonspherical scatterers are larger than the spherical scatterer case. This indicates that the nonspherical scatterer has a higher scattering effect than the spherical scatterer. Also, the effective permittivities obtained using strong fluctuation theory and discrete scatterer theory are in good agreement with each other. The noticeable discrepancies in Fig. 2(e) for frequencies greater than 3 GHz (which makes $kl_z > 1$) is due to the fact that the low frequency approximation is used to derive results for both approaches.

IV. BACKSCATTERING FROM A HALF SPACE RANDOM MEDIUM

Considering an incident electric field impinging on a half space filled with randomly distributed and oriented ellipsoid scatterers [Fig. 4]:

$$\bar{E}_{0i} = [\hat{h}(-k_{0zi})E_{hi} + \hat{v}(-k_{0zi})E_{vi}] \exp(i\bar{k}_{\rho i} \cdot \bar{\rho} - ik_{zi}z) \quad (40)$$

The unperturbed field inside the medium is

$$\bar{E}_1^{(0)} = [T_h(k_{zi})\hat{h}_1(-k_{1zi})E_{hi} + T_v(k_{zi})\hat{v}_1(-k_{1zi})E_{vi}] \exp(i\bar{k}_{\rho i} \cdot \bar{\rho} - ik_{1zi}z) \quad (41)$$

where

$$T_h(k_z) = \frac{2k_z}{k_z + k_{1z}} \quad (42a)$$

$$T_v(k_z) = \frac{2\epsilon_1 k_z}{\epsilon_1 k_z + \epsilon_0 k_{1z}} \frac{k_0}{k_1} \quad (42b)$$

The scattered field in the far-field is given as

$$\bar{E}^s = k_0^2 \int_{-\infty}^{\infty} d\bar{\rho}_1 \int_{-\infty}^0 dz_1 \bar{G}_{01}(\bar{r}, \bar{r}_1) \cdot \bar{\xi}(\bar{r}_1) \cdot \bar{F}(\bar{r}_1) \quad (43)$$

where \bar{G}_{01} is the dyadic Green's function given by [16]

$$\bar{G}_{01}(\bar{r}, \bar{r}') = \frac{e^{ik_0 r}}{4\pi r} \left[X_{01}(k_z) \hat{h}(k_z) \hat{h}_1(k_{1z}) + \frac{k_0}{k_1} Y_{01}(k_z) \hat{v}(k_z) \hat{v}_1(k_{1z}) \right] \exp(-i\bar{k}_1 \cdot \bar{r}_1) \quad (44)$$

where

$$X_{01} = \frac{2k_z}{k_z + k_{1z}} \quad (45a)$$

$$Y_{01} = \frac{2\epsilon_1 k_z}{\epsilon_1 k_z + \epsilon_0 k_{1z}} \quad (45b)$$

$$\hat{h}(k_z) = \frac{\hat{x}k_y - \hat{y}k_z}{k_\rho} \quad (46a)$$

$$\hat{v}(k_z) = \frac{-\hat{x}k_z k_x - \hat{y}k_y k_z + \hat{z}k_\rho^2}{k_0 k_\rho} \quad (46b)$$

$$\hat{h}_1(k_{1z}) = \frac{\hat{x}k_y - \hat{y}k_x}{k_\rho} \quad (46c)$$

$$\hat{v}_1(k_{1z}) = \frac{-\hat{x}k_x k_{1z} - \hat{y}k_y k_{1z} + \hat{z}k_\rho^2}{k_1 k_\rho} \quad (46d)$$

$$k_x = k_0 \cos \phi_s \sin \theta_s \quad (47a)$$

$$k_y = k_0 \sin \phi_s \sin \theta_s \quad (47b)$$

$$k_z = k_0 \cos \theta_s \quad (47c)$$

$$k_{xi} = k_0 \cos \phi_i \sin \theta_i \quad (47d)$$

$$k_{yi} = k_0 \sin \phi_i \sin \theta_i \quad (47e)$$

$$k_{zi} = k_0 \cos \theta_i \quad (47f)$$

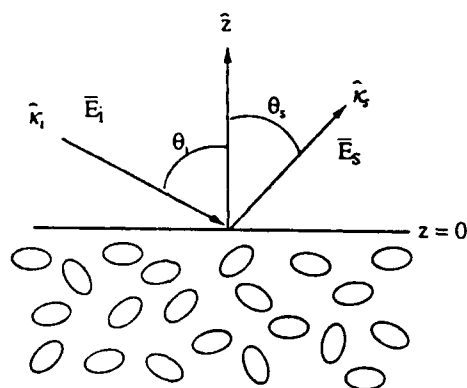


Figure 4. Configuration for scattering from half-space with randomly oriented spheroids.

Applying the distorted Born approximation to calculating the backscattering coefficients, we let

$$\bar{F}(\bar{r}) \simeq \bar{E}_1^{(0)}(\bar{r}) \quad (48)$$

Therefore, by substituting (48) into (43), the scattered field is given as

$$\begin{aligned} \bar{E}^s = \frac{e^{ik_0 r}}{4\pi r} k_0^2 \int_{-\infty}^{\infty} d\bar{\rho}_1 \int_{-\infty}^0 dz_1 \exp(-i\bar{k}_1 \cdot \bar{r}_1) \exp(i\bar{k}_{\rho i} \cdot \bar{\rho}_1 - ik_{1zi}z_1) \\ \left[X_{01} \hat{h}(k_z) \hat{h}_1(k_{1z}) + \frac{k_0}{k_1} Y_{01} \hat{v}(k_z) \hat{v}_1(k_{1z}) \right] \\ \cdot \bar{\xi}(\bar{r}_1) \cdot [T_h \hat{h}_1(-k_{1zi}) E_{hi} + T_v \hat{v}_1(-k_{1zi}) E_{vi}] \end{aligned} \quad (49)$$

The scattered field is then expressed in the following form:

$$\begin{bmatrix} E_{hs} \\ E_{vs} \end{bmatrix} = \frac{e^{ikr}}{r} \begin{bmatrix} f_{hh} & f_{hv} \\ f_{vh} & f_{vv} \end{bmatrix} \begin{bmatrix} E_{hi} \\ E_{vi} \end{bmatrix} \quad (50)$$

where E_{hs} and E_{vs} are the horizontally and vertically polarized electric fields respectively.

Note that for backscattering from a reciprocal medium f_{hv} equals to f_{vh} . The polarimetric covariance matrix in the backscattering direction is denoted as [1]

$$\begin{aligned} \overline{C} &= \begin{bmatrix} \sigma_{hh} & \sigma_{hhvv} & \sigma_{hhvv} \\ \sigma_{hhvv}^* & \sigma_{hv} & \sigma_{hvvv} \\ \sigma_{hhvv}^* & \sigma_{hvvv}^* & \sigma_{vv} \end{bmatrix} \\ &\equiv \lim_{A \rightarrow \infty} \frac{4\pi}{A} \begin{bmatrix} \langle |f_{hh}|^2 \rangle & \langle f_{hh} f_{hv}^* \rangle & \langle f_{hh} f_{vv}^* \rangle \\ \langle f_{hv} f_{hh}^* \rangle & \langle |f_{hv}|^2 \rangle & \langle f_{hv} f_{vv}^* \rangle \\ \langle f_{vv} f_{hh}^* \rangle & \langle f_{vv} f_{hv}^* \rangle & \langle |f_{vv}|^2 \rangle \end{bmatrix} \end{aligned} \quad (51)$$

Let the spectral density function be

$$\Phi_{\theta, \phi}(\vec{k}) = \frac{1}{(2\pi)^3} \int d\vec{r} R_{\theta, \phi}(\vec{r}) \exp(i\vec{k} \cdot \vec{r}) \quad (52)$$

The backscattering scattering coefficients are given by

$$\begin{aligned} \sigma_{hh} &= \pi k_0^4 |X_{01} T_h|^2 \int_0^{2\pi} d\phi \int_0^\pi d\theta \frac{\sin \theta}{4\pi} \\ &\quad \left\{ f \left| \xi_{sp} + (\xi_{sz} - \xi_{sp}) \sin^2 \theta \sin^2(\phi_i - \phi) \right|^2 \right. \\ &\quad \left. + (1-f) \left| \xi_{bp} + (\xi_{bz} - \xi_{bp}) \sin^2 \theta \sin^2(\phi_i - \phi) \right|^2 \right\} \Psi(2\vec{k}_{\rho i}, \theta, \phi) \end{aligned} \quad (53a)$$

$$\begin{aligned} \sigma_{vv} &= \pi k_0^4 |Y_{01} T_v|^2 \left| \frac{k_0}{k_1} \right|^2 \int_0^{2\pi} d\phi \int_0^\pi d\theta \frac{\sin \theta}{4\pi} \\ &\quad \left\{ f \left| \xi_{sp} + (\xi_{sz} - \xi_{sp}) \left(\frac{k_{1zi}}{k_1} \sin \theta \cos(\phi_i - \phi) + \frac{k_{\rho i}}{k_1} \cos \theta \right) \right|^2 \right. \\ &\quad \left. + (1-f) \left| \xi_{bp} + (\xi_{bz} - \xi_{bp}) \left(\frac{k_{1zi}}{k_1} \sin \theta \cos(\phi_i - \phi) + \frac{k_{\rho i}}{k_1} \cos \theta \right) \right|^2 \right\} \\ &\quad \Psi(2\vec{k}_{\rho i}, \theta, \phi) \end{aligned} \quad (53b)$$

$$\sigma_{hv} = \pi k_0^4 |X_{01} T_v|^2 \int_0^{2\pi} d\phi \int_0^\pi d\theta \frac{\sin \theta}{4\pi}$$

$$\left\{ \left[f |\xi_{sz} - \xi_{sp}|^2 + (1-f) |\xi_{bz} - \xi_{bp}|^2 \right] \sin^2 \theta \sin^2(\phi_i - \phi) \left| \frac{k_{1zi}}{k_1} \sin \theta \cos(\phi_i - \phi) + \frac{k_{\rho i}}{k_1} \cos \theta \right|^2 \right\} \Psi(2\bar{k}_{\rho i}, \theta, \phi) \quad (53c)$$

and the cross correlation between polarizations

$$\begin{aligned} \sigma_{hhvv} = \pi k_0^4 X_{01} T_h Y_{01}^* T_v^* \left(\frac{k_0}{k_1} \right)^* \int_0^{2\pi} d\phi \int_0^\pi d\theta \frac{\sin \theta}{4\pi} \\ \left\{ f \left[\xi_{sp} + (\xi_{sz} - \xi_{sp}) \sin^2 \theta \sin^2(\phi_i - \phi) \right] \right. \\ \times \left[\xi_{sp} + (\xi_{sz} - \xi_{sp}) \left(\frac{k_{1zi}}{k_1} \sin \theta \cos(\phi_i - \phi) + \frac{k_{\rho i}}{k_1} \cos \theta \right)^2 \right]^* \\ + (1-f) \left[\xi_{bp} + (\xi_{bz} - \xi_{bp}) \sin^2 \theta \sin^2(\phi_i - \phi) \right] \\ \times \left[\xi_{bp} + (\xi_{bz} - \xi_{bp}) \left(\frac{k_{1zi}}{k_1} \sin \theta \cos(\phi_i - \phi) + \frac{k_{\rho i}}{k_1} \cos \theta \right)^2 \right]^* \left. \right\} \\ \Psi(2\bar{k}_{\rho i}, \theta, \phi) \end{aligned} \quad (54a)$$

$$\sigma_{hhvv} = 0 \quad (54b)$$

$$\sigma_{hvvv} = 0 \quad (54c)$$

where

$$\Psi(2\bar{k}_{\rho i}, \theta, \phi) = \int_{-\infty}^{\infty} dk_z \frac{1}{(k_z + 2k_{1zi})(k_z + 2k_{1zi}^*)} \Phi_{\theta, \phi}(2\bar{k}_{\rho i}, k_z) \quad (55)$$

Under the low frequency approximation,

$$\Psi(2\bar{k}_{\rho i}, \theta, \phi) = \frac{\pi}{2k_{1zi}''} \Phi_{\theta, \phi}(0) \quad (56)$$

Thus

$$\begin{aligned} \sigma_{hh} = \frac{\pi^2 k_0^4}{2k_{1zi}''} |X_{01} T_h|^2 \left(f \left\{ |\xi_{sp}|^2 + \frac{1}{5} |(\xi_{sz} - \xi_{sp})|^2 + \frac{2}{3} \text{Re} [\xi_{sp}^* (\xi_{sz} - \xi_{sp})] \right\} \right. \\ \left. + (1-f) \left\{ |\xi_{bp}|^2 + \frac{1}{5} |(\xi_{bz} - \xi_{bp})|^2 + \frac{2}{3} \text{Re} [\xi_{bp}^* (\xi_{bz} - \xi_{bp})] \right\} \right) \Phi_{\theta, \phi}(0) \end{aligned} \quad (57a)$$

$$\begin{aligned} \sigma_{vv} = \frac{\pi^2 k_0^4}{2k_{1zi}''} |Y_{01} T_v|^2 \left| \frac{k_0}{k_1} \right|^2 \left(f \left\{ |\xi_{sp}|^2 + \frac{1}{5} |(\xi_{sz} - \xi_{sp})|^2 + \frac{2}{3} \text{Re} [\xi_{sp}^* (\xi_{sz} - \xi_{sp})] \right\} \right. \\ \left. + \frac{8}{15} \frac{|k_{\rho i}|^2 k_{1zi}''^2}{|k_1|^4} |\xi_{sz} - \xi_{sp}|^2 \right) + (1-f) \left\{ |\xi_{bp}|^2 + \frac{1}{5} |(\xi_{bz} - \xi_{bp})|^2 \right\} \end{aligned}$$

$$+ \frac{2}{3} \operatorname{Re} \left[\xi_{b\rho}^* (\xi_{bz} - \xi_{b\rho}) \right] + \frac{8}{15} \frac{|k_{\rho i}|^2 k_{1zi}''^2}{|k_1|^4} |\xi_{bz} - \xi_{b\rho}|^2 \left. \right\} \Phi_{\theta, \phi}(0) \quad (57b)$$

$$\sigma_{hv} = \frac{\pi^2 k_0^4}{2k_{1zi}''} |X_{01} T_v|^2 \frac{1}{15} \frac{|k_{\rho i}|^2 + |k_{1zi}|^2}{|k_1|^2} \left[f |(\xi_{sz} - \xi_{s\rho})|^2 + (1-f) |(\xi_{bz} - \xi_{b\rho})|^2 \right] \Phi_{\theta, \phi}(0) \quad (57c)$$

$$\begin{aligned} \sigma_{hhvv} = & \frac{\pi^2 k_0^4}{2k_{1zi}''} X_{01} T_h Y_{01}^* T_v^* \left(\frac{k_0}{k_1} \right)^* \left(f \left\{ |\xi_{s\rho}|^2 + \frac{1}{3} \xi_{s\rho}^* (\xi_{sz} - \xi_{s\rho}) \right. \right. \\ & + \frac{1}{3} \xi_{s\rho} (\xi_{sz} - \xi_{s\rho})^* \left[\left(\frac{k_{\rho i}}{k_1} \right)^2 + \left(\frac{k_{1zi}}{k_1} \right)^2 \right]^* \\ & + \frac{1}{15} |\xi_{sz} - \xi_{s\rho}|^2 \left[\left(\frac{k_{\rho i}}{k_1} \right)^2 + \left(\frac{k_{1zi}}{k_1} \right)^2 \right]^* \left. \right\} \\ & + (1-f) \left\{ |\xi_{b\rho}|^2 + \frac{1}{3} \xi_{b\rho}^* (\xi_{bz} - \xi_{b\rho}) + \frac{1}{3} \xi_{b\rho} (\xi_{bz} - \xi_{b\rho})^* \left[\left(\frac{k_{\rho i}}{k_1} \right)^2 + \left(\frac{k_{1zi}}{k_1} \right)^2 \right]^* \right. \\ & \left. \left. + \frac{1}{15} |\xi_{bz} - \xi_{b\rho}|^2 \left[\left(\frac{k_{\rho i}}{k_1} \right)^2 + \left(\frac{k_{1zi}}{k_1} \right)^2 \right]^* \right\} \right) \Phi_{\theta, \phi}(0) \end{aligned} \quad (57d)$$

V. NUMERICAL EXAMPLES OF POLARIMETRIC COVARIANCE MATRICES

In this section the results of Section IV are illustrated using the parameters applicable to microwave remote sensing of vegetation and forests. The orientations of nonspherical scatterers are assumed to be completely random. The correlation function (37) is used to evaluate all of the numerical results. Because four elements of the covariance matrix are zero, it is more convenient to write the polarimetric covariance matrix (51) into the following form [1]

$$\overline{C} = \sigma_{hh} \begin{bmatrix} 1 & 0 & \rho\sqrt{\gamma} \\ 0 & \epsilon & 0 \\ \rho^*\sqrt{\gamma} & 0 & \gamma \end{bmatrix} \quad (58)$$

where ϵ and γ correspond to the ratios σ_{hv}/σ_{hh} and σ_{vv}/σ_{hh} , respectively, and ρ is the complex correlation coefficient of HH and VV polarization returns. The polarimetric covariance matrix contains very important information in the classification of various terrain elements [7].

The effects of nonspherical geometry on polarimetric covariance matrices are shown in Tables 1 and 2. Included are results for five types of scatterers discussed in Section III. Note that σ_{hh} for the spherical scatterer case is bigger than the nonspherical scatterer cases. This is due to the fact that the scattering loss (imaginary part of ϵ_{eff}) for the spherical scatterer case is the smallest among all cases. The wave can penetrate deeper into the random medium with smaller scattering

loss. As a result, for a half-space configuration, the total scattering increases. Also note that the ratio σ_{vv}/σ_{hh} is very close to 1 for all cases. This is because all the scatterers are completely randomly oriented so that the number of scatterers which contribute to the HH return is the same as the number of scatterers for the VV return. The reason why the ratio is slightly greater than one is because the transmission coefficients for vertical polarization (42b) and (45b) are slightly greater than those of horizontal polarization (42a) and (45a).

| Shape | l_p (mm) | l_z (mm) | σ_{hh} (dB) | σ_{vv}/σ_{hh} | σ_{hv}/σ_{hh} | ρ |
|---------|------------|------------|--------------------|---------------------------|---------------------------|--------|
| oblate | 4 | 0.0625 | -24.6 | 1.002 | 0.108 | 0.784 |
| oblate | 2 | 0.25 | -24.2 | 1.0006 | 0.086 | 0.829 |
| sphere | 1 | 1 | -23.5 | 1.0 | 0.0 | 1.0 |
| prolate | 0.5 | 4 | -25.1 | 1.0001 | 0.214 | 0.572 |
| prolate | 0.25 | 16 | -26.0 | 1.0002 | 0.265 | 0.470 |

Table 1. Covariance matrix elements for five types of scatterers. Frequency = 1.1 GHz, $\theta_i = 40^\circ$, $f = 0.005$, $\epsilon_s = (30.8 + i1.8)\epsilon_0$, and $\epsilon_b = \epsilon_0$.

| Shape | l_p (mm) | l_z (mm) | σ_{hh} (dB) | σ_{vv}/σ_{hh} | σ_{hv}/σ_{hh} | ρ |
|---------|------------|------------|--------------------|---------------------------|---------------------------|--------|
| oblate | 4 | 0.0625 | -24.8 | 1.006 | 0.107 | 0.787 |
| oblate | 2 | 0.25 | -24.4 | 1.002 | 0.09* | 0.830 |
| sphere | 1 | 1 | -23.5 | 1.0003 | 0.0 | 1.0 |
| prolate | 0.5 | 4 | -25.3 | 1.001 | 0.212 | 0.577 |
| prolate | 0.25 | 16 | -26.1 | 1.002 | 0.262 | 0.477 |

Table 2. Covariance matrix elements for five types of scatterers. Frequency = 1.1 GHz, $\theta_i = 40^\circ$, $f = 0.01$, $\epsilon_s = (30.8 + i1.8)\epsilon_0$, and $\epsilon_b = \epsilon_0$.

The nonspherical geometry, however, has significant effects on σ_{hv}/σ_{hh} and ρ . The imaginary part of ρ is not shown in the table, since they are very close to zero. It can be seen that when the scatterers become less spherical, σ_{hv}/σ_{hh} increases from zero and ρ decreases from 1. When the eccentricity of the scatterers gets higher, the returns for HH and VV will be dominated more and more by scatterers with different orientations (i.e., different location). As a result, the correlation between HH and VV decreases. As a matter of fact, for completely randomly oriented dipoles both the ratio σ_{hv}/σ_{hh} and ρ are equal to 1/3. This is consistent with the trend shown in Table 1.

The results shown in Tables 1 and 2 are numerically integrated from (53) and (54). Because the integrands are relatively smooth analytic functions, Simpson's

rule is used for numerical integration. The total computation time for one covariance matrix is about four seconds on our VAXstation 3500. The approximate formula given in (57) are also evaluated and the approximate results are within 2% error of the exact results presented.

The parameters σ_{hv}/σ_{hh} and ρ are essentially unchanged when the fractional volume of the scatterers changes from $f = 0.5\%$ (Table 1) to $f = 1\%$ (Table 2). Results for f up to a few percent have also been evaluated and are also within a few percent difference with the numbers shown in Table 1 for those two parameters. This indicates that σ_{hv}/σ_{hh} and ρ can serve as useful parameters in identifying and distinguishing the geometry of scatterers for the remote sensing of vegetation where f is usually smaller than a few percent.

APPENDIX A: EFFECTIVE PERMITTIVITY UNDER THE LOW FREQUENCY APPROXIMATION

Assuming

$$|(\bar{\xi}_{eff})_{ij}| \ll 1 \quad (A1)$$

then, from (16),

$$\bar{\epsilon}_{eff} \simeq \epsilon_g \bar{I} + \epsilon_0 \bar{\xi}_{eff} \quad (A2)$$

Substituting (A2) and (19) into (15), then

$$\langle \bar{D}(\bar{r}) \rangle = \epsilon_g \bar{I} \langle \bar{E}(\bar{r}) \rangle + k_0^2 \epsilon_0 \int d\bar{r}' \langle \bar{\xi}(\bar{r}) \cdot PS \bar{G}_g(\bar{r}, \bar{r}') \cdot \bar{\xi}(\bar{r}') \rangle \cdot \langle \bar{E}(\bar{r}') \rangle \quad (A3)$$

Assuming the frequency is low enough so that the variation of mean field $\langle \bar{E}(\bar{r}') \rangle$ is negligible within a few correlation lengths, we can approximate (A3) as

$$\langle \bar{D}(\bar{r}) \rangle = \left(\epsilon_g \bar{I} + k_0^2 \epsilon_0 \int d\bar{r}' \langle \bar{\xi}(\bar{r}) \cdot PS \bar{G}_g(\bar{r}, \bar{r}') \cdot \bar{\xi}(\bar{r}') \rangle \right) \cdot \langle \bar{E}(\bar{r}) \rangle \quad (A4)$$

Therefore, we can define the effective permittivity of the medium under the low frequency approximation as

$$\bar{\epsilon}_{eff} \simeq \epsilon_g \bar{I} + \epsilon_0 \bar{\xi}_{eff}^{(0)} \quad (A5)$$

where

$$\bar{\xi}_{eff}^{(0)} = k_0^2 \int d\bar{r}' \langle \bar{\xi}(\bar{r}) \cdot PS \bar{G}_g(\bar{r}, \bar{r}') \cdot \bar{\xi}(\bar{r}') \rangle \quad (A6)$$

APPENDIX B: EXPRESSION FOR I_x , I_y , S_x , and S_y

For the correlation function (37) in the local coordinate, the integration of a more general case than (27) has been carried out analytically by Nghiem [8]. In this paper, results are presented for isotropic background medium only and are given by

$$I_z = - \frac{\epsilon_0}{\epsilon_g (\gamma^2 - 1) (1 + \zeta_e^2)} \left\{ \gamma^2 + (\gamma^2 - 1) \zeta_e^2 - \gamma \sqrt{-\zeta_e^2} \right\}$$

$$+ \frac{\gamma^2(1 + \zeta_e^2) + (\gamma^2 - 1)\zeta_e^2}{2(\gamma^2 - 1)\sqrt{\frac{1 + \zeta_e^2}{1 - \gamma^2}}} \left[\ln \left(1 + \sqrt{\frac{1 + \zeta_e^2}{1 - \gamma^2}} \right) - \ln \left(1 - \sqrt{\frac{1 + \zeta_e^2}{1 - \gamma^2}} \right) \right. \\ \left. - \ln \left(\sqrt{-\zeta_e^2} + \gamma \sqrt{\frac{1 + \zeta_e^2}{1 - \gamma^2}} \right) + \ln \left(\sqrt{-\zeta_e^2} - \gamma \sqrt{\frac{1 + \zeta_e^2}{1 - \gamma^2}} \right) \right] \quad (B1a)$$

$$I_\rho = - \frac{\nu_{0\rho}^2 \gamma^3}{4\nu_{g\rho}^2(1 - \gamma^2)^2(1 + \nu_{g\rho}^2)} \left\{ \frac{1}{\sqrt{\frac{\gamma^2(1 + \nu_{g\rho}^2)}{(1 - \gamma^2)}}} \left(\frac{\nu_{g\rho}^2}{\gamma^2} + 1 \right) \right. \\ \left[\ln \left(\sqrt{-\nu_{g\rho}^2} - \sqrt{\frac{\gamma^2(1 + \nu_{g\rho}^2)}{(1 - \gamma^2)}} \right) - \ln \left(\sqrt{-\nu_{g\rho}^2} + \sqrt{\frac{\gamma^2(1 + \nu_{g\rho}^2)}{(1 - \gamma^2)}} \right) \right] \\ \left. - \left[\frac{(1 - \gamma^2)\nu_{g\rho}^2}{\gamma^2} - (1 + \nu_{g\rho}^2) \right] \frac{2\sqrt{-\nu_{g\rho}^2}(1 - \gamma^2)}{\nu_{g\rho}^2 + \gamma^2} \right\} \\ - \frac{\nu_{0\rho}^2}{2\nu_{g\rho}^2(1 + \nu_{g\rho}^2)} \left\{ (1 + \nu_{g\rho}^2) - \frac{1}{2\sqrt{\frac{(1 + \nu_{g\rho}^2)}{(1 - \gamma^2)}}} \left(2\nu_{g\rho}^2 + 1 - \frac{\nu_{g\rho}^2 + 1}{1 - \gamma^2} \right) \right. \\ \times \left[\ln \left(1 + \sqrt{\frac{1 + \nu_{g\rho}^2}{1 - \gamma^2}} \right) - \ln \left(1 - \sqrt{\frac{1 + \nu_{g\rho}^2}{1 - \gamma^2}} \right) \right] \left. \right\} \\ - \frac{\nu_{0\rho}^2 \gamma^2}{4\nu_{g\rho}^2(1 - \gamma^2)(1 + \nu_{g\rho}^2)} \left\{ \frac{1}{\sqrt{\frac{(1 + \nu_{g\rho}^2)}{(1 - \gamma^2)}}} \left(2\nu_{g\rho}^2 + 1 + \frac{\nu_{g\rho}^2 + 1}{1 - \gamma^2} \right) \right. \\ \left[\ln \left(1 - \sqrt{\frac{1 + \nu_{g\rho}^2}{1 - \gamma^2}} \right) - \ln \left(1 + \sqrt{\frac{1 + \nu_{g\rho}^2}{1 - \gamma^2}} \right) \right] \\ \left. - \left(2\nu_{g\rho}^2 + 1 - \frac{\nu_{g\rho}^2 + 1}{1 - \gamma^2} \right) \frac{2(1 - \gamma^2)}{\nu_{g\rho}^2 + \gamma^2} \right\} \quad (B1b)$$

where

$$\gamma = \frac{l_\rho}{l_z} \quad (B2a)$$

$$\zeta_e^2 = k_0^2 \epsilon_g l_z^2 \quad (B2b)$$

$$\nu_{0\rho}^2 = k_0^2 l_\rho^2 \quad (B2c)$$

$$\nu_{g\rho}^2 = k_0^2 \epsilon_g l_\rho^2 \quad (B2d)$$

Note that the branch cuts of $\ln(\cdot)$ and $\sqrt{\cdot}$ are chosen along the negative real axis of the argument in the above expressions. Taking the zero frequency limit of (B1), we obtain

$$S_\rho = \frac{\epsilon_0}{2\epsilon_g a^3} \left[(1 + a^2) \tan^{-1} a - a \right] \quad (B3a)$$

$$S_z = \frac{\epsilon_0(1 + a^2)}{\epsilon_g a^3} \left[a - \tan^{-1} a \right] \quad (B3b)$$

where

$$a^2 = \gamma^2 - 1 \quad (B4)$$

APPENDIX C: EFFECTIVE PERMITTIVITY FOR DISCRETE SCATTERER THEORY

Under the low frequency assumption and in the limit of small fractional volume for scatterers, the effective permittivity for randomly oriented spheroids for discrete scatterer theory can be obtained from Equation (10) (pp. 534) in [16] by taking the small fractional volume limit. The result for spheroidal scatterers is given as

$$\frac{\epsilon_{eff}}{\epsilon_b} = 1 + f(2y_a + y_c) + f \frac{2k^3 a^2 c}{3} (2y_a^2 + y_c^2) i \quad (C1)$$

where

$$k = k_0 \sqrt{\epsilon_b} \quad (C2a)$$

$$y_a = \frac{\epsilon_s - \epsilon_b}{3\epsilon_b + \frac{3a^2 c}{2} A_a(\epsilon_s - \epsilon_b)} \quad (C2b)$$

$$y_c = \frac{\epsilon_s - \epsilon_b}{3\epsilon_b + \frac{3a^2 c}{2} A_c(\epsilon_s - \epsilon_b)} \quad (C2c)$$

For oblate spheroids ($a > c$)

$$A_c = \frac{2}{(a^2 - c^2)^{3/2}} \left[\frac{\sqrt{a^2 - c^2}}{c} - \tan^{-1} \frac{\sqrt{a^2 - c^2}}{c} \right] \quad (C3)$$

For prolate spheroids ($c > a$)

$$A_c = -\frac{1}{c^3 e^3} \left[2e + \ln \frac{1-e}{1+e} \right] \quad (C4)$$

with

$$e = \sqrt{1 - \frac{a^2}{c^2}} \quad (C5)$$

and A_a can be obtained from the following formula,

$$2A_a + A_c = \frac{2}{a^2 c} \quad (C6)$$

ACKNOWLEDGMENTS

This work was supported by the ONR Contract N00014-89-J-1107, the ARMY Corp of Engineers Contract DACA39-87-K-0022, the NASA Contract NAGW-17, the NASA Contract 958461, and the European Space Agency.

The Editor thanks M. Borgeaud, T. Le Toan, and J. J. van Zyl for reviewing the paper.

REFERENCES

1. Borgeaud, M., S. V. Nghiem, R. T. Shin, and J. A. Kong, "Theoretical models for polarimetric microwave remote sensing of earth terrain," *J. Electro. Waves Applic.*, Vol. 3, No. 1, 61-81, 1989.
2. Finkel'berg, V. M., "The dielectric constant of mixtures," *Soviet Physics-Technical Physics*, Vol. 9, No. 3, 396-402, 1964a.
3. Finkel'berg, V. M., "Mean field strength in an inhomogeneous medium," *Soviet Physics JETP*, Vol. 19, No. 2, 494-498, 1964b.
4. Finkel'berg, V. M., "Wave propagation in a random medium. The correlation group method," *Soviet Physics JETP*, Vol. 26, 268-277, 1968.
5. Ishimaru, A., *Wave Propagation and Scattering in Random Medium*, Vols. 1 and 2, Academic, New York, 1978.
6. Lang, R. H., "Electromagnetic backscattering from a sparse distribution of lossy dielectric scatterers," *Radio Science*, Vol. 16, 15-33, 1981.
7. Lim, H., A. A. Swartz, H. A. Yueh, J. A. Kong, R. T. Shin, and J. J. van Zyl, "Classification of earth terrain using synthetic aperture radar images," *J. Geophys. Res.*, Vol. 94, No. B6, 7049-7057, June 10, 1989.
8. S. V. Nghiem, *Studies of Correlation Functions in Random Medium Theory*, Masters thesis, Department of Electrical Engineering and Computer Science, Massachusetts Institute of Technology, 1988.
9. Stogryn, A., "The bilocal approximation for the electric field in strong fluctuation theory," *IEEE Trans. Antennas Propagat.*, Vol. AP-31, No. 6, 985-986, 1983.
10. Stogryn, A., "The bilocal approximation for the effective dielectric constant of an isotropic random medium," *IEEE Trans. Antennas Propagat.*, Vol. AP-32, No. 5, 517-520, 1984.
11. Tsang, L., and J. A. Kong, "Scattering of electromagnetic waves from random media with strong permittivity fluctuations," *Radio Science*, Vol. 16, No. 3, 303-320, 1981b.
12. Tsang, L., and J. A. Kong, "Effective propagation constant for coherent electromagnetic waves in media embedded with dielectric scatterers," *J. Appl. Phys.*, Vol. 53, 7162-7173, 1982a.

13. Tsang, L., J. A. Kong, and R. W. Newton, "Application of strong fluctuation random medium theory to scattering of electromagnetic waves from a half-space of dielectric mixture," *IEEE Trans. Antennas Propagat.*, Vol. AP-30, No. 2, 292-302, 1982b.
14. Tsang, L., and J. A. Kong, "Scattering of electromagnetic waves from a half space of densely distributed dielectric scatterers," *Radio Science*, Vol. 18, 1260-1272, 1983.
15. Tsang, L., J. A. Kong, and R. T. Shin, "Radiative transfer theory for active remote sensing of a layer of nonspherical particles," *Radio Science*, Vol. 19, No. 2, 629-642, 1984.
16. Tsang, L., J. A. Kong, and R. T. Shin, *Theory of Microwave Remote Sensing*, John Wiley & Sons, New York, 1985.
17. Tsang, L., M. C. Kubaschi, and J. A. Kong, "Radiative transfer theory for active remote sensing of a layer of small ellipsoidal scatterers," *Radio Science*, Vol. 16, No. 3, 321-329, 1981a.
18. Yaghjian, A. D., "Electric dyadic Green's functions in the source region," *Proc. IEEE*, Vol. 68, No. 2, 248-263, 1980.

S. H. Yueh received the SB (1982) and SM (1984) from the Electrical Engineering Department of National Taiwan University, Taiwan, and is currently working on the Ph.D. degree in electrical engineering at the Massachusetts Institute of Technology, Cambridge. His fields of interest are electromagnetic field theory and remote sensing.

J. A. Kong is Professor of Electrical Engineering and Chairman of Area IV on Energy and Electromagnetic Systems in the Department of Electrical Engineering and Computer Science at the Massachusetts Institute of Technology in Cambridge, Massachusetts. His research interest is in the field of electromagnetic wave theory and applications. He has published 6 books and over 200 refereed journal and conference papers, and is the Editor of the Wiley Series in Remote Sensing, and Chief Editor of the Elsevier book series of Progress In Electromagnetics Research (PIER).

R. T. Shin received his SB (1977), SM (1980), and Ph.D. (1984) in electrical engineering from the Massachusetts Institute of Technology. Since 1984 he has been on the Research Staff in the Air Defense Techniques Group at the MIT Lincoln Laboratory. His research interest is the areas of electromagnetic wave scattering and propagation and theoretical model development and data interpretation for microwave remote sensing. He is the coauthor of *Theory of Microwave Remote Sensing* (Wiley, 1985). Dr. Shin is a member of the IEEE, American Geophysical Union, Tau Beta Pi, Eta Kappa Nu, and Commission F of the International Union of Radio Science.

1

POLARIMETRIC REMOTE SENSING OF GEOPHYSICAL MEDIA WITH LAYER RANDOM MEDIUM MODEL

S. V. Nghiem, M. Borgeaud, J. A. Kong, and R. T. Shin

- 1.1 Introduction**
- 1.2 Polarimetric Descriptions**
 - a. Scattering matrix
 - b. Covariance Matrix
 - c. Mueller Matrix
 - d. Scattering Coefficients
- 1.3 Random Medium Model**
 - a. Formulation
 - b. Effective Permittivities
 - c. Dyadic Green's Functions
 - d. Scattering Coefficients
- 1.4 Results and Discussion**
 - a. Two-layer Configuration
 - b. Three-layer Configuration
 - c. Polarization Signatures
- 1.5 Summary**
- Appendices**
- Acknowledgments**
- References**

1.1 Introduction

With advances in polarimetric radar technology, polarimetry has become important to the remote sensing of geophysical media. Fully polarimetric radar signals convey additional information regarding the

remotely sensed media and thereby provide more accurate identification and classification of terrain types in radar imagery. The encountered geophysical media are inhomogeneous and often stratified into multiple layers. To study the fully polarimetric scattering properties of the media, the layer random medium model has been developed.

In this chapter, the three-layer random medium model applied to the fully polarimetric remote sensing of geophysical media is presented. The chapter is composed of five sections. Section 1.2 considers the polarimetric scattering descriptions in terms of the scattering, covariance, and Mueller matrices. The relations between the matrix elements and the polarimetric backscattering coefficients are shown. Section 1.3 sets forth the theoretical model formulated from Maxwell's equations to derive the polarimetric scattering coefficients. This model describes the random media by means of correlation functions in conjunction with the strong permittivity fluctuation theory. Section 1.4 discusses the results for a case of sea ice with and without snow cover. Physical insights provided by the theoretical model are used to explain the behavior of the corresponding covariance matrix and the polarization signatures calculated with the Mueller matrix. Finally, the chapter is summarized in section 1.5.

1.2 Polarimetric Descriptions

To describe electromagnetic polarization properties, various methods have been devised. In 1852, Sir George Stokes [1] introduced four quantities, known as the Stokes parameters, to characterize a beam of partially polarized light. The Stokes parameters were later (1888) modified by Lord Rayleigh [2] in his treatment of "Interference of Polarized Light". As a geometrical representation, Poincaré [3] denoted polarisation states with points on a sphere called the Poincaré sphere. In 1948, Mueller [4] considered the Stokes parameters as components of a vector which, due to "the effect of an optical instrument," could be transformed into another vector by a real 4×4 matrix. Expressed in two orthogonal polarimetric components, the incident and the scattered fields are related by the Jones matrix [5] or the complex scattering matrix [6,7]. To characterize the polarimetric scattering properties of random media, the covariance matrix is defined by the product of the polarimetric feature vector and its transposed complex conjugate [8]. Various forms of the Mueller matrix, or Stokes matrix, and other polari-

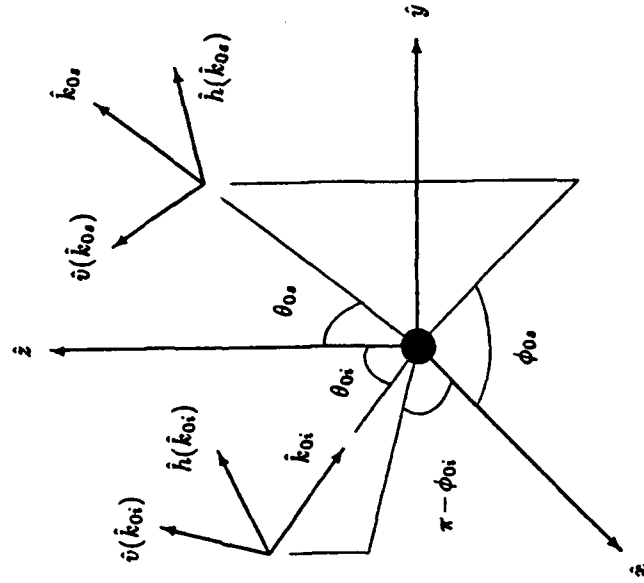


Figure 1.2.1 Coordinate systems.

metric descriptions [9-21] have been used. In the following subsections, the polarimetric descriptions used in this chapter are considered.

a. Scattering Matrix

Let an incident electric field (\vec{E}_i) propagate in the direction of incident wave vector \vec{k}_{oi} and illuminate the scatterer giving rise to the scattered field (\vec{E}_s) propagating in the direction of scattered wave vector \vec{k}_{0s} , as shown in Fig. 1.2.1. Associated with the incident field, Cartesian coordinate system ($\hat{h}(k_{0si}), \hat{v}(k_{0si}), \hat{k}_{oi}$), connoted as the incident basis, is defined with respect to vertical direction \hat{z} of the global Cartesian coordinate system ($\hat{x}, \hat{y}, \hat{z}$) as follows

$$\hat{h}(k_{0si}) = \frac{\hat{z} \times \vec{k}_{oi}}{|\hat{z} \times \vec{k}_{oi}|}, \quad \hat{v}(k_{0si}) = \frac{\vec{k}_{oi} \times \hat{h}(k_{0si})}{|\vec{k}_{oi} \times \hat{h}(k_{0si})|} \quad (1a)$$

1. Polarimetric Remote Sensing

$$\hat{k}_{0i} = \bar{k}_{0i}/|\bar{k}_{0i}| \quad \text{with} \quad \bar{k}_{0i} = k_{zi}\hat{z} + k_{yi}\hat{y} + k_{xi}\hat{x} \quad (1b)$$

Similarly, scattered basis $(\hat{h}(k_{0ss}), \hat{v}(k_{0ss}), \hat{k}_{0s})$ is determined by

$$\hat{h}(k_{0ss}) = \frac{\hat{z} \times \bar{k}_{0s}}{|\hat{z} \times \bar{k}_{0s}|}, \quad \hat{v}(k_{0ss}) = \frac{\bar{k}_{0s} \times \hat{h}(k_{0ss})}{|\bar{k}_{0s} \times \hat{h}(k_{0ss})|} \quad (1c)$$

$$\hat{k}_{0s} = \bar{k}_{0s}/|\bar{k}_{0s}| \quad \text{with} \quad \bar{k}_{0s} = k_{zs}\hat{z} + k_{ys}\hat{y} + k_{xs}\hat{x} \quad (1d)$$

In (1), the incident and the scattered wave vectors can be expressed in terms of the angles in Fig. 1.2.1 such that $\theta_{0s} = \theta_{0i}$ and $\phi_{0s} = \phi_{0i} + \pi$ in the backscattering direction.

Expressed in the incident basis, E_{hi} and E_{vi} are the components of \bar{E}_i in directions $\hat{h}(k_{0si})$ and $\hat{v}(k_{0si})$, respectively. For scattered field \bar{E}_s , the components in the scattered basis are E_{hs} along $\hat{h}(k_{0ss})$ and E_{vs} along $\hat{v}(k_{0ss})$. This coordinate connotation will be convenient for the subsequent derivation of the scattered field. The incident and scattered fields are then related by scattering matrix \bar{F} defined by

$$\begin{bmatrix} E_{hs} \\ E_{vs} \end{bmatrix} = \frac{e^{ihr}}{r} \bar{F} \cdot \begin{bmatrix} E_{hi} \\ E_{vi} \end{bmatrix} = \frac{e^{ihr}}{r} \begin{bmatrix} f_{hh} & f_{hv} \\ f_{vh} & f_{vv} \end{bmatrix} \cdot \begin{bmatrix} E_{hi} \\ E_{vi} \end{bmatrix} \quad (2)$$

where factor e^{ihr}/r is the spherical wave transformation and scattering matrix element $f_{\mu\nu}$ is for scattered polarization μ and incident polarization ν with μ and ν being h or v .

In the backscattering direction, relation $f_{hv} = f_{vh}$ holds for reciprocal media when \bar{E}_s is delineated in the incident basis. Note that the transformation of backscattered field \bar{E}_s from the scattered basis to the incident basis results in the sign changes of f_{hh} and f_{hv} . Hereafter, only backscattering is considered.

b. Covariance Matrix

The polarimetric backscattering information pertaining to a remotely sensed geophysical terrain can be conveyed in form of polarimetric feature vector \bar{X} defined with illuminated area A and the scattering matrix elements in the expression

$$\bar{X} = \lim_{A \rightarrow \infty} \sqrt{\frac{4\pi r^2}{A}} \frac{e^{ihr}}{r} \begin{bmatrix} f_{hh} \\ f_{hv} \\ f_{vv} \end{bmatrix} \quad (3)$$

1.2 Polarimetric Descriptions

As an ensemble average of the product between polarimetric feature vector \bar{X} and its transposed complex conjugate \bar{X}^\dagger , covariance matrix \bar{C} characterizes the fully polarimetric scattering properties of the geophysical media; explicitly,

$$\bar{C} = \langle \bar{X} \cdot \bar{X}^\dagger \rangle = \lim_{A \rightarrow \infty} \frac{4\pi}{A} \left\langle \begin{bmatrix} f_{hh} f_{hh}^* & f_{hh} f_{hv}^* & f_{hh} f_{vv}^* \\ f_{hv} f_{hh}^* & f_{hv} f_{hv}^* & f_{hv} f_{vv}^* \\ f_{vv} f_{hh}^* & f_{vv} f_{hv}^* & f_{vv} f_{vv}^* \end{bmatrix} \right\rangle \quad (4)$$

where the asterisk denotes the complex conjugate and the angular brackets are for the ensemble average. It is obvious from (4) that the covariance matrix is hermitian.

In the above definitions of the polarimetric feature vector and the covariance matrix, reciprocity relation $f_{hv} = f_{vh}$ has been implied for the reciprocal media under consideration. Consequently, no loss of information results from dismissing f_{vh} . It should be noted that the reciprocity relation elicits the implementation of the scattered-to-incident basis transformation.

c. Mueller Matrix

The scattering effects of geophysical terrain can also be described by the Mueller matrix which relates the Stokes vectors of the incident and the scattered fields. For the incident field, the Stokes vector is

$$\bar{I}_i = \begin{bmatrix} I_i \\ Q_i \\ U_i \\ V_i \end{bmatrix} = \begin{bmatrix} I_{hi} + I_{vi} \\ I_{hi} - I_{vi} \\ U_i \\ V_i \end{bmatrix} \quad (5)$$

where the components of \bar{I}_i are defined based on the linear polarimetric components of \bar{E}_i and the free-space intrinsic impedance η in the following equations

$$I_{hi} = \frac{1}{\eta} E_{hi} E_{hi}^*, \quad I_{vi} = \frac{1}{\eta} E_{vi} E_{vi}^* \quad (6a)$$

$$U_i = \frac{2}{\eta} \text{Re}(E_{vi} E_{hi}^*), \quad V_i = \frac{2}{\eta} \text{Im}(E_{vi} E_{hi}^*) \quad (6b)$$

For the field backscattered from reciprocal media, the Stokes vector

has the form

$$\bar{I}_s = \begin{bmatrix} I_s \\ Q_s \\ U_s \\ V_s \end{bmatrix} = \begin{bmatrix} I_{hs} + I_{vs} \\ I_{hs} - I_{vs} \\ U_s \\ V_s \end{bmatrix} \quad (7)$$

whose components are defined with the ensemble averages of the scattered field components as

$$I_{hs} = \frac{1}{\eta} \lim_{r \rightarrow \infty} \frac{4\pi r^2}{A} \langle E_{hs} E_{hs}^* \rangle \quad (8a)$$

$$I_{vs} = \frac{1}{\eta} \lim_{r \rightarrow \infty} \frac{4\pi r^2}{A} \langle E_{vs} E_{vs}^* \rangle \quad (8b)$$

$$U_s = \frac{2}{\eta} \lim_{r \rightarrow \infty} \frac{4\pi r^2}{A} \text{Re} \langle E_{vs} E_{hs}^* \rangle \quad (8c)$$

$$V_s = \frac{2}{\eta} \lim_{r \rightarrow \infty} \frac{4\pi r^2}{A} \text{Im} \langle E_{vs} E_{hs}^* \rangle \quad (8d)$$

Relating the incident to the scattered Stokes vectors, Mueller matrix \bar{M} depicts the backscattering effect by

$$\bar{I}_s = \bar{M} \cdot \bar{I}_i = \begin{bmatrix} M_{11} & M_{12} & M_{13} & M_{14} \\ M_{21} & M_{22} & M_{23} & M_{24} \\ M_{31} & M_{32} & M_{33} & M_{34} \\ M_{41} & M_{42} & M_{43} & M_{44} \end{bmatrix} \cdot \begin{bmatrix} I_i \\ Q_i \\ U_i \\ V_i \end{bmatrix} \quad (9)$$

In the incident basis, the Mueller matrix is a 4×4 matrix composed of 16 elements which are derived from equations (2,5-9) and written in terms of the scattering matrix elements as

$$M_{11} = \lim_{A \rightarrow \infty} \frac{4\pi}{A} \frac{1}{2} \langle f_{hh} f_{hh}^* + 2f_{hv} f_{hv}^* + f_{vv} f_{vv}^* \rangle \quad (10a)$$

$$M_{13} = \lim_{A \rightarrow \infty} \frac{4\pi}{A} \frac{1}{2} \langle f_{hh} f_{hh}^* - f_{vv} f_{vv}^* \rangle = M_{21} \quad (10b)$$

$$M_{13} = \lim_{A \rightarrow \infty} \frac{4\pi}{A} \text{Re} \langle f_{hh} f_{hv}^* + f_{hv} f_{vv}^* \rangle = M_{31} \quad (10c)$$

$$M_{14} = \lim_{A \rightarrow \infty} \frac{4\pi}{A} \text{Im} \langle f_{hh} f_{hv}^* + f_{hv} f_{vv}^* \rangle = -M_{41} \quad (10d)$$

$$M_{23} = \lim_{A \rightarrow \infty} \frac{4\pi}{A} \frac{1}{2} \langle f_{hh} f_{hh}^* - 2f_{hv} f_{hv}^* + f_{vv} f_{vv}^* \rangle \quad (10e)$$

1.2 Polarimetric Descriptions

$$M_{23} = \lim_{A \rightarrow \infty} \frac{4\pi}{A} \text{Re} \langle f_{hh} f_{hv}^* - f_{hv} f_{vv}^* \rangle = M_{32} \quad (10f)$$

$$M_{24} = \lim_{A \rightarrow \infty} \frac{4\pi}{A} \text{Im} \langle f_{hh} f_{hv}^* - f_{hv} f_{vv}^* \rangle = -M_{42} \quad (10g)$$

$$M_{33} = \lim_{A \rightarrow \infty} \frac{4\pi}{A} \text{Re} \langle f_{hh} f_{vv}^* + f_{hv} f_{hv}^* \rangle \quad (10h)$$

$$M_{34} = \lim_{A \rightarrow \infty} \frac{4\pi}{A} \text{Im} \langle f_{hh} f_{vv}^* \rangle = -M_{43} \quad (10i)$$

$$M_{44} = \lim_{A \rightarrow \infty} \frac{4\pi}{A} \text{Re} \langle f_{hh} f_{vv}^* - f_{hv} f_{hv}^* \rangle \quad (10j)$$

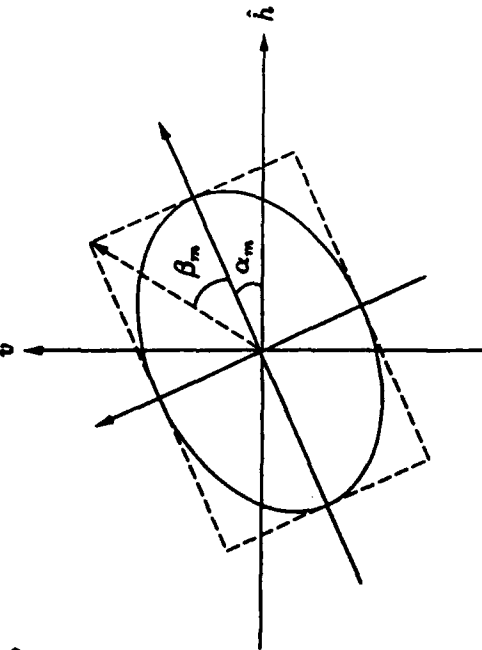
For given transmit and receive antenna polarizations, the received power is proportional to a scattering coefficient defined in terms of the Mueller matrix as [12,19,22]

$$\sigma(\alpha_r, \beta_r; \alpha_i, \beta_i) = \frac{\bar{I}_r^T \cdot \bar{T} \cdot \bar{M} \cdot \bar{I}_i}{2I_r I_i} \quad (11)$$

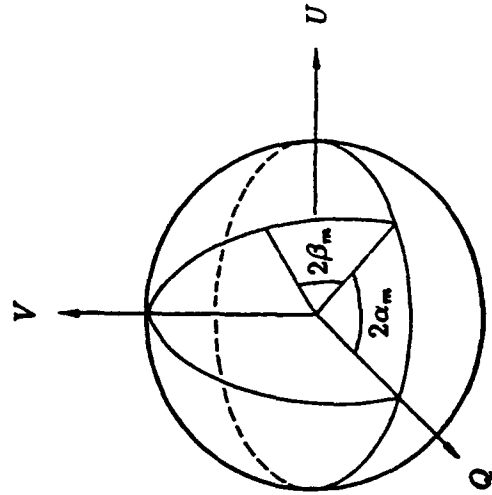
where τ denotes the transpose and Mueller matrix \bar{M} is symmetrized by diagonal matrix \bar{T} whose diagonal elements are $T_{11} = T_{33} = T_{33} = -T_{44} = 1$. Stokes vector \bar{I}_m in (11) depends on orientation angle α_m and ellipticity angle β_m (Fig. 1.2.2) as follows

$$\bar{I}_m = \begin{bmatrix} I_m \\ Q_m \\ U_m \\ V_m \end{bmatrix} = I_m \begin{bmatrix} 1 \\ \cos 2\alpha_m \cos 2\beta_m \\ \sin 2\alpha_m \cos 2\beta_m \\ \sin 2\beta_m \end{bmatrix} \quad (12)$$

with antenna operating mode $m = i$ for transmitting (incident) and $m = r$ for receiving. The orientation angles vary from 0° to 180° with 0° corresponding to h and 90° to v direction. The ellipticity angles range from -45° to 45° with 0° corresponding to linear, positive values to right-hand, and negative values to left-hand waves. The polarization states can be described geometrically by the Poincaré sphere with the upper hemisphere for right-hand polarizations and the lower for left-hand [23]. If the same antenna is used for both transmitting and receiving, the transmit and receive polarizations are identical and the corresponding scattering cross section is called the copolarized signature [22].



a Polarization ellipse



b Poincaré sphere

d. Scattering Coefficients

For polarimetric backscattering, the scattering coefficients are defined by [44]

$$\sigma_{\mu\nu\kappa} = \lim_{\substack{r \rightarrow \infty \\ A \rightarrow \infty}} \frac{4\pi r^2}{A} \frac{\langle E_{\mu} E_{\nu}^* \rangle}{E_{\tau} E_{\kappa}^*} \quad (13)$$

where subscripts μ , ν , τ , and κ can be h or v . The components of the scattered field in (13) are obtained by measuring the h and the v returns while the incident field is transmitted exclusively with h or v polarization. From (2), this measurement procedure can be described mathematically by the following equations relating the scattered to the incident field components

$$E_{\mu s} = \frac{e^{ikr}}{r} (f_{\mu\tau} E_{\tau i} + f_{\mu\kappa} E_{\kappa i})|_{E_{\tau i}=0} = \frac{e^{ikr}}{r} f_{\mu\tau} E_{\tau i} \quad (14a)$$

$$E_{\nu s} = \frac{e^{ikr}}{r} (f_{\nu\tau} E_{\tau i} + f_{\nu\kappa} E_{\kappa i})|_{E_{\tau i}=0} = \frac{e^{ikr}}{r} f_{\nu\kappa} E_{\kappa i} \quad (14b)$$

Substituting (14) in (13) renders polarimetric backscattering coefficient $\sigma_{\mu\nu\tau\kappa}$ in terms of scattering matrix components

$$\sigma_{\mu\nu\tau\kappa} = \lim_{A \rightarrow \infty} \frac{4\pi}{A} \langle f_{\mu\tau} f_{\nu\kappa}^* \rangle \quad (15)$$

By means of (15), the covariance matrix can be expressed with the backscattering coefficients as

$$\bar{C} = \begin{bmatrix} \sigma_{hhhh} & \sigma_{hhhv} & \sigma_{hhvv} \\ \sigma_{hhhv}^* & \sigma_{hhvv} & \sigma_{hvvv} \\ \sigma_{hhvv}^* & \sigma_{hvvh}^* & \sigma_{vvvv} \end{bmatrix} \quad (16)$$

in which diagonal element σ_{hhhh} , σ_{hhvv} , and σ_{vvvv} are conventional backscattering coefficient σ_{hh} , σ_{hv} , and σ_{vv} , respectively. Normalized to $\sigma = \sigma_{hhhh}$, the covariance matrix can be formed as

$$\bar{C} = \sigma \begin{bmatrix} 1 & \beta\sqrt{e} & \rho\sqrt{\gamma} \\ \beta^*\sqrt{e} & e & \xi\sqrt{\gamma e} \\ \rho^*\sqrt{\gamma} & \xi^*\sqrt{\gamma e} & \gamma \end{bmatrix} \quad (17)$$

where intensity ratio γ and e and correlation coefficient ρ , β , and ξ are

$$\gamma = \frac{\sigma_{vvvv}}{\sigma}, \quad e = \frac{\sigma_{hhvv}}{\sigma} \quad (18a)$$

Figure 1.2.2 Geometrical representations of polarizations.

$$\rho = \frac{\sigma_{hhvv}}{\sigma\sqrt{\epsilon}}, \quad \beta = \frac{\sigma_{hhhv}}{\sigma\sqrt{\epsilon}}, \quad \xi = \frac{\sigma_{hvvv}}{\sigma\sqrt{\epsilon}} \quad (18b)$$

In terms of the polarimetric backscattering coefficients, the Mueller matrix elements can also be written as

$$M_{11} = \frac{1}{2}(\sigma_{hhhh} + 2\sigma_{hhvv} + \sigma_{vvvv}) \quad (19a)$$

$$M_{12} = \frac{1}{2}(\sigma_{hhhh} - \sigma_{vvvv}) = M_{21} \quad (19b)$$

$$M_{13} = \text{Re}(\sigma_{hhhv} + \sigma_{hvvv}) = M_{31} \quad (19c)$$

$$M_{14} = \text{Im}(\sigma_{hhhv} + \sigma_{hvvv}) = -M_{41} \quad (19d)$$

$$M_{22} = \frac{1}{2}(\sigma_{hhhh} - 2\sigma_{hhvv} + \sigma_{vvvv}) \quad (19e)$$

$$M_{23} = \text{Re}(\sigma_{hhhv} - \sigma_{hvvv}) = M_{32} \quad (19f)$$

$$M_{24} = \text{Im}(\sigma_{hhhv} - \sigma_{hvvv}) = -M_{42} \quad (19g)$$

$$M_{33} = \text{Re}(\sigma_{hhvv} + \sigma_{hvvv}) \quad (19h)$$

$$M_{34} = \text{Im}(\sigma_{hhvv}) = -M_{43} \quad (19i)$$

$$M_{44} = \text{Re}(\sigma_{hhvv}) - \sigma_{hhhv} \quad (19j)$$

The use of the reciprocity relation for the media under consideration has been implied in the expressions for the covariance and the Mueller matrices. As seen from (16) and (19), both matrices are fully expressible with the complete set of polarimetric backscattering coefficients containing 9 independent parameters and therefore convey the same information regarding the terrain scattering properties. In the next section, the polarimetric backscattering coefficients will be derived with the scattered field in the scattered basis for reciprocal geophysical media with a three-layer configuration. Then, the scattered-to-incident basis transformation is applied to calculate the covariance and the Mueller matrices.

1.3 Random Medium Model

1.3 Random Medium Model

Random medium models have been used to account for the scattering due to embedded inhomogeneities in geophysical media [7,23-45]. For active and passive remote sensing, terrain media have been modeled with a two-layer anisotropic configuration [37,38]. When the permittivity fluctuations of the random media are strong, the singularity of the dyadic Green's function in the renormalization method has to be properly accounted for [40]. In this case, the scattering coefficients can be calculated under the distorted Born approximation [39-41]. For fully polarimetric remote sensing, two-layer isotropic and anisotropic random medium models have been used to derive the covariance and Mueller matrices and applied to investigate the backscattering from bare terrain fields such as sea ice and vegetation [43,44].

Presented in the following subsections is the three-layer anisotropic random medium model which can account for fully polarimetric backscattering from geophysical media under the effects of precipitation such as sea ice under snow or vegetation under fog. The model configuration (Fig. 1.3.1) has four different regions separated by three interfaces. The covering layer is modeled as an isotropic random medium. The middle layer is described as an anisotropic random medium due to the preferred alignment of the nonspherical scatterers. The underlying layer is considered as a homogeneous half space. The scattering effects of the random media are characterized by three-dimensional correlation functions with variances and correlation lengths corresponding to the fluctuation strengths and the physical geometries of the scatterers, respectively. The strong fluctuation theory is used to calculate the effective permittivities and the distorted Born approximation is then applied to obtain the complete set of polarimetric backscattering coefficients.

a. Formulation

The scattering configuration is depicted in Fig. 1.3.1. Region 0 is air with real permittivity ϵ_0 . Region 1 is a scattering medium with isotropic scatterers randomly embedded such as snow or fog whose electrical property can be characterized by inhomogeneous permittivity $\epsilon_1(\vec{r})$. Region 2 contains nonspherical scatterers constituting an anisotropic random medium such as sea ice or vegetation which has spatially dependent permittivity $\epsilon_2(\vec{r})$. Region 3 is the underlying half space with homogeneous permittivity ϵ_3 . The three regions are as-

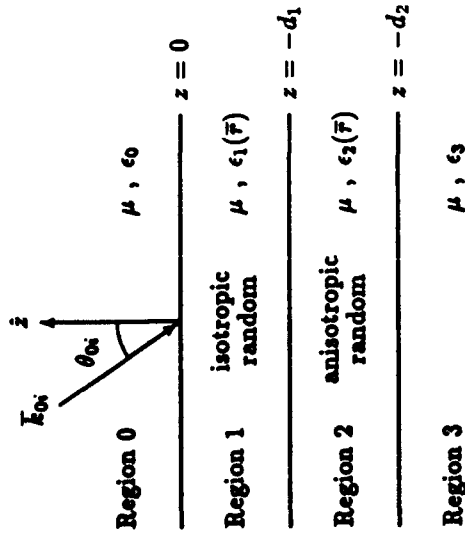


Figure 1.3.1 Scattering configuration.

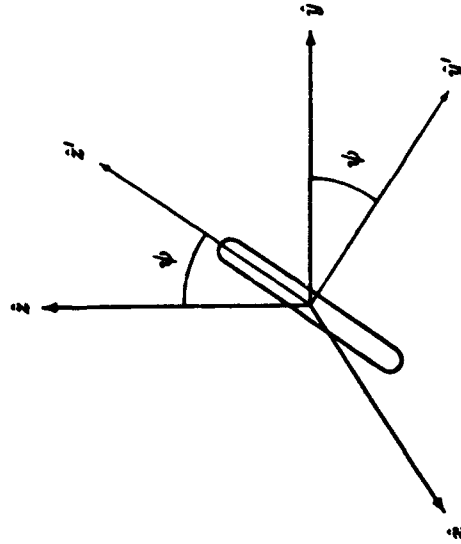


Figure 1.3.2 Geometry of scatterer in region 2.

sumed to have identical permeability μ . The infinite planar interfaces at location $z = -d_1$ and $z = -d_2$ in Cartesian coordinate system $(\hat{z}, \hat{y}, \hat{z})$ are shown in Fig. 1.3.1. Due to the preferred alignment of the nonspherical scatterers, the medium in region 2 is considered as effectively uniaxial with optic axis \hat{z}' tilted off the \hat{z} -axis by angle ψ in the $\hat{y}\hat{z}$ -plane as illustrated in Fig. 1.3.2.

1.3 Random Medium Model

13

In the phasor notation defined with $e^{-i\omega t}$ [23], time-harmonic total field $\vec{E}_0(\vec{r})$, $\vec{E}_1(\vec{r})$, and $\vec{E}_2(\vec{r})$, respectively in region 0, 1, and 2, satisfy the following wave equations

$$\nabla \times \nabla \times \vec{E}_0(\vec{r}) - k_0^2 \vec{E}_0(\vec{r}) = 0 \quad (20)$$

$$\nabla \times \nabla \times \vec{E}_1(\vec{r}) - k_0^2 \frac{\epsilon_1(\vec{r})}{\epsilon_0} \vec{E}_1(\vec{r}) = 0 \quad (21)$$

$$\nabla \times \nabla \times \vec{E}_2(\vec{r}) - k_0^2 \frac{\epsilon_2(\vec{r})}{\epsilon_0} \vec{E}_2(\vec{r}) = 0 \quad (22)$$

where the wave number is $k_0 = \omega \sqrt{\mu \epsilon_0}$ and ω is the angular frequency. In the remote sensing of geophysical media, strong permittivity fluctuations are often encountered. The strong fluctuation theory [40] is therefore necessitated in the calculations of the random-medium effective permittivities. Deterministic permittivity $\bar{\epsilon}_{g1} = \epsilon_{g1} \bar{I}$, where \bar{I} is the unit dyadic, and $\bar{\epsilon}_{g2}$ are introduced in both sides of (21) and (22), respectively, and the following vectors for $m = 1$ and $m = 2$

$$k_0^2 \bar{Q}_m(\vec{r}) \cdot \vec{E}_m(\vec{r}) = k_0^2 \left[\frac{\epsilon_m(\vec{r}) \bar{I} - \bar{\epsilon}_{gm}}{\epsilon_0} \right] \cdot \vec{E}_m(\vec{r}) \quad (23)$$

are treated as the effective sources so that wave equation (9) and (10) for the scattering random media become

$$\nabla \times \nabla \times \vec{E}_m(\vec{r}) - k_0^2 \frac{\bar{\epsilon}_{gm}}{\epsilon_0} \cdot \vec{E}_m(\vec{r}) = k_0^2 \bar{Q}_m(\vec{r}) \cdot \vec{E}_m(\vec{r}) \quad (24)$$

The permittivities in $\bar{\epsilon}_{g1}$ and $\bar{\epsilon}_{g2}$ are determined by the elimination of secular terms [40]. Physically, $\bar{\epsilon}_{g1}$ and $\bar{\epsilon}_{g2}$ are the effective permittivity tensors in the very low frequency limit where the scattering loss is negligible compared to the absorption loss [24].

In form of an integral equation, the total field in region $m = 0, 1, 2$ is the superposition of the mean field and the scattered field; explicitly,

$$\vec{E}_m(\vec{r}) = \vec{E}_m^{(0)}(\vec{r}) + k_0^2 \sum_{n=1}^2 \int_{V_n} d\vec{r}_n \bar{Q}_{mn}(\vec{r}, \vec{r}_n) \cdot \bar{Q}_n(\vec{r}_n) \cdot \vec{E}_n(\vec{r}_n) \quad (25)$$

Mean field $\vec{E}_m^{(0)}(\vec{r})$ is the solution to the homogeneous wave equations where the effective sources vanish in the absence of the scatterers.

As a particular solution to the inhomogeneous wave equations in the presence of the scatterers in region $n = 1, 2$ occupying volume V_n , the scattered field in (25) is the integrals of the products between the effective source and dyadic Green's functions $\bar{\bar{G}}_{mn}(\bar{r}, \bar{r}_n)$ defined by

$$\nabla \times \nabla \times \bar{\bar{G}}_{mn}(\bar{r}, \bar{r}_n) - k_0^2 \frac{\bar{\bar{\epsilon}}_{mn}}{\epsilon_0} \cdot \bar{\bar{G}}_{mn}(\bar{r}, \bar{r}_n) = \delta(\bar{r} - \bar{r}_n) \bar{\bar{I}} \quad (26)$$

where first subscript m in $\bar{\bar{G}}_{mn}(\bar{r}, \bar{r}_n)$ denotes the observation region containing observation point \bar{r} , second subscript n stands for source region $n = 1, 2$ containing source point \bar{r}_n , and $\delta(\bar{r} - \bar{r}_n)$ is the Dirac delta function. When $m \neq n$ signifying observation point \bar{r} is outside source region n within which \bar{r}_n is restricted, the Dirac delta function in the right-hand side of (26) vanishes. It is also obvious from (26) that an observation point in a scattering region can coincide with a source point in the same region ($m = n = 1, 2$) thus giving rise to the singularity of dyadic Green's function $\bar{\bar{G}}_{nn}(\bar{r}, \bar{r}_n)$ which can be decomposed into a principal value part and a Dirac delta part

$$\bar{\bar{G}}_{nn}(\bar{r}, \bar{r}_n) = PV \bar{\bar{G}}_{nn}(\bar{r}, \bar{r}_n) - \delta(\bar{r} - \bar{r}_n) k_0^{-2} \bar{\bar{S}}_n, \quad n = 1, 2 \quad (27)$$

Dyadic coefficient $\bar{\bar{S}}_n$ is conformed with the shape of the source exclusion volume and determined by the condition of secular-term elimination [40]. With the decomposed Green's function of (27), the singular part in the integrand on the right-hand side of (25) for $m = n$ can be extracted and then combined with total field $\bar{E}_n(\bar{r})$ on the left-hand side to form external field $\bar{F}_n(\bar{r})$ in scattering region $n = 1, 2$

$$\bar{F}_n(\bar{r}) = [\bar{\bar{I}} + \bar{\bar{S}}_n \cdot \bar{\bar{Q}}_n(\bar{r})] \cdot \bar{E}_n(\bar{r}) \quad (28)$$

In terms of external field $\bar{F}_n(\bar{r})$, the vector source of (23) can be redefined by introducing scatterer $\bar{\bar{\xi}}_n(\bar{r})$ such that

$$k_0^2 \bar{\bar{\xi}}_n(\bar{r}) \cdot \bar{F}_n(\bar{r}) = k_0^2 \bar{\bar{Q}}_n(\bar{r}) \cdot \bar{E}_n(\bar{r}) \quad (29)$$

It follows from (29) that scatterer $\bar{\bar{\xi}}_n(\bar{r})$ for the isotropic ($n = 1$) and the anisotropic ($n = 2$) random media are

$$\bar{\bar{\xi}}_n(\bar{r}) = \bar{\bar{Q}}_n(\bar{r}) \cdot [\bar{\bar{I}} + \bar{\bar{S}}_n \cdot \bar{\bar{Q}}_n(\bar{r})]^{-1} \quad (30)$$

By applying the distorted Born approximation [35, 39-41] to (25) with the new definition of the sources in (29), the total field observed in region 0 is

$$\bar{E}_0(\bar{r}) = \bar{E}_0^{(0)}(\bar{r}) + k_0^2 \sum_{n=1}^2 \int_{V_n} d\bar{r}_n \langle \bar{\bar{G}}_{0n}(\bar{r}, \bar{r}_n) \rangle \cdot \bar{\bar{\xi}}_n(\bar{r}_n) \cdot \langle \bar{F}_n(\bar{r}_n) \rangle \quad (31)$$

where isotropic effective permittivity $\bar{\bar{\epsilon}}_{d/1} = \epsilon_{d/1} \bar{\bar{I}}$ for region 1 and uniaxial permittivity $\bar{\bar{\epsilon}}_{d/2}$ for region 2 are used to calculate the mean dyadic Green's functions and the mean fields. The polarimetric scattering coefficients can then be obtained with the following correlation of the scattered field in (31)

$$\begin{aligned} \langle \bar{E}_{0a}(\bar{r}) \cdot \bar{E}_{0b}^*(\bar{r}) \rangle &= \sum_{n=1}^2 \sum_{i,j,k,l,m} k_0^4 \int_{V_n} d\bar{r}_n \int_{V_n} d\bar{r}_n' C_{ijnklm}(\bar{r}_n, \bar{r}_n') \\ &\cdot [\langle G_{0nij}(\bar{r}, \bar{r}_n) \rangle \langle F_{nkl}(\bar{r}_n) \rangle] \cdot [\langle G_{0mli}(\bar{r}, \bar{r}_n') \rangle \langle F_{nm}(\bar{r}_n') \rangle]^* \end{aligned} \quad (32)$$

For random media $n = 1$ and $n = 2$, $C_{ijnklm}(\bar{r}_n, \bar{r}_n')$ in (32) is the $ijklm$ element of fourth-rank correlation tensor $\bar{\bar{C}}_{ijnklm}(\bar{r}_n, \bar{r}_n')$ defined as

$$C_{ijnklm}(\bar{r}_n, \bar{r}_n') = \langle \epsilon_{ijnk}(\bar{r}_n) \epsilon_{nlm}^*(\bar{r}_n') \rangle \quad (33)$$

With specified correlation functions, the polarimetric scattering coefficients can thus be obtained after the effective permittivities of the random media are calculated as shown in the next subsection.

b. Effective Permittivities

The strong permittivity fluctuation theory [40] is used to derive the effective permittivities of the random media. The singularities of the dyadic Green's functions in the bilocal approximated Dyson's equations are accounted for and the low-frequency approximation is applied to obtain the results for the isotropic and the anisotropic random media. The derivations are done in the frequency domain with the Fourier-transform method. The isotropic random medium is characterized with a correlation function of spherical form and the anisotropic random medium is described with a correlation function of spheroidal form. When the spheroidal form is reduced to spherical, the anisotropic result is confirmed with the isotropic case. Following is the summary

of the effective permittivity calculations first for the isotropic and then for the anisotropic random media.

Consider an isotropic random medium composed of a host medium with permittivity ϵ_1 and randomly embedded scatterers with permittivity ϵ_2 and total fractional volume f_2 where subscript 1 is used for the isotropic random medium in accordance to the notation in Fig. 1.3.1. By introducing auxiliary permittivity $\bar{\epsilon}_2$ into the wave equation as in (24), dyadic Green's function $\bar{G}_2(\bar{r}, \bar{r}_1)$ satisfies the inhomogeneous differential equation of the form (26). Subscripts $g1$ is used here to indicate that $\bar{G}_{g1}(\bar{r}, \bar{r}_1)$ corresponds to a medium with permittivity ϵ_{g1} . To account for the singularity, $\bar{G}_{g1}(\bar{r}, \bar{r}_1) = \bar{G}_{g1}(\bar{r} - \bar{r}_1)$ is decomposed as in (27) with $\bar{S}_1 = S_1 \bar{I}$ for the Dirac delta part. By using the following definition for the Fourier transform

$$\bar{G}_{g1}(\bar{r}) \equiv \frac{1}{8\pi^3} \int_{-\infty}^{\infty} d\bar{k} \bar{G}_{g1}(\bar{k}) e^{i\bar{k} \cdot \bar{r}} \quad (34)$$

the dyadic Green's function in the frequency domain is found to be

$$\bar{G}_{g1}(\bar{k}) = \frac{\bar{I}}{D(k)} - \frac{k k}{k_{g1}^2 D(k)} \quad \text{with} \quad \begin{cases} D(k) = k^2 - k_{g1}^2 \\ k_{g1}^2 = \omega^2 \mu \epsilon_{g1} \end{cases} \quad (35)$$

Under the bilocal and the low-frequency approximations [40], the effective permittivity of the isotropic random medium is composed of a quasi-static part (ϵ_{g1}) and a correction part

$$\bar{\epsilon}_{eff1} \approx \epsilon_{g1} \bar{I} + \epsilon_0 \left[\bar{I} - \bar{\epsilon}_{eff1}^{(0)} \cdot \bar{S}_1 \right]^{-1} \cdot \bar{\epsilon}_{eff1}^{(0)} \quad (36)$$

The correction part in (36) physically accounts for the modification in the wave speed and attenuation due to the scattering effect of the scatterers. For $j, m = x, y, z$, the jm element of $\bar{\epsilon}_{eff1}^{(0)}$ is related to the Green's function (35) in the following manner

$$[\bar{\epsilon}_{eff1}^{(0)}]_{jm} = \sum_{k,l} \Gamma_{1,jlm}^{(0)} \left\{ k_0^2 \int_{-\infty}^{\infty} d\bar{k} [\bar{G}_{g1}(\bar{k})]_{kl} \bar{\Phi}_{1l}(\bar{k}) + [\bar{S}_1]_{kl} \right\} \quad (37)$$

To arrive at (37), the correlation function has been defined as

$$\Gamma_{1,jlm}(\bar{r}_1, \bar{r}_1^0) = \langle \xi_{1,jl}(\bar{r}_1) \xi_{1,lm}(\bar{r}_1^0) \rangle \quad (38a)$$

and the random medium has been assumed to be statistically homogeneous so that (38a) can be written as

$$\Gamma_{1,jlm}(\bar{r}_1, \bar{r}_1^0) = \Gamma_{1,jlm}(\bar{r}_1 - \bar{r}_1^0) \equiv \Gamma_{1,jlm}^{(0)} R_{\ell 1}(\bar{r}_1 - \bar{r}_1^0) \quad (38b)$$

where $R_{\ell 1}(\bar{r} = \bar{r}_1 - \bar{r}_1^0)$ is the normalized correlation function such that $R_{\ell 1}(0)$ is equal to 1. In (37), $\bar{\Phi}_{1l}(\bar{k})$ is the Fourier transform of the normalized correlation function $R_{\ell 1}(\bar{r})$ defined as

$$\bar{\Phi}_{\ell 1}(\bar{k}) \equiv \frac{1}{8\pi^3} \int_{-\infty}^{\infty} d\bar{r} R_{\ell 1}(\bar{r}) e^{i\bar{k} \cdot \bar{r}} \quad (39)$$

In the isotropic random medium, $\bar{\xi}_{1l}(\bar{r}_1)$ is a scalar multiple of the unit dyadic \bar{I} and non-zero coefficient $\Gamma_{1,jlm}^{(0)}$ are

$$\Gamma_{1,jlm}^{(0)} = \langle \xi_{1,jl}(\bar{r}_1) \xi_{1,lm}(\bar{r}_1) \rangle \equiv \delta_{\ell 1} \quad \begin{cases} k=j, l=m \\ j,m=x,y,z \end{cases} \quad (40)$$

For a spherically symmetric correlation function, it is seen from (36-40) that the effective permittivity of the isotropic random medium is independent of direction and expressed as a scalar multiple of \bar{I}

$$\bar{\epsilon}_{eff1} = \epsilon_{eff1} \bar{I} = \left[\epsilon_{g1} + \frac{\epsilon_0 \delta_{\ell 1} (I_0 + S_1)}{1 - \delta_{\ell 1} (I_0 + S_1)} \right] \bar{I} \quad (41)$$

where I_0 is the integral of the product between a diagonal element of the dyadic Green's function and the correlation function in the frequency domain

$$I_0 = k_0^2 \int_{\infty}^{\infty} d\bar{k} [\bar{G}_{g1}(\bar{k})]_{jj} \bar{\Phi}_{\ell 1}(\bar{k}) \quad (42)$$

Due to the isotropy of the medium, any diagonal element ($jj = xx, yy$, or zz) of the dyadic Green's function (36) can be used in (42) to yield an identical result for I_0 . For an isotropic random medium characterized by an exponential correlation function of spherical form with correlation length ℓ_1 , $R_{\ell 1}(\bar{r})$ is expressed as

$$R_{\ell 1}(\bar{r}) = \exp \left(-\frac{r}{\ell_1} \right) \quad (43a)$$

whose Fourier transform is obtained by carrying out the integration (39) in the spherical coordinates to yield

$$\Phi_{\ell 1}(\vec{k}) = \frac{\ell_1^2}{\pi^2(1 + k^2\ell_1^2)^2} \quad (43b)$$

With the use of (43b), the integration (42) is then carried out analytically by a change of variables into the spherical coordinates. The result for I_0 is

$$I_0 = \frac{\epsilon_0}{3\epsilon_{g1}} \left[-\frac{3\vartheta^2 + 1}{(\vartheta + 1)^2} + i\frac{4\vartheta\sqrt{\vartheta}}{(\vartheta + 1)^2} \right] \vartheta = k_{g1}^2\ell_1^2 \quad (44)$$

Coefficient S_1 , which conforms with the shape of the source exclusion volume, can be determined by requiring the cancelation of the frequency dependent terms in (37) so that the secular term is eliminated. For the isotropic case, S_1 is thereby obtained

$$S_1 = -\lim_{\omega \rightarrow 0} I_0 = \frac{\epsilon_0}{3\epsilon_{g1}} \quad (45)$$

The elimination of the secular term also imposes the condition of zero-mean on the scatterer tensor

$$\langle \vec{\bar{\epsilon}}_1(\vec{r}) \rangle = 0 \quad (46)$$

Condition (46) and (45) together with definition (30) and (23) for $n = 1$ determine auxiliary permittivity $\bar{\epsilon}_{g1}$ with the relation

$$\left(\frac{\epsilon_{g1} - \epsilon_{g1}}{\epsilon_{g1} + 2\epsilon_{g1}} \right) (1 - f_{s1}) + \left(\frac{\epsilon_{s1} - \epsilon_{g1}}{\epsilon_{s1} + 2\epsilon_{g1}} \right) f_{s1} = 0 \quad (47)$$

When the value of ϵ_{g1} is obtained, variance $\delta_{\ell 1}$ is found from (40)

$$\delta_{\ell 1} = 9 \frac{\epsilon_{g1}^2}{\epsilon_0^2} \left[\left(\frac{\epsilon_{g1} - \epsilon_{g1}}{\epsilon_{g1} + 2\epsilon_{g1}} \right)^2 (1 - f_{s1}) + \left(\frac{\epsilon_{s1} - \epsilon_{g1}}{\epsilon_{s1} + 2\epsilon_{g1}} \right)^2 f_{s1} \right] \quad (48)$$

In summary of the isotropic case, the isotropic effective permittivity is calculated with (41) where ϵ_{g1} , $\delta_{\ell 1}$, I_0 , and S_1 are given by (47), (48), (44), and (45), respectively.

1.3 Random Medium Model

Consider now an anisotropic random medium composed of a host medium with permittivity ϵ_{s2} and embedded nonspherical scatterers with permittivity ϵ_{g2} and total fractional volume f_{s2} . The scatterers with a preferred alignment direction and an azimuthal symmetry effectively give rise to the uniaxial anisotropy of the random medium whose optic axis is the z' axis in Cartesian coordinate system $(\hat{x}', \hat{y}', \hat{z}')$ illustrated in Fig. 1.3.2. The principle for deriving the anisotropic effective permittivity is the same as in the previous paragraph; however, the anisotropy of the medium needs be accounted for. In this case, an appropriate form of auxiliary permittivity $\bar{\epsilon}_{g2}$ is

$$\bar{\epsilon}_{g2} = \begin{bmatrix} \epsilon_{g2\rho'} & 0 & 0 \\ 0 & \epsilon_{g2\rho'} & 0 \\ 0 & 0 & \epsilon_{g2z'} \end{bmatrix} \quad (49)$$

Equation (49) is expressed in the primed coordinate system shown in Fig. 1.3.2. This coordinate system is used to calculate the effective permittivity of the anisotropic random medium and a rotation transformation with tilt angle ψ is then applied to transform the result into unprime Cartesian coordinate system $(\hat{x}, \hat{y}, \hat{z})$. Corresponding dyadic Green's function $\bar{\bar{G}}_{g2}(\vec{r}')$ is decomposed as in (27) with the Liirac delta part having uniaxial dyadic coefficient

$$\bar{\bar{S}}_2 = \begin{bmatrix} S_{2\rho'} & 0 & 0 \\ 0 & S_{2\rho'} & 0 \\ 0 & 0 & S_{2z'} \end{bmatrix} \quad (50)$$

According to the Fourier transform definition (34) where the subscript 1 is replaced by 2 and \vec{r} and \vec{k} are respectively changed to \vec{r}' and \vec{k}' , dyadic Green's function $\bar{\bar{G}}_{g2}(\vec{r}')$ has frequency-domain version $\bar{\bar{G}}_{g2}(\vec{k}')$ written as

$$\bar{\bar{G}}_{g2}(\vec{k}') = \frac{1}{(k_{\rho'}^2 + k_{\rho'}^2)D_o(\vec{k}')} \begin{bmatrix} k_{\rho'}^2 & -k_{\rho'}^2 k_{\rho'}^2 & 0 \\ -k_{\rho'}^2 k_{\rho'}^2 & k_{\rho'}^2 & 0 \\ 0 & 0 & 0 \end{bmatrix} + \frac{1}{(k_{\rho'}^2 + k_{\rho'}^2)D_o(\vec{k}')} \begin{bmatrix} k_{\rho'}^2 & k_{\rho'}^2 k_{\rho'}^2 & 0 \\ k_{\rho'}^2 k_{\rho'}^2 & k_{\rho'}^2 & 0 \\ 0 & 0 & k_{\rho'}^2 (k_{\rho'}^2 + k_{\rho'}^2) \end{bmatrix} - \frac{k_{\rho'}^2 D_o(\vec{k}')}{k_{\rho'}^2} \quad (51)$$

where $D_o(\vec{k})$, $D_e(\vec{k})$, $k_{\theta 2\rho'}^2$, and $k_{\theta 2\rho'}^2$ are defined as follows

$$D_o(\vec{k}) = k_x^2 + k_y^2 + k_z^2 - k_{\theta 2\rho'}^2 \quad (52a)$$

$$D_e(\vec{k}) = k_x^2 + \frac{k_{\theta 2\rho'}^2}{k_{\theta 2\rho'}^2} (k_x^2 + k_y^2 - k_{\theta 2\rho'}^2) \quad (52b)$$

$$k_{\theta 2\rho'}^2 = \omega^2 \mu_0 \epsilon_{\theta 2\rho'}, \quad k_{\theta 2\rho'}^2 = \omega^2 \mu_0 \epsilon_{\theta 2\rho'} \quad (52c)$$

Similar to (36), the effective permittivity of the anisotropic random medium is composed of a quasi-static part and a scattering-effect part

$$\bar{\epsilon}_{eff}(\vec{r}') = \bar{\epsilon}_{\theta 2} + \epsilon_0 \left[\bar{I} - \bar{\epsilon}_{eff}^{(0)} \cdot \bar{S}_2 \right]^{-1} \cdot \bar{\epsilon}_{eff}^{(0)} \quad (53)$$

where \vec{r}' indicates the primed coordinate system and the j m element of effective scatterer $\bar{\epsilon}_{eff}^{(0)}$ under the low-frequency approximation is of the form (37) with subscript 1 changed to 2 and $j, m = x', y', z'$

$$[\bar{\epsilon}_{eff}^{(0)}]_{jim} = \sum_{k,l} \Gamma_{\ell 2jim}^{(0)} \left\{ k_0^2 \int_{-\infty}^{\infty} d\vec{k} [\bar{G}_{\theta 2}(\vec{k})]_{kl} \bar{\Phi}_{\ell 2}(\vec{k}') + [\bar{S}_2]_{kl} \right\} \quad (54)$$

The statically homogeneous anisotropic random medium is described with fourth-rank correlation tensor $\bar{\Gamma}_{\ell 2}(\vec{r}', \vec{r}'') = \langle \bar{\epsilon}_2(\vec{r}') \bar{\epsilon}_2(\vec{r}'') \rangle$ where $\bar{\epsilon}_2(\vec{r}')_2$ is a diagonal tensor in the primed coordinates; thus, the non-zero elements of $\bar{\Gamma}_{\ell 2}(\vec{r}', \vec{r}'') = \bar{\Gamma}_{\ell 2}(\vec{r}'_2 - \vec{r}'_2'')$ are

$$\Gamma_{\ell 2jim}(\vec{r}') = \delta_{\ell 2\rho'} R_{\ell 2}(\vec{r}'), \quad jilm = \begin{cases} x'x'x'x', x'x'y'y', \\ y'y'x'x', y'y'y'y' \end{cases} \quad (55a)$$

$$\Gamma_{\ell 2jim}(\vec{r}') = \delta_{\ell 2x'} R_{\ell 2}(\vec{r}'), \quad jilm = x'x'x'x' \quad (55b)$$

$$\Gamma_{\ell 2jim}(\vec{r}') = \delta_{\ell 2z'} R_{\ell 2}(\vec{r}'), \quad jilm = \begin{cases} x'x'x'x', y'y'x'x', \\ x'x'y'y', y'y'y'y' \end{cases} \quad (55c)$$

where $\vec{r}' = \vec{r}'_2 - \vec{r}'_2''$ and $\Gamma_{\ell 2jim}(\vec{r}')$ has normalizing variance $\Gamma_{\ell 2jim}(\vec{r}' = 0) = \langle \epsilon_{2jh}(\vec{r}') \epsilon_{2im}(\vec{r}') \rangle \equiv \Gamma_{\ell 2jim}^{(0)}$ which can take on the value of $\delta_{\ell 2\rho'}$, $\delta_{\ell 2x'}$, or $\delta_{\ell 2z'}$ such that $R_{\ell 2}(0) = 1$. For an azimuthally symmetric correlation function, it is observed from (49-55) that $\bar{\epsilon}_{eff}(\vec{r}')$ is uniaxial and expressed with the permittivity tensor

$$\bar{\epsilon}_{eff}(\vec{r}') = \begin{bmatrix} \epsilon_{eff2\rho'} & 0 & 0 \\ 0 & \epsilon_{eff2x'} & 0 \\ 0 & 0 & \epsilon_{eff2z'} \end{bmatrix} \quad (56a)$$

$$\epsilon_{eff2\rho'} = \epsilon_{\theta 2\rho'} + \frac{\epsilon_0 \delta_{\ell 2\rho'} (I_{\rho'} + S_{2\rho'})}{1 - \delta_{\ell 2\rho'} (I_{\rho'} + S_{2\rho'}) S_{2\rho'}} \quad (56b)$$

$$\epsilon_{eff2x'} = \epsilon_{\theta 2x'} + \frac{\epsilon_0 \delta_{\ell 2x'} (I_{x'} + S_{2x'})}{1 - \delta_{\ell 2x'} (I_{x'} + S_{2x'}) S_{2x'}}$$

where $I_{\rho'}$ and $I_{\rho'}$ are the integrals in the frequency domain of the products between the corresponding diagonal element of the dyadic Green's function and normalized correlation function $\bar{\Phi}_{\ell 2}(\vec{k}')$ defined as in (39) with the subscript 1 changed to 2 and \vec{k} and \vec{r} to \vec{k}' and \vec{r}' . In the cylindrical coordinates, integral $I_{\rho'}$ and $I_{\rho'}$ are

$$I_{\rho'} = k_0^2 \int_0^{2\pi} d\phi' \int_0^{\infty} dk_{\rho'} k_{\rho'}' \int_{-\infty}^{\infty} dk_z' (-k_{\rho 2\rho'}^{-2}) \cdot \left[\frac{k_z'^2 - k_{\theta 2\rho'}^2}{k_z'^2 + k_{\rho}^2 (\epsilon_{\theta 2\rho'} / \epsilon_{\theta 2x'}) - k_{\theta 2\rho'}^2} \right] \bar{\Phi}_{\ell 2}(\vec{k}') \quad (57a)$$

$$I_{\rho'} = k_0^2 \int_0^{2\pi} d\phi' \int_0^{\infty} dk_{\rho'} k_{\rho'}' \int_{-\infty}^{\infty} dk_z' \cdot \left[\frac{\sin^2 \phi'}{k_z'^2 + k_{\rho}^2 - k_{\theta 2\rho'}^2} + \frac{(k_{\rho}'^{-2} - k_z'^{-2}) k_{\rho}^2 \cos^2 \phi'}{k_z'^2 + k_{\rho}^2 (\epsilon_{\theta 2\rho'} / \epsilon_{\theta 2x'}) - k_{\theta 2\rho'}^2} \right] \bar{\Phi}_{\ell 2}(\vec{k}') \quad (57b)$$

For an anisotropic random medium characterized by an exponential correlation function of spheroidal form with correlation length $\ell_{2\rho'}$ and $\ell_{2x'}$, $R_{\ell 2}(\vec{r}')$ is expressed as

$$R_{\ell 2}(\vec{r}') = \exp \left(-\sqrt{\frac{z'^2 + y'^2}{\ell_{2\rho'}^2} + \frac{z'^2}{\ell_{2x'}^2}} \right) \quad (58a)$$

whose Fourier transform is obtained by carrying out the Fourier integration in the cylindrical coordinates or by applying the scaling theorem on (43b) to yield

$$\bar{\Phi}_{\ell 2}(\vec{k}') = \frac{\ell_{2\rho'}^2 \ell_{2x'}}{\pi^2 (1 + k_{\rho}^2 \ell_{2\rho'}^2 + k_z^2 \ell_{2x'}^2)^2} \quad (58b)$$

With the use of (58b), the integrations in (57) can then be carried out analytically by effectuating the integrations over ϕ' , using contour

integration technique for the integrations over k'_z , and then performing the integrations over k'_{ρ} . The result for I_{ρ} is determined as follows

$$I_{\rho} = -\frac{2\epsilon_0}{\epsilon_{g2\rho'}}(T_s + T_d) \quad (59a)$$

$$T_s = -\frac{\alpha\gamma_L^2\sqrt{\alpha\gamma_L^2}}{2a^3}\left[\frac{\sqrt{-\zeta}}{\vartheta_e} + \frac{\vartheta_e + \zeta}{\vartheta_e\sqrt{\vartheta_e}}\left(\frac{\pi}{2} - \tan^{-1}\frac{\sqrt{-\zeta}}{\sqrt{\vartheta_e}}\right)\right] \quad (59b)$$

$$T_d = \frac{\alpha\gamma_L^2}{2a^3}\left[\frac{1+\alpha\nu_e^2}{\vartheta_e} + \frac{\vartheta_e(\alpha+2)-(b+\alpha\nu_e^2)}{\vartheta_e\sqrt{\vartheta_e}}\left(\frac{\pi}{2} - \tan^{-1}\frac{1}{\sqrt{\vartheta_e}}\right)\right] \quad (59c)$$

$$a = \alpha\gamma_L^2 - 1, \quad \alpha = \frac{\epsilon_{g2\rho'}}{\epsilon_{g2\rho'}}, \quad \gamma_L = \frac{l_{2\rho'}}{l_{2s'}}, \quad \nu_{g\rho'}^2 = k_{g2\rho'}^2 l_{2s'}^2 \quad (59d)$$

$$\zeta = \alpha\gamma_L^2\nu_{g\rho'}^2, \quad b = \frac{\alpha\gamma_L^2 + \zeta}{a}, \quad \vartheta_e = b - 1, \quad \vartheta_e = b + \zeta \quad (59e)$$

Integral I_{ρ} involves additional terms in the dyadic Green's function and the result is found to be

$$I_{\rho} = \nu_{0\rho'}^2(T_1^* - T_2^* - T_3^*) + \alpha\nu_{0\rho'}^2\left[(T_1^* - T_2^* - T_3^*) + \frac{1}{\zeta}(T_s + T_d - \frac{1}{2})\right] \quad (60a)$$

$$T_1^* = \frac{\alpha\gamma_L^2\sqrt{\alpha\gamma_L^2}}{2a^3\vartheta_e}\left[-\frac{\sqrt{-\zeta}}{b} + \frac{1}{\sqrt{\vartheta_e}}\left(\frac{\pi}{2} - \tan^{-1}\frac{\sqrt{-\zeta}}{\sqrt{\vartheta_e}}\right)\right] \quad (60b)$$

$$T_2^* = \frac{1}{2a\vartheta_e}\left[1 - \frac{1}{\sqrt{\vartheta_e}}\left(\frac{\pi}{2} - \tan^{-1}\frac{1}{\sqrt{\vartheta_e}}\right)\right] \quad (60c)$$

$$T_3^* = \frac{\alpha\gamma_L^2}{2a^3\vartheta_e}\left[-\frac{1}{b} + \frac{1}{\sqrt{\vartheta_e}}\left(\frac{\pi}{2} - \tan^{-1}\frac{1}{\sqrt{\vartheta_e}}\right)\right] \quad (60d)$$

$$T_{1,2,3}^* = T_{1,2,3}^*(\alpha = 1), \quad \nu_{0\rho'} = k_0 l_{2\rho'} \quad (60e)$$

Diagonal element $S_{g2\rho'}$ and $S_{g2s'}$ of dyadic coefficient $\bar{\bar{S}}_2$ in the singular part of the Green's function for the anisotropic medium are obtained by requiring the cancelation of the frequency dependent terms

1.3 Random Medium Model

in (54) to eliminate the secular terms. Derived from (54), (59), and (60), coefficient $S_{g2\rho'}$ and $S_{g2s'}$ are

$$S_{2\rho'} = -\lim_{\omega \rightarrow 0} I_{\rho'} = \frac{\epsilon_0}{2\epsilon_{g2\rho'}a\sqrt{a}}[(1+a)\tan^{-1}\sqrt{a} - \sqrt{a}] \quad (61a)$$

$$S_{2s'} = -\lim_{\omega \rightarrow 0} I_{s'} = \frac{\epsilon_0(1+a)}{\epsilon_{g2s'}a\sqrt{a}}[\sqrt{a} - \tan^{-1}\sqrt{a}] \quad (61b)$$

Similar to (46), the zero-mean condition is imposed on scatterer $\bar{\bar{\xi}}_2(\bar{r})$ for the elimination of the secular terms. This condition together with (61) and definition (30) and (23) for $n = 2$ in the primed coordinate system determine auxiliary permittivity $\bar{\bar{\epsilon}}_{g2}$ in the following manner

$$\frac{(\epsilon_{g2} - \epsilon_{g2\rho'})(1 - f_{g2})}{\epsilon_0 + S_{2\rho'}(\epsilon_{g2} - \epsilon_{g2\rho'})} + \frac{(\epsilon_{g2} - \epsilon_{g2\rho'})f_{g2}}{\epsilon_0 + S_{2\rho'}(\epsilon_{g2} - \epsilon_{g2\rho'})} = 0 \quad (62a)$$

$$\frac{(\epsilon_{g2} - \epsilon_{g2s'})(1 - f_{g2})}{\epsilon_0 + S_{2s'}(\epsilon_{g2} - \epsilon_{g2s'})} + \frac{(\epsilon_{g2} - \epsilon_{g2s'})f_{g2}}{\epsilon_0 + S_{2s'}(\epsilon_{g2} - \epsilon_{g2s'})} = 0 \quad (62b)$$

Numerical values of $\epsilon_{g2\rho'}$, $\epsilon_{g2s'}$, $S_{2\rho'}$, and $S_{2s'}$ are obtained by solving (61) and (62) iteratively. A suggested scheme for the iteration is to initially assign $\epsilon_{g2\rho'} = \epsilon_{g2s'} = \epsilon_{g2}$ then use (61) to find $S_{2\rho'}$ and $S_{2s'}$ which are subsequently employed to recalculate $\epsilon_{g2\rho'}$ and $\epsilon_{g2s'}$ with (62) rearranged as

$$\epsilon_{g2\rho'} = \epsilon_{g2} + \frac{f_{g2}(\epsilon_{g2} - \epsilon_{g2\rho'})}{(1 - f_{g2})} \frac{\epsilon_0 + S_{2\rho'}(\epsilon_{g2} - \epsilon_{g2\rho'})}{\epsilon_0 + S_{2\rho'}(\epsilon_{g2} - \epsilon_{g2\rho'})} \quad (63a)$$

$$\epsilon_{g2s'} = \epsilon_{g2} + \frac{f_{g2}(\epsilon_{g2} - \epsilon_{g2s'})}{(1 - f_{g2})} \frac{\epsilon_0 + S_{2s'}(\epsilon_{g2} - \epsilon_{g2s'})}{\epsilon_0 + S_{2s'}(\epsilon_{g2} - \epsilon_{g2s'})} \quad (63b)$$

The iteration is repeated until a required accuracy is achieved. Equation (63) indicates that small fractional volume f_{g2} leads to a fast convergence rate for the iterative solution and explains why the background permittivity has been chosen as the initial value for the auxiliary permittivities. After $\epsilon_{g2\rho'}$, $\epsilon_{g2s'}$, $S_{2\rho'}$, and $S_{2s'}$ are computed, variance $\delta\epsilon_{2\rho'}$, $\delta\epsilon_{2s'}$, and $\delta\epsilon_{2c'}$ are found from (55)

$$\delta\epsilon_{2\rho'} = \left[\frac{\epsilon_{g2} - \epsilon_{g2\rho'}}{\epsilon_0 + S_{2\rho'}(\epsilon_{g2} - \epsilon_{g2\rho'})} \right]^2 (1 - f_{g2}) + \left[\frac{\epsilon_{g2} - \epsilon_{g2\rho'}}{\epsilon_0 + S_{2\rho'}(\epsilon_{g2} - \epsilon_{g2\rho'})} \right]^2 f_{g2} \quad (64a)$$

$$\delta\epsilon_{2s'} = \left[\frac{\epsilon_{g2} - \epsilon_{g2s'}}{\epsilon_0 + S_{2s'}(\epsilon_{g2} - \epsilon_{g2s'})} \right]^2 (1 - f_{g2}) + \left[\frac{\epsilon_{g2} - \epsilon_{g2s'}}{\epsilon_0 + S_{2s'}(\epsilon_{g2} - \epsilon_{g2s'})} \right]^2 f_{g2} \quad (64b)$$

In summary of the anisotropic case, the anisotropic effective permittivity tensor is calculated in the primed coordinate system of Fig. 1.3.2 with (56) where $\epsilon_{2\rho'}$, $\epsilon_{2z'}$, $S_{2\rho'}$, and $S_{2z'}$ are obtained by iterating (63) and (61) and then $\delta_{2\rho'}$, $\delta_{2z'}$, $\delta_{2\rho'}$, $I_{\rho'}$, and $I_{z'}$ are determined by (64a-c), (60), and (59), respectively. To transform the result into the unprimed coordinate system, the following operation is applied

$$\bar{\epsilon}_{eff} = \bar{T}_{\psi} \cdot \bar{\epsilon}_{eff}(\hat{r}') \cdot \bar{T}_{\psi}^{-1} \quad \text{with} \quad \bar{T}_{\psi} = \begin{bmatrix} 1 & 0 & 0 \\ 0 & \cos \psi & \sin \psi \\ 0 & -\sin \psi & \cos \psi \end{bmatrix} \quad (65)$$

where \bar{T}_{ψ} is the transformation matrix which rotates a vector by angle ψ from the primed coordinates to the unprimed coordinates. After the rotation, the anisotropic effective permittivity, which is a symmetric tensor in the $(\hat{x}, \hat{y}, \hat{z})$ system, is related to tilt angle ψ by

$$\bar{\epsilon}_{eff} = \begin{bmatrix} \epsilon_{eff2xx} & 0 & 0 \\ 0 & \epsilon_{eff2yy} & \epsilon_{eff2yz} \\ 0 & \epsilon_{eff2yz} & \epsilon_{eff2zz} \end{bmatrix} \quad (66a)$$

$$\begin{aligned} \epsilon_{eff2xx} &= \epsilon_{eff2\rho'} & \epsilon_{eff2yz} &= \epsilon_{eff2z\rho'} \\ \epsilon_{eff2yy} &= (\epsilon_{eff2\rho'} - \epsilon_{eff2z\rho'}) \cos \psi \sin \psi & \\ \epsilon_{eff2yy} &= \epsilon_{eff2\rho'} \cos^2 \psi + \epsilon_{eff2z\rho'} \sin^2 \psi & \\ \epsilon_{eff2zz} &= \epsilon_{eff2\rho'} \sin^2 \psi + \epsilon_{eff2z\rho'} \cos^2 \psi & \end{aligned} \quad (66b)$$

In this subsection, the effective permittivities of the isotropic and anisotropic random media have been derived. It is necessary to note that the principal branch cut of square root \sqrt{w} for complex number w has been chosen such that $-\pi < \arg w \leq \pi$ where $\arg w$ denotes the argument of w . Also, inverse tangent $\tan^{-1} w$ for complex number w is determined by

$$\tan^{-1} w = \frac{1}{2i} \ln w_a \quad \text{with} \quad w_a = \frac{1+iw}{1-iw} \quad (67)$$

where $\ln w_a$ is the natural logarithm of w_a on the principal Riemann sheet $|w_a| > 0$ and $-\pi < \arg w_a < \pi$.

Auxiliary permittivity $\epsilon_{\rho 1}$ of the isotropic random medium as obtained is the same as the Polder and van Santen mixing formula [41];

thus, auxiliary permittivity $\epsilon_{\rho 2}$ of the anisotropic random medium obtained in a similar manner can be considered as a more generalized version. Related to the auxiliary permittivity and the shape of the exclusion volume, the dyadic coefficient of the Dirac delta part in the Green's function is also derivable with a surface integration over a limiting equicorrelation surface and proved to satisfy the following condition [42]

$$2 \frac{\epsilon_{\rho \rho}}{\epsilon_0} S_{\rho} + \frac{\epsilon_{zz}}{\epsilon_0} S_z = 1 \quad (68)$$

where $\epsilon_{\rho \rho} = \epsilon_{\rho z}$ and $S_{\rho} = S_z = S_1$ for the isotropic case or $\epsilon_{\rho \rho} = \epsilon_{\rho 2\rho'}$, $\epsilon_{zz} = \epsilon_{2z'}$, $S_{\rho} = S_{2\rho'}$, and $S_z = S_{2z'}$ for the anisotropic case.

As mentioned earlier, the anisotropic effective permittivity becomes isotropic when the spheroidal correlation function is reduced to spherical. This is the case when $\ell_{2\rho'}$ approaches $\ell_{2z'}$ and it is trivial to show that

$$\lim_{\ell_{2\rho'} \rightarrow \ell_{2z'}} S_{2\rho'} = \lim_{\ell_{2\rho'} \rightarrow \ell_{2z'}} S_{2z'} \quad (69a)$$

$$\lim_{\ell_{2\rho'} \rightarrow \ell_{2z'}} \epsilon_{\rho 2\rho'} = \lim_{\ell_{2\rho'} \rightarrow \ell_{2z'}} \epsilon_{\rho 2z'} \quad (69b)$$

The limit (69a) has the form of (45) and consequently the variances in (64) have the same limit of the form (48) since $\epsilon_{\rho 2\rho'}$ and $\epsilon_{2z'}$ approach to the same limit as indicated in (69b). To prove that $I_{\rho'}$ and $I_{z'}$ have the same expression of the form (44) as $\ell_{2\rho'} \rightarrow \ell_{2z'}$, attention must be given to the above chosen branch cuts. For instance, $\sqrt{-\zeta}$ is $-i\sqrt{\zeta}$ instead of $i\sqrt{\zeta}$; this is because $w = -\zeta \rightarrow -k_{\rho 2\rho'}^2 \ell_{2z'}^2$ as $\ell_{2\rho'} \rightarrow \ell_{2z'}$ and w is thus in the third quadrant of the complex w plane so that \sqrt{w} is consequently in the fourth quadrant due to the chosen branch cut of the square root. The value of $\sqrt{-\zeta}$ so obtained is identical to $-i\sqrt{\zeta}$ and not to $i\sqrt{\zeta}$. The proof is then straight forward.

In deriving the effective permittivities, the low-frequency and the bilocal approximations have been used. The low-frequency approximation is valid when $k_{\rho 1} \ell_1 \ll 1$ for the isotropic case or $k_{\rho 2\rho'} \ell_{2\rho'} \ll 1$ and $k_{\rho 2\rho'} \ell_{2z'} \ll 1$ for the anisotropic case. This approximation results in the ignorance of the spatial dispersive characteristics of the inhomogeneous media. In this case, the bilocal approximation further requires that $|\bar{\epsilon}_{eff}|_{\text{lim}} \ll 1$ with $n = 1$ for the isotropic or $n = 2$ for the anisotropic case. This condition allows more simplification on

1. Polarimetric Remote Sensing

the permittivity results (41) and (56) where the denominators can be approximated to be unity.

When the low-frequency condition is removed, the spatial dispersion of the random media is manifested in the dependence of the effective scatterers on wave vector \vec{k} as

$$[\bar{\epsilon}_{eff}(\vec{k})]_{jm} = \sum_{k,j'} \Gamma_{\alpha j'jm}^{(0)} \left\{ \frac{k_0^2}{2} \int_{-\infty}^{\infty} d\vec{k}' [\bar{\epsilon}_{gm}(\vec{k}')]_{kl} \cdot [\bar{\Phi}_{\ell n}(\vec{k}' - \vec{k}) + \bar{\Phi}_{\ell n}(\vec{k} + \vec{k})] + [\bar{S}_n]_{kl} \right\} \quad (70)$$

The effective permittivities are still calculated with (36) or (53) with the effective scatterer (70) replacing the low-frequency version. In this case, the bilocal approximation is valid when $|\bar{\epsilon}_{eff}(\vec{k})|_{jm} \ll 1$. From (36), (53), and (70), it is observed that the effective permittivities are even functions of wave vector \vec{k} and can be expressed with symmetric tensors. The random media under consideration are therefore reciprocal as physically expected. Besides the above approximation, the use of the Fourier transform in this subsection implies that the media are unbounded in the calculations of the effective permittivities. In the next subsection, the effective permittivities is used to obtain the dyadic Green's function of the layer random medium which accounts for the multiple reflections, refractions, and transmissions at the medium interfaces.

c. Dyadic Green's Functions

In this subsection, the mean dyadic Green's Functions (DGFs), needed in the calculation of the scattered field correlation (32), is presented for the three-layer configuration. Rather than directly calculating $\langle \bar{G}_{0n}(\vec{r}, \vec{r}_0) \rangle$ for observation point \vec{r} in region 0 and source point \vec{r}_0 in region n , $\langle \bar{G}_{n0}(\vec{r}, \vec{r}_0) \rangle$ are obtained for the source in region 0 and the observation in region n and the needed DGFs are then deduced from the symmetric relation [46]

$$\langle \bar{G}_{mn}(\vec{r}, \vec{r}_0) \rangle = \langle \bar{G}_{nm}^T(\vec{r}_0, \vec{r}) \rangle \quad (71)$$

In this method [23,24,36], vector wave equations are first written for the DGFs subjected to the appropriate boundary conditions at the interfaces and radiation conditions at infinite distances above and below

1.3 Random Medium Model

the interfaces. Next, the Cartesian coordinate systems corresponding to upgoing and downgoing waves in the layers are shown. The DGFs can then be solved in terms of transmission and reflection coefficients for the upgoing and downgoing waves. This procedure for obtaining the DGFs are detailed in the subsequent paragraphs.

Consider the source in region 0 at \vec{r}_0 above interface $z = 0$. The DGFs observed in region $n = 0, 1, 2, 3$ are governed by vector wave equations as follows

$$\nabla \times \nabla \times \langle \bar{G}_{00}(\vec{r}, \vec{r}_0) \rangle - k_0^2 \cdot \langle \bar{G}_{00}(\vec{r}, \vec{r}_0) \rangle = \delta(\vec{r} - \vec{r}_0) \bar{I}, \quad z \geq 0 \quad (72a)$$

$$\nabla \times \nabla \times \langle \bar{G}_{10}(\vec{r}, \vec{r}_0) \rangle - k_0^2 \frac{\epsilon_{d11}}{\epsilon_0} \cdot \langle \bar{G}_{10}(\vec{r}, \vec{r}_0) \rangle = 0, \quad 0 \geq z \geq -d_1 \quad (72b)$$

$$\nabla \times \nabla \times \langle \bar{G}_{20}(\vec{r}, \vec{r}_0) \rangle - k_0^2 \frac{\epsilon_{d12}}{\epsilon_0} \cdot \langle \bar{G}_{20}(\vec{r}, \vec{r}_0) \rangle = 0, \quad -d_1 \geq z \geq -d_2 \quad (72c)$$

$$\nabla \times \nabla \times \langle \bar{G}_{30}(\vec{r}, \vec{r}_0) \rangle - k_0^2 \frac{\epsilon_{d3}}{\epsilon_0} \cdot \langle \bar{G}_{30}(\vec{r}, \vec{r}_0) \rangle = 0, \quad -d_2 \geq z \quad (72d)$$

The boundary conditions call for the continuity of $\hat{z} \times \langle \bar{G}_{n0} \rangle$ and $\hat{z} \times \nabla \times \langle \bar{G}_{n0} \rangle$ at the interfaces where the tangential electric and magnetic fields are continuous, respectively. The boundary conditions can be written explicitly as

$$\left. \begin{aligned} \hat{z} \times \langle \bar{G}_{00}(\vec{r}, \vec{r}_0) \rangle &= \hat{z} \times \langle \bar{G}_{10}(\vec{r}, \vec{r}_0) \rangle \\ \hat{z} \times \nabla \times \langle \bar{G}_{00}(\vec{r}, \vec{r}_0) \rangle &= \hat{z} \times \nabla \times \langle \bar{G}_{10}(\vec{r}, \vec{r}_0) \rangle \end{aligned} \right\} \text{ at } z = 0 \quad (73a)$$

$$\left. \begin{aligned} \hat{z} \times \langle \bar{G}_{10}(\vec{r}, \vec{r}_0) \rangle &= \hat{z} \times \langle \bar{G}_{20}(\vec{r}, \vec{r}_0) \rangle \\ \hat{z} \times \nabla \times \langle \bar{G}_{10}(\vec{r}, \vec{r}_0) \rangle &= \hat{z} \times \nabla \times \langle \bar{G}_{20}(\vec{r}, \vec{r}_0) \rangle \end{aligned} \right\} \text{ at } z = -d_1 \quad (73b)$$

$$\left. \begin{aligned} \hat{z} \times \langle \bar{G}_{20}(\vec{r}, \vec{r}_0) \rangle &= \hat{z} \times \langle \bar{G}_{30}(\vec{r}, \vec{r}_0) \rangle \\ \hat{z} \times \nabla \times \langle \bar{G}_{20}(\vec{r}, \vec{r}_0) \rangle &= \hat{z} \times \nabla \times \langle \bar{G}_{30}(\vec{r}, \vec{r}_0) \rangle \end{aligned} \right\} \text{ at } z = -d_2 \quad (73c)$$

To express the solutions for the DGFs physically in terms upgoing of and downgoing waves, Cartesian coordinate systems are defined to coincide with directions of electromagnetic fields and Poynting vectors. In the same manner as (1), coordinate system $(\hat{h}(k_{nz}^w), \hat{v}(k_{nz}^w), \hat{k}_n^w)$, corresponding to upgoing ($w = u$) and downgoing ($w = d$) waves in the isotropic media ($n = 0, 1, 3$), are determined by

$$\hat{h}(k_{nz}^w) = \frac{\hat{z} \times \hat{k}_n^w}{|\hat{z} \times \hat{k}_n^w|}, \quad \hat{v}(k_{nz}^w) = \frac{\hat{k}_n^w \times \hat{h}(k_{nz}^w)}{|\hat{k}_n^w \times \hat{h}(k_{nz}^w)|} \quad (74a)$$

$$\hat{k}_n^w = \bar{k}_n^w / |\bar{k}_n^w| \quad \text{with} \quad \bar{k}_n^w = k_x \hat{x} + k_y \hat{y} + k_{nz} \hat{z} \quad (74b)$$

where the z components of the wave vectors are related as follows

$$k_{nz}^w = -k_{nz}^d = k_{nz} = \sqrt{k_x^2 - k_y^2 - k_z^2}, \quad \text{with} \quad k_n^2 = \begin{cases} \omega^2 \mu \epsilon_n, & n=0, 3 \\ \omega^2 \mu \epsilon_{eff1}, & n=1 \end{cases} \quad (75)$$

For the effective anisotropic medium ($n=2$) with optic axis \hat{z}' , the ordinary and extraordinary waves propagating in the upgoing and downgoing directions call for four different coordinate systems. Corresponding to the ordinary waves, coordinate system $(\hat{o}(k_{2z}^w), \hat{e}(k_{2z}^w), \hat{k}_2^w)$ are defined by

$$\hat{o}(k_{2z}^w) = \frac{\hat{z}' \times \bar{k}_2^w}{|\hat{z}' \times \bar{k}_2^w|}, \quad \hat{e}(k_{2z}^w) = \frac{\bar{k}_2^w \times \hat{o}(k_{2z}^w)}{|\bar{k}_2^w \times \hat{o}(k_{2z}^w)|} \quad (76a)$$

$$\hat{k}_2^w = \bar{k}_2^w / |\bar{k}_2^w| \quad \text{with} \quad \bar{k}_2^w = k_x \hat{x} + k_y \hat{y} + k_{2z}^w \hat{z} \quad (76b)$$

where the z components of the ordinary upgoing ($w=ou$) and the ordinary downgoing ($w=od$) wave vectors are

$$k_{2z}^{ow} = -k_{2z}^{od} = k_{2z} = \sqrt{k_x^2 - k_y^2} \quad \text{with} \quad k_2^2 = \omega^2 \mu \epsilon_{eff2ss} \quad (77)$$

Corresponding to the extraordinary waves in the anisotropic medium, coordinate system $(\hat{o}(k_{2z}^w), \hat{e}(k_{2z}^w), \hat{s}_2^w)$ are defined by

$$\hat{o}(k_{2z}^w) = \frac{\hat{z}' \times \bar{k}_2^w}{|\hat{z}' \times \bar{k}_2^w|}, \quad \hat{e}(k_{2z}^w) = \frac{\bar{s}_2^w \times \hat{o}(k_{2z}^w)}{|\bar{s}_2^w \times \hat{o}(k_{2z}^w)|}, \quad \hat{s}_2^w = \bar{s}_2^w / |\bar{s}_2^w| \quad (78)$$

where the extraordinary upgoing ($w=eu$) and the extraordinary downgoing ($w=ed$) wave vectors are determined by

$$\bar{k}_2^w = k_x \hat{x} + k_y \hat{y} + k_{2z}^w \hat{z} \quad \text{with} \quad w = eu, ed \quad (79a)$$

$$k_{2z}^{ow} = -\frac{\epsilon_{eff2ss} k_y + \frac{1}{\epsilon_{eff2ss}}}{\epsilon_{eff2ss}} \cdot \sqrt{k_x^2 \epsilon_{eff2ss} \epsilon_{eff2ss} - k_y^2 \epsilon_{eff2ss} \epsilon_{eff2ss} - k_y^2 \epsilon_{eff2ss} \epsilon_{eff2ss}} \quad (79b)$$

$$k_{2z}^{od} = -\frac{\epsilon_{eff2ss} k_y - \frac{1}{\epsilon_{eff2ss}}}{\epsilon_{eff2ss}} \cdot \sqrt{k_x^2 \epsilon_{eff2ss} \epsilon_{eff2ss} - k_y^2 \epsilon_{eff2ss} \epsilon_{eff2ss} - k_y^2 \epsilon_{eff2ss} \epsilon_{eff2ss}} \quad (79c)$$

and unit ray vector \hat{s}_2^w [23] of the extraordinary waves are parallel to

$$\bar{s}_2^w = \bar{\epsilon}_{eff2} \cdot \bar{k}_2^w = \epsilon_{eff2ss} k_x \hat{x} + (\epsilon_{eff2yy} k_y + \epsilon_{eff2yz} k_{2z}^w) \hat{y} + (\epsilon_{eff2zy} k_y + \epsilon_{eff2zz} k_{2z}^w) \hat{z}, \quad \text{with} \quad w = eu, ed \quad (80)$$

The above definitions of the unit vectors are physically descriptive. Unit vector \hat{h} is parallel to TE , \hat{v} to TM , \hat{o} to ordinary, and \hat{e} to extraordinary wave polarizations. For wave vector \bar{k}_n^w , all the lateral components are set identical to $\bar{k}_p = \hat{x} k_x + \hat{y} k_y$ in accordance to the phase matching condition and the z components are calculated from dispersion relations. Poynting vectors are all in the directions of wave vectors except for extraordinary waves whose Poynting vectors are in the directions of \bar{s}_2^w given by (80).

With the defined unit vectors, solutions for the DGFs have the following forms expressed in terms of upgoing and downgoing waves as

$$\begin{aligned} \langle \bar{G}_{00}(\bar{r}, \bar{r}_s) \rangle &= \frac{i}{8\pi^2} \int_{-\infty}^{\infty} dk_{0z} \int_{-\infty}^{\infty} dk_y \frac{e^{-i\bar{k}_0^d \cdot \bar{r}}}{k_{0z}} \\ &\left\{ \hat{h}(k_{0z}^d) e^{i\bar{k}_0^d \cdot \bar{r}} \hat{h}(k_{0z}^d) \right. \\ &+ \left[R_{hh}(\bar{k}_p) \hat{h}(k_{0z}^u) e^{i\bar{k}_0^u \cdot \bar{r}} + R_{hu}(\bar{k}_p) \hat{v}(k_{0z}^u) e^{i\bar{k}_0^u \cdot \bar{r}} \right] \hat{h}(k_{0z}^d) \\ &+ \hat{v}(k_{0z}^d) e^{i\bar{k}_0^d \cdot \bar{r}} \hat{v}(k_{0z}^d) \\ &+ \left[R_{vh}(\bar{k}_p) \hat{h}(k_{0z}^u) e^{i\bar{k}_0^u \cdot \bar{r}} + R_{vv}(\bar{k}_p) \hat{v}(k_{0z}^u) e^{i\bar{k}_0^u \cdot \bar{r}} \right] \hat{v}(k_{0z}^d) \left. \right\} \\ &z_s > z \geq 0 \end{aligned} \quad (81a)$$

$$\begin{aligned} \langle \bar{G}_{10}(\bar{r}, \bar{r}_s) \rangle &= \frac{i}{8\pi^2} \int_{-\infty}^{\infty} dk_{0z} \int_{-\infty}^{\infty} dk_y \frac{e^{-i\bar{k}_0^d \cdot \bar{r}}}{k_{0z}} \\ &\left\{ \left[D_{1hh}(\bar{k}_p) \hat{h}(k_{1z}^d) e^{i\bar{k}_1^d \cdot \bar{r}} + D_{1hu}(\bar{k}_p) \hat{v}(k_{1z}^d) e^{i\bar{k}_1^d \cdot \bar{r}} \right] \hat{h}(k_{0z}^d) \right. \\ &+ \left[U_{1hh}(\bar{k}_p) \hat{h}(k_{1z}^u) e^{i\bar{k}_1^u \cdot \bar{r}} + U_{1hu}(\bar{k}_p) \hat{v}(k_{1z}^u) e^{i\bar{k}_1^u \cdot \bar{r}} \right] \hat{h}(k_{0z}^d) \\ &+ \left[D_{1vh}(\bar{k}_p) \hat{h}(k_{1z}^d) e^{i\bar{k}_1^d \cdot \bar{r}} + D_{1vu}(\bar{k}_p) \hat{v}(k_{1z}^d) e^{i\bar{k}_1^d \cdot \bar{r}} \right] \hat{v}(k_{0z}^d) \left. \right\} \end{aligned}$$

$$+ \left[U_{1hh}(\bar{k}_p) \hat{h}(k_{1z}^d) e^{i\bar{k}_1^u \cdot \bar{r}} + U_{1vv}(\bar{k}_p) \hat{v}(k_{1z}^u) e^{i\bar{k}_1^u \cdot \bar{r}} \right] \hat{v}(k_{0z}^d) \} \quad 0 \geq z \geq -d_1 \quad (81b)$$

$$\begin{aligned} \langle \bar{G}_{30}(\bar{r}, \bar{r}_0) \rangle = & \frac{i}{8\pi^2} \int_{-\infty}^{\infty} dk_x \int_{-\infty}^{\infty} dk_y \frac{e^{-i\bar{k}_0^d \cdot \bar{r}_0}}{k_{0z}} \\ & \left\{ \left[D_{2hh}(\bar{k}_p) \hat{h}(k_{2z}^d) e^{i\bar{k}_2^d \cdot \bar{r}} + D_{2hv}(\bar{k}_p) \hat{v}(k_{2z}^d) e^{i\bar{k}_2^d \cdot \bar{r}} \right] \hat{h}(k_{0z}^d) \right. \\ & + \left[U_{2hh}(\bar{k}_p) \hat{h}(k_{2z}^u) e^{i\bar{k}_2^u \cdot \bar{r}} + U_{2hv}(\bar{k}_p) \hat{v}(k_{2z}^u) e^{i\bar{k}_2^u \cdot \bar{r}} \right] \hat{h}(k_{0z}^d) \\ & + \left[D_{2vh}(\bar{k}_p) \hat{h}(k_{2z}^d) e^{i\bar{k}_2^d \cdot \bar{r}} + D_{2vv}(\bar{k}_p) \hat{v}(k_{2z}^d) e^{i\bar{k}_2^d \cdot \bar{r}} \right] \hat{v}(k_{0z}^d) \\ & \left. + \left[U_{2vh}(\bar{k}_p) \hat{h}(k_{2z}^u) e^{i\bar{k}_2^u \cdot \bar{r}} + U_{2vv}(\bar{k}_p) \hat{v}(k_{2z}^u) e^{i\bar{k}_2^u \cdot \bar{r}} \right] \hat{v}(k_{0z}^d) \right\} \quad -d_1 \geq z \geq -d_2 \quad (81c) \end{aligned}$$

$$\begin{aligned} \langle \bar{G}_{30}(\bar{r}, \bar{r}_0) \rangle = & \frac{i}{8\pi^2} \int_{-\infty}^{\infty} dk_x \int_{-\infty}^{\infty} dk_y \frac{e^{-i\bar{k}_0^d \cdot \bar{r}_0}}{k_{0z}} \\ & \left\{ \left[T_{1hh}(\bar{k}_p) \hat{h}(k_{1z}^d) e^{i\bar{k}_1^d \cdot \bar{r}} + T_{1hv}(\bar{k}_p) \hat{v}(k_{1z}^d) e^{i\bar{k}_1^d \cdot \bar{r}} \right] \hat{h}(k_{0z}^d) \right. \\ & \left. + \left[T_{1vh}(\bar{k}_p) \hat{h}(k_{1z}^d) e^{i\bar{k}_1^d \cdot \bar{r}} + T_{1vv}(\bar{k}_p) \hat{v}(k_{1z}^d) e^{i\bar{k}_1^d \cdot \bar{r}} \right] \hat{v}(k_{0z}^d) \right\} \quad -d_2 \geq z \quad (81d) \end{aligned}$$

DGF coefficient R 's, U 's, D 's, and T 's can be calculated directly from the boundary conditions in (73). To facilitate the calculation and the interpretation, the matrix method [23] is used to express the DGF coefficients in terms of Fresnel reflection and transmission coefficients. These expressions are determined by considering amplitude vector \bar{A}_n of upgoing waves and \bar{B}_n of downgoing waves in region $n = 0, 1, 2, 3$. In this method, amplitude vectors of waves propagating away and toward each interface as shown in Fig. 1.3.3 are related with matrix equations

$$\begin{bmatrix} \bar{A}_0 \\ \bar{B}_1 \end{bmatrix} = \begin{bmatrix} \bar{R}_{01} & \bar{T}_{10} \\ \bar{T}_{01} & \bar{R}_{10} \end{bmatrix} \cdot \begin{bmatrix} \bar{B}_0 \\ \bar{A}_1 \end{bmatrix} \quad (82a)$$

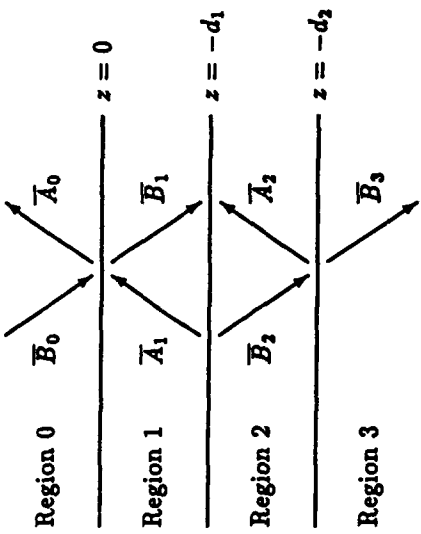


Figure 1.3.3 Amplitude vector \bar{A}_n are for upgoing waves, \bar{B}_n are for downgoing waves, and the arrows represent the propagation directions.

$$\begin{bmatrix} \bar{A}_1 \\ \bar{B}_2 \end{bmatrix} = \begin{bmatrix} \bar{R}_{12} & \bar{T}_{21} \\ \bar{T}_{12} & \bar{R}_{21} \end{bmatrix} \cdot \begin{bmatrix} \bar{B}_1 \\ \bar{A}_2 \end{bmatrix} \quad (82b)$$

$$\begin{bmatrix} \bar{A}_2 \\ \bar{B}_3 \end{bmatrix} = \begin{bmatrix} \bar{R}_{23} \\ \bar{T}_{33} \end{bmatrix} \cdot \bar{B}_3 \quad (82c)$$

Observed from (81), the amplitude vectors are also connected to incident amplitude vector \bar{B}_0 by

$$\bar{A}_0 \equiv \bar{R}_0 \cdot \bar{B}_0 = \begin{bmatrix} R_{hh}(\bar{k}_p) & R_{vh}(\bar{k}_p) \\ R_{hv}(\bar{k}_p) & R_{vv}(\bar{k}_p) \end{bmatrix} \cdot \bar{B}_0 \quad (83a)$$

$$\bar{B}_1 \equiv \bar{D}_1 \cdot \bar{B}_0 = \begin{bmatrix} D_{1hh}(\bar{k}_p) & D_{1vh}(\bar{k}_p) \\ D_{1hv}(\bar{k}_p) & D_{1vv}(\bar{k}_p) \end{bmatrix} \cdot \bar{B}_0 \quad (83b)$$

$$\bar{A}_1 \equiv \bar{U}_1 \cdot \bar{B}_0 = \begin{bmatrix} U_{1hh}(\bar{k}_p) & U_{1vh}(\bar{k}_p) \\ U_{1hv}(\bar{k}_p) & U_{1vv}(\bar{k}_p) \end{bmatrix} \cdot \bar{B}_0 \quad (83c)$$

$$\bar{B}_2 \equiv \bar{D}_2 \cdot \bar{B}_0 = \begin{bmatrix} D_{2hh}(\bar{k}_p) & D_{2vh}(\bar{k}_p) \\ D_{2hv}(\bar{k}_p) & D_{2vv}(\bar{k}_p) \end{bmatrix} \cdot \bar{B}_0 \quad (83d)$$

$$\bar{A}_2 \equiv \bar{U}_2 \cdot \bar{B}_0 = \begin{bmatrix} U_{2hh}(\bar{k}_p) & U_{2vh}(\bar{k}_p) \\ U_{2hv}(\bar{k}_p) & U_{2vv}(\bar{k}_p) \end{bmatrix} \cdot \bar{B}_0 \quad (83e)$$

$$\bar{B}_3 \equiv \bar{T}_3 \cdot \bar{B}_0 = \begin{bmatrix} T_{hh}(\bar{k}_p) & T_{vh}(\bar{k}_p) \\ T_{hv}(\bar{k}_p) & T_{vv}(\bar{k}_p) \end{bmatrix} \cdot \bar{B}_0 \quad (83f)$$

Equation system (82) is readily solved for the downgoing and upgoing amplitude vectors in terms of \bar{B}_0 and the results are then compared to (83) to obtain the following DGF coefficient matrices

$$\bar{R}_0 = \bar{R}_{01} + \bar{T}_{10} \cdot (\bar{R}_{13} + \bar{T}_{31} \cdot \bar{R}_{33} \cdot \bar{T}_{12}) \cdot \bar{D}_1 \quad (84a)$$

$$\bar{D}_1 = [\bar{I} - \bar{R}_{10} \cdot (\bar{R}_{13} + \bar{T}_{31} \cdot \bar{R}_{33} \cdot \bar{T}_{12})]^{-1} \cdot \bar{T}_{01} \quad (84b)$$

$$\bar{U}_1 = [\bar{R}_{13} + \bar{T}_{31} \cdot \bar{R}_{33} \cdot \bar{T}_{12}] \cdot \bar{D}_1 \quad (84c)$$

$$\bar{D}_2 = \bar{T}_{12} \cdot \bar{D}_1 \quad (84d)$$

$$\bar{U}_2 = \bar{R}_{23} \cdot \bar{T}_{12} \cdot \bar{D}_1 \quad (84e)$$

$$\bar{T}_3 = \bar{T}_{23} \cdot \bar{T}_{12} \cdot \bar{D}_1 \quad (84f)$$

where $\bar{T} = (\bar{I} - \bar{R}_{31} \cdot \bar{R}_{23})^{-1}$ and the reflection and transmission matrices are

$$\bar{R}_{01} = \begin{bmatrix} R_{01hh} & 0 \\ 0 & R_{01vv} \end{bmatrix}, \quad \bar{R}_{10} = \begin{bmatrix} R_{10hh} & 0 \\ 0 & R_{10vv} \end{bmatrix} \quad (85a)$$

$$\bar{T}_{01} = \begin{bmatrix} T_{01hh} & 0 \\ 0 & T_{01vv} \end{bmatrix}, \quad \bar{T}_{10} = \begin{bmatrix} T_{10hh} & 0 \\ 0 & T_{10vv} \end{bmatrix} \quad (85b)$$

$$\bar{R}_{12} = \begin{bmatrix} e^{i2k_{1z}^u d_1} R_{12hh} & e^{i2k_{1z}^u d_1} R_{12vh} \\ e^{i2k_{1z}^u d_1} R_{12hv} & e^{i2k_{1z}^u d_1} R_{12vv} \end{bmatrix} \quad (85c)$$

$$\bar{R}_{21} = \begin{bmatrix} e^{i(k_{2z}^{od} - k_{2z}^{ou})} d_1 R_{21oo} & e^{i(k_{2z}^{od} - k_{2z}^{ou})} d_1 R_{21eo} \\ e^{i(k_{2z}^{od} - k_{2z}^{ou})} d_1 R_{21eo} & e^{i(k_{2z}^{od} - k_{2z}^{ou})} d_1 R_{21ee} \end{bmatrix} \quad (85d)$$

$$\bar{T}_{12} = \begin{bmatrix} e^{i(k_{2z}^{od} - k_{2z}^d)} d_1 T_{12ho} & e^{i(k_{2z}^{od} - k_{2z}^d)} d_1 T_{12vo} \\ e^{i(k_{2z}^{od} - k_{2z}^d)} d_1 T_{12ho} & e^{i(k_{2z}^{od} - k_{2z}^d)} d_1 T_{12vv} \end{bmatrix} \quad (85e)$$

$$\bar{T}_{31} = \begin{bmatrix} e^{i(k_{1z}^u - k_{2z}^{ou})} d_1 T_{31oh} & e^{i(k_{1z}^u - k_{2z}^{ou})} d_1 T_{31ev} \\ e^{i(k_{1z}^u - k_{2z}^{ou})} d_1 T_{31oh} & e^{i(k_{1z}^u - k_{2z}^{ou})} d_1 T_{31ev} \end{bmatrix} \quad (85f)$$

$$\bar{R}_{23} = \begin{bmatrix} e^{i(k_{2z}^{ou} - k_{2z}^{od})} d_2 R_{23oo} & e^{i(k_{2z}^{ou} - k_{2z}^{od})} d_2 R_{23eo} \\ e^{i(k_{2z}^{ou} - k_{2z}^{od})} d_2 R_{23eo} & e^{i(k_{2z}^{ou} - k_{2z}^{od})} d_2 R_{23ee} \end{bmatrix} \quad (85g)$$

$$\bar{T}_{23} = \begin{bmatrix} e^{i(k_{2z}^d - k_{2z}^{od})} d_2 T_{23oh} & e^{i(k_{2z}^d - k_{2z}^{od})} d_2 T_{23ev} \\ e^{i(k_{2z}^d - k_{2z}^{od})} d_2 T_{23oh} & e^{i(k_{2z}^d - k_{2z}^{od})} d_2 T_{23ev} \end{bmatrix} \quad (85h)$$

1.3 Random Medium Model

in which the exponents carry phase factors due to the locations of the interfaces and Fresnel reflection and transmission coefficient R 's and T 's are given in appendix A. The above results vividly describe the physical processes of wave interaction in the layer media. For instance, amplitude vector \bar{B}_2 of downgoing waves in region 2 is spelled out from (83d) and (84d) as

$$\bar{B}_2 = \bar{T} \cdot \bar{T}_{12} \cdot \bar{D}_1 \cdot \bar{B}_0 \quad (86)$$

which can be interpreted as the incident wave \bar{B}_0 from region 0 propagates down into region 1 ($\bar{D}_1 \cdot \bar{B}_0$), transmits through the interface between region 1 and region 2 ($\bar{T}_{12} \cdot \bar{D}_1 \cdot \bar{B}_0$), and multiply reflects between the interfaces of region 2 ($\bar{T} \cdot \bar{T}_{12} \cdot \bar{D}_1 \cdot \bar{B}_0$). This completes the derivation of the DGFs corresponding to the source in region 0 in integral form (81).

For latter calculations of the scattering coefficients involving the effective sources in the scattering regions ($n = 1, 2$), dyadic Green's function ($\bar{G}_{01}(\bar{r}, \bar{r}_s)$) and ($\bar{G}_{02}(\bar{r}, \bar{r}_s)$) need be obtained by applying the symmetry relation (71) requiring the transposition of the corresponding DGFs in the last paragraph and the sign changes of k_x and k_y respectively to $-k_x$ and $-k_y$. After the integrations are carried out with the two-dimensional saddle point method [9,23], the results for the DGFs in the radiation field are

$$\langle \bar{G}_{0n}(\bar{r}, \bar{r}_s) \rangle = \frac{e^{ik_0 r}}{4\pi r} e^{-i\bar{k}_p \cdot \bar{r}} \bar{y}_n(\bar{k}_p, z_s), \quad n = 1, 2 \quad (87)$$

where $\bar{r}_s = \hat{z}z_s + \hat{y}y_s$, and dyadic coefficient $\bar{y}_n(\bar{k}_p, z_s)$ are defined as

$$\begin{aligned} \bar{y}_1(\bar{k}_p, z_s) = & + \hat{h}(k_{0z}^u) \left[D_{1hh}(-\bar{k}_p) \hat{h}(k_{1z}^u) e^{-ik_{1z}^u z_s} - D_{1hv}(-\bar{k}_p) \hat{v}(k_{1z}^u) e^{-ik_{1z}^u z_s} \right] \\ & + \hat{h}(k_{0z}^u) \left[U_{1hh}(-\bar{k}_p) \hat{h}(k_{1z}^d) e^{-ik_{1z}^d z_s} - U_{1hv}(-\bar{k}_p) \hat{v}(k_{1z}^d) e^{-ik_{1z}^d z_s} \right] \\ & - \hat{v}(k_{0z}^u) \left[D_{1vh}(-\bar{k}_p) \hat{h}(k_{1z}^u) e^{-ik_{1z}^u z_s} - D_{1vv}(-\bar{k}_p) \hat{v}(k_{1z}^u) e^{-ik_{1z}^u z_s} \right] \\ & - \hat{v}(k_{0z}^u) \left[U_{1vh}(-\bar{k}_p) \hat{h}(k_{1z}^d) e^{-ik_{1z}^d z_s} - U_{1vv}(-\bar{k}_p) \hat{v}(k_{1z}^d) e^{-ik_{1z}^d z_s} \right] \end{aligned} \quad (88a)$$

$$\begin{aligned}
\vec{F}_2(\vec{k}_p, z_0) \equiv & \\
& + \hat{h}(k_{2z}^u) \left[D_{2ho}(-\vec{k}_p) \hat{o}(k_{2z}^u) e^{-ik_{2z}^u z_0} - D_{2ho}(-\vec{k}_p) \hat{e}(k_{2z}^u) e^{-ik_{2z}^u z_0} \right] \\
& + \hat{h}(k_{2z}^d) \left[U_{2ho}(-\vec{k}_p) \hat{o}(k_{2z}^d) e^{-ik_{2z}^d z_0} - U_{2ho}(-\vec{k}_p) \hat{e}(k_{2z}^d) e^{-ik_{2z}^d z_0} \right] \\
& - \hat{v}(k_{2z}^u) \left[D_{2vo}(-\vec{k}_p) \hat{o}(k_{2z}^u) e^{-ik_{2z}^u z_0} - D_{2vo}(-\vec{k}_p) \hat{e}(k_{2z}^u) e^{-ik_{2z}^u z_0} \right] \\
& - \hat{v}(k_{2z}^d) \left[U_{2vo}(-\vec{k}_p) \hat{o}(k_{2z}^d) e^{-ik_{2z}^d z_0} - U_{2vo}(-\vec{k}_p) \hat{e}(k_{2z}^d) e^{-ik_{2z}^d z_0} \right] \quad (88b)
\end{aligned}$$

In summary, the DGFs are obtained in (88) where all the coefficients are determined by (83-85) and appendix A. With the available DGFs, the scattering coefficients are derived in the next subsection.

d. Scattering Coefficients

The polarimetric backscattering coefficients are defined by (13) based on ensemble averages of scattered fields. As indicated in (32), the averages are calculated with spatial integrations over products of the DGFs, the mean fields, and the correlation functions. The DGFs have been obtained; next shown are the mean field and the correlation functions. The integrations are then carried out to derive the scattering coefficients.

The mean external fields in the scattering regions ($n = 1, 2$) can be approximated as the corresponding homogeneous solutions to the wave equations

$$\nabla \times \nabla \times \langle \vec{F}_n(\vec{r}) \rangle - k_0^2 \frac{\bar{\epsilon}}{\epsilon_0} \langle \vec{F}_n(\vec{r}) \rangle = 0, \quad n = 1, 2 \quad (89)$$

which are solved subjected to the boundary conditions at interface $z = 0, -d_1, -d_2$. For incident field $\vec{E}_{0i} = [\hat{h}(k_{0zi}) \vec{E}_h + \hat{v}(k_{0zi}) \vec{E}_v] e^{ik_{0z} z}$, the mean fields can be written as

$$\langle \vec{F}_n(\vec{r}) \rangle = e^{ik_{0z} z} \vec{P}_n(\vec{k}_p, z), \quad n = 1, 2 \quad (90)$$

where subscript i indicates the incident wave, $\vec{p} = \hat{z}x + \hat{y}y$ is the lateral space, $\vec{k}_p = \hat{z}k_{pz} + \hat{y}k_{py} = k_0(\hat{z} \sin \theta_0 \cos \phi_0 + \hat{y} \sin \theta_0 \sin \phi_0)$ is the lateral component of incident wave vector \vec{k}_{0i} , and polarization vector $\vec{P}_n(\vec{k}_p, z)$ are determined by

1.3 Random Medium Model

$$\begin{aligned}
\vec{P}_1(\vec{k}_p, z) \equiv & \\
& + E_{hi} \left[D_{1hh}(\vec{k}_p) \hat{h}(k_{1zi}^d) e^{ik_{1zi}^d z} + D_{1ho}(\vec{k}_p) \hat{v}(k_{1zi}^d) e^{ik_{1zi}^d z} \right] \\
& + E_{hi} \left[U_{1hh}(\vec{k}_p) \hat{h}(k_{1zi}^u) e^{ik_{1zi}^u z} + U_{1ho}(\vec{k}_p) \hat{v}(k_{1zi}^u) e^{ik_{1zi}^u z} \right] \\
& + E_{vi} \left[D_{1vh}(\vec{k}_p) \hat{h}(k_{1zi}^d) e^{ik_{1zi}^d z} + D_{1vo}(\vec{k}_p) \hat{v}(k_{1zi}^d) e^{ik_{1zi}^d z} \right] \\
& + E_{vi} \left[U_{1vh}(\vec{k}_p) \hat{h}(k_{1zi}^u) e^{ik_{1zi}^u z} + U_{1vo}(\vec{k}_p) \hat{v}(k_{1zi}^u) e^{ik_{1zi}^u z} \right] \quad (91a) \\
\vec{P}_2(\vec{k}_p, z) \equiv & \\
& + E_{hi} \left[D_{2hh}(\vec{k}_p) \hat{o}(k_{2zi}^d) e^{ik_{2zi}^d z} + D_{2ho}(\vec{k}_p) \hat{e}(k_{2zi}^d) e^{ik_{2zi}^d z} \right] \\
& + E_{hi} \left[U_{2hh}(\vec{k}_p) \hat{o}(k_{2zi}^u) e^{ik_{2zi}^u z} + U_{2ho}(\vec{k}_p) \hat{e}(k_{2zi}^u) e^{ik_{2zi}^u z} \right] \\
& + E_{vi} \left[D_{2vh}(\vec{k}_p) \hat{o}(k_{2zi}^d) e^{ik_{2zi}^d z} + D_{2vo}(\vec{k}_p) \hat{e}(k_{2zi}^d) e^{ik_{2zi}^d z} \right] \\
& + E_{vi} \left[U_{2vh}(\vec{k}_p) \hat{o}(k_{2zi}^u) e^{ik_{2zi}^u z} + U_{2vo}(\vec{k}_p) \hat{e}(k_{2zi}^u) e^{ik_{2zi}^u z} \right] \quad (91b)
\end{aligned}$$

with z components of the wave vectors defined in the same manner as (75), (77), and (79b,c) by changing k_{nz}^u, k_{nz}^d , and k_y respectively to k_{nz}^u, k_{nz}^d , and k_{py} .

The correlation functions are defined by (33) in the spatial domain. To facilitate the integration of (32), Fourier transforms of the correlation functions are introduced for the statistically homogeneous scattering media under consideration

$$C_{\ell n j k m}(\vec{r}_n, \vec{r}_n) = \int_{-\infty}^{\infty} d\vec{\beta} \Phi_{n j k m}(\vec{\beta}) e^{-i\vec{\beta} \cdot (\vec{r}_n - \vec{r}_n)}, \quad n = 1, 2 \quad (92)$$

For the isotropic random medium ($n = 1$), the non-zero elements of spectral density $\Phi_{1 j k m}(\vec{\beta})$ are simply

$$\Phi_1(\vec{\beta}) = \Phi_{1 j j m m}(\vec{\beta}) = \delta_1 \Phi_{\ell 1}(\vec{\beta}) \quad (93)$$

where $\Phi_{\ell 1}(\vec{\beta})$ is defined as in (39) and functionally given by (43b) in conformity with the correlation function used to find the isotropic effective permittivity. For a two-constituent medium, variance δ_1 is

$$\delta_1 = 9 \left| \frac{\epsilon_1}{\epsilon_0} \right|^2 \left[\left| \frac{\epsilon_1 - \epsilon_2}{\epsilon_1 + 2\epsilon_2} \right|^2 (1 - f_1) + \left| \frac{\epsilon_1 - \epsilon_2}{\epsilon_1 + 2\epsilon_2} \right|^2 f_1 \right] \quad (94)$$

For the anisotropic random medium ($n = 2$), the correlation functions (92) specified in the untilted coordinate system $(\hat{x}, \hat{y}, \hat{z})$ are derived by applying the rotation transformation \bar{T}_ψ on scatterer $\bar{\xi}_2(\vec{r}_2)$ in the untilted coordinate system $(\hat{x}', \hat{y}', \hat{z}')$ so that

$$\bar{\xi}_2(\vec{r}_2) = \bar{T}_\psi \cdot \bar{\xi}_2(\vec{r}_2') \cdot \bar{T}_\psi^{-1} = \begin{bmatrix} \xi_{2xx}(\vec{r}_2) & 0 & 0 \\ 0 & \xi_{2yy}(\vec{r}_2) & \xi_{2yz}(\vec{r}_2) \\ 0 & \xi_{2zy}(\vec{r}_2) & \xi_{2zz}(\vec{r}_2) \end{bmatrix} \quad (95)$$

where the elements of $\bar{\xi}_2(\vec{r}_2)$ have the form of (66b) with $\omega/2$ replaced by ξ_2 . The scatterer elements in the untilted coordinates are then used in (33) to find the anisotropic correlation functions whose spectral densities can be obtained from the following spectral densities defined in the tilted coordinates as

$$\Phi_{2r'}(\vec{\beta}) = \Phi_{2r'r'r'}(\vec{\beta}) = \delta_{2r'} \Phi_{\xi_2}(\vec{\beta}) \quad (96a)$$

$$\Phi_{2r'}(\vec{\beta}) = \Phi_{2r'r'r'}(\vec{\beta}) = \delta_{2r'} \Phi_{\xi_2}(\vec{\beta}) \quad (96b)$$

$$\Phi_{2r'}(\vec{\beta}) = \Phi_{2r'r'r'}(\vec{\beta}) = \delta_{2r'} \Phi_{\xi_2}(\vec{\beta}) \quad (96c)$$

where $\Phi_{\xi_2}(\vec{\beta})$ is functionally determined by (58b) in conformity with the correlation function used to calculate the anisotropic effective permittivity. For the two-constituent anisotropic random medium, the variances in (96) are

$$\delta_{2r'} = \left| \frac{\epsilon_{23} - \epsilon_{22r'}}{\epsilon_0 + S_{2r'}(\epsilon_{23} - \epsilon_{22r'})} \right|^2 (1 - f_{23}) + \left| \frac{\epsilon_{23} - \epsilon_{22r'}}{\epsilon_0 + S_{2r'}(\epsilon_{23} - \epsilon_{22r'})} \right|^2 f_{23} \quad (97a)$$

$$\delta_{2r'} = \left| \frac{\epsilon_{23} - \epsilon_{22r'}}{\epsilon_0 + S_{2r'}(\epsilon_{23} - \epsilon_{22r'})} \right|^2 (1 - f_{23}) + \left| \frac{\epsilon_{23} - \epsilon_{22r'}}{\epsilon_0 + S_{2r'}(\epsilon_{23} - \epsilon_{22r'})} \right|^2 f_{23} \quad (97b)$$

$$\delta_{2r'} = \left[\frac{\epsilon_{23} - \epsilon_{22r'}}{\epsilon_0 + S_{2r'}(\epsilon_{23} - \epsilon_{22r'})} \right] \left[\frac{\epsilon_{23} - \epsilon_{22r'}}{\epsilon_0 + S_{2r'}(\epsilon_{23} - \epsilon_{22r'})} \right]^* (1 - f_{23}) + \left[\frac{\epsilon_{23} - \epsilon_{22r'}}{\epsilon_0 + S_{2r'}(\epsilon_{23} - \epsilon_{22r'})} \right] \left[\frac{\epsilon_{23} - \epsilon_{22r'}}{\epsilon_0 + S_{2r'}(\epsilon_{23} - \epsilon_{22r'})} \right]^* f_{23} \quad (97c)$$

Due to the invariant property of the Fourier transform under the rotation transformation, spectral density $\Phi_{2jlm}(\vec{\beta})$ in the untilted coordinates can functionally be related to those given in (96) with

$$\Phi_{\xi_2}(\vec{\beta}) = \Phi_{\xi_2}(\beta'_x = \beta_x \cos \psi - \beta_y \sin \psi, \beta'_y = \beta_y \sin \psi + \beta_x \cos \psi) \quad (98)$$

In the untilted coordinates, the rotation transformation together with the above invariant property give the anisotropic spectral densities

$$\Phi_{2jilm}(\vec{\beta}) = \delta_{2jilm} \Phi_{\xi_2}(\vec{\beta}) \quad (99)$$

where non-zero variance δ_{2jilm} are dependent on the tilt angle ψ as

$$\delta_{2xxxx} = \delta_{2r'} \quad (100a)$$

$$\delta_{2xyxy} = \delta_{2r'}^* \cos^2 \psi + \delta_{2r'} \sin^2 \psi \quad (100b)$$

$$\delta_{2xyyz} = \delta_{2xyzy} = \delta_{2r'}^* = \delta_{2r'}^* \sin^2 \psi = (\delta_{2r'} - \delta_{2r'}) \sin \psi \cos \psi \quad (100c)$$

$$\delta_{2zzzz} = \delta_{2r'}^* \sin^2 \psi + \delta_{2r'} \cos^2 \psi \quad (100d)$$

$$\delta_{2xyyz} = \delta_{2r'} \cos^4 \psi + \delta_{2r'} \sin^4 \psi + (\delta_{2r'} + \delta_{2r'}^*) \sin^2 \psi \cos^2 \psi \quad (100e)$$

$$\delta_{2xyyz} = \delta_{2xyzy} = \delta_{2r'}^* = \delta_{2r'}^* \sin^2 \psi = (\delta_{2r'} - \delta_{2r'}) \sin \psi \cos \psi \quad (100f)$$

$$\delta_{2xyyz} = \delta_{2r'}^* \sin^2 \psi \cos^2 \psi + \delta_{2r'} \cos^4 \psi + \delta_{2r'}^* \sin^4 \psi \quad (100g)$$

$$\delta_{2xyyz} = \delta_{2r'}^* \sin^2 \psi \cos^2 \psi + \delta_{2r'} \cos^4 \psi + \delta_{2r'}^* \sin^4 \psi \quad (100h)$$

$$\delta_{2xyyz} = \delta_{2r'}^* \sin^2 \psi \cos^2 \psi + \delta_{2r'} \cos^4 \psi + \delta_{2r'}^* \sin^4 \psi \quad (100i)$$

$$\delta_{2xyyz} = \delta_{2r'}^* \sin^2 \psi \cos^2 \psi + \delta_{2r'} \cos^4 \psi + \delta_{2r'}^* \sin^4 \psi \quad (100j)$$

The correlation of the scattered field can now be found by substituting into (32) the dyadic Green's functions (87), the means fields (90), and the correlation functions (92). To enable the calculation of the scattering coefficients according to (13), correlations of the scattered field components are actualised in the manner of (14)

$$\begin{aligned} \langle E_{\mu\alpha}(\vec{r}) E_{\nu\beta}^*(\vec{r}') \rangle &= \frac{E_{\tau\alpha} E_{\tau\beta}^*}{(4\pi r)^2} \\ &\left\{ k_0^2 \int_{-\infty}^{\infty} d\vec{\beta}_p \int d\vec{p}_1 \int d\vec{p}_1' e^{i(\vec{k}_{p1} - \vec{k}_p - \vec{\beta}_p) \cdot \vec{r}_1} e^{-i(\vec{k}_{p1'} - \vec{k}_p - \vec{\beta}_{p1'}) \cdot \vec{r}_1'} \right. \\ &\quad \left. \sum_{j,m} \int_{-\infty}^{\infty} d\vec{\beta}_j \int_{-\infty}^{\infty} d\vec{z}_1 \int_{-\infty}^{\infty} d\vec{z}_1' \Phi_1(\vec{\beta}) e^{-i\vec{\omega} \cdot (\vec{r}_1 - \vec{r}_1')} \right\} \end{aligned}$$

$$\begin{aligned}
& \cdot g_{1\mu j}(\bar{k}_\rho, z_1) \mathcal{F}_{1\tau j}(\bar{k}_\rho, z_1) g_{1\nu m}(\bar{k}_\rho, z_1^*) \mathcal{F}_{1\sigma m}^*(\bar{k}_\rho, z_1^*) \\
& + k_0^4 \int_{-\infty}^{\infty} d\bar{\beta}_\rho \int d\bar{\beta}_z \int d\bar{\beta}_z^* e^{i(\bar{k}_\rho - \bar{k}_\rho - \bar{\beta}_\rho) \cdot \bar{r}_\rho} e^{-i(\bar{k}_\rho - \bar{k}_\rho - \bar{\beta}_\rho) \cdot \bar{r}_\rho} \cdot \bar{\beta}_z^* \\
& \sum_{j,h,l,m} \int_{-\infty}^{\infty} d\bar{\beta}_z \int_{-\infty}^{\infty} d\bar{\beta}_z^* \int_{-\infty}^{\infty} d\bar{\beta}_z^* \Phi_{2jklm}(\bar{\beta}) e^{-i\bar{\beta} \cdot (z_1 - z_2^*)} \\
& \cdot g_{2\mu j}(\bar{k}_\rho, z_2) \mathcal{F}_{2\tau h}(\bar{k}_\rho, z_2) g_{2\nu l}(\bar{k}_\rho, z_2^*) \mathcal{F}_{2\sigma m}^*(\bar{k}_\rho, z_2^*) \} \quad (101)
\end{aligned}$$

where $\bar{\beta} = \bar{\beta}_\rho + \bar{\beta}_z$, $\bar{\beta}_\rho = \bar{\beta}_\rho + \bar{\beta}_\rho$, subscript μ, ν, τ , and κ can be h or v , and DGF element $g_{\mu\nu j}(\bar{k}_\rho, z_n)$ and normalized mean field component $\mathcal{F}_{\tau j}(\bar{k}_\rho, z_n)$ for $n = 1, 2$ and $j = \hat{x}, \hat{y}, \hat{z}$ are defined as

$$g_{\mu\nu j}(\bar{k}_\rho, z_n) = [\hat{\mu}(k_{0z}^n) \cdot \bar{g}_n(\bar{k}_\rho, z_n)] \cdot \hat{j} \quad (102a)$$

$$\mathcal{F}_{\tau j}(\bar{k}_\rho, z_n) = E_{\tau j}^{-1}(\bar{F}_n(\bar{r}_n)) \cdot \hat{j} |_{E_n=0} \quad (102b)$$

The integrations in (101) are carried out with the procedure in [37]: the integrals over \bar{r}_n give Dirac delta function $4\pi^2 \delta(\bar{k}_\rho - \bar{k}_\rho - \bar{\beta}_\rho)$, the integrals over $\bar{\beta}_\rho$ then effectuate $\bar{\beta}_\rho = \bar{k}_\rho - \bar{k}_\rho$, and the integrals over \bar{r}_n form illuminated area A . Then (101) becomes

$$\begin{aligned}
(E_{\mu\sigma}(\bar{r}) E_{\nu\sigma}^*(\bar{r})) &= E_{\tau j} E_{\tau j}^* \frac{k_0^4 A}{4\pi^2} \\
& \left\{ \sum_{j,m} \int_{-\infty}^{\infty} d\bar{\beta}_\rho \int_{-\infty}^{\infty} d\bar{\beta}_z \int_{-\infty}^{\infty} d\bar{\beta}_z^* \Phi_{1jlm}(\bar{\beta}_\rho = \bar{k}_\rho - \bar{k}_\rho, \bar{\beta}_z) e^{-i\bar{\beta}_z \cdot (z_1 - z_1^*)} \right. \\
& \cdot g_{1\mu j}(\bar{k}_\rho, z_1) \mathcal{F}_{1\tau j}(\bar{k}_\rho, z_1) g_{1\nu m}(\bar{k}_\rho, z_1^*) \mathcal{F}_{1\sigma m}^*(\bar{k}_\rho, z_1^*) \\
& + \sum_{j,h,l,m} \int_{-\infty}^{\infty} d\bar{\beta}_z \int_{-\infty}^{\infty} d\bar{\beta}_z^* \int_{-\infty}^{\infty} d\bar{\beta}_z^* \Phi_{2jklm}(\bar{\beta}_\rho = \bar{k}_\rho - \bar{k}_\rho, \bar{\beta}_z) e^{-i\bar{\beta}_z \cdot (z_2 - z_2^*)} \\
& \cdot g_{2\mu j}(\bar{k}_\rho, z_2) \mathcal{F}_{2\tau h}(\bar{k}_\rho, z_2) g_{2\nu l}(\bar{k}_\rho, z_2^*) \mathcal{F}_{2\sigma m}^*(\bar{k}_\rho, z_2^*) \} \quad (103)
\end{aligned}$$

It is observed from the forms of g 's and \mathcal{F} 's that all the polarization vectors and coefficient D 's and U 's can be taken out of the integrations

in (103). Retained inside the integrations are the spectral densities and the exponential terms which account for the upgoing and downgoing propagation of the mean fields and the scattered fields. Furthermore, $\phi_{0\rho} = \phi_{0i} + \pi$ and $\theta_{0\rho} = \theta_{0i}$ in the backscattering direction so that $\bar{k}_\rho = -\bar{k}_{\rho i}$ and $k_{\rho z}^* = k_{\rho z i}^*$ for wave type $w = u, d$ in region $n = 1$ or $w = ou, od, eo, ed$ in region $n = 2$. Also note that the z components of the upgoing and the downgoing wave vectors in region 1 differ only by a minus sign. Consequently, the following integrals are defined to simplify the calculation

$$T_1^{abcd} \equiv \int_{-\infty}^{\infty} d\bar{\beta}_z \Phi_1(2\bar{k}_{\rho i}, \bar{\beta}_z) \int_{-\infty}^{\infty} d\bar{z}_1 e^{-i(\bar{\beta}_z - \kappa_{ab}) \cdot \bar{z}_1} \int_{-\infty}^{\infty} d\bar{z}_2^* e^{i(\bar{\beta}_z - \kappa_{cd}) \cdot \bar{z}_2^*} \quad (104a)$$

$$\text{with : } \begin{cases} \kappa_{ab} = (a+b)k_{1z}; & a, b = -1, 1 \\ \kappa_{cd} = (c+d)k_{1z}; & c, d = -1, 1 \end{cases} \quad (104b)$$

$$T_2^{pqrs} \equiv \int_{-\infty}^{\infty} d\bar{\beta}_z \Phi_2(2\bar{k}_{\rho i}, \bar{\beta}_z) \int_{-\infty}^{\infty} d\bar{z}_2 e^{-i(\bar{\beta}_z - \kappa_{pq}) \cdot \bar{z}_2} \int_{-\infty}^{\infty} d\bar{z}_2^* e^{i(\bar{\beta}_z - \kappa_{rs}) \cdot \bar{z}_2^*} \quad (105a)$$

$$\text{with : } \begin{cases} \kappa_{pq} = -k_{2zi}^* + k_{2zi}^* & ; p, q = ou, od, eu, ed \\ \kappa_{rs} = -k_{2zi}^* + k_{2zi}^* & ; r, s = ou, od, eu, ed \end{cases} \quad (105b)$$

For the isotropic random medium, integral T_1^{abcd} involves 16 quantities since a, b, c , and d each has two possibilities of -1 and 1 . The integrations over vertical space z_1 and z_2^* are readily carried out and the integration over $\bar{\beta}_z$ is performed with the residue theorem in the contour integration method. From appendix D, the result for T_1^{abcd} is

$$\begin{aligned}
T_1^{abcd} &= i \frac{2\delta_1}{\pi \bar{L}_1} \left[\frac{e^{-i(\kappa_{ab} - \kappa_{cd}) \cdot \bar{d}_1}}{(\kappa_{ab} - \kappa_1)^2 (\kappa_{cd} - \kappa_1^*)^2 (\kappa_{ab} - \kappa_{cd})} \right. \\
& \left. + \frac{1}{(\kappa_{cd} - \kappa_1)^2 (\kappa_{cd} - \kappa_1^*)^2 (\kappa_{cd} - \kappa_{ab})} - \mathcal{P}_1(\kappa_1) - \mathcal{Q}_1(\kappa_1^*) \right] \quad (106a)
\end{aligned}$$

where $\kappa_1 = iL^{-1} \sqrt{1 + 4k_{\rho i}^2 L^2}$ and quantities $\mathcal{P}_1(\kappa_1)$ and $\mathcal{Q}_1(\kappa_1^*)$ are

$$\begin{aligned}
\mathcal{P}_1(\kappa_1) &= \frac{id_1 e^{i(\kappa_1 - \kappa_{ab}) \cdot \bar{d}_1}}{(2\kappa_1)^2 (\kappa_1 - \kappa_{ab})(\kappa_1 - \kappa_{cd})} \\
& + \frac{1 - e^{i(\kappa_1 - \kappa_{ab}) \cdot \bar{d}_1} + e^{-i(\kappa_{ab} - \kappa_{cd}) \cdot \bar{d}_1}}{(2\kappa_1)^2 (\kappa_1 - \kappa_{ab})(\kappa_1 - \kappa_{cd})}
\end{aligned}$$

$$\cdot \left[\frac{1}{\kappa_1} + \frac{1}{\kappa_1 - \kappa_{ob}} + \frac{1}{\kappa_1 - \kappa_{cd}} \right] \quad (106b)$$

$$\begin{aligned} Q_1(\kappa_1^*) &= \frac{id_1 e^{-i(\kappa_1^* - \kappa_{od})d_1}}{(2\kappa_1^*)^2 (\kappa_1^* - \kappa_{ob})(\kappa_1^* - \kappa_{cd})} \\ &+ \frac{e^{-i(\kappa_1^* - \kappa_{od})d_1}}{(2\kappa_1^*)^2 (\kappa_1^* - \kappa_{ob})(\kappa_1^* - \kappa_{cd})} \\ &\cdot \left[\frac{1}{\kappa_1^*} + \frac{1}{\kappa_1^* - \kappa_{ob}} + \frac{1}{\kappa_1^* - \kappa_{cd}} \right] \quad (106c) \end{aligned}$$

For the anisotropic random medium, integral T_{2jilm}^{pqr} involves 256 quantities since p, q, r , and s each has four possibilities of ou, od, eu , and ed . As in the isotropic case, the integrations over vertical space z_2 and z_2^* are readily carried out and the integration over β_2 is performed with the residue theorem in the contour integration method. From appendix D, the result for T_{2jilm}^{pqr} is

$$\begin{aligned} T_{2jilm}^{pqr} &= i \frac{2\delta_{2jilm} \ell_{2p}' \ell_{2r}'}{\pi \ell_2^2} \left[\frac{e^{-i(\kappa_{r1} - \kappa_{r1})d_2}}{(\kappa_{pq} - \kappa_2)(\kappa_2 - \kappa_{pq} - \kappa_2^*)(\kappa_{pq} - \kappa_2)} \right. \\ &+ \left. \frac{e^{i(\kappa_{r1} - \kappa_{r1})d_1}}{(\kappa_{r1} - \kappa_2)^2 (\kappa_{r1} - \kappa_2^*)(\kappa_{r1} - \kappa_{pq})} - \mathcal{P}_2(\kappa_2) - Q_2(\kappa_2^*) \right] \quad (107a) \end{aligned}$$

where square of length \mathcal{L}_2 is $\mathcal{L}_2^2 = \ell_{2p}'^2 \sin^2 \psi + \ell_{2r}'^2 \cos^2 \psi$, pole κ_2 is $\kappa_2 = \mathcal{L}_2^{-2} [-k_{rp}(\ell_{2p}'^2 - \ell_{2r}'^2) \sin(2\psi) + i\sqrt{(1+4k_{rp}^2 \ell_{2p}'^2) \mathcal{L}_2^2 + 4k_{rp}^2 \ell_{2r}'^2}]$, and quantities $\mathcal{P}_2(\kappa_2)$ and $Q_2(\kappa_2^*)$ are determined as follows

$$\begin{aligned} \mathcal{P}_2(\kappa_2) &= \frac{i(d_2 - d_1)e^{-i(\kappa_2 - \kappa_{r1})d_1}e^{i(\kappa_2 - \kappa_{r1})d_2}}{(2i\ell m \kappa_2)^2 (\kappa_2 - \kappa_{pq})(\kappa_2 - \kappa_{r1})} \\ &+ \frac{[e^{-i(\kappa_{r1} - \kappa_{r1})d_1} + e^{-i(\kappa_{r1} - \kappa_{r1})d_2}]}{[(2i\ell m \kappa_2)^2 (\kappa_2 - \kappa_{pq})(\kappa_2 - \kappa_{r1})]} \\ &- \frac{e^{-i(\kappa_2 - \kappa_{r1})d_1}e^{i(\kappa_2 - \kappa_{r1})d_2}}{(2i\ell m \kappa_2)^2 (\kappa_2 - \kappa_{pq})(\kappa_2 - \kappa_{r1})} \\ &\cdot \left[\frac{1}{i\ell m \kappa_2} + \frac{1}{\kappa_2 - \kappa_{pq}} + \frac{1}{\kappa_2 - \kappa_{r1}} \right] \quad (107b) \end{aligned}$$

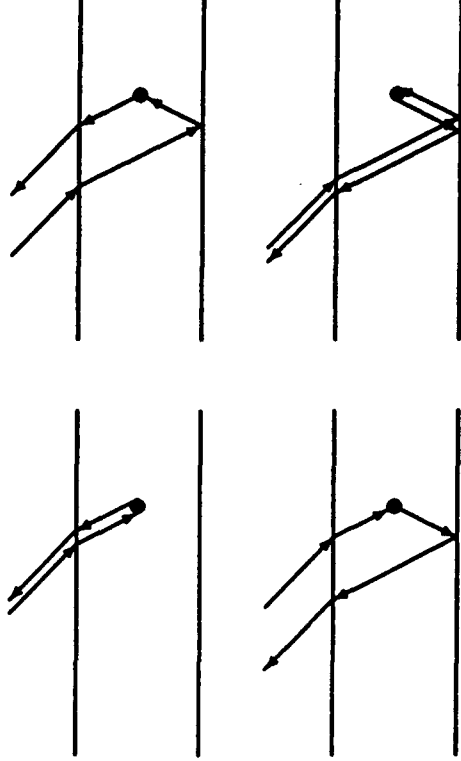


Figure 1.3.4 Wave scattering processes.

$$\begin{aligned} Q_2(\kappa_2^*) &= \frac{i(d_2 - d_1)e^{i(\kappa_2^* - \kappa_{r1})d_1}e^{-i(\kappa_2^* - \kappa_{r1})d_2}}{(2i\ell m \kappa_2^*)^2 (\kappa_2^* - \kappa_{pq})(\kappa_2^* - \kappa_{r1})} \\ &+ \frac{e^{i(\kappa_2^* - \kappa_{r1})d_1}e^{-i(\kappa_2^* - \kappa_{r1})d_2}}{(2i\ell m \kappa_2^*)^2 (\kappa_2^* - \kappa_{pq})(\kappa_2^* - \kappa_{r1})} \\ &\cdot \left[\frac{1}{i\ell m \kappa_2^*} + \frac{1}{\kappa_2^* - \kappa_{pq}} + \frac{1}{\kappa_2^* - \kappa_{r1}} \right] \quad (107c) \end{aligned}$$

The polarimetric backscattering coefficients are now obtained by applying results (106) and (107) to (103) and then making use of definition (13). From the observation on the forms of the DGF and mean field coefficients, the scattering coefficients can be expressed conveniently as

$$\sigma_{\mu\nu\alpha} = \pi k_0^4 \sum_{a,b,c,d} \sum_{ou,od} \sum_{eu,eu} \sum_{ed,ed} \sum_{p,q,r,s} \sum_{j,k,l,m} \Psi_{1\mu\nu}^{ab} \Psi_{1\nu\alpha}^{cd} \Psi_{2\mu r,jk}^{ou,ou} \Psi_{2jlm}^{eu,eu} \quad (108)$$

where all coefficient Ψ 's are given in appendix B and C. The scattering coefficients obtained in (108) is for the scattered field expressed in

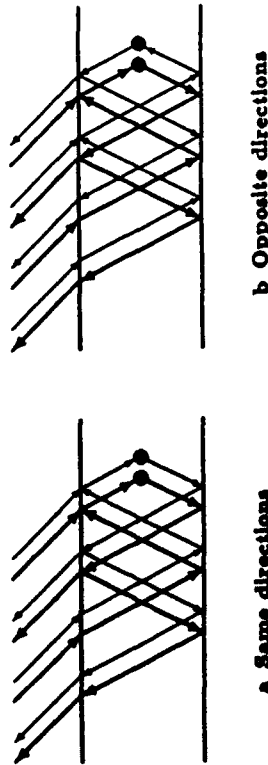


Figure 1.3.5 Correlations of waves multiply interacting with the boundaries. Thin arrows represent complex conjugates of thick-arrow terms.

the scattered basis. To change to the incident basis, simply take the negative of σ_{HVV} and σ_{VHV} . As calculated, the scattering coefficients are composed of 16 terms from the isotropic random medium and 256 terms from the anisotropic random medium. For the isotropic random medium, a scattered field can be an upgoing or a downgoing wave which is excited by an upgoing or a downgoing mean field as depicted in Fig. 1.3.4. Therefore, there are 4 possibilities for the total scattered field and its correlation thus consists of 16 terms. For the anisotropic random medium, a scattered field can be an upgoing or a downgoing wave excited by an upgoing or a downgoing mean field and each wave type can be ordinary or extraordinary. Therefore, there are 16 possibilities for the total scattered field and thus its correlation consists of 256 terms. Furthermore, all multiple interactions between the waves and the boundaries are accounted for and all correlations of waves with same and different propagation directions are included. For instances, Fig. 1.3.5a represents a correlation of waves multiply interacting with the boundaries and propagating in the same directions and Fig. 1.3.5b illustrates a correlation of waves propagating in opposite directions.

In this section, the random medium model is formulated and the polarimetric backscattering coefficients are obtained under the distorted Born approximation with the strong permittivity fluctuation theory. In the next section, the model is applied to study the polarimetric backscattering properties from layer random media. Consideration is also given to the polarization signatures of the media and their relations to the corresponding covariance matrices are explained.

1.4 Results and Discussion

1.4 Results and Discussion

a. Two-layer Configuration

For geophysical media with a two-layer configuration, the three-layer model is applied with the top scattering layer removed by setting its thickness and variances to zero. The reduced model is used to investigate the polarimetric backscattering directly from an unconvolved anisotropic random medium such as sea ice. Consider an electromagnetic wave of 9 GHz incident on a random medium composed of an ice background with permittivity $\epsilon_{2b} = (3.15 + i0.002)\epsilon_0$ and a 3.0%-volume fraction of vertically oriented ($\psi = 0$) brine inclusions with permittivity $\epsilon_{2i} = (38 + i41)\epsilon_0$ and correlation length $\ell_{2i'} = 0.5$ mm and $\ell_{2i''} = 1.5$ mm for which the strong fluctuation theory (SFT) gives the variances of $\delta_{2i'} = 1.48$, $\delta_{2i''} = 14.9$, and $\delta_{2i'''} = 4.57 - i1.08$ and the uniaxial effective permittivity tensor with $\epsilon_{2i'} = (3.37 + i0.034)\epsilon_0$ and $\epsilon_{2i''} = (3.85 + i0.374)\epsilon_0$ as shown in Fig. 1.4.1. The thickness of the random medium is 1.7 m and the permittivity of the underlying sea water is $\epsilon_3 = (45.0 + i40.0)\epsilon_0$. To point out the anisotropy effect on the polarimetric backscattering, a comparison is made with an isotropic random medium with the same parameters except $\ell_{2i'} = \ell_{2i''} = 0.5$ mm for which the SFT yields $\delta_{2i'} = \delta_{2i''} = \delta_{2i'''} = 2.53$ and $\epsilon_{2i'} = \epsilon_{2i''} = (3.43 + i0.047)\epsilon_0$. For both the untitled anisotropic and the isotropic random media, cross term σ_{HV} , σ_{HHV} , and σ_{HHVV} are zero under the first-order distorted Born approximation rendering the covariance matrix of the form

$$\bar{C} = \begin{bmatrix} \sigma_{\text{HH}} & 0 & \sigma_{\text{HHVV}} \\ 0 & 0 & 0 \\ \sigma_{\text{HHVV}}^* & 0 & \sigma_{\text{VV}} \end{bmatrix} \quad \text{or} \quad \bar{C} = \sigma \begin{bmatrix} 1 & 0 & \rho\sqrt{\gamma} \\ 0 & 0 & 0 \\ \rho^*\sqrt{\gamma} & 0 & \gamma \end{bmatrix} \quad (109)$$

Conventional backscattering coefficient σ_{HH} and σ_{VV} are plotted as a function of incident angle in Fig. 1.4.2 for the two-layer untitled anisotropic (a) and the isotropic (b) cases. As observed from Fig. 1.4.2, σ_{VV} crosses over σ_{HH} for the anisotropic case whereas, for the isotropic case, σ_{VV} is higher than σ_{HH} over the range of incident angles under consideration. The distinction of the conventional backscattering coefficients, σ_{VV} and σ_{HH} , associated with the two different random media is, however, not as obvious as that of the polarimetric correlation coefficient ρ as indicated in Fig. 1.4.3 where the untitled anisotropic random medium manifests its characteristics in ρ with magnitude and

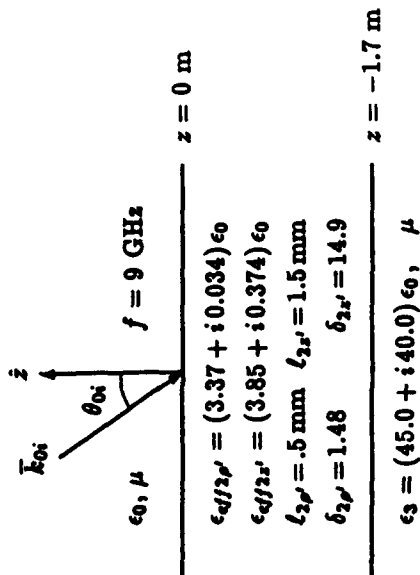


Figure 1.4.1 Parameters for the two-layer configuration.

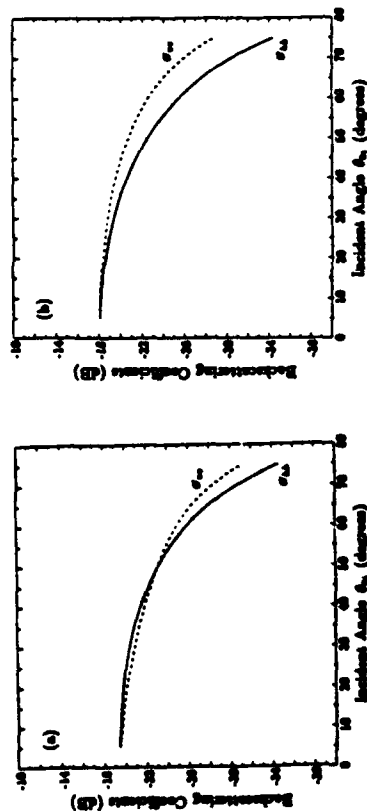


Figure 1.4.2 Conventional backscattering coefficients: (a) untitled anisotropic random medium, (b) isotropic random medium.

phase inversely related to the incident angle while the isotropic random medium ρ simply has the value of approximately 1.0 over the range of incident angles. These results can be explained based on the physical characteristics of the random media. In the anisotropic random medium, the effective complex wave vectors of the ordinary and the extraordinary waves are different; therefore, the h -polarized wave

corresponding to the ordinary wave and the v -polarized wave corresponding to the extraordinary wave have different propagation velocities and attenuation rates which result in the separation of the scattering centers of the two wave types. At normal incident angle, there is no distinction between the h and the v waves for the untitled random medium, the two waves are correlated, and thus the correlation coefficient ρ has the value of unity. As the incident angle is increased, the two waves become increasingly distinctive and less correlated; thus, the correlation coefficient takes on a complex value with decreased magnitude and phase. For the isotropic random medium, the distinction between the h and the v waves is only due to the boundary effect and the good correlation of two wave types leads to the correlation coefficient of value close to unity.

To illustrate the effect of the scatterers tilted in a preferred alignment direction, consider now the anisotropic random medium as described in the previous example but with non-zero tilt angle. For instance, let $\psi = 10^\circ, 20^\circ$ and $\phi_0i = 0^\circ$. In this case, the correlation coefficient ρ also contains information about the tilting as shown in Fig. 1.4.3. It is observed that the maximum magnitude of ρ is at normal incidence in the untitled case and moves to a larger incident angle as the tilted angle becomes larger. Also, the phase of ρ does not change sign for the case of $\psi = 0^\circ$ whereas, in the tilted cases, the phase of ρ changes sign at the incident angle where the magnitude of ρ is maximum. Furthermore, it should be noted that the tilting results in non-zero cross terms and the corresponding covariance matrix become fully populated. As shown in this subsection, the covariance matrix describes the fully polarimetric scattering property of the remotely sensed media and thus can be used for the identification and the classification of terrain types.

b. Three-layer Configuration

To identify the effect of the covering top layer on the backscattering from the lower layer, the components of covariance matrices are compared between a two-layer configuration such as the bare sea ice in section 1.4a and a three-layer configuration such as the sea ice with snow cover. In Fig. 1.4.4, the covering dry-snow layer is a low-loss isotropic random medium of thickness $d_1 = 0.1 \text{ m}$ composed of an air background with permittivity $\epsilon_{1b} = \epsilon_0$ and a 20%-volume fraction of ice particles with permittivity $\epsilon_{1i} = (3.15 + i0.002)\epsilon_0$ and correlation

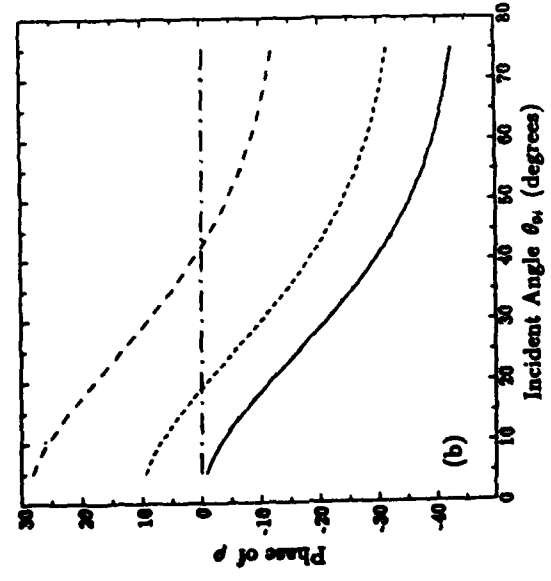
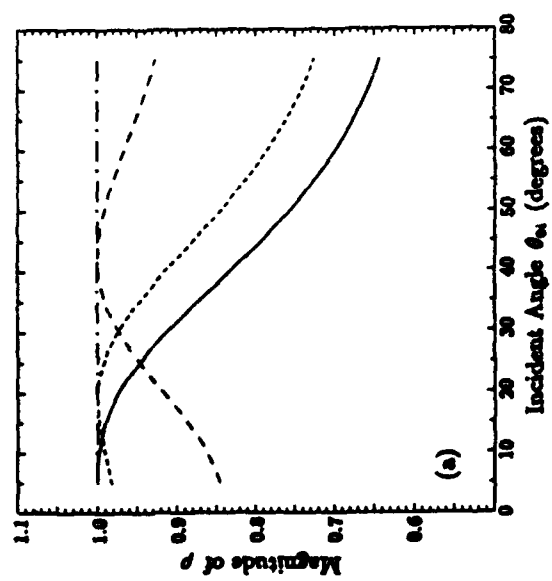


Figure 1.4.5 Correlation coefficients ρ : (a) magnitude, (b) phase. Dash-dot curves are for the isotropic, continuous for the untitled, short-dash for the 10°-tilted, and long-dash for the 20°-tilted random media.

1.4 Results and Discussion

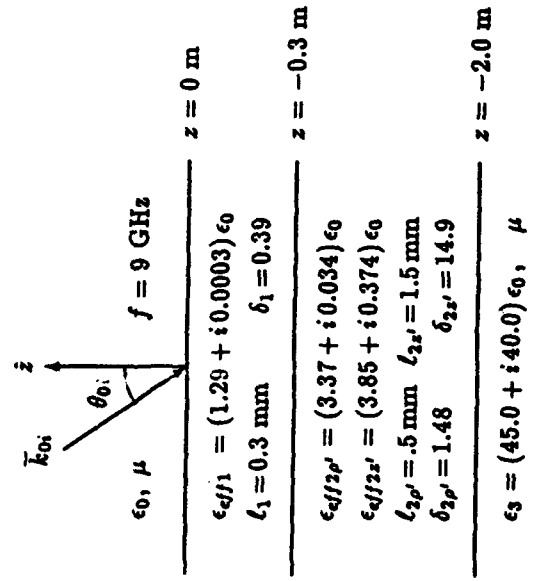


Figure 1.4.4 Parameters for the three-layer configuration.

length $l_1 = 0.3$ mm for which the SFT gives the variance of $\delta_1 = 0.39$ and the isotropic effective permittivity of $\epsilon_{eff1} = (1.29 + i0.0003)\epsilon_0$; the middle and the underlying regions are, respectively, the sea ice with vertical brine inclusion over the sea water with the same physical parameters as in the two-layer configuration.

Displayed in Fig. 1.4.5 are the plots of σ_{HH} and σ_{VV} as a function of incident angle for the two-layer and the three-layer configurations. The comparison shows that both σ_{HH} and σ_{VV} are enhanced due to the effect of the dry-snow cover whose ice particles introduce more backscattering. Moreover, the boundary effect is recognized in form of the oscillations on σ_{HH} and σ_{VV} . The oscillations can also be seen clearly on the phase of the correlation coefficient ρ in Fig. 1.4.6b. As compared to the two-layer case, the absolute value of the phase of ρ for the three layer is smaller over the range of incident angle. Physically, this is due to the isotropic covering layer, which characteristically exhibits its isotropy in ρ with a small phase, partially masks the scattering effect of the lower anisotropic random medium. The magnitude of ρ , however, exhibits very weak oscillations while clearly retaining

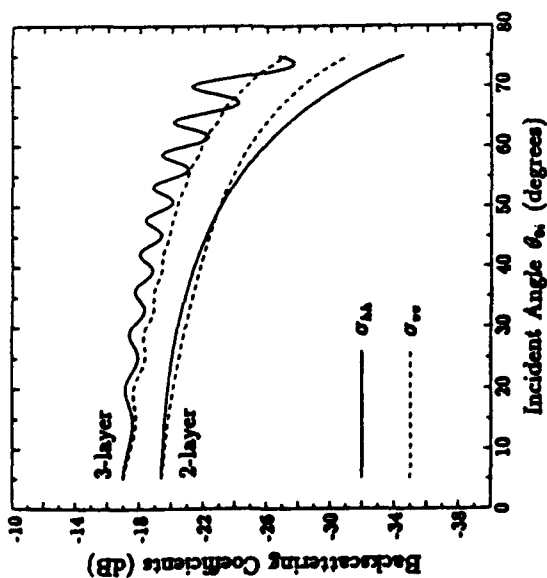


Figure 1.4.5 Conventional backscattering coefficients for the two-layer and three-layer configurations.

the almost same characteristics as observed directly from the two-layer configuration as seen in Fig. 1.4.6b. Thus, the correlation coefficient ρ can carry information from both the covering low-loss isotropic layer and the lower tilted anisotropic layer in a rather distinctive manner. If the top layer is more lossy, both σ_{HH} and σ_{VV} can be diminished and the boundary-effect oscillations can be depressed. As illustrated, the three-layer model can account for the effect of the top scattering layer covering a geophysical medium whose characteristics can be recognized from the polarimetric covariance matrix.

c. Polarization Signatures

For given polarizations of the transmitter and the receiver, (11) can be used to synthesise the scattering coefficient which is similar to the polarization signature defined in [22]. When orientation angle $\alpha_i = \alpha_r = \alpha_c$ and $\beta_i = \beta_r = \beta_c$, the copolarized signature can be displayed with a three-dimensional plot with the vertical axis for the normalized signature and the horizontal plane for α_c and β_c . In

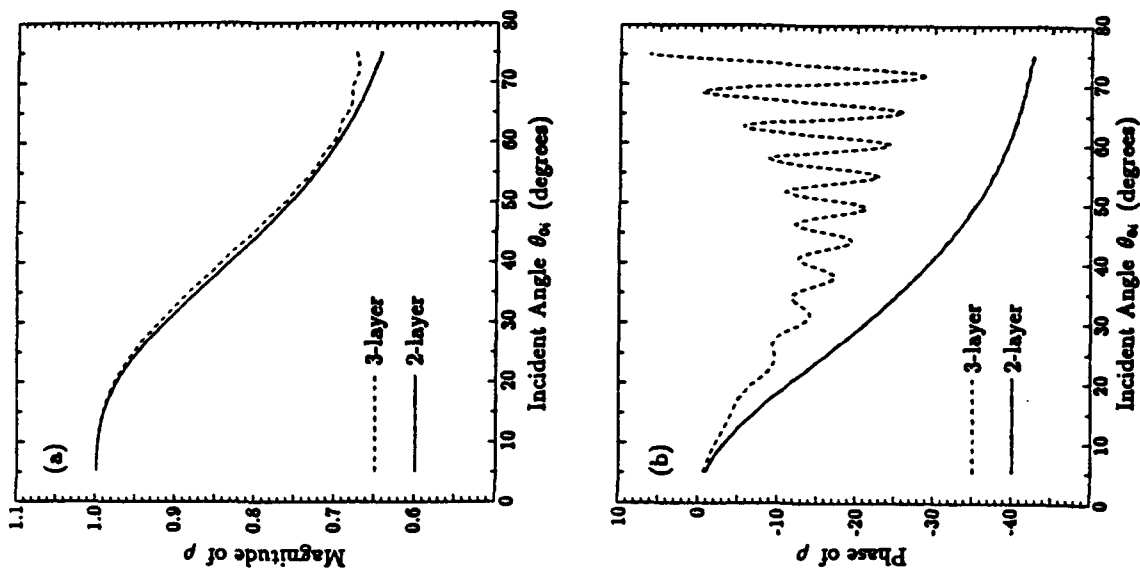


Figure 1.4.6 Correlation coefficients ρ : (a) magnitude, (b) phase. Continuous curves are for the two-layer and dash curves are for the three-layer configurations.

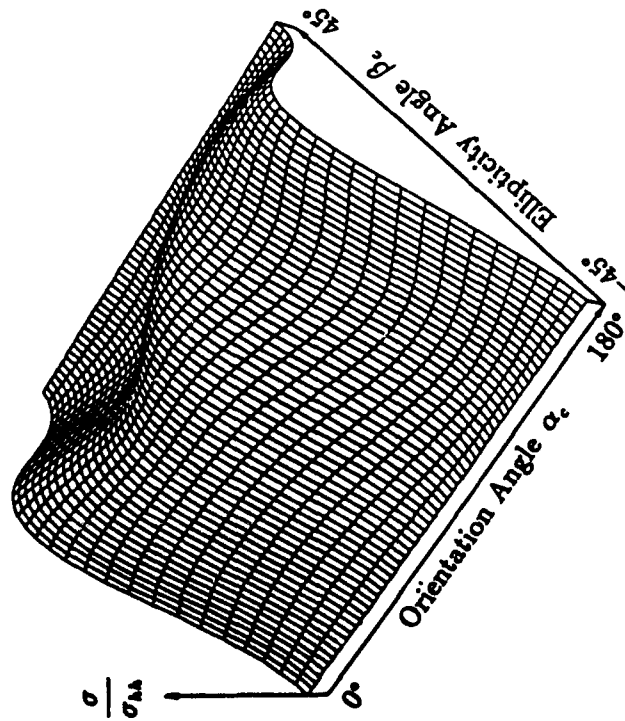


Figure 1.4.7 Copolarized signature normalized to σ_{AA} for the two-layer configuration at $\theta_{0i} = 40^\circ$.

this subsection, the copolarized signature is shown for the bare sea ice and compared with that of the snow-covered sea ice. The forms of the displayed signatures and their relations to the corresponding covariance matrices will be explained.

Consider the 9-GHz wave incident at $\theta_{0i} = 40^\circ$ on the sea ice with vertical brine inclusions. The corresponding covariance matrix is

$$\bar{C} = 7.12 \times 10^{-3} \begin{bmatrix} 1 & 0 & (0.83 \angle -29.5^\circ)\sqrt{7} \\ 0 & 0 & 0 \\ (0.83 \angle +29.5^\circ)\sqrt{7} & 0 & 0 \end{bmatrix} \quad \gamma = 0.915 \quad (110)$$

The copolarized signature is shown in Fig. 1.4.7 where the variation is seen in both α_c and β_c . To illustrate the variation in α_c , the copolarized signature normalized to σ_{AA} for linear polarization is plotted

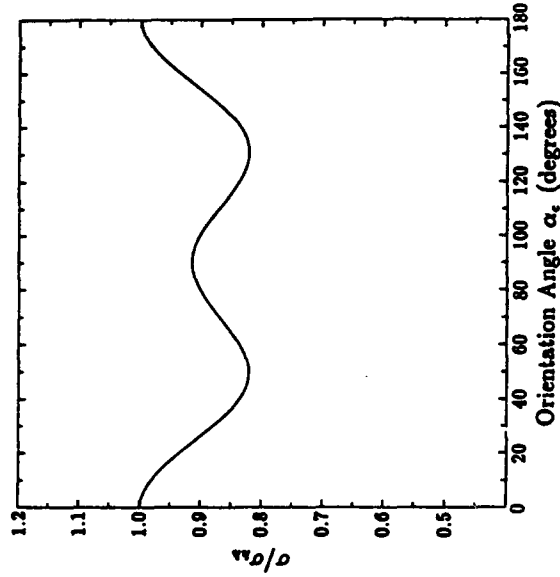


Figure 1.4.8 Linearly copolarized signature normalized to σ_{AA} for the two-layer configuration at $\theta_{0i} = 40^\circ$.

in Fig. 1.4.8 where the normalized signature at $\alpha = 90^\circ$ has the value of 0.915 which is the ratio $\gamma = \sigma_{vv}/\sigma_{AA}$ in covariance matrix (110) and the undulation also depends on the correlation coefficient ρ . For the variation in β_c , the signature at a fixed value of α_c increases to a maximum and then decreases. The variation over the polarization plane (α_c, β_c) makes the signature look like being distorted. To describe this distortion, a "signature distortion track" is defined as the plot of β_c at which the signature is maximum as a function of α_c such that $\partial\sigma(\alpha_c, \beta_c)/\partial\beta_c = 0$. This plot tracks the locations of the local maxima of the copolarized signature over the polarization plane. The result of the signature distortion track for the bare sea ice is shown in Fig. 1.4.9 which indicates that a maximum copolarized scattering coefficient can be obtained with an h ($\alpha_c = 0^\circ, 180^\circ$) or v ($\alpha_c = 90^\circ$) polarization and with an elliptical polarization for other orientation angles. To explain the cause of the distortion, the phase of ρ in the covariance matrix (110) is artificially set to zero which consequently gives the signature in Fig. 1.4.10a where the distortion disappears as seen in Fig. 1.4.10b. Thus, the distortion is due to the non-zero phase of ρ which

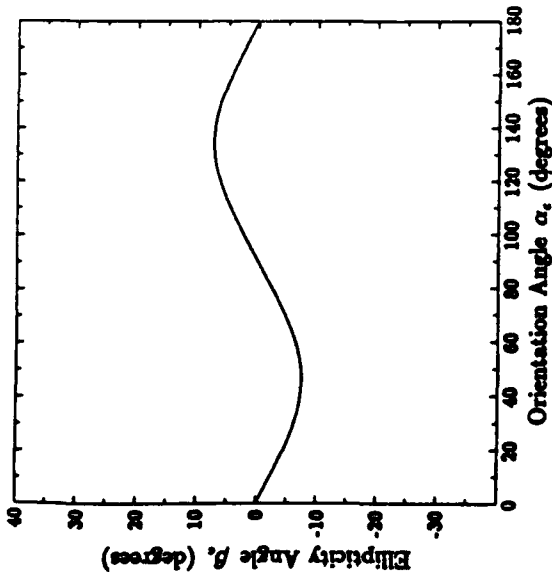


Figure 1.4.9 Signature distortion track of the two-layer configuration.

can come from the anisotropy of the random medium as discussed in subsection 1.4a. Furthermore, the distortion track is symmetric about the v polarization ($\alpha = 90^\circ, \beta = 0^\circ$) due to the azimuthal symmetry of the untilted anisotropic random medium. Consider an azimuthally symmetric random medium whose polarimetric backscattering properties are characterized with a covariance matrix of the form [45]

$$\bar{C} = \sigma_{hh} \begin{bmatrix} 1 & 0 & \rho\sqrt{\gamma} \\ 0 & e & 0 \\ \rho^*\sqrt{\gamma} & 0 & \gamma \end{bmatrix} \quad (111)$$

which is more general than (109). In this case, the distortion track equation is

$$\begin{aligned} \partial\sigma/\partial\beta_c &= \sigma_{hh} \sin 2\beta_c [(\gamma - 1) \cos 2\alpha_c - (\gamma + 1 - 4e) \cos^2 2\alpha_c \cos 2\beta_c \\ &\quad - 2\sqrt{\gamma} \operatorname{Re} \rho \cos 2\beta_c (1 + \sin^2 2\alpha_c)] + 2\sigma_{hh} \sqrt{\gamma} \operatorname{Im} \rho \sin 2\alpha_c \cos 4\beta_c = 0 \end{aligned} \quad (112)$$

from which the properties of the signature distortion track can be deduced. If $\operatorname{Im}(\rho) = 0$, (112) has solution $\beta_c = 0$ for any given orientation angle α_c and the track is just the straight line at β_c of

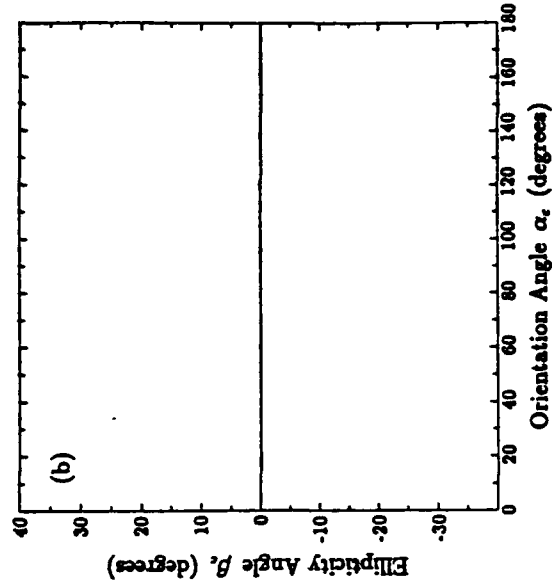
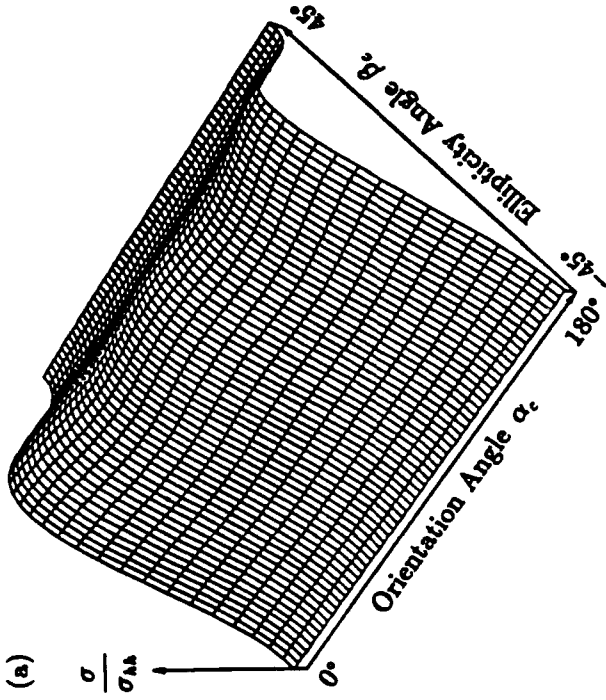


Figure 1.4.10 For the covariance matrix (110) with the phase of ρ set to zero: (a) Copolarised signature normalised to σ_{hh} , (b) Signature distortion track.

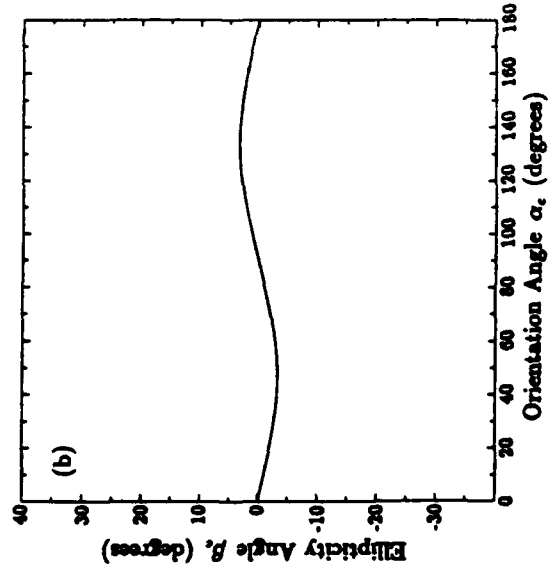
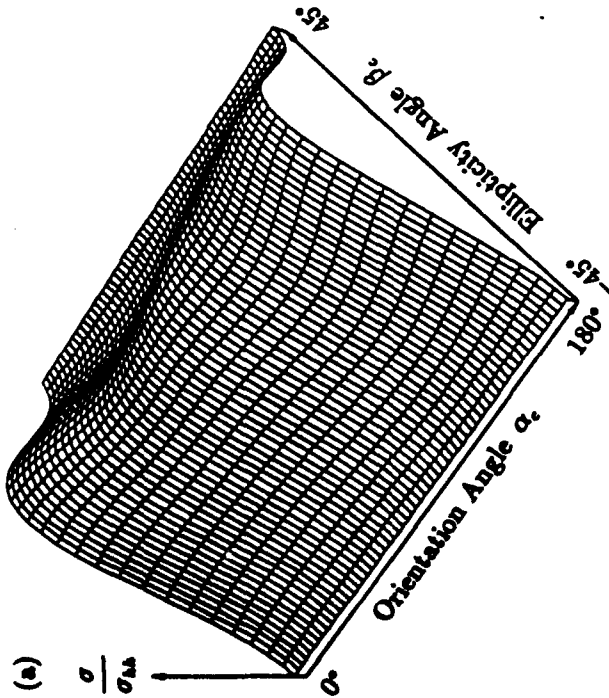


Figure 1.4.11 For the three-layer configuration: (a) Copolarized signature normalised to $\sigma_{\Lambda\Lambda}$, (b) Signature distortion track.

1.4 Results and Discussion

zero value signifying the disappearance of the distortion. Also, the invariance of (112) under the change of α_c and β_c respectively to $(180^\circ - \alpha_c)$ and $-\beta_c$ implies the symmetry about the v polarization ($\alpha_c = 90^\circ, \beta_c = 0^\circ$). When $e = 0$ as in (109), these properties of the distortion track still remain.

The pedestal is also observed in Fig. 1.4.6. To explain the existence of the pedestal, the pedestal height is calculated from (11) by setting $\beta_c = \pm 45^\circ$ (circular polarizations) for the case of (111)

$$\sigma(\beta_c = \pm 45^\circ)/\sigma_{\Lambda\Lambda} = e + \frac{1}{4}[(\gamma + 1) - 2\sqrt{\gamma}\text{Re}\rho] \quad (113)$$

Obviously from (113), the pedestal height is composed of two terms: the first term e can come from the depolarization due to multiple scattering [45] and the second term can come from the anisotropy of the random medium. For the untilted anisotropic random medium under consideration, the pedestal height is therefore non-zero even though the cross term e is not accounted for. In this case, the pedestal is due to the anisotropy and the boundary effects.

For the snow covered sea ice with the three-layer configuration in Fig. 1.4.4, the covariance matrix at the incident angle of $\theta_{0i} = 40^\circ$ is

$$\overline{\mathbf{C}} = 1.34 \times 10^{-2} \begin{bmatrix} 1 & 0 & 0 & (0.84 \angle -13.2^\circ)\sqrt{\gamma} \\ 0 & 0 & 0 & 0 \\ (0.84 \angle +13.2^\circ)\sqrt{\gamma} & 0 & 0 & \gamma \end{bmatrix} \quad (114)$$

The corresponding copolarized signature and the signature distortion track are displayed in Fig. 1.4.11. Compared to the two-layer case, the three-layer signature is less distorted and the pedestal height is lower. This is due to the masking effect of the isotropic covering layer which renders the anisotropic characteristics of the lower scattering layer less pronounced.

The polarization signatures of the two-layer and the three-layer random medium configurations have been shown in this subsection. The forms of the copolarized signatures and the pedestal heights are explained with the components of the covariance matrices from which the polarimetric scattering properties are readily recognized.

1.5 Summary

In this chapter, the fully polarimetric backscattering coefficients have been obtained with the layer random medium model. The top layer is modelled as an isotropic random medium, the middle layer as an anisotropic random medium, and the underlying layer as a homogeneous medium. The strong fluctuation theory is used to calculate the effective permittivities of the scattering layers and the distorted Born approximation is applied to derive the scattered fields. The dyadic Green's functions are used in the calculations and the backscattering processes are explained. The model can be applied to the remote sensing of both bare and covered geophysical media as illustrated for the case of bare and snow covered sea ice. The physical information conveyed in the elements of the covariance matrices are discussed especially for the correlation coefficient ρ . The copolarization signatures for the layer random media are obtained with the Mueller matrices and explained with the scattering coefficients contained in the covariance matrices. Since the fully polarimetric scattering coefficients convey more information about the remotely sensed media as compared to the conventional scattering coefficients, the polarimetry provides a better means for the identification and classification of the geophysical media.

Appendix A: Transmission and Reflection Coefficients

The transmission and reflection coefficients are obtained by matching the boundary conditions at the interfaces where the tangential components of the electric and magnetic fields are continuous. The boundary conditions for the zeroth-order mean fields can be written explicitly as

$$\left. \begin{aligned} \hat{z} \times \langle \vec{F}_0(\vec{r}) \rangle &= \hat{z} \times \langle \vec{F}_1(\vec{r}) \rangle \\ \hat{z} \times \nabla \times \langle \vec{F}_0(\vec{r}) \rangle &= \hat{z} \times \nabla \times \langle \vec{F}_1(\vec{r}) \rangle \end{aligned} \right\} \text{ at } z = 0 \quad (\text{A.1a})$$

$$\left. \begin{aligned} \hat{z} \times \langle \vec{F}_1(\vec{r}) \rangle &= \hat{z} \times \langle \vec{F}_2(\vec{r}) \rangle \\ \hat{z} \times \nabla \times \langle \vec{F}_1(\vec{r}) \rangle &= \hat{z} \times \nabla \times \langle \vec{F}_2(\vec{r}) \rangle \end{aligned} \right\} \text{ at } z = -d_1 \quad (\text{A.1b})$$

$$\left. \begin{aligned} \hat{z} \times \langle \vec{F}_2(\vec{r}) \rangle &= \hat{z} \times \langle \vec{F}_3(\vec{r}) \rangle \\ \hat{z} \times \nabla \times \langle \vec{F}_2(\vec{r}) \rangle &= \hat{z} \times \nabla \times \langle \vec{F}_3(\vec{r}) \rangle \end{aligned} \right\} \text{ at } z = -d_2 \quad (\text{A.1c})$$

The boundary conditions are satisfied by coefficients composed of

half-space Fresnel coefficients and phase factors as expressed in (85). The phase factors in the exponents account for the wave propagation to the boundaries. The Fresnel reflection and transmission coefficients have been derived as shown in [36]. For the coordinate systems defined in this chapter, the Fresnel coefficients are given as follows:

At boundary $z=0$ between the isotropic media of region 0 and region 1

$$R_{01\text{hh}} = -R_{10\text{hh}} = \frac{k_{0z} - k_{1z}}{k_{0z} + k_{1z}} \quad (\text{A.2a})$$

$$R_{01\text{vv}} = -R_{10\text{vv}} = \frac{k_1^2 k_{0z} - k_0^2 k_{1z}}{k_1^2 k_{0z} + k_0^2 k_{1z}} \quad (\text{A.2b})$$

$$T_{01\text{hh}} = \frac{2k_{0z}}{k_{0z} + k_{1z}}, \quad T_{10\text{hh}} = \frac{2k_{1z}}{k_{1z} + k_{0z}} \quad (\text{A.2c})$$

$$T_{01\text{vv}} = \frac{2k_0 k_1 k_{0z}}{k_1^2 k_{0z} + k_0^2 k_{1z}}, \quad T_{10\text{vv}} = \frac{2k_1 k_0 k_{1z}}{k_0^2 k_{1z} + k_1^2 k_{0z}} \quad (\text{A.2d})$$

At boundary $z=-d_1$ between isotropic region 1 and anisotropic region 2

$$\begin{aligned} R_{12\text{hh}} &= -1 + \frac{k_2^2 k_{\text{av}} T_{12\text{hv}}}{k_p U_d} \sin \psi \\ &+ \frac{T_{12\text{ho}}}{k_p G_d} (k_p^2 \cos \psi + k_y k_{2z}^2 \sin \psi) \end{aligned} \quad (\text{A.3a})$$

$$\begin{aligned} R_{12\text{hv}} &= \frac{k_1 k_{\text{av}} k_{2z}^2 T_{12\text{ho}}}{k_p k_{1z} G_d} \sin \psi \\ &+ \frac{k_1 T_{12\text{he}}}{k_p k_{1z} U_d} (k_p^2 k_{2z}^2 \cos \psi - k_y k_{2z}^2 \sin \psi) \end{aligned} \quad (\text{A.3b})$$

$$\begin{aligned} R_{12\text{vh}} &= \frac{k_2^2 k_{\text{av}} T_{12\text{ve}}}{k_p U_d} \sin \psi \\ &+ \frac{T_{12\text{vo}}}{k_p G_d} (k_p^2 \cos \psi + k_y k_{2z}^2 \sin \psi) \end{aligned} \quad (\text{A.3c})$$

$$\begin{aligned} R_{12\text{vv}} &= 1 + \frac{k_1 k_{\text{av}} k_{2z}^2 T_{12\text{vo}}}{k_p k_{1z} G_d} \sin \psi \\ &+ \frac{k_1 T_{12\text{ve}}}{k_p k_{1z} U_d} (k_p^2 k_{2z}^2 \cos \psi - k_y k_{2z}^2 \sin \psi) \end{aligned} \quad (\text{A.3d})$$

$$R_{21\text{oo}} = \frac{G_d E_o (k_{2z}^2 - k_{1z})}{G_u D_d (k_{2z}^2 + k_{1z})} \quad (\text{A.3e})$$

$$R_{210e} = \frac{2k_u k_{2z}^o U_d}{G_u D_e} (k_{1z} - k_{2z}^o) \quad (A.3f)$$

$$\cdot (k_y \sin \psi - k_{1z} \cos \psi) \sin \psi$$

$$R_{210e} = \frac{k_z^2 k_u G_d}{U_u D_e} (k_{2z}^{ed} - k_{2z}^{eu}) (k_{1z} - k_{2z}^o)$$

$$\cdot (k_y \sin \psi + k_{1z} \cos \psi) \sin \psi \quad (A.3g)$$

$$R_{210e} = -\frac{U_d I_e}{U_u D_e} \quad (A.3h)$$

$$T_{120e} = \frac{2k_{1z} G_d}{k_p D_e (k_{1z} + k_{2z}^o)} \left[k_p^2 (k_{2z}^2 k_{1z} - k_1^2 k_{2z}^{ed}) \cos \psi \right. \\ \left. + k_y (k_1^2 k_{2z}^o - k_{2z}^2 k_{1z} k_{2z}^{ed}) \sin \psi \right] \quad (A.3i)$$

$$T_{120e} = \frac{2k_u k_{1z} U_d}{k_p D_e} (k_p^2 + k_{1z} k_{2z}^o) \sin \psi \quad (A.3j)$$

$$T_{120e} = -\frac{2k_1 k_{2z}^2 k_{1z} G_d (k_{1z} - k_{2z}^{ed})}{k_p D_e (k_{1z} + k_{2z}^o)} \sin \psi \quad (A.3k)$$

$$T_{120e} = \frac{2k_1 U_d}{k_p D_e} (k_p^2 k_{1z} \cos \psi + k_y k_{1z} k_{2z}^o \sin \psi) \quad (A.3l)$$

$$T_{210e} = \frac{k_z^2 k_u R_{210e}}{k_p U_d} \sin \psi + \frac{1}{k_p G_u} (k_p^2 \cos \psi - k_y k_{2z}^o \sin \psi) \\ + \frac{R_{210e}}{k_p G_d} (k_p^2 \cos \psi + k_y k_{2z}^o \sin \psi) \quad (A.3m)$$

$$T_{210e} = \frac{k_1 k_u k_{2z}^o R_{210e}}{k_p k_{1z} G_d} \sin \psi - \frac{k_1 k_u k_{2z}^o}{k_p k_{1z} G_u} \sin \psi \\ - \frac{k_1 R_{210e}}{k_p k_{1z} U_d} (k_y k_{2z}^o \sin \psi - k_p^2 k_{2z}^{ed} \cos \psi) \quad (A.3n)$$

$$T_{210e} = \frac{k_z^2 k_u}{k_p U_u} \sin \psi + \frac{k_z^2 k_u R_{210e}}{k_p U_d} \sin \psi \\ + \frac{R_{210e}}{k_p G_d} (k_p^2 \cos \psi + k_y k_{2z}^o \sin \psi) \quad (A.3o)$$

$$T_{210e} = \frac{k_1 k_u k_{2z}^o R_{210e}}{k_p k_{1z} G_d} \sin \psi$$

$$- \frac{k_1}{k_p k_{1z} U_u} (k_y k_{2z}^o \sin \psi - k_p^2 k_{2z}^{eu} \cos \psi) \\ - \frac{k_1 R_{210e}}{k_p k_{1z} U_d} (k_y k_{2z}^o \sin \psi - k_p^2 k_{2z}^{ed} \cos \psi) \quad (A.3p)$$

At boundary $z = -d_2$ between anisotropic region 2 and isotropic region 3

$$R_{230o} = \frac{G_u G_e (k_{2z}^o - k_{3z})}{G_d F_e (k_{2z}^o + k_{3z})} \quad (A.4a)$$

$$R_{230e} = \frac{2k_u k_{2z}^o U_u}{G_d F_e} (k_{2z}^o - k_{3z}) \\ \cdot (k_y \sin \psi + k_{3z} \cos \psi) \sin \psi \quad (A.4b)$$

$$R_{230e} = \frac{k_z^2 k_u G_u}{U_d F_e} (k_{2z}^{ed} - k_{2z}^{eu}) (k_{2z}^o - k_{3z}) \\ \cdot (k_y \sin \psi - k_{3z} \cos \psi) \sin \psi \quad (A.4c)$$

$$R_{230e} = -\frac{U_u H_e}{U_d F_e} \quad (A.4d)$$

$$T_{230e} = \frac{k_z^2 k_u R_{230e}}{k_p U_u} \sin \psi + \frac{1}{k_p G_d} (k_p^2 \cos \psi + k_y k_{2z}^o \sin \psi) \\ + \frac{R_{230e}}{k_p G_u} (k_p^2 \cos \psi - k_y k_{2z}^o \sin \psi) \quad (A.4e)$$

$$T_{230e} = \frac{k_3 k_u k_{2z}^o R_{230e}}{k_p k_{3z} G_u} \sin \psi - \frac{k_3 k_u k_{2z}^o}{k_p k_{3z} G_d} \sin \psi \\ + \frac{k_3 R_{230e}}{k_p k_{3z} U_u} (k_y k_{2z}^o \sin \psi - k_p^2 k_{2z}^{eu} \cos \psi) \quad (A.4f)$$

$$T_{230e} = \frac{k_z^2 k_u R_{230e}}{k_p U_u} \sin \psi + \frac{k_z^2 k_u}{k_p U_d} \sin \psi \\ + \frac{R_{230e}}{k_p G_u} (k_p^2 \cos \psi - k_y k_{2z}^o \sin \psi) \quad (A.4g)$$

$$T_{230e} = \frac{k_3 k_u k_{2z}^o R_{230e}}{k_p k_{3z} G_u} \sin \psi \\ + \frac{k_3 R_{230e}}{k_p k_{3z} U_u} (k_y k_{2z}^o \sin \psi - k_p^2 k_{2z}^{eu} \cos \psi)$$

$$+ \frac{k_3}{k_p k_{3z} U_d} (k_y k_{2z}^2 \sin \psi - k_p^2 k_{2z}^2 \cos \psi) \quad (\text{A.4h})$$

In the above expressions, the following definitions have been used

$$G_d \equiv \sqrt{k_m^2 + (k_y \cos \psi + k_{2z}^0 \sin \psi)^2} \quad (\text{A.5a})$$

$$G_u \equiv \sqrt{k_m^2 + (k_y \cos \psi - k_{2z}^0 \sin \psi)^2} \quad (\text{A.5b})$$

$$U_d \equiv \left\{ \frac{\epsilon_{eff2p'}}{\epsilon_{eff2p'} - \epsilon_{eff2s'}} (k_p^2 + k_{2z}^2 - k_2^2) \left[k_p^2 + k_{2z}^2 - k_2^2 \left(1 + \frac{\epsilon_{eff2s'}}{\epsilon_{eff2p'}} \right) \right] \right\}^{\frac{1}{2}} \quad (\text{A.5c})$$

$$U_u \equiv \left\{ \frac{\epsilon_{eff2p'}}{\epsilon_{eff2p'} - \epsilon_{eff2s'}} (k_p^2 + k_{2z}^2 - k_2^2) \left[k_p^2 + k_{2z}^2 - k_2^2 \left(1 + \frac{\epsilon_{eff2s'}}{\epsilon_{eff2p'}} \right) \right] \right\}^{\frac{1}{2}} \quad (\text{A.5d})$$

$$\begin{aligned} D_e &\equiv k_p^2 (k_2^2 k_{1z} - k_1^2 k_{2z}^2) \cos^2 \psi \\ &+ \left[k_2^2 (k_{1z} - k_{2z}^2) (k_m^2 + k_{1z} k_{2z}^2) + k_y^2 k_{2z}^2 (k_2^2 - k_1^2) \right] \sin^2 \psi \\ &+ k_y (k_{1z} + k_{2z}^2) (k_{2z}^2 - k_{2z}^2) (k_p^2 + k_{1z} k_{2z}^2) \cos \psi \sin \psi \quad (\text{A.5e}) \end{aligned}$$

$$\begin{aligned} E_e &\equiv k_p^2 (k_2^2 k_{1z} - k_1^2 k_{2z}^2) \cos^2 \psi \\ &+ \left[k_2^2 (k_{1z} - k_{2z}^2) (k_m^2 - k_{1z} k_{2z}^2) - k_y^2 k_{2z}^2 (k_2^2 - k_1^2) \right] \sin^2 \psi \\ &- k_y (k_{1z} - k_{2z}^2) (k_{2z}^2 + k_{2z}^2) (k_p^2 - k_{1z} k_{2z}^2) \cos \psi \sin \psi \quad (\text{A.5f}) \end{aligned}$$

$$\begin{aligned} I_e &\equiv k_p^2 (k_2^2 k_{1z} - k_1^2 k_{2z}^2) \cos^2 \psi \\ &+ \left[k_2^2 (k_{1z} - k_{2z}^2) (k_m^2 + k_{1z} k_{2z}^2) + k_y^2 k_{2z}^2 (k_2^2 - k_1^2) \right] \sin^2 \psi \\ &+ k_y (k_{1z} + k_{2z}^2) (k_{2z}^2 - k_{2z}^2) (k_p^2 + k_{1z} k_{2z}^2) \cos \psi \sin \psi \quad (\text{A.5g}) \end{aligned}$$

$$\begin{aligned} F_e &\equiv k_p^2 (k_2^2 k_{3z} + k_3^2 k_{2z}^2) \cos^2 \psi \\ &+ \left[k_2^2 (k_{3z} + k_{2z}^2) (k_m^2 + k_{3z} k_{2z}^2) + k_y^2 k_{2z}^2 (k_2^2 - k_3^2) \right] \sin^2 \psi \\ &- k_y (k_{3z} + k_{2z}^2) (k_{2z}^2 + k_{2z}^2) (k_p^2 + k_{3z} k_{2z}^2) \cos \psi \sin \psi \quad (\text{A.5h}) \end{aligned}$$

$$G_e \equiv k_p^2 (k_2^2 k_{3z} + k_3^2 k_{2z}^2) \cos^2 \psi$$

Appendix B

$$\begin{aligned} &+ [k_2^2 (k_{3z} + k_{2z}^2) (k_m^2 - k_{3z} k_{2z}^2) - k_y^2 k_{2z}^2 (k_2^2 - k_3^2)] \sin^2 \psi \\ &+ k_y (k_{3z} - k_{2z}^2) (k_{2z}^2 - k_{2z}^2) (k_p^2 - k_{3z} k_{2z}^2) \cos \psi \sin \psi \quad (\text{A.5i}) \end{aligned}$$

$$\begin{aligned} H_e &\equiv k_p^2 (k_2^2 k_{3z} + k_3^2 k_{2z}^2) \cos^2 \psi \\ &+ [k_2^2 (k_{3z} + k_{2z}^2) (k_m^2 + k_{3z} k_{2z}^2) + k_y^2 k_{2z}^2 (k_2^2 - k_3^2)] \sin^2 \psi \\ &- k_y (k_{3z} + k_{2z}^2) (k_{2z}^2 + k_{2z}^2) (k_p^2 + k_{3z} k_{2z}^2) \cos \psi \sin \psi \quad (\text{A.5j}) \end{aligned}$$

Appendix B: Coefficient $\Psi_{1,\mu}^{ab}$

The coefficients are derived from (88a) for the DGF, (91a) for the mean field, and (102) for their components which are combined to form $\Psi_{1,\mu}^{ab}$ in the manner determined by the first term in (101) and the definition in (104). All the exponential functions have been incorporated into $T_{1,\mu}^{ab}$ and $\Psi_{1,\mu}^{ab}$ are thus composed of D 's, U 's, \hat{h} 's, and \hat{v} 's. For backscattering, D 's and U 's are evaluated at \vec{k}_ρ and \hat{h} 's and \hat{v} 's can be expressed in terms of incident polar angle θ_{0i} and incident azimuthal angle ϕ_{0i} as

$$\hat{h}(k_{1z}^u) = \begin{bmatrix} \sin \phi_{0i} \\ -\cos \phi_{0i} \\ 0 \end{bmatrix}, \quad \hat{v}(k_{1z}^u) = \frac{1}{k_1} \begin{bmatrix} k_{1z} \cos \phi_{0i} \\ k_{1z} \sin \phi_{0i} \\ k_0 \sin \theta_{0i} \end{bmatrix} \quad (\text{B.1a})$$

$$\hat{h}(k_{1z}^d) = \begin{bmatrix} \sin \phi_{0i} \\ -\cos \phi_{0i} \\ 0 \end{bmatrix}, \quad \hat{v}(k_{1z}^d) = \frac{1}{k_1} \begin{bmatrix} -k_{1z} \cos \phi_{0i} \\ -k_{1z} \sin \phi_{0i} \\ k_0 \sin \theta_{0i} \end{bmatrix} \quad (\text{B.1b})$$

$$\hat{h}(k_{1zi}^u) = \begin{bmatrix} -\sin \phi_{0i} \\ \cos \phi_{0i} \\ 0 \end{bmatrix}, \quad \hat{v}(k_{1zi}^u) = \frac{1}{k_1} \begin{bmatrix} -k_{1z} \cos \phi_{0i} \\ -k_{1z} \sin \phi_{0i} \\ k_0 \sin \theta_{0i} \end{bmatrix} \quad (\text{B.1c})$$

$$\hat{h}(k_{1zi}^d) = \begin{bmatrix} -\sin \phi_{0i} \\ \cos \phi_{0i} \\ 0 \end{bmatrix}, \quad \hat{v}(k_{1zi}^d) = \frac{1}{k_1} \begin{bmatrix} k_{1z} \cos \phi_{0i} \\ k_{1z} \sin \phi_{0i} \\ k_0 \sin \theta_{0i} \end{bmatrix} \quad (\text{B.1d})$$

The unit vectors of the polarization bases for the upgoing and downgoing waves are shown in Fig. 1.B.1 to help ease the derivation and illustrate the backscattering processes. As seen from the figure, a and b respectively describe scattered and incident wave types which can be upgoing or downgoing wave constituting the four processes depicted in

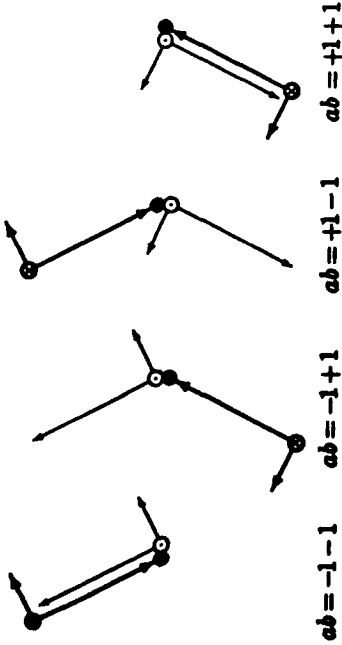


Figure 1.3.1 Polarisation bases for incident (thick lines) and scattered (thin lines) waves: \hat{k} = cross or dot circles, $\hat{\theta}$ = short arrows, \hat{k} = long arrows; black circles are for scatterer.

Fig. 1.3.4. The algebra is straight forward and the results for $\Psi_{1\mu\nu}^{ab}$ can be written as follows:

For h -polarised return due to h -polarised transmission (hh)

$$\Psi_{1hh}^{-1-1} = -D_{1hh}^2(\bar{k}_\mu) - D_{1hv}^2(\bar{k}_\mu) \quad (B.2a)$$

$$\begin{aligned} \Psi_{1hh}^{-1+1} = & -D_{1hh}(\bar{k}_\mu)U_{1hh}(\bar{k}_\mu) \\ & -k_1^{-2}(k_0^2 \sin^2 \theta_{0i} - k_{1z}^2) D_{1hv}(\bar{k}_\mu)U_{1hv}(\bar{k}_\mu) \end{aligned} \quad (B.2b)$$

$$\Psi_{1hh}^{+1-1} = -U_{1hh}(\bar{k}_\mu)D_{1hh}(\bar{k}_\mu) \quad (B.2c)$$

$$\begin{aligned} \Psi_{1hh}^{+1+1} = & -U_{1hh}^2(\bar{k}_\mu) - U_{1hv}^2(\bar{k}_\mu) \\ & -k_1^{-2}(k_0^2 \sin^2 \theta_{0i} - k_{1z}^2) U_{1hv}(\bar{k}_\mu)D_{1hv}(\bar{k}_\mu) \end{aligned} \quad (B.2d)$$

For h -polarised return due to v -polarised transmission (hv)

$$\Psi_{1hv}^{-1-1} = -D_{1hh}(\bar{k}_\mu)D_{1vh}(\bar{k}_\mu) - D_{1hv}(\bar{k}_\mu)D_{1vv}(\bar{k}_\mu) \quad (B.3a)$$

$$\begin{aligned} \Psi_{1hv}^{-1+1} = & -D_{1hh}(\bar{k}_\mu)U_{1vh}(\bar{k}_\mu) \\ & -k_1^{-2}(k_0^2 \sin^2 \theta_{0i} - k_{1z}^2) D_{1hv}(\bar{k}_\mu)U_{1vv}(\bar{k}_\mu) \end{aligned} \quad (B.3b)$$

$$\Psi_{1hv}^{+1-1} = -U_{1hh}(\bar{k}_\mu)D_{1vh}(\bar{k}_\mu) \quad (B.3c)$$

$$\begin{aligned} \Psi_{1hv}^{+1+1} = & -U_{1hh}(\bar{k}_\mu)U_{1vh}(\bar{k}_\mu) - U_{1hv}(\bar{k}_\mu)U_{1vv}(\bar{k}_\mu) \\ & -k_1^{-2}(k_0^2 \sin^2 \theta_{0i} - k_{1z}^2) U_{1hv}(\bar{k}_\mu)D_{1vv}(\bar{k}_\mu) \end{aligned} \quad (B.3d)$$

For v -polarised return due to h -polarised transmission (vh)

$$\Psi_{1vh}^{-1-1} = D_{1vh}(\bar{k}_\mu)D_{1hh}(\bar{k}_\mu) + D_{1vv}(\bar{k}_\mu)D_{1hv}(\bar{k}_\mu) \quad (B.4a)$$

$$\begin{aligned} \Psi_{1vh}^{-1+1} = & D_{1vh}(\bar{k}_\mu)U_{1hh}(\bar{k}_\mu) \\ & + k_1^{-2}(k_0^2 \sin^2 \theta_{0i} - k_{1z}^2) D_{1vv}(\bar{k}_\mu)U_{1hv}(\bar{k}_\mu) \end{aligned} \quad (B.4b)$$

$$\Psi_{1vh}^{+1-1} = U_{1vh}(\bar{k}_\mu)D_{1hh}(\bar{k}_\mu) \quad (B.4c)$$

$$\begin{aligned} \Psi_{1vh}^{+1+1} = & U_{1vh}(\bar{k}_\mu)U_{1hh}(\bar{k}_\mu) + U_{1vv}(\bar{k}_\mu)U_{1hv}(\bar{k}_\mu) \\ & + k_1^{-2}(k_0^2 \sin^2 \theta_{0i} - k_{1z}^2) U_{1vv}(\bar{k}_\mu)D_{1hv}(\bar{k}_\mu) \end{aligned} \quad (B.4d)$$

For v -polarised return due to v -polarised transmission (vv)

$$\Psi_{1vv}^{-1-1} = D_{1vh}^2(\bar{k}_\mu) + D_{1vv}^2(\bar{k}_\mu) \quad (B.5a)$$

$$\begin{aligned} \Psi_{1vv}^{-1+1} = & D_{1vh}(\bar{k}_\mu)U_{1vh}(\bar{k}_\mu) \\ & + k_1^{-2}(k_0^2 \sin^2 \theta_{0i} - k_{1z}^2) D_{1vv}(\bar{k}_\mu)U_{1vv}(\bar{k}_\mu) \end{aligned} \quad (B.5b)$$

$$\Psi_{1vv}^{+1-1} = U_{1vh}(\bar{k}_\mu)D_{1vh}(\bar{k}_\mu) \quad (B.5c)$$

$$\begin{aligned} \Psi_{1vv}^{+1+1} = & U_{1vh}^2(\bar{k}_\mu) + U_{1vv}^2(\bar{k}_\mu) \\ & + k_1^{-2}(k_0^2 \sin^2 \theta_{0i} - k_{1z}^2) U_{1vv}(\bar{k}_\mu)D_{1vv}(\bar{k}_\mu) \end{aligned} \quad (B.5d)$$

With $k_i^2 = k_0^2 \sin^2 \theta_{0i} + k_{1z}^2$ and the definitions of $W^{(+1)} = U$ and $W^{(-1)} = D$, all of the above expressions for Ψ 's can be summarized as

$$\begin{aligned} \Psi_{1\mu\nu}^{ab} = & \pm W_{\mu h}^{(a)}(\bar{k}_\mu)W_{\nu h}^{(b)}(\bar{k}_\mu) \\ & \pm k_1^{-2}(k_0^2 \sin^2 \theta_{0i} + abk_{1z}^2) W_{\mu v}^{(a)}(\bar{k}_\mu)W_{\nu v}^{(b)}(\bar{k}_\mu) \end{aligned} \quad (B.6)$$

where the minus signs are for $\mu = h$ and the plus signs are for $\mu = v$.

Appendix C: Coefficients $\Psi_{2\mu\nu,jh}^{pq}$

The coefficients are derived from (102), (88b), and (91b) for the components of the DGF and the mean field which are combined according to the second term in (101) and the definition in (105) to form $\Psi_{2\mu\nu,jh}^{pq}$. The results for the coefficients can be expressed as follows:

For the h -polarised return due to the h -polarised transmission (hh)

$$\Psi_{2hh,jh}^{qu} = D_{2ho}(-\bar{k}_p)U_{2ho}(\bar{k}_\mu)o_j(k_{2z}^{qu})o_h(k_{2z}^{qu}) \quad (C.1)$$

$$\Psi_{2hh,jh}^{qu} = D_{2ho}(-\bar{k}_p)D_{2ho}(\bar{k}_\mu)o_j(k_{2z}^{qu})o_h(k_{2z}^{qu}) \quad (C.2)$$

$$\Psi_{2\alpha_1 j k}^{ou ou} = -D_{2\alpha_1}(-\bar{k}_p)U_{2\alpha_1}(\bar{k}_p)o_j(k_{2z}^{ou})e_k(k_{2z}^{ou}) \quad (C.51)$$

$$\Psi_{2\alpha_1 j k}^{ou od} = -D_{2\alpha_1}(-\bar{k}_p)D_{2\alpha_1}(\bar{k}_p)o_j(k_{2z}^{ou})e_k(k_{2z}^{od}) \quad (C.52)$$

$$\Psi_{2\alpha_1 j k}^{od ou} = -U_{2\alpha_1}(-\bar{k}_p)U_{2\alpha_1}(\bar{k}_p)o_j(k_{2z}^{od})o_k(k_{2z}^{ou}) \quad (C.53)$$

$$\Psi_{2\alpha_1 j k}^{od od} = -U_{2\alpha_1}(-\bar{k}_p)D_{2\alpha_1}(\bar{k}_p)o_j(k_{2z}^{od})o_k(k_{2z}^{od}) \quad (C.54)$$

$$\Psi_{2\alpha_1 j k}^{ou ou} = -U_{2\alpha_1}(-\bar{k}_p)U_{2\alpha_1}(\bar{k}_p)o_j(k_{2z}^{ou})e_k(k_{2z}^{ou}) \quad (C.55)$$

$$\Psi_{2\alpha_1 j k}^{od od} = -U_{2\alpha_1}(-\bar{k}_p)D_{2\alpha_1}(\bar{k}_p)o_j(k_{2z}^{od})e_k(k_{2z}^{od}) \quad (C.56)$$

$$\Psi_{2\alpha_1 j k}^{ou ou} = D_{2\alpha_1}(-\bar{k}_p)U_{2\alpha_1}(\bar{k}_p)e_j(k_{2z}^{ou})o_k(k_{2z}^{ou}) \quad (C.57)$$

$$\Psi_{2\alpha_1 j k}^{ou od} = D_{2\alpha_1}(-\bar{k}_p)D_{2\alpha_1}(\bar{k}_p)e_j(k_{2z}^{ou})o_k(k_{2z}^{od}) \quad (C.58)$$

$$\Psi_{2\alpha_1 j k}^{ou ou} = D_{2\alpha_1}(-\bar{k}_p)U_{2\alpha_1}(\bar{k}_p)e_j(k_{2z}^{ou})e_k(k_{2z}^{ou}) \quad (C.59)$$

$$\Psi_{2\alpha_1 j k}^{ou od} = D_{2\alpha_1}(-\bar{k}_p)D_{2\alpha_1}(\bar{k}_p)e_j(k_{2z}^{ou})e_k(k_{2z}^{od}) \quad (C.60)$$

$$\Psi_{2\alpha_1 j k}^{od ou} = U_{2\alpha_1}(-\bar{k}_p)U_{2\alpha_1}(\bar{k}_p)e_j(k_{2z}^{od})o_k(k_{2z}^{ou}) \quad (C.61)$$

$$\Psi_{2\alpha_1 j k}^{od od} = U_{2\alpha_1}(-\bar{k}_p)D_{2\alpha_1}(\bar{k}_p)e_j(k_{2z}^{od})o_k(k_{2z}^{od}) \quad (C.62)$$

$$\Psi_{2\alpha_1 j k}^{od ou} = U_{2\alpha_1}(-\bar{k}_p)U_{2\alpha_1}(\bar{k}_p)e_j(k_{2z}^{od})e_k(k_{2z}^{ou}) \quad (C.63)$$

$$\Psi_{2\alpha_1 j k}^{od od} = U_{2\alpha_1}(-\bar{k}_p)D_{2\alpha_1}(\bar{k}_p)e_j(k_{2z}^{od})e_k(k_{2z}^{od}) \quad (C.64)$$

where o_j (or o_k) and e_j (or e_k) are the $j, k = x, y, z$ components of unit vector \hat{o} and \hat{e} defined in section 1.3c. For backscattering, $\bar{k}_p = -\bar{k}_p$ and $o_j(k_{2z}^{ou}), o_j(k_{2z}^{od}), e_j(k_{2z}^{ou})$, and $e_j(k_{2z}^{od})$ are evaluated for the backscattered waves similarly to the procedure in appendix B.

Appendix D: Integrations of T_1^{od} and T_2^{ou}

a. Integrations of T_1^{od}

The integrations over z_1 and z_1^0 in (103a) are carried out to give

$$T_1^{od} = \int_{-\infty}^{\infty} d\beta_z \Phi_1(2\bar{k}_p, \beta_z) \cdot \frac{1 - e^{i(\beta_z - \kappa_{ab})d_1}}{\beta_z - \kappa_{ab}} \cdot \frac{1 - e^{-i(\beta_z - \kappa_{cd})d_1}}{\beta_z - \kappa_{cd}} \quad (D.1)$$

Using (93) and (43b) for the isotropic correlation functions in (D.1) yields

$$T_1^{od} = \delta_1 \ell_1^2 \pi^{-2} (\mathcal{A}_1 + \mathcal{B}_1) \quad (D.2)$$

Appendix D

where \mathcal{A}_1 and \mathcal{B}_1 are integrals over β_z defined as

$$\mathcal{A}_1 = \int_{-\infty}^{\infty} d\beta_z \frac{1 - e^{i(\beta_z - \kappa_{ab})d_1} + e^{i(\kappa_{cd} - \kappa_{ab})d_1}}{(\beta_z^2 \ell_1^2 + 1 + 4k_p^2 \ell_1^2)^2 (\beta_z - \kappa_{ab})(\beta_z - \kappa_{cd})} \quad (D.3)$$

$$\mathcal{B}_1 = \int_{-\infty}^{\infty} d\beta_z \frac{-e^{-i(\beta_z - \kappa_{cd})d_1}}{(\beta_z^2 \ell_1^2 + 1 + 4k_p^2 \ell_1^2)^2 (\beta_z - \kappa_{ab})(\beta_z - \kappa_{cd})} \quad (D.4)$$

The integrations over β_z in (D.3) and (D.4) are carried out with the contour integration method. For \mathcal{A}_1 , the imaginary part of β_z has to be positive for the integral to converge. Thus, \mathcal{A}_1 can be taken as the integral along the positively oriented contour composed of the real β_z axis and the infinite semi-circle on the upper half of the complex β_z plane and centered at origin $\beta_z = 0$. Note that the integral over the semi-circle vanishes on account of Jordan's lemma. The chosen contour encloses simple poles at $\beta_z = \kappa_{ab}, \kappa_{cd}$ (if the imaginary parts of the simple poles are positive) and a double pole at $\beta_z = \kappa_1 = i\ell^{-1} \sqrt{1 + 4k_p^2 \ell_1^2}$. Integral \mathcal{A}_1 is therefore composed of the residue contribution from the enclosed poles. According to the residue theorem, the result for \mathcal{A}_1 is

$$\begin{aligned} \mathcal{A}_1 = 2\pi i \left\{ \frac{e^{i(\kappa_{cd} - \kappa_{ab})d_1}}{(\kappa_{ab}^2 \ell_1^2 + 1 + 4k_p^2 \ell_1^2)^2 (\kappa_{ab} - \kappa_{cd})} \right. & \quad (\text{if } \text{Im} \kappa_{ab} > 0) \\ + \frac{1}{(\kappa_{cd}^2 \ell_1^2 + 1 + 4k_p^2 \ell_1^2)^2 (\kappa_{cd} - \kappa_{ab})} & \quad (\text{if } \text{Im} \kappa_{cd} > 0) \\ - \frac{id_1 e^{i(\kappa_1 - \kappa_{ab})d_1}}{\ell_1^4 (\kappa_1 - \kappa_{ab})^2 (\kappa_1 - \kappa_{ab})(\kappa_1 - \kappa_{cd})} \\ - \frac{1 - e^{i(\kappa_1 - \kappa_{ab})d_1} + e^{i(\kappa_{cd} - \kappa_{ab})d_1}}{\ell_1^4 (\kappa_1 - \kappa_{ab})^2 (\kappa_1 - \kappa_{ab})(\kappa_1 - \kappa_{cd})} \\ \left. \cdot \left[\frac{2}{\kappa_1 - \kappa_1^*} + \frac{1}{\kappa_1 - \kappa_{ab}} + \frac{1}{\kappa_1 - \kappa_{cd}} \right] \right\} & \quad (D.5) \end{aligned}$$

For \mathcal{B}_1 , the same contour integration method is used except that the infinite semi-circle is in the lower half of the complex β_z plane for convergence of the integral. The integration contour is now negatively oriented along the real β_z axis and the lower semi-circle enclosing simple poles at $\beta_z = \kappa_{ab}, \kappa_{cd}$ (if the imaginary parts of the simple

poles are negative) and a double pole at $\beta_z = \kappa_1^* = -i\ell^{-1}\sqrt{1+4k^2\ell_1^2}$. The result for B_1 is

$$B_1 = 2\pi i \left\{ \frac{e^{i(\kappa_{cd}-\kappa_{ab})d_1}}{(\kappa_{ab}^2\ell_1^2 + 1 + 4k^2\ell_1^2)^2(\kappa_{ab} - \kappa_{cd})} \quad (\text{if } \text{Im}\kappa_{ab} < 0) \right. \\ + \frac{1}{(\kappa_{ab}^2\ell_1^2 + 1 + 4k^2\ell_1^2)^2(\kappa_{cd} - \kappa_{ab})} \quad (\text{if } \text{Im}\kappa_{cd} < 0) \\ - \frac{id_1 e^{-i(\kappa_1^* - \kappa_{cd})d_1}}{\ell_1^2(\kappa_1^* - \kappa_1)^2(\kappa_1^* - \kappa_{ab})(\kappa_1^* - \kappa_{cd})} \\ - \left. \frac{e^{-i(\kappa_1^* - \kappa_{cd})d_1}}{\ell_1^2(\kappa_1^* - \kappa_1)^2(\kappa_1^* - \kappa_{ab})(\kappa_1^* - \kappa_{cd})} \cdot \left[\frac{2}{\kappa_1^* - \kappa_1} + \frac{1}{\kappa_1^* - \kappa_{ab}} + \frac{1}{\kappa_1^* - \kappa_{cd}} \right] \right\} \quad (\text{D.6})$$

Substituting (D.6) and (D.5) in (D.4) yields T_{2jlm}^{ppr} which is rearranged to obtaining the result in (105) for the isotropic random medium.

b. Integrations of T_{2jlm}^{ppr}

The integrations over z_2 and z_2^* in (103a) are carried out to give

$$T_{2jlm}^{\text{ppr}} = \int_{-\infty}^{\infty} d\beta_z \tilde{S}_{2jlm}(2\bar{k}_{\mu i}, \beta_z) \cdot \frac{e^{i(\beta_z - \kappa_{\tau\tau})d_1} - e^{i(\beta_z - \kappa_{\tau\tau})d_2}}{\beta_z - \kappa_{\tau\tau}} \cdot \frac{e^{-i(\beta_z - \kappa_{\tau\tau})d_1} - e^{-i(\beta_z - \kappa_{\tau\tau})d_2}}{\beta_z - \kappa_{\tau\tau}} \quad (\text{D.7})$$

Using (99), (98), and (58b) for the anisotropic correlation functions in (D.7) yields

$$T_{2jlm}^{\text{ppr}} = \delta_{2jlm} \ell_{2\mu}^2 \ell_{2\nu}^2 \pi^{-2} (A_2 + B_2) \quad (\text{D.8})$$

where integral A_2 and B_2 are defined as

$$A_2 = \int_{-\infty}^{\infty} d\beta_z \frac{e^{i(\kappa_{\tau\tau} - \kappa_{\tau\tau})d_1} - e^{i(\kappa_{\tau\tau} d_1 - \kappa_{\tau\tau} d_2)} e^{i(d_2 - d_1)\beta_z} + e^{i(\kappa_{\tau\tau} - \kappa_{\tau\tau})d_2}}{D^2(2\bar{k}_{\mu i}, \beta_z)(\beta_z - \kappa_{\tau\tau})(\beta_z - \kappa_{\tau\tau})} \quad (\text{D.9})$$

$$B_2 = \int_{-\infty}^{\infty} d\beta_z \frac{-e^{i(\kappa_{\tau\tau} d_2 - \kappa_{\tau\tau} d_1)} e^{-i(d_2 - d_1)\beta_z}}{D^2(2\bar{k}_{\mu i}, \beta_z)(\beta_z - \kappa_{\tau\tau})(\beta_z - \kappa_{\tau\tau})} \quad (\text{D.10})$$

References

69

In (D.9) and (D.10), $D(2\bar{k}_{\mu i}, \beta_z)$ is a quadratic expression in β_z given by

$$D(2\bar{k}_{\mu i}, \beta_z) = \ell_{2\mu}^2 \beta_z^2 + 2k_{\mu i}(\ell_{2\mu}^2 - \ell_{2\nu}^2) \sin(2\psi) \beta_z + \left[1 + 4k_{\mu i}^2 \ell_{2\mu}^2 + 4k_{\mu i}^2 (\ell_{2\mu}^2 \cos^2 \psi + \ell_{2\nu}^2 \sin^2 \psi) \right] \quad (\text{D.11})$$

with $\ell_{2\mu}^2 = \ell_{2\mu}^2 \sin^2 \psi + \ell_{2\nu}^2 \cos^2 \psi$. The integrations over β_z in (D.9) and (D.10) are carried out with the contour integration method as in the last section of this appendix. In consideration of the convergence, the contour for A_2 is taken to be positively oriented along the real β_z axis and the upper infinite semi-circle and that for B_2 is negatively oriented along the real β_z axis and the lower infinite semi-circle. Integral T_{2jlm}^{ppr} is thus composed of the contribution from the residues of two simple poles at $\beta_z = \kappa_{\tau\tau}$, $\kappa_{\tau\tau}$, and two double poles corresponding to the two zeros of quadratic equation $D(2\bar{k}_{\mu i}, \beta_z) = 0$ at $\beta_z = \kappa_2$, κ_2^* for $\kappa_2 = \ell_{2\mu}^{-2} \left[-k_{\mu i}(\ell_{2\mu}^2 - \ell_{2\nu}^2) \sin(2\psi) + i\sqrt{(1+4k_{\mu i}^2 \ell_{2\mu}^2) \ell_{2\mu}^2 + 4k_{\mu i}^2 \ell_{2\nu}^2 \ell_{2\mu}^2} \right]$. The residue theorem then gives the result in (107) for the anisotropic random medium. Note that the anisotropic result approaches the isotropic result in the limits of $\ell_{2\mu} \rightarrow \ell_{2\nu}$ and $d_1 \rightarrow 0$.

Acknowledgments

This work was supported by the NASA Contract 958461, the ARO Contract DAAL03-88-J-0057, the ARMY Corp of Engineers Contract DACA39-87-K-0022, the NASA Contract NAGW-1617, and the ONR Contract N00014-89-J-1107.

References

- [1] Stokes, G., "On the Composition and Resolution of Streams of Polarized Light from Different Sources," *Proceedings of the Cambridge Philosophical Society*, 1, 140-147, 1852.
- [2] Rayleigh, Lord, *Scientific Papers by Lord Rayleigh*, III, Dover Publications, New York, 1964.

- [3] Poincaré, H., *Théorie Mathématique de la Lumière*, 2, Paris, 1892.
- [4] Mueller, H., "The Foundation of Optics," *Journal of the Optical Society of America*, 38, 661, 1948.
- [5] Jones, R. C., "A New Calculus for the Treatment of Optical systems—Part I. Description and Discussion of the Calculus," *Journal of the Optical Society of America*, 31, 488–493, 1941.
- [6] van de Hulst, H. C., *Light Scattering by Small Particles*, Dover Publications, New York, 1981.
- [7] Ishimaru, A., *Wave Propagation in Random Media*, 1–2, Academic Press, New York, 1978.
- [8] Kong, J. A., A. A. Swartz, H. A. Yueh, L. M. Novak, and R. T. Shin, "Identification of Terrain cover Using the Optimum Polarimetric Classifier," *Journal of Electromagnetic Waves and Applications*, 2, 171–194, 1987.
- [9] Born, M., and E. Wolf, *Principle of Optics*, Pergamon Press, New York, 1980.
- [10] Chandrasekhar, S., *Radiative Transfer*, Dover Publications, New York, 1960.
- [11] Deirmendjian, D., *Electromagnetic Scattering on Spherical Polydispersions*, American Elsevier, New York, 1969.
- [12] Kennaugh, E. M., "Effects of the type of polarisation on echo characteristics," Report 389-9, Antenna Lab., Ohio State University, 1951.
- [13] Rumsey, V. H., "Part I—Transmission between Elliptically Polarized Antennas," *Proc. I.R.E.*, 39, 535–540, 1951.
- [14] Deschamps, G. A., "Part II—Geometrical Representation of the Polarisation of a Plane Electromagnetic Wave," *Proc. I.R.E.*, 39, 540–544, 1951.
- [15] Walker, M. J., "Matrix Calculus and the Stokes Parameters of Polarized Radiation," *American Journal of Physics*, 22, 170–174, 1954.
- [16] Deschamps, G. A., and P. E. Mast, "Poincaré Sphere Representation of Partially Polarized Fields," *IEEE Trans. Antennas Propag.*, AP-21, 1973.

- [17] Huynen, J. R., "Phenomenological Theory of Radar Targets," in *Electromagnetic Scattering*, edited by P. L. E. Uslenghi, Academic Press, New York, 1978.
- [18] Hauge, P. S., "Mueller Matrix Ellipsometry with Imperfect Compensator," *Journal of the Optical Society of America*, 68, 1519–1528, 1978.
- [19] Ioannidis, G. A., and D. E. Hammers, "Optimum Antenna Polarizations for Target Discrimination in Clutter," *IEEE Trans. Antennas Propag.*, AP-27, 357–363, 1979.
- [20] Kostinski, A. B., and W.-M. Boerner, "On Foundations of Radar Polarimetry," *IEEE Trans. Antennas Propag.*, AP-34, 1986.
- [21] Kim, K., L. Mandel, and E. Wolf, "Relationship between Jones and Mueller Matrices for Random Media," *Journal of the Optical Society of America A*, 4, 433–437, 1987.
- [22] van Zyl, J. J., H. A. Zebker, and C. Elachi, "Imaging Radar Polarization Signatures: Theory and Observation," *Radio Science*, 22, 529–543, 1987.
- [23] Kong, J. A., *Electromagnetic Wave Theory*, Wiley-Interscience, New York, 1986.
- [24] Tsang, L., J. A. Kong, and R. T. Shin, *Theory of Microwave Remote Sensing*, Wiley-Interscience, New York, 1985.
- [25] Tatarskii, V. I., *Wave Propagation in a Turbulent Medium*, McGraw-Hill, New York, 1961.
- [26] Tatarskii, V. I., *The Effects of Turbulent Atmosphere on Wave Propagation*, U.S. Department of Commerce, National Technical Information Service, Springfield, Virginia, 1971.
- [27] Keller, J. B., "Wave Propagation in Random Media," *Proceedings of Symposia in Applied Mathematics, American Mathematical Society*, 13, 227–246, 1962.
- [28] Frisch, U., "Wave Propagation in Random Medium," in *Probabilistic Methods in Applied Mathematics*, edited by A. T. Bharucha-Reid, 1, 75–198, Academic, New York, 1968.
- [29] Stogryn, A., "Electromagnetic Scattering by Random Dielectric Constant Fluctuations in a Bounded Medium," *Radio Science*, 9, 509–518, 1974.

- [30] Tsang, L., and J. A. Kong, "Microwave Remote Sensing of a Two-Layer Random Medium," *IEEE Trans. Antennas Propagat.*, AP-24, 283-287, 1976.
- [31] Fung, A. K., and H. S. Fung, "Application of First Order Renormalisation Method to Scattering from a Vegetation-like Half Space," *IEEE Transactions on Geoscience Electronics*, GE-15, 189-195, 1977.
- [32] Zuniga, M. A., T. M. Habashy, and J. A. Kong, "Active Remote Sensing of Layered Random Media," *IEEE Transactions on Geoscience Electronics*, GE-17, 296-302, 1979.
- [33] Zuniga, M. A., J. A. Kong, and L. Tsang, "Depolarization Effects in the Active Remote Sensing of Random Media," *Journal of Applied Physics*, 51, 2315-2325, 1980.
- [34] Vallese, F., and J. A. Kong, "Correlation Function Studies for Snow and Ice," *Journal of Applied Physics*, 52, 4921-4925, 1981.
- [35] Lang, R. H., "Electromagnetic Backscattering from a Sparse Distribution of Lossy Dielectric Scatterers," *Radio Science*, 16, 25-30, 1981.
- [36] Lee, J. K., and J. A. Kong, "Dyadic Greens' Functions for Layered Anisotropic Medium," *Electromagnetics*, 3, 111-130, 1983.
- [37] Lee, J. K., and J. A. Kong, "Active Microwave Remote Sensing of an Anisotropic Random Medium Layer," *IEEE Transactions on Geoscience and Remote Sensing*, GE-23, 910-923, 1985.
- [38] Lee, J. K., and J. A. Kong, "Passive Microwave Remote Sensing of an Anisotropic Random Medium Layer," *IEEE Transactions on Geoscience and Remote Sensing*, GE-23, 924-932, 1985.
- [39] Tsang, L., and J. A. Kong, "Application of Strong Fluctuation Random Medium Theory to Scattering from Vegetation-like Half Space," *IEEE Transactions on Geoscience and Remote Sensing*, GE-19, 62-69, 1981.
- [40] Tsang, L., and J. A. Kong, "Scattering of Electromagnetic Waves from Random Media with Strong Permittivity Fluctuations," *Radio Science*, 16, 303-320, 1981.
- [41] Tsang, L., J. A. Kong, and R. W. Newton, "Application of Strong Fluctuation Random Medium Theory to Scattering of Electro-

- magnetic Waves from a Half-Space of Dielectric Mixture," *IEEE Trans. Antennas Propagat.*, AP-30, 292-302, 1982.
- [42] Stogryn, A., "A Note on the Singular Part of the Dyadic Green's Function in Strong Fluctuation Theory," *Radio Science*, 18, 1283-1286, 1983.
- [43] Borgeaud, M., R. T. Shin, and J. A. Kong, "Theoretical Models for Polarimetric Radar Clutter," *Journal of Electromagnetics Waves and Applications*, 1, 73-89, 1987.
- [44] Borgeaud, M., S. V. Nghiem, R. T. Shin, and J. A. Kong, "Theoretical Models for Polarimetric Microwave Remote Sensing of Earth Terrain," *Journal of Electromagnetic Waves and Applications*, 3, 61-81, 1989.
- [45] Borgeaud, M., J. A. Kong, R. T. Shin, and S. V. Nghiem, "Theoretical Models for Polarimetric Microwave Remote Sensing of Earth Terrain," *Proceedings of the 1988 NATO Advanced Research Workshop*, Nuremberg, F. R. Germany, September, 1988.

Office of Naval Research

DISTRIBUTION LIST

| | |
|---|----------|
| <u>Charles A. Luther</u> Code: 1121 R5 Office of Naval Research 800 North Quincy Street Arlington, VA 22217 | 3 copies |
| Administrative Contracting Officer E19-628 Massachusetts Institute of Technology Cambridge, MA 02139 | 1 copy |
| Director Naval Research Laboratory Washington, DC 20375 Attn: Code 2627 | 6 copies |
| Defense Technical Information Center Bldg. 5, Cameron Station Alexandria, VA 22314 | 2 copies |